A Moving-Trap Zeeman Decelerator

ARIN MIZOURI

MIZOURI, ARIN (2016) A Moving-Trap Zeeman Decelerator. Doctoral thesis, Durham University.

A Moving-Trap Zeeman Decelerator

Arin Mizouri

A thesis submitted in partial fulfilment
of the requirements for the degree of
Doctor of Philosophy

Department of Physics
Durham University

December 2, 2016

Abstract

This thesis reports on the design, construction and implementation of a moving-trap Zeeman decelerator which uses 3D magnetic traps to guide and decelerate paramagnetic particles from a supersonic beam. The decelerator will ultimately be used in a quantum simulator device, where a system of strongly-interacting quantum particles, where their interactions can be tuned, is formed using polar molecules. The decelerator is a potential loading stage for a molecular magneto-optical trap (MOT), where high densities of molecules can be cooled down to the sub milliKelvin temperatures. The molecules can then be further cooled sympathetically with laser-cooled atoms into the microKelvin regime, allowing their trapping in an optical lattice.

This thesis mainly describes the design, construction, and implementation of the decelerator. The technicalities of the beam machine, the decelerator coils, and the driving electronics are described in detail. A homebuilt fast-ionisation gauge (FIG) detector allows the characterisation and optimisation of pulsed beams produced by a cryogenically cooled pulsed valve. We produce supersonic beams of metastable argon atoms (Ar*), made by the electronic excitation of the atoms using a homebuilt pulsed electric discharge assembly, stabilised by a hot filament. This enables the discharge to operate more stably at voltages as low as 400 V and at discharge pulse durations as short as 20 μs, which combine to create a cold packet of Ar* atoms. An optimised slow beam of Ar* with a measured velocity of 306±8 m/s and a translational temperature of 4 K is formed. The decelerator has a detection chamber that allows different means of detecting atoms and molecules: michrochannel-plate (MCP), single-pass laser-induced fluorescence (LIF), cavity-enhanced laser-induced fluorescence (CELIF), and a quadrupole mass spectrometer (QMS) with the ability to photo-ionise. We demonstrate that the CELIF detection technique, which combines a cavity ring-down (CRD) setup and a LIF setup, using a standard UV pulsed dye laser, can be an effective detection method for molecules with fluorescence lifetimes on the order of hundreds of nanoseconds. Using CELIF, we measure the absolute density of SD radicals in a pulsed supersonic jet down to the limit-of-detection of 10^5 cm^{-3}. In the 0.002 cm^3 probe volume, this corresponds to *ca.* 200 molecules, and the quantum-noise-limited absorption coefficient is $\alpha_{\min} = 7.9 \times 10^{-11}$ cm^{-1} in 200 s of acquisition time.

The biggest advantage of this type of decelerator is in the fact that the paramagnetic atoms are confined in all three dimensions continuously throughout the length of the decelerator. We present our proof-of-principle experimental results where we demonstrate, using a single deceleration stage with a length of 123 mm, the manipulation of Ar* atoms in the $^3P_2$ metastable state using 3D magnetic fields, and using continuously modulated magnetic fields which produce a travelling potential. It is successfully shown that the Ar* signal intensity is greatly increased, nearly by a factor two by using a 290 mm long quadrupole magnetic guide which provides transverse confinement of the atoms. With the addition of the decelerator coils, magnetic confinement along the longitudinal beam axis is achieved, forming 3D-traps. The 3D-guiding of the low-field-seeking states of $^3P_2$ state of Ar* is carried out at constant velocities ranging from 320 m/s up to 400 m/s along a single decelerator module. The longitudinal temperatures were ∼500 mK. While attempting the deceleration of the traps, though no real deceleration was observed for this short decelerator length, the fields did show a manipulation effect. This gives us the confidence that with a longer decelerator, we will see very prominent bunching.

The work presented in this thesis is a major step forward in the demonstration of an efficient Zeeman decelerator which can bring large numbers of molecules to low velocities. It will be an ideal loading step for a molecular MOT where high densities of molecules can be cooled down to the sub milliKelvin temperatures. A beam of CaF molecules from a buffer gas source, starting at an initial velocity of 150 m/s, could be decelerate to a standstill using a 1 m long decelerator. This would only require eight decelerator modules. Aside from its use as a loading step for a molecular MOT, for building a quantum simulator device, this new type of decelerator can be used for various applications. One of these is in cold chemistry. The methyl radical is one of the most important and fundamental intermediates in chemical reactions. With regards to magnetic deceleration, the methyl radical has a similar magnetic-moment-to-mass ratio to argon, so with an appropriate choice of a seed gas we should be able reproduce the results we have so far with argon and demonstrate deceleration of our first molecule.

Declaration

I confirm that no part of the material offered has previously been submitted by myself for a degree in this or any other University. Where material has been generated through joint work, the work of others has been indicated.

Arin Mizouri
Durham, December 2, 2016

To my parents, sisters, and brother.

Acknowledgements

The four year journey which has led to this thesis involved many people. Hereby, I would like to take this chance to thank those who have contributed to the success of this project. First and foremost, I would like to express my gratitude to my supervisor, David Carty for his guidance and support throughout my PhD. I was lucky to come across someone who could see my strengths as an independent researcher and ignore my weaknesses as a student that couldn't fit in well in an education system that measured people's intellectual ability with timed examinations. David gave me the chance to pursue my passion, and in doing so, literally helped make one of my dreams come true. It has been a pleasure having him as my supervisor.

I am particularly thankful to Lewis McArd. To put it simply, he was the superman of the project. Without his impressive hard work on the electronics and simulations, we would not have gotten far in the time given. Anyone would be lucky to have him in their group. The two post-doc researchers who worked on the decelerator project in the duration of my PhD were Ulrich Krohn and Vijay Sing. I thank Ulrich for his genius which helped push the project forward and for writing the Monte-Carlo simulations code. He also started off the work on the electronics. I thank Vijay for his contributions in building the experiment and for taking some of the measurements while I was writing my thesis. Many thanks also go to the project students who helped tighten flanges and assisted me in the lab (Katherine, Ingeborg, Dominic). Last but not least, I thank everyone in the AtMol group who made my four years fruitful and enjoyable.

The CELIF chapter plays a big part in my thesis. For this I would like to thank Eckart Wrede, Dennis Deng, Hendrick Nahler and Jack Eardley. Though Eckart Wrede wasn't officially my supervisor, he was acting as a supervisor for a big part of my PhD. I have learned a lot from him and his enthusiastic approach to every challenging situation. It was a pleasure to work alongside his post-doc, Dennis during the CELIF measurements. He taught me plenty, not only on the technical side, but also from his philosophical ideas. I also thank our summer student, Jack Eardley for making some of the CELIF measurements. Lastly, I want to thank Jan Verlet and his group in chemistry, for letting me steal vacuum parts and gas line fittings from their prep room.

Having built an experiment from scratch, I depended on the mechanical workshop for the majority of my PhD. I am grateful to Paul White for most of the parts that were built for the experiment. I also thank everyone else in the Mechanical workshop in the Physics department, for machining the many parts which make up the decelerator. Specials thanks also go to Lee Mcalpine and Neil Holmes from the Chemistry mechanical workshop. The work done by the electronics workshops of both the chemistry and the physics departments was invaluable to the project. The decelerator would not have existed without the electronics, and so I would like to express my sincere gratitude to John Scott and Duncan Kennedy. I would also like to thank Kelvin Appleby for his contributions to the development of the decelerator source. Last but not least, I would like to thank Barry Moss who designed the decelerator electronics circuit.

It took a lot of moral support to get through these four years, and for this I would now like to thank all of my friends who supported me through these challenging years. I must first thank Manfred, one of my best friends who has supported me since my first year at Durham, both as a class mate and a friend. Thanks for helping me solve all of those nasty integrals and my personal ‘problems’. Next, I want to thank Latifa for always being there for me in the last eighteen years to help me through the most stressful times. I also thank all my other close friends in Durham who supported me in their own special ways and helped me get through this challenging journey, including: Sam, Natalie, Nada, Milda, Reem, Eszter, Tatiana, Sherihan, Semra, Rania and Olga. Last but not least, I thank my most encouraging and supportive study buddy, Demet, who shared with me my joy and pain through the journey.

My biggest gratitude goes to my family. Without them I wouldn’t have been exactly where I want to be at this point in my life. My parents sacrificed a lot to give their children a better life. We have all come very far, both literally and metaphorically. I am forever grateful for all of their unconditional love and support. Thank you mum, dad, Helin, Nalin, Oscar, and Alan.

Contents

Page

List of Tables

Page

List of Figures

Page

Chapter 1

A General Introduction

Our moving-trap Zeeman decelerator project is part of a programme entitled "MicroKelvin Molecules in a Quantum Array" (MMQA) where a common goal of building a device called a quantum simulator is shared by the research groups of Ed Hinds, Mike Tarbutt, Jeremy Hutson, Simon Cornish, Eckart Wrede and David Carty. This chapter starts by introducing the field of cold molecules, followed by the MMQA programme where we lay out the route recognised by the programme towards the production of ultracold molecules. There are a variety of methods of cooling molecules using different means. One method is Zeeman deceleration which uses inhomogeneous magnetic fields to slow down paramagnetic species. In this chapter, we will carefully examine the "conventional" Zeeman decelerator, a pulsed-type decelerator, highlighting its main features in order to understand its limitations on the deceleration efficiency. Finally, we will present a new approach that we are taking which promises to solve this by using real 3D moving traps. These confine the molecules in all dimensions throughout the deceleration time.

1.1 Making Molecules Cold

The laser cooling of atoms was developed in the 1980's, [1] opening various avenues to explore fascinating physics in the ultra-cold regime including atomic clocks, [2] different quantum phases of matter such as the Mott insulator, [3] and Bose-Einstein condensates (BEC), [4] amongst various other applications. The impact of producing ultracold molecules is expected to be as large and profound as that made by the work achieved with ultracold atoms. [5,6] Furthermore, unlike atoms, molecules offer rotational and vibrational degrees of freedom in addition to the translational ones, giving them unique properties which may enable the study of new physical phenomena and lead to exciting new discoveries. These degrees of freedom provide additional tuneable experimental parameters. Furthermore, polar molecules have large permanent electric-dipole moments arising from the non-spherical symmetry, which provide long-range strong dipole-dipole interactions, a feature which is vital in the building of a quantum-simulator device.

Although there is no definite definition of ‘cold’ and ‘ultracold’ temperatures, in this research field, ‘cold’ molecules are commonly placed in the temperature range 1 mK-1 K and ‘ultracold’ molecules $<$1 mK. These classifications are defined as such to distinguish different temperature regimes where interesting physical phenomena emerge, and where the molecules can be manipulated by external fields. It is important to note here that this refers to the translational temperature. Statistical thermodynamics teaches that temperature is a parameter which determines the distribution of the molecules in a system over the available energy levels. The translational temperature for a gas is a parameter in the description of the velocity distribution of the gas, defined by the Maxwell-Boltzmann distribution. A low temperature means a narrow velocity distribution. However, one must remember that the molecules are not in thermal equilibrium, and that in this case the stated temperature is only used to describe the amount of kinetic energy that the stated degree of freedom possesses. For instance, a supersonic beam (discussed in detail in chapter two) is internally cold with a small velocity spread, but the molecules have a large kinetic energy in the forward motion.

The production of ultracold molecules started in 1987, where photoassociation was the leading technique. [7–9] Over the last 20 years, researchers in the field of chemical physics and physical chemistry have investigated a range of techniques to cool down molecules. The number of techniques is increasing rapidly in time. Following the success with the laser-cooling of atoms, the obvious first choice would be to extend this to molecules. However, laser-cooling works by inducing absorption-emission cycles in an atom repeatedly, in order to give an efficient momentum transfer from thousands of photons in the laser beam to the much 'heavier' atom. This requires a closed-cycle which is why it cannot be as easily extended to the cooling of molecules. The presence of rotational and vibrational degrees of freedom in molecules result in decays to unwanted sublevels, making it difficult to find the required closed cycling transitions required for laser cooling. However, there are exceptions with some molecules which posses Franck-Condon Factors (FCFs) that suppress decays to excited vibrational states. [10,11] Nonetheless, there are still leaks to excited vibrational levels and each additional populated level requires a repump laser to return the population to the main cooling cycle. This makes it difficult to completely cool down the molecules, since not enough photons are scattered to provide a strong enough force. To date, the laser cooling of molecules has been demonstrated for SrF [12,13], YO [14,15], and CaF. [16]

The methods of cooling molecules can be divided into two groups: direct methods which take the molecules and directly cool them using electromagnetic fields, and the indirect methods that associate laser-cooled atoms into molecules. Magnetoassociation or 'Feshbach resonance' is one method which uses laser-cooled atoms and associates them by applying appropriate external magnetic-fields under specific conditions in such a way that the energies of the non-bound state of the pair of atoms and the bound state of the molecule become identical. [17–20] Recently, a group at Durham university successfully used magnetoassociation to create a sample of over 1000 ultracold ^{87}Rb^{133}Cs molecules in the lowest rovibrational ground state from an atomic mixture of ^{87}Rb and ^{133}Cs. [21] Although the indirect methods are better developed and can achieve lower temperatures below $1\,\mu$K, and at high densities, they are limited since they only use atoms that themselves can be laser-cooled. These include the alkali metals, alkaline earth metals and a few others. On the other hand, the direct methods can be applied to a wider range of molecules that can be more complex and often chemically more interesting. Unfortunately, the temperatures and densities attainable via direct methods are limited and the major challenge for the future is to achieve further cooling to reach the ultracold regime.

1.2 Applications of Decelerated Molecules

Though our Zeeman decelerator was built as part of a project with the aim of building a quantum simulator device, the decelerator on its own can serve as a useful tool in other applications. Samples of cold molecules from Zeeman decelerators are particularly attractive for applications in low-energy collisions and higher resolution spectroscopy. High-resolution spectroscopy benefits from using supersonic beams due to their cold internal degrees of freedom, long interaction times and reduced Doppler widths, which allow more accurate measurements. When atomic or molecular transitions are induced by electromagnetic radiation, the precision of the measurement is limited by the interaction time of the atom or molecule with the applied electromagnetic radiation. Zeeman decelerators reduce the forward velocity of supersonic beams, increasing the interaction time with the sample, thus decreasing the transit-time broadening and thereby improving the spectral resolution. This makes Zeeman decelerators an attractive tool for precision spectroscopic measurements.

Precise measurements of fundamental energy intervals serve as tests for quantum electrodynamics and may be used to set limits on the time variation of fundamental constants. Measuring the variation of fundamental constants, such as the fine-structure constant, α, may help us understand whether the universe is expanding on a cosmological timescale. [22] The most accurate spectroscopic measurement made to date is the hydrogen-deuterium 1S-2S isotope shift, [23] measured by using the slow tail of a thermal beam of hydrogen or deuterium atoms produced in a radio-frequency discharge source. The use of a slow, cold sample from a Zeeman decelerator would significantly improve the precision of this measurement. There has been a proposal for a high-resolution spectroscopy measurement on Zeeman-decelerated tritium. [24] High-precision spectroscopy can also be used in the study of fundamental physics, such as the search for the electric dipole-moment (EDM) of the electron. [25] A non-vanishing EDM of the electron would indicate a violation of time-reversal symmetry (T-violation) and therefore imply that the Standard Model of particle physics is incomplete. One molecular candidate for an EDM measurement is the YbF molecule. [26] Cold samples of dipolar molecules have strong intramolecular electric fields that can enhance the effects arising from the EDM of the electron by orders of magnitude. Recently, Bulleid *et al.* decelerated YbF molecules using AG Stark deceleration followed by travelling-wave Stark deceleration. [27] The increase in the spectroscopic resolution of measurements using slow, cold beams from a decelerator has also been demonstrated in a spectroscopic measurement of ^{15}ND$_3$, using a Stark decelerator. [28] By decelerating the beam from 280 m/s to 52m/s, the interaction time with the applied microwave field was increased, which enabled the resolution of the hyperfine structure on the inversion transition in ^{15}ND$_3$ for the first time. [28]

At temperatures below 1 K the collision energy of molecules becomes less significant than the perturbations due to external fields, and thus, molecular collisions can be effectively controlled with electromagnetic fields. This is of particular interest to reaction dynamicists. In many chemical reactions, thermal fluctuations are required for reactants to overcome an activation energy barrier in order to form the products. Classically, reaction rates vanish exponentially at low temperatures for such reactions. However, at low temperatures, the large de-Broglie wavelength of the molecules is comparable to the range of the inter-particle interactions, and thus, the quantum-mechanical nature of the particles becomes increasingly important. Consequently, classically forbidden reactions can be made possible because tunnelling through energy barriers on the potential energy surface becomes the dominant reaction pathway. Furthermore, one can also study other quantum effects such as non-classical reflections and resonances. [29] Deceleration techniques, such as Zeeman deceleration, can thus provide a route to study the effects of the quantum-mechanical nature of particles in chemical reactions. These low temperature reactions are also important in astronomical processes. [30] Zeeman decelerators are particularly useful for the study of barrier-less radical reactions at low temperatures since all radicals are paramagnetic due to having at least one unpaired electron, and thus, can be decelerated.

The methods that produce slow beams, particularly deceleration techniques, also tend to give very state-pure samples of molecules. In a low-temperature collision with very few quantum states, thermal averaging is avoided and thus more accurate data can be obtained that could lead to better understanding of the collision process. Therefore, with decelerators, the study of elastic, inelastic and reactive collisions in crossed and merged beam configurations can be made possible at high levels of accuracy and previously unattainable temperatures. This was first demonstrated in Stark decelerated OH molecules with Xenon atoms, where the threshold behaviour in the inelastic-scattering cross sections of the OH molecules was accurately measured with an overall energy resolution of about 13 wavenumbers. [31] Furthermore, decelerators enable the study of crossed-beam scattering studies as a function of collision energy. The effect of trapping electric or magnetic fields on collisions outcomes was seen in measurements of low-energy inelastic collisions between trapped [32] and velocity-tunable [33] OH molecules with supersonic beams of atomic He and molecular D_2.

For further discussions about collisions in the cold and ultracold regime please refer to the two review articles here. [6, 34] Other methods and applications of cold molecules will not be further discussed in this thesis, the reader is referred to the given literature: [5,35–37] for further discussions on the various methods and applications of cold molecules.

1.3 A Route Towards a Quantum Simulator Device: MMQA

Another application of cold molecules is in quantum simulations. All the matter surrounding us and within us is governed by quantum physics. Quantum phenomena can endure even in bulk materials where there is a large number of particles. It is possible to understand the behaviour of the bulk from the quantum physics of the constituents only if the particles interact with their nearest neighbours. However, if the interactions are strong and long-range, the particles not only interact with the nearest neighbours, but with every other particle in the material. This means that every particle interacts appreciably with every other particle, making it a nearly impossible task to understand the behaviour of the bulk from that of the constituents. High temperature superconductivity and the fractional quantum Hall effect, which are still not well understood, are two examples of phenomena which emerge from such strongly-interacting quantum systems. The complex behaviour of many-body quantum systems is one of the greatest challenges remaining in modern physics, due to the difficulty in modelling these systems computationally.

To try and understand these systems, we can create a physical model of strongly-interacting quantum particles in which we can control and tune their interactions. This idea of using a quantum simulator as a physical model of strongly-interacting quantum particles was first proposed by Richard Feynman. [38] For the construction of a quantum simulator, polar molecules are favourable over atoms. This is because an electric dipole moment can be induced in a polar molecule by a static DC electric field, allowing the molecules to strongly interact with each other via long-range dipole-dipole interactions. The electric dipole moment also allows the molecules to strongly interact with external fields such as DC electric fields and AC microwave fields, allowing their manipulation. When the molecules have spin, one has the chance to explore systems of interacting spins on a lattice, which are of great interest to the condensed matter community. [39–41] These lattice-spin models are used as simplified models to describe the characteristic behaviour of more complicated interacting physical systems. One real-world example, the fractional quantum Hall effect, can be modelled using a spin half lattice. [39] This can be realised by trapping $X^2\Sigma$ molecules such as CN, CaF and SO, in an optical lattice. The molecules will be confined in a two-dimensional optical-dipole trap and are therefore required to have temperatures in the microKelvin regime. With a two-dimensional trap, an array of 300×300 molecules contains 10^5 molecules. This is a number that can be detected reasonably easily. [42]

The aim of the MMQA was to build a device called a quantum simulator, an instrument that can cool down polar molecules to microKelvin temperatures and below, arrange them in a regular array, forming a strongly-interacting quantum system where their motion, orientation, and the way they interact can be controlled. The building of a quantum simulator requires ten million molecules in the initial trap, presumed to be about 100 mK deep, in order to have enough molecules for sympathetic cooling. [42] The five years of investigation so far have identified a promising route towards the production of ultracold molecules. This is illustrated in a flow chart diagram in figure 1.1. It begins with a supersonic beam or a buffer gas source with a slower velocity, which is decelerated to below the capture velocity of a molecular MOT. Another option is to use a cryogenic source, which will provide beams of greater density than supersonic sources. A buffer gas source can produce a dense beam of atoms or molecules at low temperatures. One of the projects

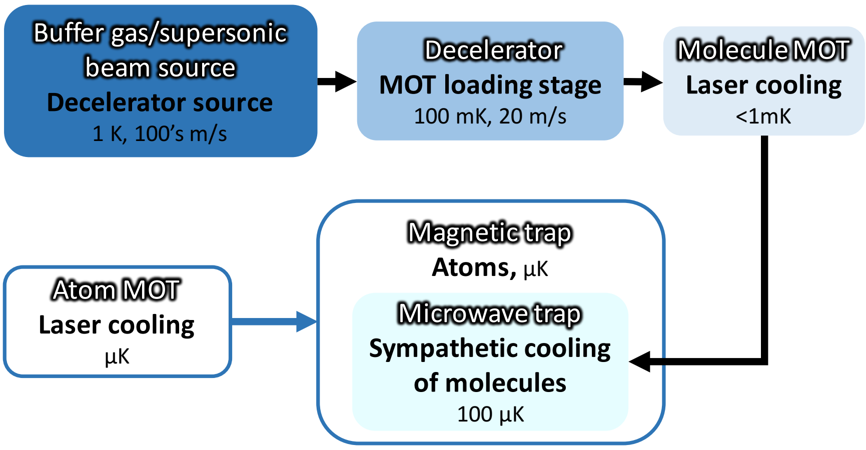

Figure 1.1: A route towards the production of ultracold molecules. Our decelerator is the loading stage for the molecular MOT.

within the MMQA programme involves building an intense cryogenic beam source using buffer gas cooling which can inject a beam into our decelerator. [43] In buffer-gas cooling, the atoms or molecules are laser-ablated into a cryogenic cell which contains a buffer gas (e.g. He), and are cooled by collisions with them. Following experimental and theoretical (fluid dynamics) studies of beam formation from a cryogenic buffer gas cell, the cell design was optimised for the extraction of the beam. [44] The latest design of the cell is able to produce a beam as slow as 150 m/s. [45]

As illustrated in figure 1.1, the decelerator is the loading stage for a magneto-optical-trap (MOT), where the molecules are further cooled with lasers. The decelerator traps have depths in the tens of milliKelvin. The required velocity for trapping depends on the trap depth. For a trap depth of a fraction of 1 K, molecular velocities below 20 m/s are required for trapping. The laser cooling of the molecules in a MOT will allow us to reach temperatures as low as a few milliKelvin. Molecular MOTs can be realised for any molecular species which can be laser-cooled. Our molecule of choice is CaF, following the recent success of the laser-cooling of this molecule by a project within the MMQA. [16] Magneto-optical trapping of molecules was only recently achieved for SrF molecules. [13, 46]

The final stage towards microKelvin temperatures is the sympathetic cooling of the molecules using laser-cooled atoms. As illustrated in figure 1.1, by bringing the milliKelvin molecules into contact with a buffer gas of pre-cooled ultracold atoms inside a trap, a new thermal equilibrium can be achieved with the aid of elastic collisions. [47] The atom MOT can be transferred to a magnetic quadrupole trap that can be moved along a motorised track to overlap these atoms with the molecules. This requires us to be able to contain the molecules in a suitable trap. A drawback of the sympathetic cooling technique is inelastic collisions, which prevent the cooling by releasing kinetic energy that could eject molecules from the trap and/or transfer the molecules into an untrapped state. A static magnetic trap can only trap the low-field-seeking molecules and not the ground-state molecules which are always strong-field seeking. For sympathetic cooling, we need to be able to trap the molecules in their absolute ground states because in this state they can only undergo elastic collisions and will thus remain trapped. The most suitable trap for ground-state molecules with a large depth is a microwave trap, as suggested by DeMille *et al.* [48] This is because microwave traps can provide large trap depths (up to several Kelvin) as well as large trapping volumes (up to several cm^3) for polar molecules, enabling efficient loading from a decelerated packet of cold polar molecules. In the microwave trap the ground-state molecules are confined near the maximum intensity of a microwave field. A Fabry-Perot microwave trap has been successfully built for ground-state atoms and molecules by one of the projects within the MMQA programme. [49] This microwave trap has an open geometry, allowing an easy overlap of the molecules with the laser-cooled atoms.

Recently, the theoretical team within the MMQA programme modelled the sympathetic cooling of ground-state CaF molecules by ultracold Li and Rb atoms. [50] Here, the molecules were confined in a microwave trap while the atoms were magnetically trapped. The simulation findings suggested that Rb is a more effective coolant than Li for ground-state molecules. If large enough densities are present, one could evaporatively cool the molecules in the microwave trap. Alternatively, forced evaporative cooling of the atoms could sympathetically cool the molecules further. The evaporative cooling of excited OH molecules was recently demonstrated successfully using a magnetic trap. However, this was only achieved for this specific molecule due to its uniquely favourable ratio of elastic to inelastic scattering cross-section. [51] Once the molecules are cold enough, the lasers forming the lattice can be switched on, forming a quantum array of polar molecules.

1.4 The Development of Zeeman Decelerators

The first demonstration of deceleration was in 1999 by Meijer and colleagues, where for the first time, the forward motion of neutral polar molecules was manipulated using time-varying inhomogeneous electric fields, using a Stark decelerator. [52] This device can produce slow polar molecules starting from a supersonic beam using time-dependent switching of static inhomogeneous electric fields, created by a series of pairs of parallel electrodes placed along the beam axis. Stark decelerators require the molecule to have a permanent dipole moment. The working principles of the Stark and Zeeman decelerators are analogous to each other. Stark decelerators use the Stark effect while Zeeman decelerators use the Zeeman effect. The Stark effect arises due to the interaction of the electric dipole moment of a molecule with an electric field, while the Zeeman effect arises due to the interaction of the magnetic dipole moment of a molecule with a magnetic field.

Stark decelerators have a longer history than Zeeman decelerators. The design of the Zeeman decelerator was inspired by the success of Stark decelerators. Hogan *et al.* have given a comprehensive list of decelerated atoms and molecules based on the various deceleration methods. [53] The Meijer group was the first to decelerate beams of polar molecules, such as metastable CO and ND_3, by rapidly switching electric fields of several tens of kV/cm in a Stark decelerator. [52, 54] Since its invention, the Stark decelerator has been developed and improved by changing the switching sequence of electrodes. Different switching sequences lead to different modes of operation, for example, in one mode only every third electrode is used to decelerate while the other electrodes are used to focus the molecular beam. This mode improved the beam intensity at the end of the decelerator by effectively decoupling the transverse motion from the longitudinal motion. [55] Different designs of the decelerator were also developed which were also based on the same principle of utilising the Stark shift to manipulate the motion of the molecular beam using external fields. One example is the alternate-gradient variant of the Stark decelerator for high-field-seeking states. [56] Decelerators using three-dimensional moving traps were first built in a chip-based decelerator [57] and this was later followed by decelerators using ring electrodes. [58] Furthermore, a wire Stark decelerator has also been demonstrated where the electrodes are replaced by thin wires which reduced the size of the decelerator by a factor of ten than the conventional Stark decelerator. It is also worth noting that in addition to the Stark and Zeeman decelerators, there is also the Optical-Stark decelerator, [59] the Rydberg-Stark decelerator, [60] and the microwave decelerator. [61] These decelerators will not be further discussed in this thesis, the discussions that follow will focus on the various types of Zeeman decelerators that have been constructed and operated by various groups worldwide.

It was the successful work on multistage Stark deceleration followed by the development of traveling-wave Stark decelerators that led to the development of multistage Zeeman decelerators. The Zeeman decelerator was developed to decelerate paramagnetic species using external inhomogeneous magnetic fields. For Zeeman decelerators, the atom or molecule needs to have a magnetic dipole moment i.e. the spin must not be zero. The unpaired electron in all radicals gives them a non-zero spin, making Zeeman deceleration a general method to produce cold atomic and molecular radicals. Furthermore, it can be used for a wide range of molecules with a magnetic dipole moment for which Stark deceleration cannot be applied. All decelerator methods start with beams formed by supersonic expansion. This will be discussed extensively in chapter two. Briefly here, pulsed supersonic expansion provides an attractive starting point for deceleration methods due to their narrow longitudinal and transverse velocity spreads (corresponding to temperatures of $\sim$1 K), joined with high particle density and low internal (rovibrational) temperatures. However the mean velocity of these beams can range from 100's to 1000's of m/s. Decelerators are designed to extract this longitudinal kinetic energy by capturing a range of velocities around the mean velocity and slowing them down to a lower values.

Group	Description	Reference
Raizen	**2007** - Ne* decelerated from 461 m/s to 406 m/s over 18 stages (28 cm).	[62]
	2008 - Ne* decelerated from 447 m/s to 55 m/s over 64 stages (64 cm).	[63]
	2008 - O_2 decelerated from 389 m/s to 83 m/s over 64 stages (64 cm).	[64]
Narevicius	**2011** - Ne* decelerated from 429 m/s to 53 m/s using a co-moving trap with 213 overlapping quadrupoles extending over 114 cm.	[65]
	2015 - Simultaneous deceleration of O_2 and Ar* from 430 m/s to 100 m/s using a co-moving trap with 480 overlapping quadrupoles extending over 2.4 m.	[66]
Merkt	**2007** - H decelerated from 313 m/s to 225 m/s over 6 stages (4.8 cm).	[67]
	2007 - H and D decelerated from 422 m/s to 273 m/s and 367 m/s respectively, over 7 stages (5.6 cm).	[68]
	2008 - H decelerated from 435 m/s to 107 m/s over 12 stages (9 cm).	[69]
	2008 - H trapped after deceleration from 520 m/s to 100 m/s over 12 stages.	[70]
	2010 - D trapped after deceleration from 475 m/s to 0 m/s over 24 stages (19 cm).	[71]
	2011 - Ne* decelerated from 580 m/s to 105 m/s over 91 stages (towers between).	[72]
	2012 - O_2 decelerated from 390 m/s and 450 m/s to velocities in the range 150-280 m/s over 90 stages.	[73]
	2014 - He_2 decelerated from 500 m/s to 100 m/s over 55 stages (40 cm).	[74]
Vanhaecke	**2011** - Guided beam of Ar* atoms at 463 m/s in a 3D moving trap decelerator (published). Decelerated Ar* beam from 400 m/s to 364 m/s over 2 stages extending a distance of 28 cm (PhD thesis).	[75]
Momose	**2013** - Methyl radicals CH_3 decelerated from 510 m/s to 480 m/s over 15 stages.	[76]
	2015 - Decelerated O_2 beam from 320 m/s to 0 m/s then confined in 3D over 80 stages.	[77]
	2016 - Methyl radicals CH_3 decelerated from 510 m/s to 0 m/s over 80 stages then confined in 3D.	Unpublished
Softley	**2014** - H decelerated from 500 m/s to 350 m/s over 12 stages (each 8.5 mm length).	[78]
	2015 - He* decelerated from 490 m/s to 370 m/s over 12 stages (each 8.5 mm length).	[79]
Carty	**2015** - 3D guiding of Ar* at velocities in the range 320-400 m/s over 1 stage (12.3 cm length).	This thesis

Table 1.1: Summary of various Zeeman decelerators built by different groups with a reference to the given published work. The asterisk indicates a metastable state.

Table 1.1 summarises all the Zeeman decelerators which have been built by various groups. The first demonstration of magnetic deceleration using a Zeeman decelerator was in 2007. This was carried out in the same year in the groups of Raizen (UT Austin, USA) and Merkt (ETH, Switzerland) where atomic hydrogen [67] and metastable neon [62] were decelerated, respectively. The ‘Description’ column in table 1.1 lists the all the achievements by these two groups with a reference to the literature. One difference between the design of the Merkt group Zeeman decelerator and that of Raizen’s/Narevicius’ group is the former have their coils outside vacuum while the latter group have them inside. Another difference is the Raizen/Narevicius group uses magnetic shielding/field-enhancing material around the coils. Finally, the Merkt group uses currents of around 300 A while Raizen uses 700 A, achieving magnetic field strengths of up to 2.2 T and 5.2 T, respectively. The group of Narevicius branched out from the group of Raizen and recently demonstrated the simultaneous deceleration of O_2 molecules and metastable Ar (Ar*) atoms in a moving trap decelerator. [66] The success of these two groups sparked interest in other groups worldwide, including Vanhaecke (Orsay, France), Softley (Oxford, UK), Momose (UBC, Canada) and our own decelerator. The published findings of these groups are also summarised in table 1.1. The most recent published achievement is the deceleration of methyl radicals from 510 m/s to 480m/s over 80 stages. [76] This was the first time a polyatomic free radical was decelerated using Zeeman deceleration. Though unpublished, further experiments by the group of Momose have decelerated the methyl radicals to a standstill (the paper is in preparation).

1.5 The Working Principle of Zeeman Deceleration

Multistage Zeeman deceleration relies on the interaction between paramagnetic species and time-dependent inhomogeneous magnetic fields. Here, the Zeeman effect arises due to the interaction of the magnetic dipole moment of a molecule with a magnetic field. In the absence of the magnetic field, all magnetic sub-levels (M_J) of an atom are degenerate, a consequence of the lack of a space-quantisation axis. When an external magnetic field is applied, the degeneracy is broken and the energy levels are split in a way that depends on whether the projection of the spin is parallel or anti-parallel to the applied magnetic field. The population in the various resulting energy levels is distributed equally. The magnitude of splitting is given by the Zeeman shift

$$\Delta E = g\mu_B M_J B_z, \tag{1.1}$$

where g is the Landé g-factor, μ_B is the Bohr magneton, M_J is the magnetic sub-level quantum number, and B_z is the applied magnetic field in the z-direction. All atoms and molecules have metastable states of energy. These have long lifetimes as a result of selection rules which forbid the de-excitation of the state. The two metastable states of Ar are $^3P_0$ and $^3P_2$. The Zeeman deceleration method relies on the Zeeman shift in the presence of an inhomogeneous magnetic field, $\vec{B}$, exerting a force, $\vec{F}$, on a particle with an effective magnetic moment, $\vec{\mu}_{\text{eff}}$, that is proportional to the gradient of the magnetic field on the atoms or molecules

$$\vec{F} = -\nabla(\vec{\mu}_{\text{eff}}.\vec{B}). \tag{1.2}$$

Hence, the state with the biggest effective magnetic moment will experience the greatest force, and thus, be decelerated more easily. Figure 1.2 shows the Zeeman effect in the $^3P_2$ state, as calculated using equation 1.1. The low-field-seeking state, $M_J = 2$, with the largest effective magnetic moment of 3 Bohr magnetons is illustrated in black, this is the most suitable state for the decelerator. The Zeeman sub-levels are divided into two groups with particles in high-field-seeking states (HFS, $M_J = -1, -2$) minimising their energy in a high magnetic field and low-field seeking states (LFS, $M_J = 1, 2$) that minimise their energy in low magnetic fields. The overall effect on LFS states is that the inhomogeneous magnetic field exerts a force on the atom and pushes it back towards the low field region. Any paramagnetic species will exhibit Zeeman splitting in the presence of a magnetic field.

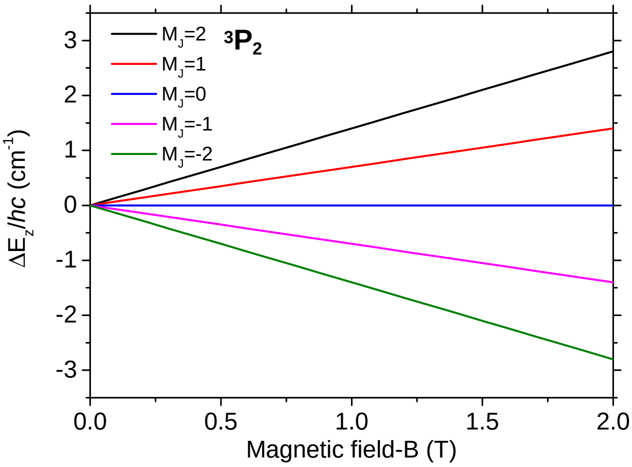

Figure 1.2: The Zeeman effect in the $^3P_2$ state. The low-field-seeking state $M_J = 2$ with the largest magnetic moment is depicted in black. Plotted using equation 1.1.

Figure 1.3a illustrates a simplified schematic diagram of an experimental setup that uses a Zeeman decelerator. The setup consists of a source where a pulsed supersonic expansion is used to produce an atomic or molecular beam. The beam propagates through a skimmer before reaching the decelerator solenoids. Here, inhomogeneous magnetic fields are produced by an array of coils. A detector placed downstream can then record the arrival times of the atoms or molecules, giving a time-of-flight distribution. The mean velocity and temperature can then be extracted from this distribution.

In figure 1.3b, the solid and dashed coils and potential hills depict two subsequent configurations of a deceleration sequence. Only one solenoid is switched on at a time, giving rise to a single-peaked Zeeman energy, W(z). High currents are pulsed through these solenoids to produce large magnetic fields. When a paramagnetic LFS atom or molecule approaches the magnetic field produced by the solenoids, it climbs up this potential hill and loses kinetic energy at the expense of gaining Zeeman potential energy up to the field maximum. If the field is not switched off after the atom or molecule reaches the field maximum, it would climb back down the potential and regain its initial kinetic energy. To avoid this, the field must be switched off sharply before it reaches the field maximum. The field is switched on and off repeatedly in a series of stages, removing substantial amounts of kinetic energy

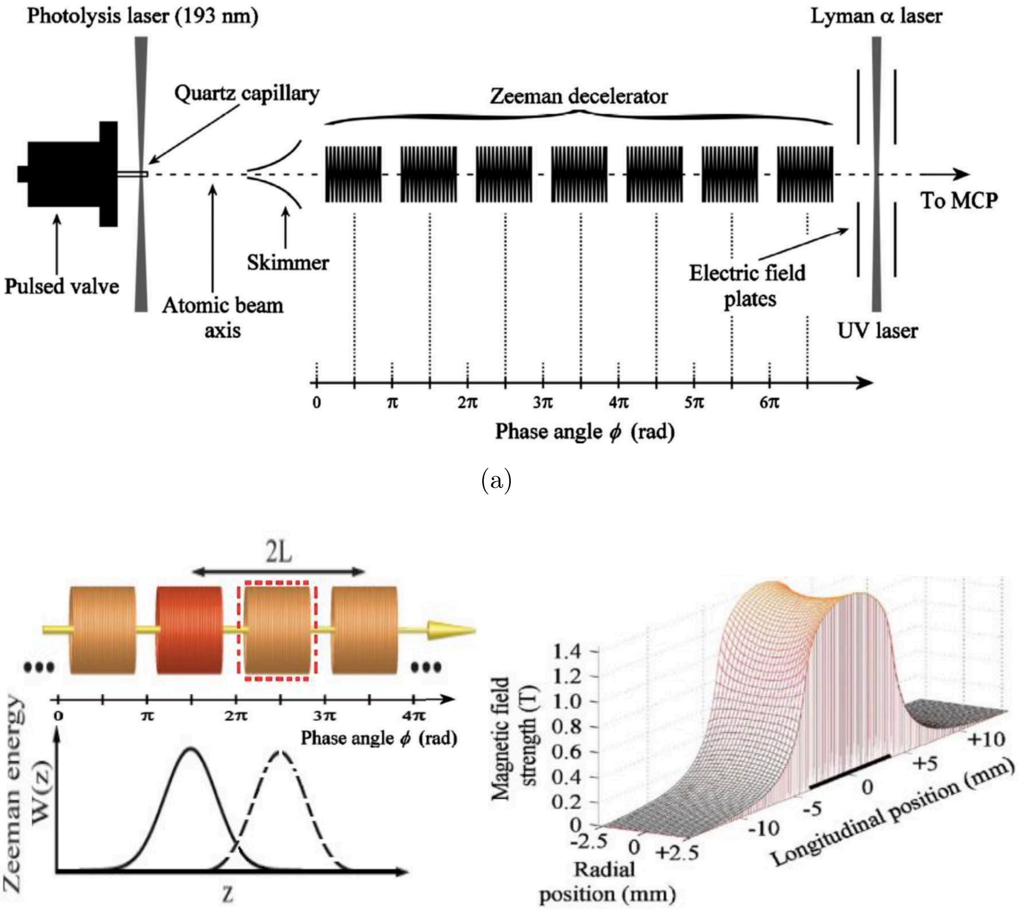

(a)

(b)

(c)

Figure 1.3: a) Schematic of an experimental setup using a multistage Zeeman decelerator. It includes a pulsed supersonic expansion source producing a beam which propagates through a skimmer. This is followed by the decelerator and a micro-channel plate (MCP) detector downstream. In the lower part, the phase angle is indicated with respect to the first solenoid (taken from [68]). b) Schematic of the geometry and standard mode of operation of a multistage Zeeman decelerator (taken from [80]). The propagation direction is indicated by a yellow arrow. The solid and dashed coils and potential hills depict two subsequent configurations of a deceleration sequence. Only one solenoid is switched on at a time, giving rise to a single peaked Zeeman energy W(z). c) The calculated magnetic field strength inside every solenoid of the Zeeman decelerator showing the longitudinal and radial magnetic field distributions for an operating current of 250 A (taken from [68]). The position and the spatial extension of the solenoid is indicated by the thick black line on the axis representing the longitudinal position.

from the atoms or molecules until they are brought to rest. The number of stages determines the finally velocity.

Phase stability is an important concept in decelerators. It dictates that only particles with a certain range of relative velocities and spatial positions can be decelerated by the fields. The initial phase-space distribution of the gas can be preserved throughout the deceleration process by operating the decelerators in a phase-stable manner. A representative particle is chosen, named the 'synchronous particle', with an initial longitudinal velocity equal to the mean of the distribution. The amount of kinetic energy lost by a particle in a given deceleration stage depends on its position along the beam axis when the magnetic field is switched off. Rather than a spatial coordinate, this position is given a phase angle due to the periodicity of the decelerator. A phase angle of 0 ° corresponds to the midpoint between two adjacent solenoids and 90 ° corresponds to the centre of an active solenoid where the magnetic field is at its maximum. This is indicated in the lower part of figures 1.3a and b, where the phase angle is indicated with respect to the first solenoid. Particles slightly ahead of the synchronous particle will experience a slightly greater deceleration, while particles slightly behind will experience less deceleration. This results in the particles oscillating around the synchronous particle. These particles are phase stable. The deceleration pulse sequence is calculated for a specific quantum state that gains most Zeeman energy in the inhomogeneous magnetic field i.e. the state with the largest magnetic moment. Furthermore, the switching sequence for the solenoids is calculated for a specific velocity that matches the synchronous molecule and a specific phase angle i.e. the point at which the field is switched off.

In the phase-space plots depicted in figure 1.4, particle trajectories have been simulated in 1D and 3D for different switch off times indicated by a different phase angle. [80] The synchronous molecules are in the centre, while the non-synchronous molecules trajectories are given a relative phase and velocity. The bold line in each plot is called the separatrix and is the boundary between the stable and unstable regions in phase space. The decelerator acceptance is defined as the region in phase space at the entrance from which particles are guided to the last trap of the decelerator. The 1D simulations (figure 1.4a) show that the phase space acceptance decreases with increasing phase angle, which is accompanied by a decrease in deceleration stages.

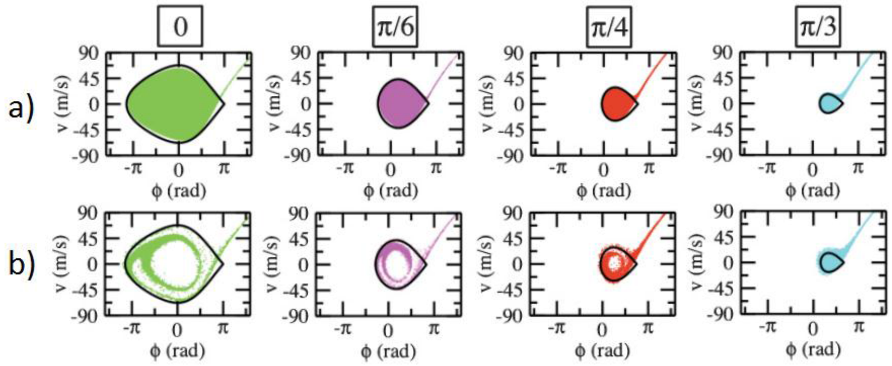

Figure 1.4: Comparison of the 1D phase stability model with particle trajectory simulations for selected values of the phase angle, ϕ_0, in a) 1D and b) 3D assuming instantaneous switch off times for the currents. The bold line in each graph shows the separatrix. Adapted from reference [80].

When transverse motion is taken into account, one can see many losses indicated by the white regions within the separatrix. These can be understood by looking at the magnetic field distribution in figure 1.3c which shows that the radial fields change along the length of the solenoids. The longitudinal and radial magnetic field distribution are shown for an operating current of 250 A (taken from [68]). The concave nature of the radial profile high-field region inside the solenoid naturally guides atoms in LFS levels and ensures transverse stability, providing radial confinement during the deceleration process. However, the convex magnetic field outside the solenoid leads to a reduction in the longitudinal phase-space acceptance of the decelerator at low phase angles due to defocusing transverse forces. Consequently, the longitudinal and transverse motions are not independent. At low velocities, the atoms or molecules are over-focussed. Other features that can be seen in figure 1.4 are the white bands known as halos. These are a result of the parametric amplification that is brought about by large amplitude oscillation around synchronous molecules, leading to large gain in transverse velocity. When the finite rise and fall times (around 5-10 μs) of the switched fields are taken into account, this leads to an increase in the phase-space acceptance due to the increased effective phase angle experienced by the non-synchronous molecules that travel further into the solenoid as it is being switched off.

To summarise, the problematic feature with this type of Zeeman decelerator is that the longitudinal and radial motions are not completely independent; the same solenoids are used for deceleration and transverse confinement.

The radial confinement is not the same throughout the deceleration. The switching of the magnetic fields effectively produces a moving quasi-potential. However, the particles are not confined in all dimensions throughout the deceleration. This leads to various losses that greatly reduce the deceleration efficiency. Different modes of operation have been used to increase the deceleration efficiency, [80] where the longitudinal and transverse motions are decoupled by using different stages or solenoids for deceleration and focussing. More recently, Dulitz *et al.* demonstrated that by applying a low, anti-parallel magnetic field in one of the solenoid coils, a temporally varying quadrupole field is formed, improving particle confinement in the transverse direction. [78] This was shown to significantly increase the overall acceptance of the Zeeman decelerator. However, to fully overcome the problems limiting the deceleration efficiency already discussed, a different approach can be taken where the supersonic beams are stopped without any radial losses by initially trapping them in a 3D trap and then decelerating the trap along with the confined beam. This will be described in detail in the next section.

1.5.1 Moving Trap Decelerators

A more recent approach to Zeeman deceleration, which uses moving 3D traps promises to solve the problem of the limited efficiency by using a true travelling potential well. This new approach provides a decelerator with a larger phase-space acceptance than the conventional pulsed-type decelerators and appears to avoid the focussing difficulties of the conventional design. As previously mentioned, this different approach was implemented first in decelerators based on the Stark effect involving both microscopic and macroscopic moving electrostatic traps. [57, 58] By reducing the loss processes, one subsequently increases the phase-space acceptance of the decelerator. With a magnetic trap decelerator, it has been shown that the phase-space region containing the decelerating species is larger by up to two orders of magnitude as compared to other available decelerating methods. [65]

So far, two different coil designs have been used to produce a 3D moving trap Zeeman decelerator: that of Lavert-Ofir *et al.* [65] and that of Trimeche *et al.* [75]. These two designs differ in the coil arrangement. The diagram on the left of figure 1.5a shows the Lavert-Ofir *et al.* design. Here, moving 3D magnetic confinement is obtained by switching a series of spatially

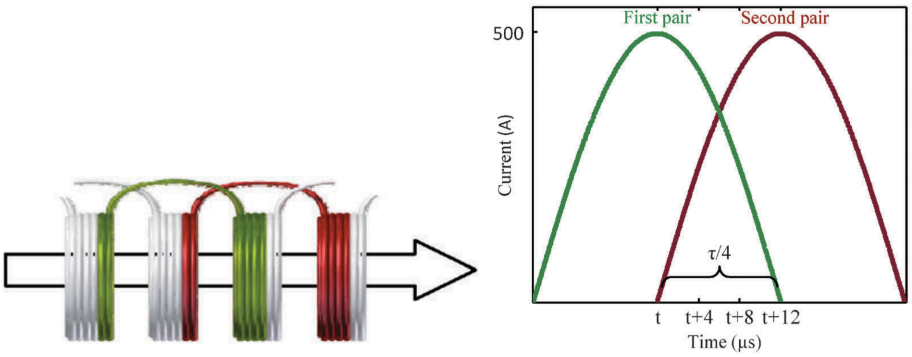

(a) (b)

Figure 1.5: a) Lavert-Ofir *et al.* design: two spatially overlapping quadrupole traps. Each trap consists of two coils with current running in opposite directions (anti-Helmholtz pair) b) Time sequence between two overlapping quadrupole traps. Taken from [65].

overlapping quadrupole traps, and activating them in a temporally overlapping pulse sequence. Each magnetic trap is produced from two coils in an anti-Helmholtz configuration and is axially shifted from the next trap by half of the coil-to-coil distance. Two adjacent spatially overlapping quadrupole pairs are each driven with a half sine-shape current pulse; figure 1.5b shows the time sequence between the two overlapping quadrupole traps used to produce the moving magnetic trap. To decelerate the trap, the overlap time is increased, which requires increasing the pulse duration and the pulse-to-pulse time difference. 3D trajectory simulations and measurements showed that the moving magnetic potential minimum position oscillates during the deceleration. The oscillations occur during the transfer between two adjacent coils and are intrinsic to this design approach. [65] Furthermore, the potential shape changes during the propagation.

Another possible geometry to form a 3D moving trap consists of groups of wires that are wound in double helices that are flattened, as illustrated in figure 1.6b. The bottom coils are identical to the top coils but with the opposite handedness. A schematic of the vertical cross-section of the Trimeche *et al.* coil arrangement can be seen in figure 1.6a which illustrates the molecular beam in relation to the decelerator coils. The flat helical coils mostly provide longitudinal confinement. Figure 1.6c shows the working principles of this decelerator. The top coils consist of four groups of eight wires labelled A to D that are interleaved in a right-handed double helix.

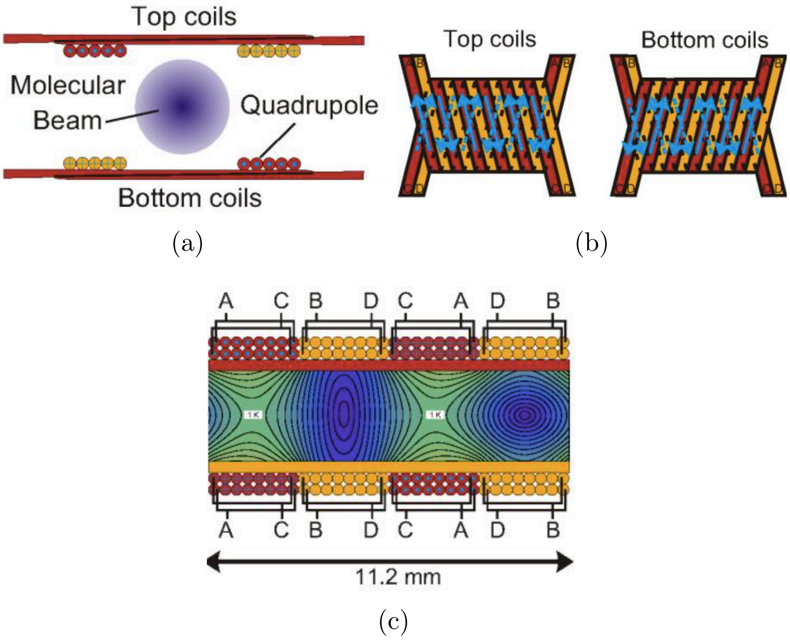

(a) (b)

(c)

Figure 1.6: a) A cross-sectional view of the decelerator along the molecular beam axis. b) Top and bottom coils. c) Vertical cross-section of the Trimeche *et al.* design, running down the length of the decelerator through the centre of the quadrupole and coils showing the magnetic potential in which the molecules are trapped for different snapshots in time. The wire groups are labelled A to D.

The identically labelled wire groups are connected in such a manner that the current in them is equal in magnitude but opposite in direction at any given time. The wire geometry is arranged in such a way that a magnetic field minimum is effectively formed from the current running into and out of the page, as in an anti-Helmholtz coil. Time-dependent currents are run through both sets of coils sinusoidally at a certain frequency. This results in a travelling sinusoidal magnetic-wave propagating in the z-direction with a series of confining potentials at the velocity of the travelling wave. The moving trap is created with an initial velocity that matches the centre of mass velocity of the atomic or molecular supersonic beam. By applying a constant frequency, the potential well moves at a constant speed that can be matched to the speed of the incoming molecules. Chirping-down the frequency allows the moving potential well, along with the molecules trapped within, to be decelerated.

Full 3D confinement is achieved by the addition of a quadrupole field which is independent of the deceleration coils. As depicted in figure 1.6a, the quadrupole guide consists of long wires that confine the molecules transversely, sandwiched between two sets of coils in such a way that together they provide the required 3D potential well for LFS molecules. A quadrupole trap consists of two coils with current running in opposite directions in an anti-Helmholtz configuration. It has a zero magnetic field at the centre that then increases linearly in all directions. All the HFS states are expelled from the trap, leaving behind only the LFS species trapped in the region of lower magnetic field in the trap centre. This radial magnetic field has no axial component.

On a final note, when discussing the different methods of cooling molecules, it is important to consider how the phase-space density changes. The phase-space density is defined as the number of molecules per unit volume per unit momentum space. i.e. it describes the number of particles in a given interval in Cartesian and velocity space. Phase-space density is an important concept as it allows us to determine whether a cooling technique does in fact 'cool' the system with an increase in the phase space density or whether it preserves the phase space density. Liouville's theorem states that the phase-space density remains constant for a system of particles evolving under the action of non-dissipative forces that do not depend on their velocities. [81] Hence 'real cooling' requires the introduction of a force resembling friction that is proportional to the velocity of a particle e.g. photons in spontaneous emission cycles. Therefore, for decelerator methods such as Zeeman deceleration that rely on conservative forces, the achievable phase-space densities are limited by the phase-space characteristics of the sample prior to deceleration, as in agreement with Liouville's theorem. The decelerator works by capturing a range of the velocities around the mean of the beam, and then centring this around a lower velocity.

1.6 In this Thesis

Based on the limitations of a conventional pulsed-type Zeeman decelerator described, we decided to proceed with building the new type of Zeeman decelerator which uses real 3D moving traps. On initial inspection, the Lavert-Ofir *et al.* design seemed superior due to its larger scale, and thus larger spatial acceptance, and the convenience of its circular coil design. However, it was decided to go with a similar design to the that of Trimeche *et al.* for reasons which will be discussed in detail in chapter four. This thesis presents the work carried out towards the building of our decelerator. The research carried out is structured as follows: chapter two contains an introduction to supersonic expansion both in continuous and pulsed beams. This chapter presents the results on the characterisation of a pulsed beam of argon atoms, using a home-built fast-ionisation-gauge (FIG) as a detector. More importantly, a home-built electric excitation source is presented along with its characterisation. The aim of the work in this chapter is to produce a slow beam of metastable argon atoms from supersonically expanded pulses that can be then captured by the decelerator traps. Chapter three presents the research carried out on a project involving the attempts to build a fast-pulsed cantilever piezo valve. The gas pulse characterisation is carried out using the FIG detector.

In chapter four, the design specifications of our decelerator are explained in detail. First, the working principle of our decelerator is discussed. The aim of this chapter is to outline the technical details of the decelerator design and describe the justification for the chosen design. The vacuum system is described in detail. The design of the quadrupole guide coils and the independent decelerator coils are described and the specific design choices are justified. The independent electronics driving high pulsed currents through the decelerator and quadrupole guide coils are then presented. The following chapter, chapter five, begins by describing the Zeeman effect in more detail. This is then followed by the presentation of data characterising our decelerator using time-of-flight techniques. 2D and 3D guiding of metastable argon are successfully achieved. Chapter six begins by discussing standard, well established detection techniques used to measure absolute densities in gas samples: laser-induced fluorescence (LIF) and cavity ring-down-spectroscopy (CRDS), followed by cavity-enhanced laser-induced fluorescence (CELIF), a cross-correlated combination of the two methods. The chapter explains the methodology of CELIF with the presentation of published work where we measured the absolute density of SD radicals in a supersonic jet. [82] Finally, the thesis is concluded in chapter seven with a summary of all the findings. An outlook, including the near-future and far-future plans of the decelerator are also outlined.

Chapter 2

A Metastable Rare-Gas Atom Source for a Decelerator

In all beam-deceleration methods, a prerequisite is a dense but collision-free gas beam with a small velocity spread in the propagation direction. For the purpose of our moving magnetic trap decelerator, short pulses would only fill one of the moving traps, making the analysis of the time-of-flight (TOF) distributions much easier. These pulses need to have a small spatial and velocity spread that will be accepted by the decelerator traps in order to maximise the number of captured molecules. Pulsed supersonic beams formed in an adiabatic expansion meet these conditions, and by serving as a convenient platform for entraining paramagnetic atoms and molecules, they have been successfully used in many experiments for over fifty years. [83, 84] This chapter is devoted to the production of an optimised source of metastable argon atoms (Ar*), where their low-field-seeking states can be captured by the magnetic fields of our decelerator. A pulsed supersonic jet valve will be presented, including the development of a home-made electric discharge as an excitation source that uses electron-impact in a plasma in order to excite ground-state atoms to long-lived metastable states.

2.1 Supersonic Expansion and Pulsed Beams

Supersonic beams are an indispensable technique in modern chemical physics. The success of many experiments involving supersonic beams lies in the

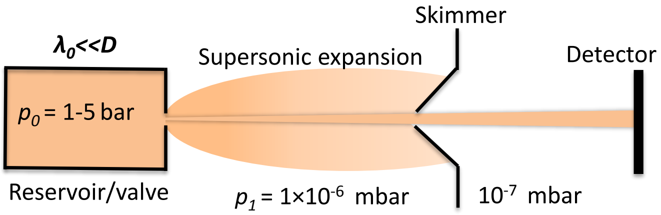

Figure 2.1: Schematic diagram showing supersonic expansion from a valve at high backing pressure (1-5 bar) into a low pressure (1×10^{-6} mbar) region, including a skimmer which collimates the beam and a detector downstream.

remarkable simplicity and benefits of an adiabatic expansion, where thermal and internal energy is converted into directed mass flow, leading to the production of molecular beams with low temperatures and at high speeds. Molecular beams with well-defined kinetic energies can be prepared, a vital capability in crossed beam experiments. One can reach temperatures under 1 Kelvin with high densities that are enough to observe collision processes in great detail and enhance the precision of spectroscopic measurements. In the discussions that will follow, the key concepts in the theory of supersonic beams are outlined, with the treatment based on two books by Miller and Morse. [83, 84] A more vigorous discourse can be read from the referenced books.

In general, atomic and molecular beams are generated by letting a gas escape from a big reservoir at a certain pressure through a small orifice into a vacuum chamber at a much lower pressure. Inside the reservoir, the velocities can be described by a broad Maxwellian velocity distribution, given by

$$f(v) = \sqrt{\left(\frac{m}{2\pi kT}\right)^3} 4\pi v^2 e^{-\frac{mv^2}{2kT}}, \tag{2.1}$$

where v is the velocity, m is the mass, k is Boltzmann's constant, and T the temperature. If the mean free-path, λ_0, is larger than the orifice diameter, D i.e. $\lambda_0 >> D$ the resulting beam is effusive. In this case, every now and then molecules escape through the orifice, without suffering from collisions while they exit the reservoir. However, when the reservoir pressure is increased to a point at which the mean free path of the particle in the reservoir is much smaller than the orifice diameter i.e. $\lambda_0 << D$, the

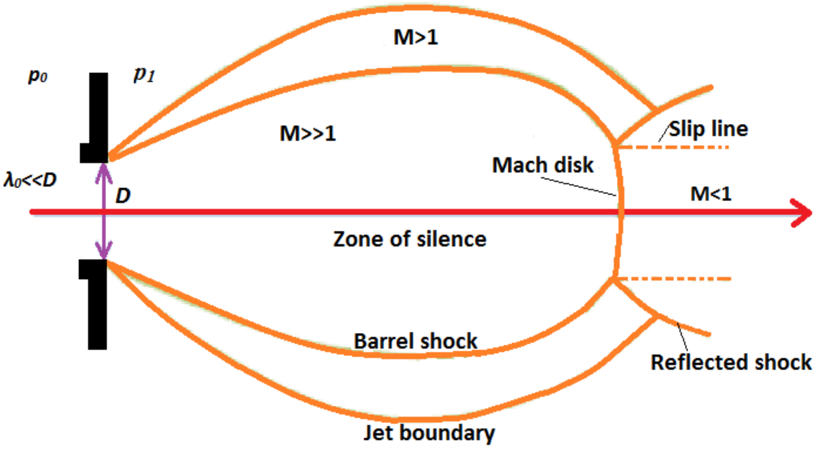

Figure 2.2: A supersonic, continuous beam emitted from an orifice. The jet has rotational symmetry about the z axis showing: barrel shock, slip lines, jet boundary, Mach disk, Mach reflection and the zone of silence. Here, the reservoir pressure, p_0, is much greater than the background pressure, p_1, i.e. $p_0 >> p_1$.

molecules escaping through the orifice collide frequently. Many collisions occur at the orifice, pushing the molecules through the orifice, leading to a supersonic expansion of the gas, as illustrated in figure 2.1. In a monoatomic gas, this leads to the production of high velocity supersonic beams and a narrow velocity spread in the co-moving frame of the gas, corresponding to a low translational temperature. In a molecular gas, from many inelastic collisions that occur, the internal energy, including rotational and vibrational energies are transferred to translational motion. This makes the molecular beam translationally warmer than an atomic beam.

Supersonic expansion will occur if the high backing pressure (p_0) and the lower background pressure (p_1) ratio p_0/p_1 is sufficiently large ($>$ 2.1). [83] Due to this pressure difference, the gas is accelerated towards the orifice and on exit, the mean pressure reaches the local speed of sound i.e. the Mach number M=1. At low differential pressures, an increase in the reservoir pressure leads to a higher beam velocity. However, if one reaches a critical pressure difference, the atoms are accelerated to the local speed of sound and can no longer respond to local boundary conditions. Downstream from the orifice, the Mach number increases beyond unity and the beam is supersonic. Ideally, $p_1 = 0$, but in real experiments, the background pressure always has some finite values. Thus, the ideal model breaks down at the point in the expansion where the gas density reaches that of the background gas. This results in collisions that randomise the velocity distribution and increase the entropy, and also lead to shock zones, as illustrated in figure 2.2 where the particles are rapidly decelerated. These shock waves: the *Barrel shock* and the *Mach disk* confine the region of supersonic expansion.

In the space between the nozzle and the *Mach disk*, the number of collisions is very low and known as the zone of silence which ends at the *Mach disk*. The position of the *Mach disk*, Z_M, is given by [83]

$$Z_M = 0.67D\sqrt{\frac{p_0}{p_1}}. \tag{2.2}$$

Typical pressures we use are $p_0 = 4\,\text{bar}$ and $p_1 = 10^{-6}\,\text{mbar}$, and a nozzle orifice of 0.5 mm, placing the Mach disk approximately 21 m downstream of the nozzle orifice, outside the building.

When source pressures are high, gas viscosity and heat transfer effects can be neglected, therefore the gas flow may be treated as an adiabatic, isentropic expansion. This adiabatic assumption leads to the conservation of energy, implying that for a gas flow under adiabatic conditions, the sum of the internal energy of the gas and the kinetic energy remain constant during the expansion. For an ideal, perfect gas, the internal energy of the system, which is defined by the specific enthalpy (in J/kg), is given by

$$U = c_p T, \tag{2.3}$$

where c_p is the specific heat capacity and, T, is the temperature. For a reservoir temperature of T_0, and a temperature of T, of an expanding gas at a supersonic flow velocity, v, energy conversion gives the expression

$$c_p T + \frac{v^2}{2} = c_p T_0, \tag{2.4}$$

assuming that, c_p, at constant pressure is independent of temperature, this can be rewritten as

$$v = \sqrt{2c_p(T_0 - T)}. \tag{2.5}$$

For an ideal gas, $c_p = k_B/m\gamma(\gamma - 1)$ holds, where k_B is Boltzmann's constant and γ the ratio of heat capacities of the gas species, c_p/c_v, with $\gamma = 5/3$

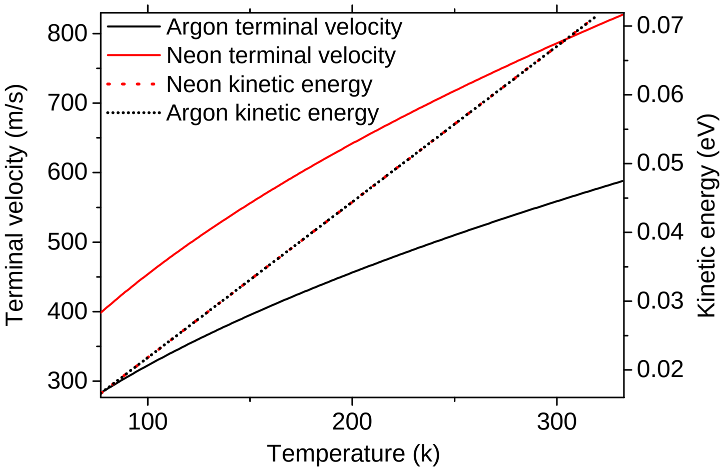

Figure 2.3: Calculated terminal velocity in the supersonic expansion of argon gas (black solid line) and neon gas (red solid line) at liquid nitrogen temperatures (77 K) and up to room temperature, calculated using equation 2.6. The calculated kinetic energies at these velocities (dotted lines) are also shown.

for a monoatomic gas and $\gamma = 7/5$ for a diatomic gas (in the vibrational ground state). During the expansion in the low-pressure region, the density of the gas decreases, making collisions in the gas less frequent, after which the gas reaches a terminal temperature T_t. The corresponding pressure is low compared to p_0. From $T/T_0 = (p/p_0)^{(\gamma-1)/\gamma}$, it can be deduced that $T_t << T_0$, [84] so the terminal velocity of the beam can be approximated as

$$v_t = \sqrt{\frac{2kT}{m}\frac{\gamma}{\gamma-1}}. \tag{2.6}$$

Equation 2.6 tells us that lowering the temperature of the initial gas reduces the terminal velocity. Given that we want to use the supersonic beam in a decelerator, it is advantageous to start out with a beam at a low velocity, since the initial kinetic energy and therefore the decelerator length increases quadratically with the supersonic beam terminal velocity. This can be achieved by reducing the reservoir's temperature which can be done by using a cryogenic valve. Figure 2.3 shows a plot of the calculated terminal velocities using equation 2.6 for argon (black solid line) and neon (solid red line) at temperatures in the range 77 - 340 K. The kinetic energy of the two gases at these velocities are very similar, as illustrated as a dotted black line for argon and dashed red line for neon. However, colder temperatures could have a detrimental effect, depending on the pressure and gas species, the gas

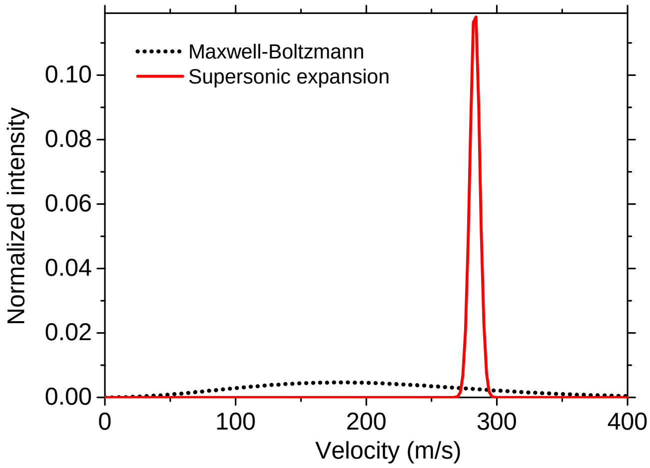

Figure 2.4: Comparison between the velocity distribution of an argon supersonic beam (red line, equation 2.7) with a Maxwell-Boltzmann distribution (black dotted line, equation 2.1), both at 77 K, illustrating a substantial narrowing of the velocity distribution that has taken place by the time the expansion has reached its limit. The graphs are normalised to their area.

can start to condense inside the valve, thus lowering the pressure. If the temperature is too low, the vapour pressure might not be sufficient enough for supersonic expansion. Therefore at lower temperatures, the lowest velocity which can be achieved is limited by the gas' condensation temperature. The mass dependence of the terminal velocity tells us that a heavy atom with a high boiling point can have similar velocity to a lighter and colder atom. However, the divergence of beams made with heavier gases is greater as the heavier atoms transfer more energy to the molecules in the direction perpendicular to the propagation direction, increasing the beam's divergence. [85] It is important to note here that the equations given above are only strictly valid for continuous nozzles, although nowadays most supersonic valves are pulsed to achieve higher brightness, as will be explained below.

The velocity distribution for a supersonic beam can be approximated by a distribution of the form [86]

$$f(v)dv = Av^3 \mathrm{e}^{\frac{-m}{2kT}(v-v_t)^2} dv, \tag{2.7}$$

where m is the mass, T is the translational temperature, A is a normalisation constant, and v_t is the terminal velocity (given by equation 2.6). Figure 2.4 illustrates the velocity distribution of argon gas at 77 K (black dotted line) inside the reservoir or valve which is described by equation 2.1 and its comparison with the terminal velocity distribution of a supersonic beam (red solid line), as described by equation 2.7. The graph illustrates a substantial narrowing of the velocity distribution that has taken place by the time the expansion has reached its limit with a much higher mean velocity centred around 283 m/s. The purpose of the decelerator is to capture as much of the range of velocities and centre the mean velocity at a lower mean velocity.

The signal we detect is a TOF of the atoms, thus we need an equation which describes the time-dependent signal produced by the atoms or molecules. Equation 2.7 can be transformed from a velocity to time space, giving an equation which describes the time-dependence of the signal according to

$$g(t)dt = \frac{L}{t^2} f\left(\frac{L}{t}\right) dt = A\frac{L^4}{t^5} \mathrm{e}^{-4\ln 2\frac{(t-t_0)^2}{w(t)^2}} dt, \tag{2.8}$$

where $w(t) = \sqrt{8\ln 2\, k\, T\, t^2/(M v_0^2)}$ is the time-dependent temporal width (full-width-half-maximum (FWHM)) of the pulse due to the thermal spread of forward velocities. [25] Later in this chapter, this form of time-dependence distribution of the signal is seen to fit our TOF distributions very well.

Another way to lower the beam velocity of a chosen species is by dilution of the desired sample with a heavier ‘carrier gas’. Typical fractions of the carrier gas vary from 50% to 99% allowing a compromise between flux and beam velocity. With high fractions, the sample is entrained in the flow of the carrier gas and adapts its thermodynamical properties resulting in a lower terminal velocity, as well as more efficient cooling of the internal degree of freedom providing a denser sample. Nevertheless, one has to be careful with the choice of the carrier gas. If the mass ratio between the lighter and heavier gas becomes too small, the lighter species is pushed out of the beam during supersonic expansion, i.e. the lighter atom travels on the outer boundary of the beam, resulting in a very broad velocity distribution. This is called velocity slip. For a molecular source, a pure molecular expansion can be carried out, however, seeding the molecules into supersonic jets of atoms cools down their translational and rotational temperatures more effectively. In the seeded beam, the heavier molecules are accelerated by the lighter atoms, giving a cold molecular beam at the terminal velocity of the heavier carrier gas. A lower temperature is reached for the atomic species due to the differences in the heat capacity ratio between the two species. Seeding is relatively simplistic and can be used to cool many different molecules, including radicals created in photodissociation. When seeding molecules in a carrier gas, rare gas atoms are chosen due to their inertness.

In continuous molecular beam sources the beam intensity, as well as the degree of cooling, is limited by the size and the pumping capabilities of the vacuum pumps. Ideally, the beam needs to be produced in a near perfect vacuum in order to minimise collisions between the beam particles and the warm background gas molecules. Furthermore, the constant gas load of a continuous beam leads to an unwanted background detector signal, limiting the experimental sensitivity. On the other hand, pulsed sources can achieve substantially higher peak intensities and reduce the background detector signals simply by reducing the duty cycle. The system, then, has time to pump away background gas between pulses. Pulsed beams are characterised by their duty factor, $D_F = \tau/T$, which is the ratio between the pulse duration, τ and the period, T. A great advantage of pulsed molecular beams is their low duty factor, which allows the use of high backing pressures, giving comparatively strong expansions and high instantaneous intensities to be reached with moderate pumping capabilities and low sample consumption. The degree of cooling in the supersonic expansion depends on the number of inelastic collisions, which convert internal energy into kinetic energy, higher pressures mean higher densities and, more collisions and therefore, more cooling. Thus, low temperatures are achieved with a bigger orifice diameter and a greater backing pressure i.e. their product, p_0D, is made as large as possible. [84]

In experiments using pulsed beams, a very important experimental parameter is the time spreading of a single beam pulse, measured at the beam detector. Short pulsed beams are essential for our decelerator since only molecules that are within the decelerator acceptance will be captured and decelerated; short pulses are required in order to fill only one potential well at a time. In addition, the excess particles can cause further losses by colliding with slowed molecules further downstream whilst also increasing background pressure, leading to more trap loss. The pulse time spread is determined by the valve opening time and the distribution of velocities present in the beam. The velocity distribution is determined by how well-formed the supersonic expansion and the degree of cooling is. For this, one requires sufficient opening times for the hydrodynamic flow through the nozzle to become fully developed. This raises an issue relating to the general operation of pulsed beam sources concerning the dynamical properties of the gas flow at different times in the pulse and in particular, the possibility of reaching a quasi-steady flow condition similar to the one occurring for continuous sources.

2.1.1 A Commercial Pulsed Valve: the General Valve

Many valve designs have been used in the production of pulsed supersonic beams based on different mechanisms, including piezoelectric materials and solenoid valves. [87–91] A commonly used and commercially available pulsed valve driven by means of a solenoid is the General Valve (*Parker*, Series 9). A schematic of the valve is displayed in figure 2.5. The General Valve, a magnetically activated plunger valve, is the most widely used design in the field of atomic and molecular beams. As illustrated in figure 2.5, the exit nozzle is a small channel with two conical ends through the front face plate of the valve. A small Teflon cylinder acts as the shutting poppet with a conical tip that fits into the nozzle channel in the closed position, held by the armature (in black). The front plate has a screw thread, which allows the adjustment of the main valve body in order to get a proper operation of the shutting poppet. The nominal diameter of the circular cross section at the narrowest part of the nozzle is 0.5 mm.

The valve is pulsed by varying a current through a solenoid. When no current is applied, a spring exerts a force on the poppet and blocks the nozzle orifice. When a current is applied to the solenoid, a magnetic field is generated, causing the armature in which the poppet is held, to be pulled back into the valve, retracting the sealing poppet thus opening the valve and allowing the flow of gas. The valve is driven by a commercially available driver (IOTA-ONE, *Parker*) which feeds a higher kick voltage pulse providing the initial force required to move the mass of the armature against the closing spring, and a lower hold voltage that keeps the valve open. The driver triggers the valve with a fixed high voltage kick pulse of approximately 275 V (DC) with a standard set maximum length of 180 μs and a constant hold voltage amplitude of 10 V. The only parameter, which can be varied, is the total ‘on-time’, which is the hold voltage pulse width. This valve can be used at room temperature and be driven using pulses as short as 160 μs and can be operated at frequencies up to 120 Hz with backing pressures up to 86 bars.

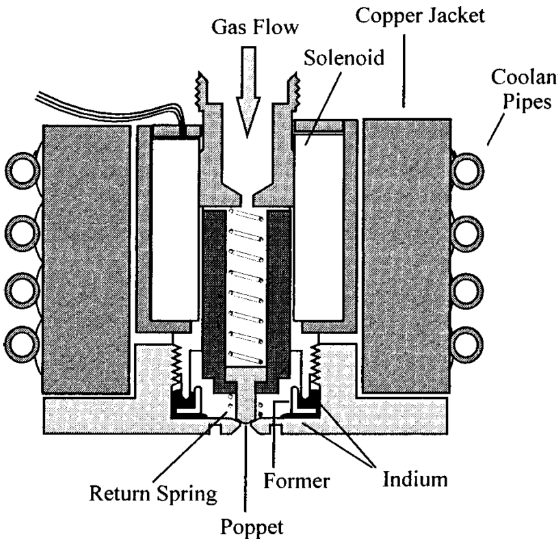

Figure 2.5: Schematic diagram of the General Valve (*Parker*, series 9) with a cooling copper jacket (dark grey) around the main body of the valve. The solenoid wraps around the chamber in which the armature (in black) sits within. The poppet sits inside the armature. In the series 99 valve, a copper gasket sits where the 'former' and indium are depicted in this diagram. [92]

The wide use of the General Valve has revealed that achieving a steady flow is limited by the mechanical displacement of the armature, which means that the valve does not fully open for short pulses which we would typically use i.e. that the effective exit area in the 'full open' position is smaller than the nominal size of the orifice due to an insufficient retreat of the closing poppet. [93] This was one of the motivations for building our new home-made cantilever piezo valve, which will be presented in chapter 3.

2.2 Pulse Characterisation with a Fast-Ionisation-Gauge Detector

In order to optimise the source, it is useful to be able to characterise the gas pulse produced by the valve, and this can be done using a fast-ionisation-gauge detector (FIG). Though there was once a commercially available FIG by *Beam Dynamics Inc*, these were out of production when the building of our decelerator started. Additionally, due to the compact size of our decelerator source chamber, this FIG would not have fit inside the chamber, therefore, we had to develop our own home-made compact FIG.

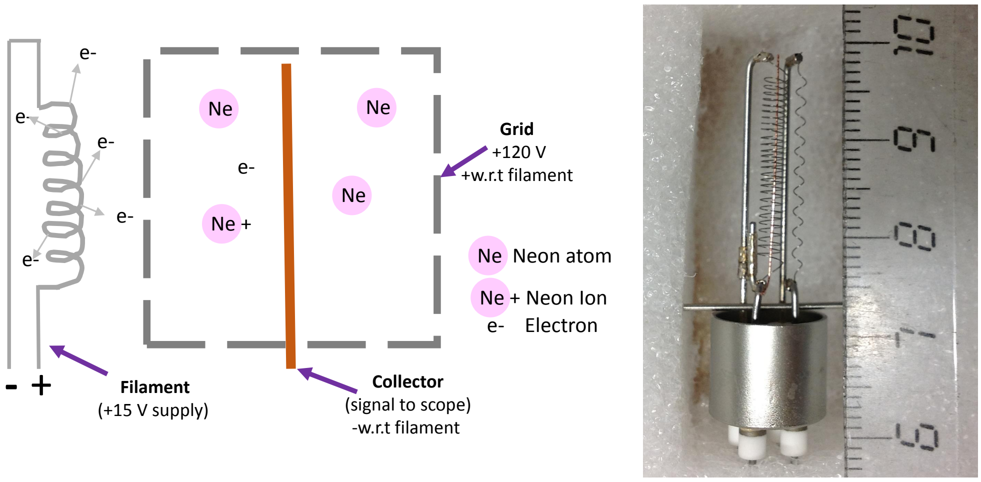

(a) (b)

Figure 2.6: a) A schematic overview of the operation mechanism of the FIG. The filament supplies electrons which are accelerated towards the positive anode grid. Ionised gas particles are detected by the collector wire in the centre of the grid. b) A photograph of the FIG with its dimension indicated by a ruler.

Our FIG design is based on the specifications provided in a paper by Gentry. [87] As depicted in figures 2.6a and b: it is essentially a high vacuum gauge consisting of a grid, a filament and a collector on which the grid dimensions have been reduced to increase speed of response. The schematic diagram in figure 2.6a illustrates the operation mechanism of the FIG. The gauge operates by measuring the pressure through ions produced within the grid. An electron current is produced by the filament which is accelerated towards the positively charged grid, some of which collide with atoms within, therefore ionizing them. The ions formed within the grid are detected by the collector in the centre of the grid as they collide with it and neutralise. The detected ion signal is proportional to the gas pressure provided the temperature and the electron current from the filament are constant. The response time has to be sufficiently fast such that it does not introduce appreciable broadening in the measured distributions. The gauge head design was drawn and sent to a company specialising in making gauges (*SS Scientific*) to manufacture the three components and spot weld them onto a commercially available electrical feedthrough (*Allectra*). For more technical drawings of the FIG, please see *Appendix C*.

In typical molecular beam experiments, the FIG sits far from the nozzle, therefore an amplifier is required to see the FIG signal at the lower beam

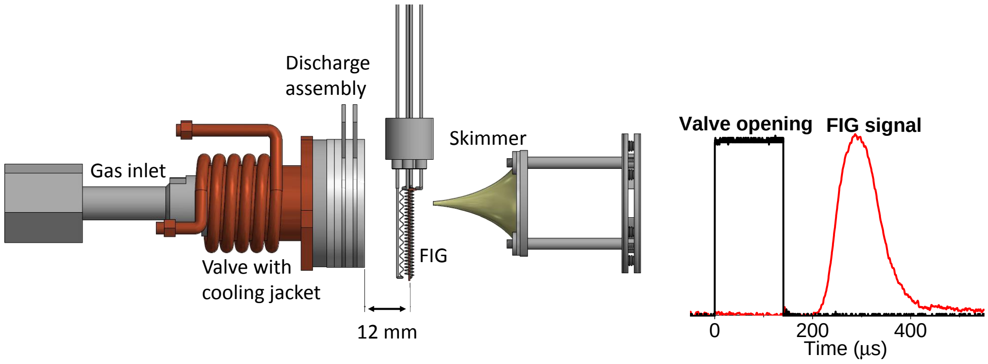

(a) (b)

Figure 2.7: a) Schematic diagram showing the position of the FIG in the source chamber. b) A typical detected FIG signal (red) and the trigger pulse (black) fed to the valve.

densities downstream. However, in our compact source chamber design, the FIG sits very close to nozzle, eliminating the need for an amplifier. Nonetheless the FIG was designed with a working fast amplifier circuit, as described by Gentry, and this was operated successfully in a separate machine where the FIG was sat further downstream. The operation of the FIG also requires a controller, the design of which was based on the one by *Beam Dynamics* and was constructed in our electronics workshop.

Figure 2.7a shows the FIG, as it is mounted in the source chamber. The FIG sits on a rotatable rod that allows us to move the FIG out of the molecular beam path in the decelerator source chamber when the deceleration experiments are running. When making the measurements, the FIG was positioned in the most intense part of the beam. Figure 2.7b shows the detected FIG signal when the valve was triggered by a square trigger pulse from the pulse generator (*Quantum Composers 9520*) with a width of 140 μs (black trace). The valve was at a temperature of 155 K with an argon backing pressure of 3 bar. At 155 K, the terminal velocity of argon is around 400 m/s, thus, the beam would take 34 μs to travel the distance between the valve assembly exit and the FIG. This indicates a time response of 165 μs for the valve that was used under these specific conditions.

The FIG controller allows the FIG filament current to be varied in the range 0 - 5 mA. When operating the FIG, the current is increased enough in such a way that a high signal to noise ratio is obtained. Typically a current under 2 mA was used in order to avoid saturation. Figure 2.8a shows the FIG

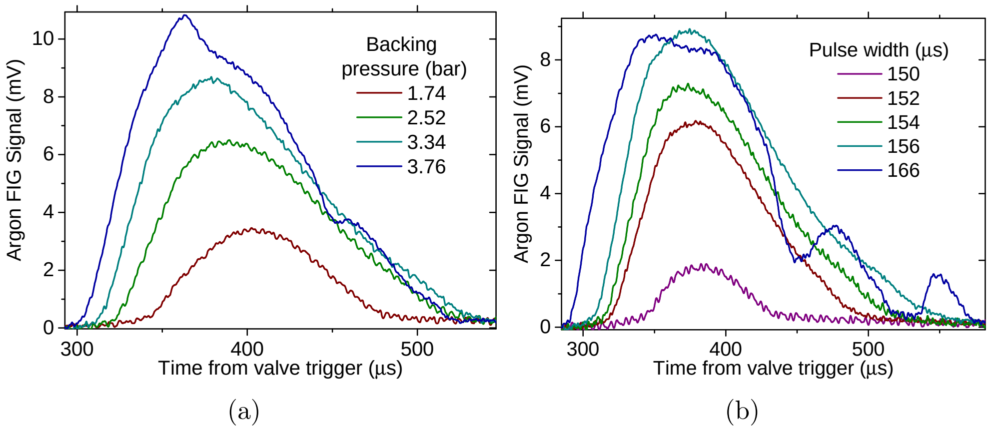

(a)

(b)

Figure 2.8: a) Argon FIG signal for different valve backing pressures a fixed valve trigger pulse width of 158 μs. b) Argon FIG signal for different valve opening trigger pulse widths.

signal for argon gas at different valve backing pressures. The gas pulse shape appears to deteriorate after a pressure of 3.34 bar, as the distribution starts to show a second peak. This is related to the fact that the valve operation is also pressure dependent, as the higher pressures can affect the movement of the parts inside the valve body. The bouncing of the poppet indicated by secondary peaks. Another demonstration of the bouncing of the poppet can be seen from the FIG traces in figure 2.8b where the FIG signal for argon has been measured at different valve opening trigger pulse widths. Increasing the length of the opening trigger pulse increases the intensity, as more gas escapes through the nozzle. When the pulse width is increased beyond 158 μs, the poppet starts to bounce, as seen in the secondary and tertiary peaks in the traces. The valve opening trigger pulse width is optimised by varying the pulse width and choosing the width that results in the most intense beam before the profile deviated from a single peaked gaussian which is made to be as symmetric as possible.

2.2.1 Cooling the General Valve Series 99

The mean speeds of the beams required for our decelerator can only be attained at low temperatures with the use of liquid nitrogen cooling. As the valve cools down, this effectively increases the distance between the armature and the nozzle, by changing the springs' properties, which makes the valve behave as though the opening time is longer. The series 9 version of the valve,

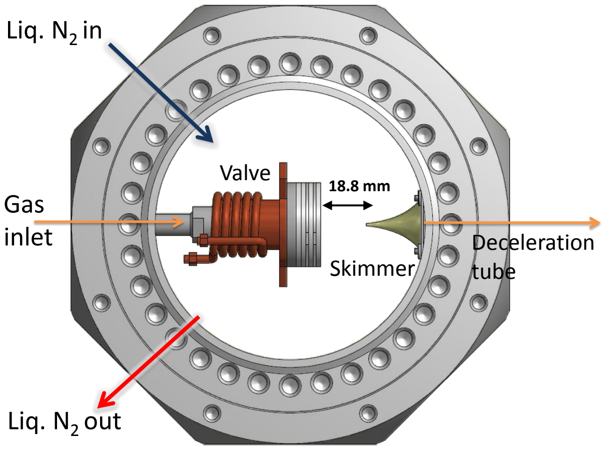

Figure 2.9: A schematic diagram of the source chamber showing the mounted valve with the discharge assembly attached to the front face, and the cooling jacket which is wrapped around it.

as it was illustrated in figure 2.5 on page 33, was not designed for operation at cryogenic temperatures. In the series 99 version of the valve, the faceplate is screwed onto the main body of the valve, and compresses a copper gasket in order to prevent gas leaking out. This valve was also designed to work at room temperature, therefore a simple modification of using a thinner gasket was made to improve its performance at low temperatures since the performance of the valve depends critically on how the valve nozzle is fixed to the body, which unfortunately cannot be easily optimised with this valve design. The only adjustment left on the valve was the length of the opening trigger pulse on the commercially available valve driver.

The General Valve series 99 was cooled by using a cooling jacket that was designed in such a way that it cools the body of the valve as well as the front face plate of the valve, as can be seen in figure 2.9. A photograph of the source chamber can be seen in *Appendix D*. The cooling jacket consists of a machined main part that slides onto the body of the valve and a copper pipe (3.175 mm I.D. and 0.4572 mm wall thickness) that is silver welded onto it with extended arms attached to the source chamber liquid-nitrogen feedthroughs. Liquid nitrogen is forced through the copper tube by pressurising a dewar (*Wessington Cryogenics*, ES 35 KF) that forces the cold liquid through the copper tube wrapping the cooling jacket, then exiting from the second feedthrough and vaporising into the air. One thermocouple (N-type) is attached to the cooling jacket and a second one to the front face flange

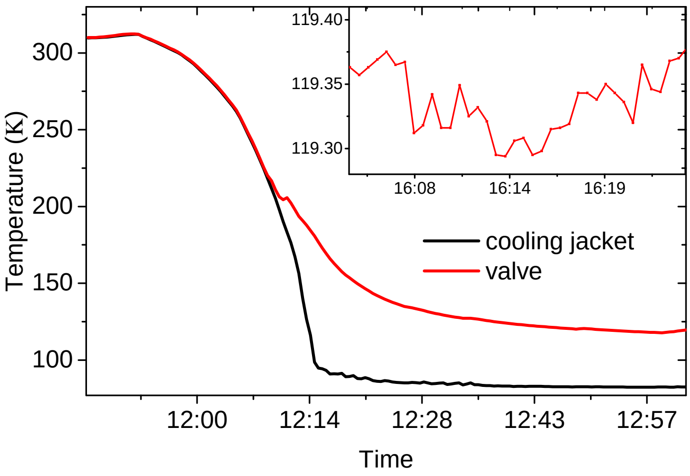

Figure 2.10: Measured temperature over time using the thermocouples on the cooling jacket (black line) and front face-plate flange of the General Valve (red line). Inset: valve temperature fluctuation when a stable glow discharge was being operated during the source optimisation measurements.

of the valve. Two heaters (47 ohm, 20 W, TO220, *Digi-Key*) are attached to the cooling jacket on either side, allowing the heating of the valve in order to control the temperature and thus, the velocity of the gas pulse. In order to measure the temperature and control the heaters, we use a programmable temperature controller (PTC10, *Stanford Research Systems*) which uses a feedback loop, where the output power supplied to a heater is continually adjusted to keep a predetermined set-point value for temperature reading that is input.

Figure 2.10 shows the change in temperature of the valve as it is cooled down with liquid nitrogen. The valve was running before the cooling started. Initially, both the cooling jacket and the valve decrease in temperature at the same rate. Shortly before 12:14, the discharge was activated. The cooling rate then slowed down for the valve, which is closer to the discharge electrodes and the discharge filament and therefore experiences more heat load. The lowest temperature measured on the cooling jacket was 82 K, which is 5 degrees above liquid nitrogen temperature (77 K). The valve takes longer to cool down and only reaches the lowest temperature of 117 K for this length of cooling time due to the constant heat load from the discharge and filament. The inset in figure 2.10 shows the temperature fluctuation while the valve is in operation with a stable discharge at low voltages, which only fluctuates

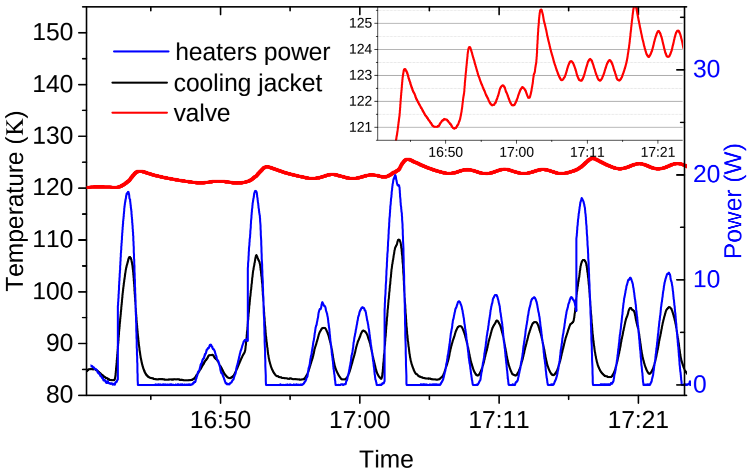

Figure 2.11: Measured temperature over the time period of the measurements using the thermocouples on the cooling jacket (black) and face plate of the General Valve series 99 (red). The inset shows valve temperature fluctuation when a stable discharge is operating.

by 0.1 K. It is important to ensure that the temperature does not fluctuate too much in order to maintain a constant mean velocity of the beam in such a way that the decelerator traps can capture the initial gas pulse with the desired mean velocity.

Though for our measurement with argon atoms we want to be operating the valve at the lowest temperatures achieved by using liquid nitrogen, the heaters will be necessary when using molecules with higher boiling points, and therefore, could condense on the inner walls of the valve when cooling down to liquid nitrogen temperatures (77 K). The graph in figure 2.11 demonstrates the response of the temperature stabilisation system to changes in the set temperature. The valve temperature is shown by the red trace and the cooling jacket temperature by the black trace. Initially, the valve temperature was set to 120 K. The temperature controller feeds the heaters power (blue trace) to maintain the constant set temperature. The big spikes in both measured temperatures are a result of electrical noise and not a dramatic instant increase in temperature. The temperature was then set to different temperatures, increasing by increments of 1 K from 120 K to 124 K at times which correspond to the big spikes in the heater power. The inset in the graph shows that the fluctuations in temperature for each set temperature

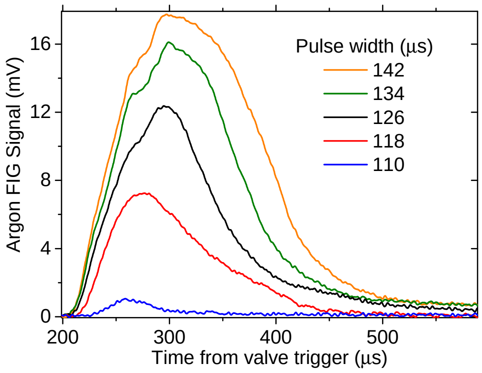

Figure 2.12: Argon FIG signal from the cooled valve at 117 K for different trigger pulse widths.

is only 1 degree. This is a bigger temperature fluctuation than the instances when the heaters are not used to maintain a constant temperature.

The biggest contribution to the heating of the General Valve is the heating of the solenoid coil as current is pulsed through it. It is also worth noting that the movement of the poppet and armature also add a heat load to the valve, imposing a limit on the temperature reached, an effect that has been observed by various groups. [92] This effect can be lowered by running the valve at a low repetition rate as reducing the valve pulsing repetition rates gives the valve more time to cool between pulses and, thus, should reduce the temperature and velocity of the carrier gas. In measurements by Bulleid, it was found that by increasing the repetition rate from 1 Hz to 10 Hz, the velocity increased from 340 m/s to 425 m/s. [94]

At room temperature, the valve started to open at trigger pulse widths of 150 μs with an optimum width of 156 μs, as is was seen in figure 2.8b on page 36. When cooling the valve, the trigger pulse width is adjusted to a smaller value, in this case to 128 μs, in such a way that the valve only starts to open at the lower temperatures. As the valve cools down, the valve then becomes "correctly adjusted". Once the valve has reached an equilibrium temperature, the trigger pulse width can then optimised. Figure 2.12 shows the FIG signal from the cooled valve at different pulse widths at an equilibrium temperature of 117 K. Increasing the trigger pulse width increases the temporal width of the gas pulse. Comparison with figure 2.8b on page 36 indicates that the optimum trigger pulse width is shorter for the cooled valve. Additionally, the signal starts 100 μs earlier, indicating a faster response time for the cold valve. This is possibly a result of the lower resistance of the solenoid at the lower temperatures. Increasing the pulse by 30 μs increases the gas intensity by an order of magnitude. For trigger pulse widths shorter than 110 μs the valve does not open.

We have also constructed a home-made valve driver which allows more flexibility in manipulating the beam characteristics. Using the home-made driver, the kick voltage amplitude and width can both be varied in addition to the hold voltage width. Attempts were made to produce identical traces for the output by using the home-made and commercial valve drivers, but it could not be achieved due to the sensitivity of the valve behaviour to even very small differences in the kick and hold and the combination of the two. While investigating the gas profile at lower temperatures with the home-made driver, the valve behaviour was even more sensitive with even a few volts or microsecond changes leading to dramatic changes in the gas profile. The background pressures in the source chamber were too high for a clean supersonic expansion, it was thus decided to stick to the IOTA-ONE driver. The data for this is presented in *Appendix A*.

2.3 Exciting Atoms with Electric Discharges

The first species chosen to test the decelerator with was metastable argon due to its high magnetic moment to mass ratio. The choice of using an atomic source was because of the ease of production as well as detection. Metastable-state argon (Ar*) and neon (Ne*) can both be produced using a pulsed electric discharge excitation source and detected on a micro-channel-plate detector (MCP, see section 2.3.1). Table 2.1 shows the energies of the different metastable states of argon and neon in eV and their respective lifetimes. Although argon is heavier than neon, its terminal velocity is smaller at 77 K, making it easier to decelerate to rest. Figure 2.3 on page 28 showed the terminal velocity and the kinetic energy for argon and neon at different temperatures. At 77 K the terminal velocity and kinetic energy of argon and neon are 283 m/s and $16.6\times10^{-}3\,\mathrm{eV}$, and 398 m/s and $16.4\times10^{-}3\,\mathrm{eV}$, respectively. The lowest decelerator trap velocity we can produce depends on the how fast we can switch the current, with faster beams requiring faster switching of current, imposing a challenge on the electronics. This will be further discussed in chapter 4. Pulsed discharge sources can also be used in

Atom	State	Energy (eV)	Lifetime (s)
Ne	Ne^+	>21.56 [96]	
	$^3P_2$	16.62 [97]	14.7 [98]
	$^3P_0$	16.72 [97]	long [97]
Ar	Ar^+	>15.76 [96]	
	$^3P_2$	11.55 [97]	38 [98]
	$^3P_0$	11.72 [97]	long [97]

Table 2.1: Energies of different states of argon and neon including the lifetimes of the metastable states.

the production of molecular radicals such as OH radicals and SD radicals. [95] For the production of these molecular radicals, the pulsed discharge source provides a simple, cheap, and intense stable source.

The excitation source is an electronic excitation via a high voltage discharge where a voltage is applied between two electrodes. In the presence of a gas, conduction across the gap occurs once the applied voltage exceeds the breakdown voltage of the gas, forming ions as well as metastable states of atoms. The two things required to initiate a discharge are charged particles with sufficient energy and a sufficiently high density of neutral gas particles. For particles with high ionisation potentials, the electrons need to be accelerated to high enough kinetic energy. One of the fundamental processes involved in a DC discharge is electron avalanche, where the electrons drift in an electric field towards the anode and gain enough kinetic energy from this field to cause the ionisation of the atoms by collisions. This leads to a fast multiplication of ions and electrons. Another fundamental process is secondary electron emission. This can occur through several processes: [99] thermionic emission due to the heating of the electrode; field emission where electrons are released due to the strong electric field gradient near the electrode; and electron emission due to the impact of high energy particles on the electrode surface. Secondary electron emission can help stabilise the discharge.

Electric discharges can operate in different regimes, including: glow discharge at low voltage and low current where there is high stability and arc discharges where there are large spikes in current that add heat to the gas pulse and erode the electrodes. Arc discharges are likely to occur at high voltages, for the glow discharge typical voltages are it the range of 300 - 600 V and currents in the milliamp regime. The glow discharge that we desire is characterised by a homogeneous plasma forming between the electrode surfaces. The plasma consists of positive ions and negative electrons in a sea of neutral atoms.

A DC discharge source for the production of metastable states is relatively simple to make since the voltage is constantly on. However, it presents the disadvantage of a lot of heating of the gas pulse and, therefore, generates a gas pulse with a wide velocity spread. In the context of our decelerator, short discharges are preferable in order to fill up one trap at a time. Pulsed high-density beams using electric discharge sources are much more difficult to realise than a continuous gas discharge, since the build up of charge is interrupted between the high voltage pulses. The longer the length of the pulsed discharge, the easier it is to achieve a stable discharge that can be reliably used as an electron impact excitation to metastable states. However, when the temporal pulse width of the voltage pulse is comparable or smaller than the time required for the build-up of charge carriers in the gas pulse, it is no longer possible to achieve a stable quasi-steady-state stable electric discharge. This problem can be resolved by the addition of an electron emitter, which provides free electron injection, massively improving the efficiency and the stability of the excitation of the atoms to the metastable states, giving a reliable, intense, and short-pulse beam of metastable atoms. In previous published work by Halfmann *et al.*, it was revealed that the addition of a hot wire emits electrons that seed the discharge, allowing a strong enhancement in the discharge stability as well as efficiency. [100]

2.3.1 Detecting Metastable Atoms with a Micro-Channel Plate Detector

Ions and highly excited states of atoms can be detected by using michrochannel plate detectors (MCP) consisting of several millions of parallel glass channels with diameters of 10 μm packed in a honeycomb structure, as illustrated in figure 2.13. When an electron, a positive ion or an excited atom with enough energy enters a channel and strikes a wall, an electron is emitted that then travels in a parabolic trajectory until it strikes the channel wall, emitting a secondary electron. The voltage difference accelerates electrons produced. Figure 2.13 shows how this process is repeated, resulting in a cas-

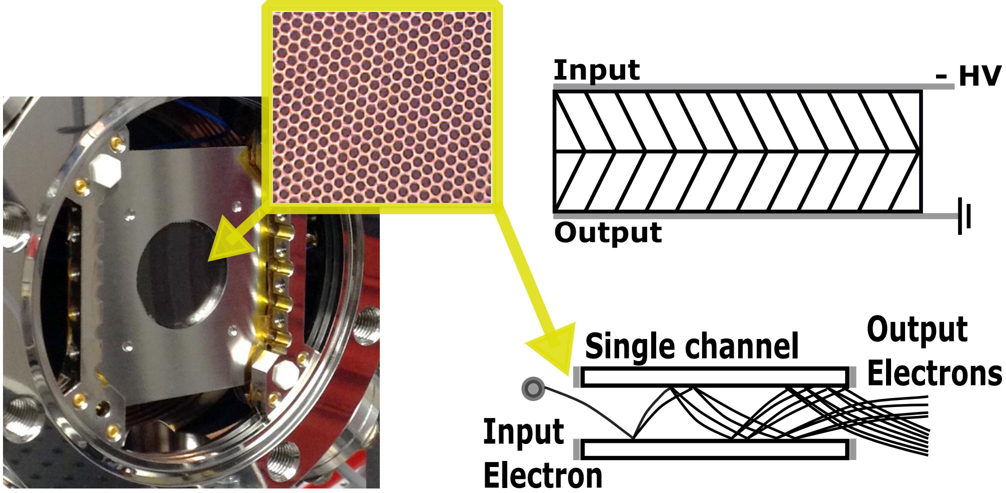

Figure 2.13: Left: photograph of the MCP assembly as it is mounted inside the detection chamber. The assembly sits on a plate that is electrically insulated from the chamber. An optical microscope image of our MCPs shows the channels in the honeycomb structure. Top right: a high voltage power supply connections with up to 2 kV across the MCP plates in the two stacked MCPs in a chevron configuration. Bottom right: schematic of the amplification of the signal through the electron cascade. The grey lines represent the electrodes.

cade of several thousand electrons that are collected by an anode, producing a strong detection signal for the particle's arrival time. [101]

In our decelerator detection chamber, we have mounted a two-stage MCP detector, as shown on the left in figure 2.13 (*Hamamatsu* compact MCP assembly F12334-11), located 416 ± 5 mm downstream from the discharge centre, with an active area with a diameter of 20 mm. The thin and flat compact assembly allows us to mount this detector very close to the exit of the decelerator tube, in order to maximise the number of detected atoms. The two MCP plates in the compact assembly are stacked in a chevron-configuration where the two plates are connected in series (top right of 2.13), a large potential difference of 1.7 kV is supplied from one side of the plate to the other with the high voltage connection to the plate and the other end grounded though the SMA grounded shielding. The highest safe voltage that can be applied is 2.1 kV, however, if the signal level is strong, the voltage must be reduced to avoid signal saturation. The signal generated by the MCPs is collected through an SMA coaxial cable that is passed through a voltage follower sitting just outside the vacuum chamber before being digitised with an oscilloscope (*LeCroy, WaveRunner* 610Zi). The voltage follower consists of a high speed buffer amplifier (*Burr Brown*, OPA633) that provides electrical impedance transformation from one circuit to another in order to match the high impedance signal coming out of the MCP to low impedance. This difference in impedance would otherwise cause signal reflection to occur as a transmitted signal is reflected back towards its origin due to differences in impedance along the transmission line. We systematically tested different chips to chose the one with a fast enough response that does not distort our MCP signal. Our voltage follower is further discussed in *Appendix B*.

2.3.2 A Stable Glow Discharge with a Pulsed Electric Discharge

Figure 2.14a shows a photograph of our discharge source with a schematic diagram illustrated in figure 2.14b. The discharge assembly consists of two circular metal electrodes separated by a 2.5 mm thick boron nitride insulating layer. Another insulating separator is placed between the high voltage electrode upstream and the valve, and one after the grounded electrode downstream in order to prevent unwanted discharges. The inner diameters of the electrodes are 4 mm and larger for the insulator separating the electrodes, which results is better discharge efficiency. [102] The live electrode is upstream and is supplied with a positive voltage pulse in such a way that, when the discharge is pulsed upon the arrival of the gas pulse, the electrons accelerate from the ground electrode to the positive electrode, against the gas flow, thus increasing the discharge efficiency. We installed a filament (AGA092, *Agar Scientific*) near the electrodes to serve as an electron emitter, providing additional electron current between the electrodes which helps to initiate and to maintain a stable discharge. The expansion can be disrupted if an object or surface is positioned too close to the valve nozzle, therefore, the filament was placed off the beam axis. In addition, it has been found that by placing the filament further downstream from the region of the electric discharge is most efficient, as further downstream is a region of lower density where the extra electrons are more essential in the stable discharge operation. A variable current power supply was made for the filament to be used with an output current in the range 0 - 3 A. A photograph of the source chamber can be seen in *Appendix D*.

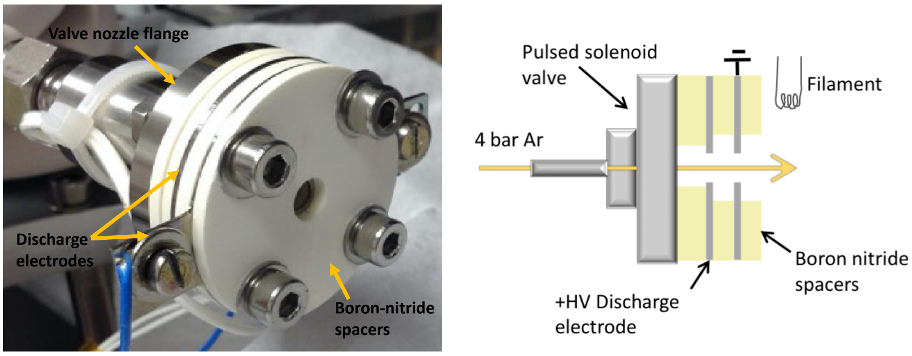

(a) (b)

Figure 2.14: a) A photograph showing the General Valve and the discharge assembly which is directly mounted onto the valve front face plate, including the discharge stainless-steel disc electrodes and the boron nitride insulating spacers which electrically isolated the electrodes from one another, as well as from the valve body. b) A schematic diagram of the discharge assembly. The spacers' thickness' from left to right are: 4 mm, 2 mm and 2 mm.

In order to operate the discharge source, a home-made power supply is used to provide power to a commercially bought 1.5 kV high-voltage pulse generator (*Directed Energy Inc.* PVX-4150 Pulse Generator) which can be used to produce high voltage pulses with fast rise times when triggered by a square trigger pulse from our pulse generator (*Quantum Composers* 9520). The high voltage pulse is then fed to the live electrode via a variable resistor (9 kΩ - 10 MΩ) with a dial that allows us to limit the discharge current to currents in the range 10 - 40 mA in order to avoid arc discharges. Additionally, the edges of the discharge electrode inner holes were polished to make them smoother in order to prevent the glow discharge from changing to an arc, that is unstable, hard to maintain, and could lead to big fluctuations in the metastable-state atom production. The high voltage pulse generator includes outputs that allow us to monitor the discharge voltage and current, a useful feature to monitor sharp spikes in current which would indicate arc discharges. Figure 2.15 shows the discharge voltage for a trigger pulse width of 75 μs (black trace), the discharge current from a single shot (red) and average over 100 (blue trace). As can be seen, the discharge current amplitude is around 40 mA. Arc discharges (not seen here) would appear as sharp peaks with peaks current values greater than 1 A.

The most precise way to measure the velocity of a pulsed supersonic jet is by changing the flight distance in vacuo by precisely defined increments,

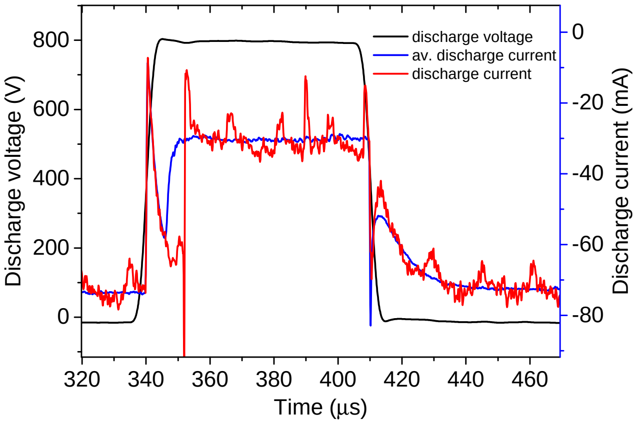

Figure 2.15: A high voltage discharge pulse applied to the discharge electrodes (black), the monitored discharge current (red), and an average current pulse (blue).

using a linear translation stage. [103] This eliminates the need to know the nozzle to detector distance. However, we simply use a measured distance of 416 mm as depicted in figure 2.16a, which shows a schematic diagram of the experiment in the Ar* beam characterisation, including a timing scheme showing the sequence of pulses involved in the operation of the discharge, as well as the discharge current. In figure 2.16b the MCP signal records the TOF distribution of the Ar* atoms, positioned 416 mm downstream from the midpoint between the discharge electrodes. The experimental procedure begins with the triggering of the pulsed valve (black trace). The red pulse is the high voltage pulse for the discharge which is triggered after a variable delay. The centre of discharge trigger pulse is taken as the point in time when the metastable state atoms are created and therefore marks the zero of time. The duration of this high-voltage pulse can be varied from widths as short as 20 μs (shortest stable discharge) up to DC. The blue trace is the discharge current and the green trace the MCP signal which shows the TOF of the Ar* atoms. For the MCP signal, the first peak corresponds to photons, which occur within the discharge time and the second peak to the Ar* atoms. By fitting a time-dependence distribution of the signal according to equation 2.8, the Ar* peak centre is used to calculate the mean velocity for a flight distance of L=416 mm. The metastable atoms could have been created at any time within the duration of the discharge voltage pulse, thus with a more defined point in time at which the metastable atoms are created, one can know this velocity more precisely.

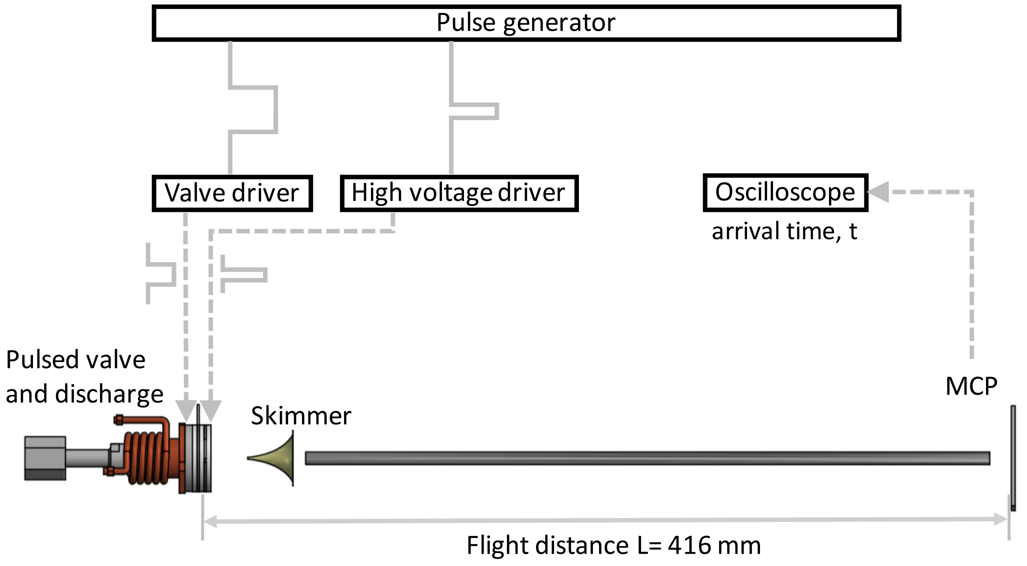

(a)

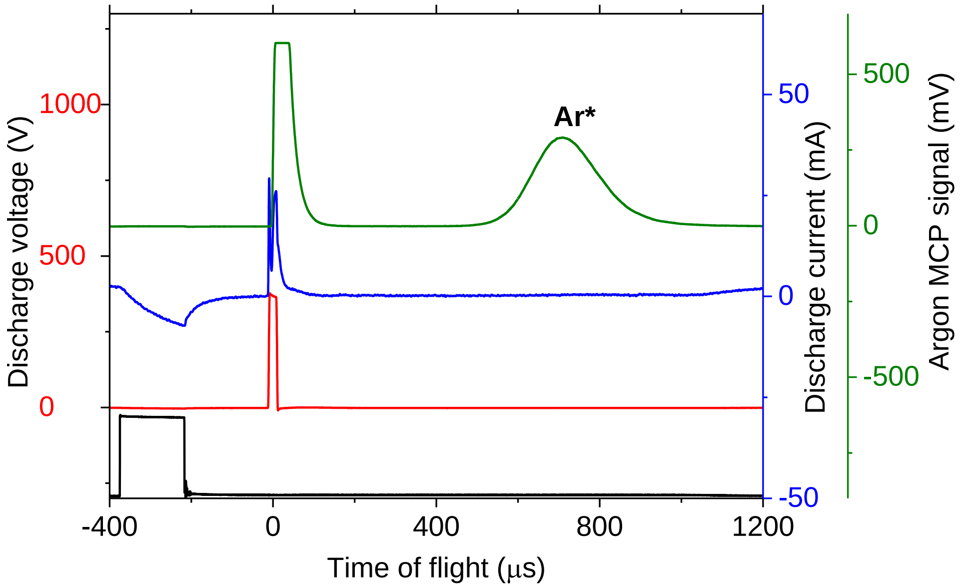

(b)

Figure 2.16: a) Timing scheme for the measurement of arrival time distribution over a distance of 416 mm in a pulsed supersonic jet experiment using the discharge excitation source showing the cooled valve, skimmer, and MCP detector downstream, including the timing of the trigger pulsed from the pulse generator. b) Plot of the trigger pulse for the valve opening (black), the high voltage pulse applied across the discharge electrodes (red), the discharge current (blue) and the detected MCP signal (green) showing the arrival time distribution for the photon signal and the Ar* peak. The centre of the discharge pulse is taken as the zero of time.

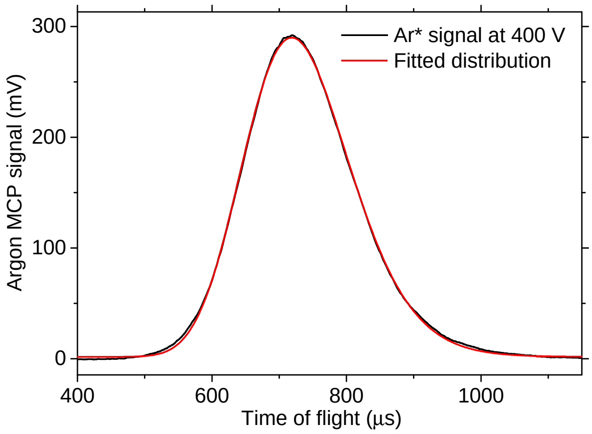

Figure 2.17: Ar* MCP signal (black) for the an optimised stable glow discharge and the fitted distribution according to equation 2.8 (red).

Once a stable glow discharge is initiated by applying a large enough voltage pulse to the electrodes with a high enough filament current, all the parameters which can be varied are optimised in order to give a strong metastable peak signal that is stable enough such that it does not vary noticeably between shots. The shot-to-shot fluctuation of the source was found to be ∼4 %. The parameters which can be varied and optimised are: valve backing pressure, discharge pulse width, discharge pulse voltage, discharge and valve trigger delays, filament current, and the variable resistor value limiting the discharge current. Initially, this was done at room temperature to characterise the discharge source. Here, the TOF of the atoms over a distance of 416 mm is from the centre of the discharge, where the metastable state atoms are created to the detector. Figure 2.17 shows an optimised signal at 330 K. Equation 2.8 on page 30 was used to fit a time-dependence distribution of the signal, from the peak centre arrival time we calculated a velocity of 565±14 m/s and a temperature of 4 k. The calculated terminal velocity for argon at 330 K using equation 2.6 is 586 m/s. This is higher than the measured velocity by 21 m/s. One reason for this could be that the supersonic expansion is not fully formed, a result of the non-optimal valve or the stack of electrodes in front of the nozzle with different diameters which manipulate the expansion. Nonetheless, this velocity is too fast for the electronics to be able to produce such fast moving traps. However, this can be reduced to a more desirable velocity by cooling the valve and the discharge assembly, as described in section 2.2.1.

2.3.3 Slow Beam of Ar*

Measurements were made to characterise the discharge source at cryogenic temperatures in order to obtain an optimised slow beam of Ar*. The valve was first cooled-down using the procedure described in section 2.2.1 A valve opening trigger pulse width of 128 μs was chosen from optimising the signal on the FIG while maintaining a source chamber background pressure of 1×10^{-5} mbar. The Ar* signal was optimised by varying the different discharge parameters: discharge pulse width, the valve-to-discharge delay, the discharge-stabilising filament current, the discharge current, the discharge voltage and the backing pressure. The optimum discharge pulse width is the shortest one which can be stabilised. This is because having the discharge on for shorter times heats the beam less. Additionally, a shorter discharge lowers the uncertainty in the velocity and also gives a translationally colder beam. Furthermore, shorter discharge pulses ensure that only one decelerator trap will be filled at a time. The optimum valve-to-discharge delay is chosen such that the discharge pulse is applied in the centre of the gas pulse where the intensity is highest. The discharge current can be varied by varying a variable resistor between the high voltage pulse output and the live electrode. The optimum resistor value is chosen in such a way that the discharge can be stabilised with a strong Ar* signal and no arching. This was found to be using a resistance of around 10 kΩ.

In the following results graphs, both the effect of varying the discharge voltage and the backing pressure on the Ar* signal were measured. The averaged signal over 100 shots is plotted for each data set and the signal is analysed to give the integrated area (a relative measure of the number of Ar* atoms in the gas pulse), the translational temperature by fitting equation 2.8 (on page 30) and the mean arrival time from which the velocity is calculated using a flight distance of L = 416 mm.

One of the most important parameters in the operation of the discharge is the discharge voltage since varying the discharge voltage has a big effect on the nature of the discharge, and could cause the discharge to transition from a stable glow, to an unstable arc discharge. Figures 2.18a and b show the effect of varying the DC voltage on the Ar* signal. The general trend that can be seen is, that more Ar* atoms are produced which have a higher mean velocity with increasing discharge voltage. This is expected since, at

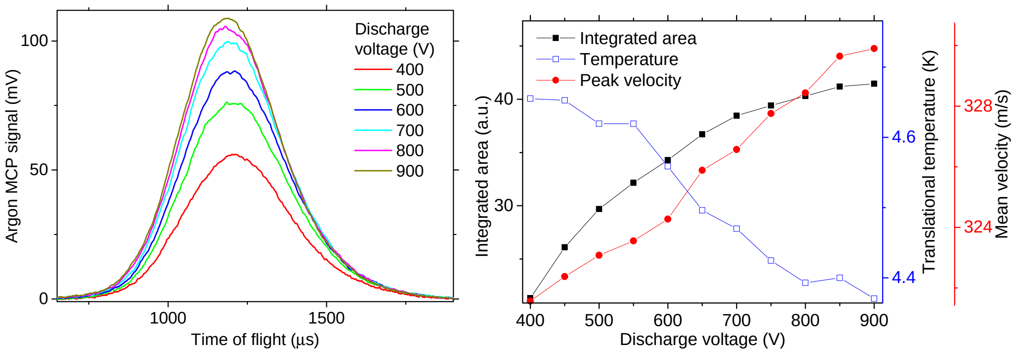

(a) (b)

Figure 2.18: a) Detected Ar* signal for different discharge voltages. Inset: discharge current for the corresponding voltage values. b) Integrated area (black), translational temperature (green) and mean velocity (orange) of the Ar* signal.

higher voltages, the electrons are more energetic and, thus, they are more likely to ionise or excite the atoms. When operating the discharge, one has to compromise between using a lower voltage or a shorter discharge pulse. Shorter discharge pulses are more stable at higher voltages. However, higher voltages could lead to arc discharges, which can heat the beam and lead to signal instability. Finally, the slight decrease in the translational temperature could be explained by the increasing number of Ar* atoms at higher voltages. These lead to more collisions in the region between the electrodes, resulting in more effective cooling as they supersonically expand into the source chamber. The optimum voltage is chosen to be the lowest one which can give a stable enough discharge with a good signal-to-noise ratio.

Figures 2.19a and b show the effect of increasing the argon backing pressure on the Ar* signal where the number of Ar* produced initially increases with increasing pressures, leading to higher densities. At pressures higher than 2.6 bar, the signal starts to decrease, as illustrated by the decreasing integrated area (black line), a result of the increased density leading to the collisional quenching of the metastable states from collisions between the excited atoms and the neutral atoms. The translational temperature and mean velocity both increase with increasing pressure. These behaviours are most likely due to the valve operation dependence on the backing pressure. Increasing the pressure leads to a more complete supersonic expansion which results in a faster beam.

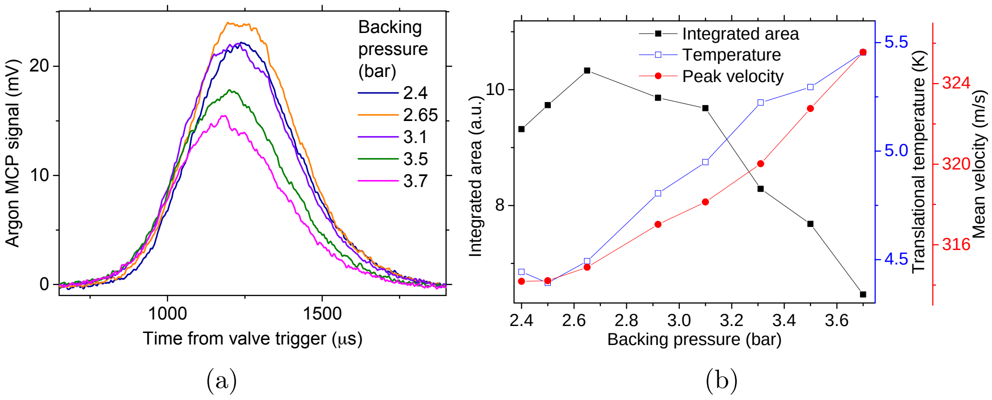

(a)

(b)

Figure 2.19: a) Detected Ar* signal at different valve backing pressures b) Integrated area (black), translational temperature (green) and mean velocity (orange) of the Ar* signal.

Figure 2.20 shows an optimised signal at 115 K. The operating conditions were: 128 μs valve trigger pulse width, 20 μs discharge pulse width at a voltage of 400 V, 2.5 bar backing pressure, 1.3 A discharge filament current, and a discharge current-limiting resistor of 9 kΩ. Equation 2.8 on page 30 was used to fit a time-dependence distribution of the signal, from which the mean arrival time was used to calculate a velocity of 306±8 m/s and a temperature of 4 K. The signal was found to be stable over a time duration of more than several minutes, provided the valve temperature can be kept constant. The terminal velocity for argon at 115 K was calculated using equation 2.6 (on page 28) is 345 m/s. This is higher than the measured velocity by 39 m/s.

However, it is important to remember that the current calculations for supersonic beams are for continuous beams. For short pulses, the attainment of quasi-continuous stationary flow is mandatory when a meaningful value of beam temperature or flow velocity is required. Very short pulses do not allow for the evolution of stationary flow and, therefore, result in the incorrect theoretical calculation for the beam properties. This issue was addressed in a paper by Christen et al., where they demonstrated that the equivalent behaviour of a continuous nozzle-source could be achieved in a restricted section of the gas pulse. [104] One requirement for a complete expansion, with optimum translational cooling is, that the valve needs to be fully open, in such a way that the gas flow rate is limited by the orifice diameter and no other obstructions. The flow needs to reach a steady-state condition where one reaches maximum mass flow within the pulse width. However, in the Gen-

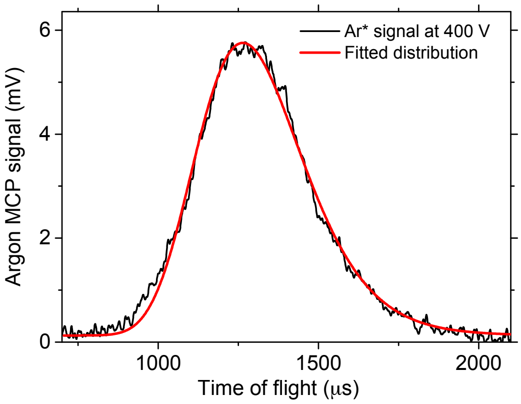

Figure 2.20: Optimised Ar* signal (black) for a stable glow discharge and the fitted distribution using equation 2.8 (red).

eral Valve design, the nozzle-sealing poppet never retreats far enough into the valve to allow this. Thus, the expansion is not complete, either from the discharge assembly attached to the nozzle with the different inner diameters, or from the non-optimal operation of the valve at cryogenic temperatures. When the discharge was operated at 330 K, the difference in the measured and calculated velocity was only 21 m/s. This supports the suspicion of the non-optimal operation of the valve contributing to the incomplete expansion which gives a slower and translationally hotter beam.

The time-dependence distribution of the signal that were fit to the TOF data using equation 2.8 (on page 30) are good expect for the faster end of the distribution. In order to measure the temperature, one would ideally use two detectors separated in distance along the molecular beam path. With a single detector placed far from the source, an upper limit that is close to the temperature can be determined. The TOF profile is a convolution of the function of the time spread due to the temperature and the initial width which is determined by the discharge pulse width. This results in the width of a single TOF profile that can only give an upper limit to the temperature. However, since the detector is sufficiently far from the source, this upper limit is very close to the true temperature.

2.4 Conclusions and Requirements of the Decelerator

In conclusion, we have developed and characterised a controllable discharge-based source of Ar* atoms. The introduction of a hot filament into the source chamber allows the discharge to operate more stably and at a lower voltage, reducing the heating of the Ar* atoms during their production. We can operate the discharge at voltages as low as 400 V and discharge pulse durations as short as 20 μs, which together combine to create a colder packet of Ar* atoms. This source will be used to test and optimise the decelerator. The optimisation of the cold valve required the development of a home-made FIG which allows us to characterise the valve at different temperatures and operate it at optimum conditions. The excitation source that was developed was an electric discharge that was successfully stabilised with a filament. The need for producing a beam of Ar* atoms with a low mean velocity will be further discussed in chapter four. The main aim of the development of the source for the decelerator was to obtain a slow enough beam of a metastable-state rare-gas source with low-field-seeking states that can be captured by the decelerator traps, bearing the limitations of the decelerator electronics. Our decelerator would benefit from having an Ar* beam with both a low mean longitudinal velocity and a high phase-space density. The optimised slow beam in figure 2.20 has a velocity of 306±8 m/s and a translational temperature of 4 K. In decelerators, ideally one wants to match the decelerator acceptance to the emittance of the source. We want the pulsed source of molecules to be narrowly distributed both in position and velocity. The contributions to the spread in the arrival times of the atoms or molecules are: the temporal spread of the signal at the detector, the spatial spread at the source, the forward velocity distribution in the pulse, and the temporal resolution of the detector. The temporal resolution of the MCPs is small enough that it can be neglected.

In 1D, there is one degree of freedom, therefore, kT is equal to the kinetic energy, thus

$$kT = \frac{1}{2} m \sigma_{\mathrm{v}}^2, \tag{2.9}$$

where σ_{v} is the velocity spread, m is the mass, and T is the translational temperature. We can capture and decelerate the M_j=1, 2 low-field seeking states of the $^3P_2$ metastable state. The Landé factor for the $^3P_2$ state is 1.5 which leads to an effective magnetic moment of 3 Bohr magnetons for the M_j=2 and 1.5 Bohr magnetons for M_j=1 state. Using the Zeeman shift (equation 1.1, page 14, chapter 1) in the $^3P_2$ state of argon, the magnetic field required to produce traps depths for a specific translational temperature can be written as

$$B = \frac{\frac{1}{2}m\sigma_v^2}{\frac{3}{2}M_j\mu_B} = \frac{kT}{\frac{3}{2}M_j\mu_B}. \tag{2.10}$$

For our optimised cold beam with a temperature of 4 K (40 m/s velocity spread), equation 2.10 gives a field of 1.98 T for the M_j=2 state and 3.97 T for the M_j=1 state. These fields are rather high and challenging to produce at the required frequencies for our limited electronics. A colder source of Ar* beam with a translational temperature of 1 K would only require a trap depth of 2 T to trap both low field seeking states, a more achievable target. Chapter 4 will discuss the fields and currents (500 A peak) produced by our coils and the electronics restriction which currently limits our trap depths to 0.7 T, or 1.4 K for the M_j=2 state and 0.7 K for the M_j=1 state.

Simulations of the magnetic fields will be discussed in chapter 4. For our target 1 m length decelerator, the deceleration required to decelerate a 306 m/s beam to a standstill is 4.68×10^4 m/s^2. For a 100 mK trap depth target at the end of the deceleration, the initial trap depths need to be 1.74 K for the $M_j = 2$ state which corresponds to fields and currents of 0.86 T and 616 A and 3.47 K for the M_j=1 state which correspond to a peak field of 1.72 T and current of 1231 A. A matching source emittance must, therefore, not be hotter than 3.47 K in order to capture both M_j sub-levels. This in clearly colder than the source we have. However, the decelerator traps will still capture some of the velocity which are within the decelerator acceptance.

Ideally, the decelerator trap velocity must match the mean velocity of the beam. In order to match the trap velocity to the mean velocity of the gas pulse, the field producing currents in the decelerator coils need to be modulated at frequencies of around 7 kHz (discussed later). For the decelerator, beams with slower initial mean velocity are more efficiently decelerated as the deceleration force used is smaller, and thus, a smaller deceleration is expected to lead to much smaller loss from the pseudo deceleration potential that lowers the trap depth.

As well as the velocity matching of the decelerator traps to the source, the decelerator traps must also be spatially matched. The spatial extent of the spacing between the electrodes is 2.5 mm. With a forward velocity of 306 m/s, the time it takes to get to the first decelerator trap is 292 μs. With a translational velocity spread of σ_v =40 m/s, the spatial spread at the first trap should be is ~30 mm. We will later see that the spatial extent of the decelerator traps in the longitudinal direction is smaller than this.

Chapter 3

An Alternative Short-Pulsed Valve

This chapter presents the characterisation of our homebuilt cantilever piezo valve. The widely used solenoid-based General Valve is unable to produce short gas pulses, motivating us to develop a cantilever piezo valve. This type of valve can produce short gas pulses which allow the matching of the acceptance of the small decelerator traps with the short gas pulse. One problem encountered with the General Valve is the insufficient retreat of the closing stem, preventing the valve from fully opening, as discussed in the previous chapter. Furthermore, using a shorter gas pulse allows the use of higher backing pressures, producing a more intense supersonic beam with a narrow velocity distribution (i.e. a translationally colder beam). The piezoelectric ceramic is characterised by carrying out response-time measurements as well as displacement measurements at different driving electric field strengths, using a confocal microscope with static DC electric fields measurements, and while pulsing the cantilever piezo with pulsed electric fields. Finally, our homebuilt FIG detector is used to characterise the gas pulse.

3.1 A Cantilever Piezo Valve

As discussed in the previous chapter, pulsed supersonic beams have advantages over continuous beams, including sample consumption, the reduction of pumping requirements of the vacuum apparatus, signal intensity and transla-

Operation mechanism	**Pulse width (μs)**	**Reference**
Cantilever piezo	>7	[88]
	60	[108]
Electromagnetic plunger	>10	[109]
	30-100	[110]
	30-150	[111]
Lorentz force	>10	[87]
	50	[112]

Table 3.1: A collection of three different types of fast valves used in the production of pulsed supersonic beams showing the pulse width and a reference to the article it was taken from.

tional cooling. Additionally, pulsed beams allow the synchronised seeding of molecules into supersonic beams by pulsed laser photolysis. Table 3.1 shows a collection of three different types of fast valves used in the production of pulsed supersonic beams along with the pulse width and a reference to the article it was taken from. While comparing the performance of pulsed valves, one must consider the moving parts of the valve mechanism and the effective opening and closing of the valve determining the actual shape of the gas pulse. There are a few valves described in the literature which use piezo ceramics. For instance, the piezodisk pulsed valve is based on a cylindrical piezo disk which is flexed when a voltage pulse is applied and is able to produce pulse widths of about 100 - 150 μs at repetition rates of up to 1 kHz. [105] These valves use mechanisms that are relatively slow and preclude in general the production of pulses shorter than 100 μs. Over the past few decades, various designs of pulsed valves have been developed, with the aim of decreasing the pulse duration. One of these sources is the cantilever piezo valve, numerous designs of which have been used to produce short pulsed supersonic beams. [106, 107] From the given types of valves, the cantilever piezo valve is the one with the simplest design, which is the main motivation behind choosing this valve. Our design resembles that of the cantilever piezo valve, developed by D. Irimia *et al.*, which is capable of producing 7 μs FWHM pulses at high repetition rates of 5 kHz. This fast valve was demanded by the high repetition rate laser systems they were using, with frequencies well above 1 KHz. [88]

The theory of continuous supersonic beams was discussed in the previous chapter. For short pulses, the attainment of quasi-continuous stationary flow is mandatory when a meaningful value of beam temperature or flow velocity is required. This is because the current model calculations for supersonic beams assume a continuous, steady-flow. However, very short pulses do not allow for the evolution of stationary flow, and therefore result in the incorrect theoretical calculation for the beam properties. This issue was addressed in a paper by Christen *et al.* only in 2013 despite the wide-spread use of fast-acting valves producing short gas pulses. [104] The predictions are often based on the assumption that the gas is ideal and the valve behaviour is ideal. Christen *et al.* demonstrated that the equivalent behaviour of a continuous nozzle-source could be achieved in a restricted section of the gas pulse. One requirement for a complete expansion is, with optimum translational cooling; the valve needs to be fully open, in such a way that the gas flow rate is limited by the orifice diameter and no other obstructions. This is referred to as "choked flow". The flow needs to reach a steady-state condition where one reaches maximum mass flow within the pulse width. As discussed in the previous chapter, in the General Valve design, the nozzle-sealing poppet never retreats far enough into the valve to allow this.

In addition to the physical requirement of the opening of the valve, there is a minimum opening time required for the pulsed valve to achieve a constant flow velocity. For example, once the valve is open, a further time is required to reach uniform flow velocities within the central section of the gas pulse. This is the time interval required for the flow to reach a steady condition. [113, 114] It depends on the nature of the gas and on the source parameters, such as pressure, temperature, and the diameter of the source orifice. It is the minimum limit on the pulse duration which is required for a pulsed nozzle to produce a supersonic beam comparably ‘cold’ to that obtained from a continuous flow nozzle source. The minimum time required for the valve to completely open is the sum of three terms: the ‘initiation’ time required for the gas behind the nozzle to be accelerated to the sonic exit velocity, the time required to establish a buffer zone containing sufficient molecules to act as collision partners during expansion (assuming continuous flow conditions) and the time for which the pulse must be on to ensure that, in the region over which the expansion takes place, the density in the buffer zone is not diminished by the velocity dispersion at the pulse edges. For valve opening times longer than this sum, the terminal velocity and temperatures are independent of the pulse length. This minimum time required to produce

Gas species	**Pressure (bar)**	$\Delta t_{min}(\mu\text{s})$
He	0.27	2.5
	2.7	4.1
Ar	0.27	9.0
	2.7	15.1
Ne	0.27	7.6
	2.7	18.1

Table 3.2: Minimum pulse durations predicted by the sudden freeze model for a 0.5 mm nozzle diameter at temperature of 300 K. Tabulated values taken from a reference. [113]

a complete expansion is tabulated in table 3.2; for helium, argon and neon. [113]

3.2 The Design of Our Piezo Valve

Before piezoelectric ceramics can be operated, they are poled; causing the domains to be oriented in a certain direction. In a series configuration, illustrated on the left in figure 3.1, the two piezo layers are oppositely polarised in such a way that when a field is applied, it gives rise to oppositely directed transverse strains, resulting in the bending of the free end. On the other hand, a parallel-poled bimorph, shown on the right in figure 3.1, has two layers that are polarised in the same direction. In this configuration, the applied electric field across the two piezo layers can be applied in a way such that it is always along the poling direction, allowing the use of very high fields to give bigger deflections. In addition, when the piezo is driven at high field strengths, we benefit from the nonlinear static response of the piezoelectric material, shown to be due to mechanical domain reorientation as studied by Yao *et al.* [115] In contrast to series poled bimorphs, the deflection per applied voltage is greater by a factor of two for the parallel-poled bimorphs because the full driving voltage is applied across each plate.

For a linear response and static operation, the deflection of a cantilever, δ, can be expressed as [116]

$$\delta \propto d_{31}\frac{l^2}{t}, \tag{3.1}$$

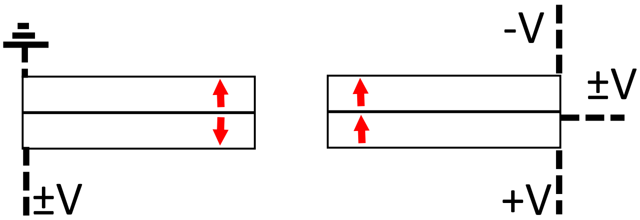

Figure 3.1: Cantilever piezoelectric ceramics in series (left) and parallel (right) configuration, showing the difference in the way in which the electric field is applied. The red arrows indicate the direction of the poling field. With the sealing silicone glued to the bottom face of the piezo, for the parallel biomorph (right), a negative voltage would seal the valve nozzle while a positive voltage would open it.

where l is the free length, t is the total thickness of the cantilever, and d_{31} is the transverse piezoelectric coefficient. The first natural resonance frequency, ν_1, can be written as

$$\nu_1 \propto \frac{t}{l^2}. \tag{3.2}$$

The blocking force, F_{bl}, for a cantilever piezo with a width w, is given by

$$F_{bl} \propto \frac{wt^2}{l}. \tag{3.3}$$

Expressions 3.1 and 3.3 show that both the blocking force and the displacement are strongly dependent on the dimensions of the cantilever piezo. Since we want to design a valve that will allow stationary flow conditions, large displacements are required. In the design of Gerlich *et al.*, [106] the free length was 8 mm with a resonance frequency of 3.6 kHz. In the valve of Irimia, [88] the free length was reduced to 6 mm to be able to operate their valve at a repetition rate of 5 kHz, the resonance frequency had to be well above this (at 7.7 kHz in their case). The deflection of the cantilever piezo scales with the square of the free length, therefore, any reduction in the free length leads to a great loss in the defection. Since the original cantilever piezo valve by Gerlich, new ceramics have emerged with bigger piezoelectric coefficients, enabling bigger displacements at smaller applied electric field strengths.

For our application in the 1-5 bar backing pressure range, we aimed for an optimal compromise of the design of the cantilever between sufficient displacement and a sufficient blocking force. In terms of resonance frequency, we will only operate the valve at the highest frequency of 10 Hz, therefore we do not require the resonance frequency to be high, thus we can have a cantilever with a long free length to give large displacements. Simple calculations were carried out to find the ideal piezoelectric ceramic for our purposes using the exact form of equations 3.1-3.3 given in the reference [116]; different types of ceramics were compared with different transverse piezoelectric coefficients. The force of the silicone disc against the nozzle is 0.88 N for a 1.5 mm effective exit diameter (from the cone) and a backing pressure of 5 bars. Thus, the blocking force must be greater than this in order to allow the valve to open. For even higher pressures of 10 bars this would be 1.76 N. Having the internal nozzle with a larger diameter is advantageous for choked flow, but it also means that a bigger blocking force is required for the valve to open. The optimum dimensions were chosen for the piezoelectric ceramic to give a blocking force of 1.2 N, a 1 kHz resonance frequency and the maximum displacement possible.

When operating piezoelectric ceramics, the transverse piezoelectric coefficient determines the deflection. We chose a parallel-poled PZT507 from *Morgan Electroceramics* as it has one of the largest piezoelectric constants, quoted at a value of 360×10^{-12} m/V by the manufacturer. [117] The design of our homebuilt piezo valve is displayed in figure 3.2; it is based on the original valve by Gerlich *et al.* [106] and resembles the valve by Irimia. [88] Initially, we made a prototype of the Gerlich valve since we had some series-poled piezo bimorph samples at hand, and then we moved to the newer design based on the one by Irimia with the main difference being a copper gasket to seal the valve body instead of an O-ring, in order to allow the cryogenic cooling of the valve. The knife edge that cuts into the copper gasket can be seen in the photograph in figure 3.2a. Unlike the valve by Irimia *et al.*, our homebuilt valve was designed to operate both at room and cryogenic temperatures, although to date, the testing and characterisation have only been carried out at room temperature.

The photograph in figure 3.2a shows the inside of the valve with the piezo cantilever clamped down. In order to make the electrical contacts, the wires were soldered on the gold plated contacts. When soldering, the heat must not be kept on for too long (<2 s) to avoid the risk of local depolarisation. This

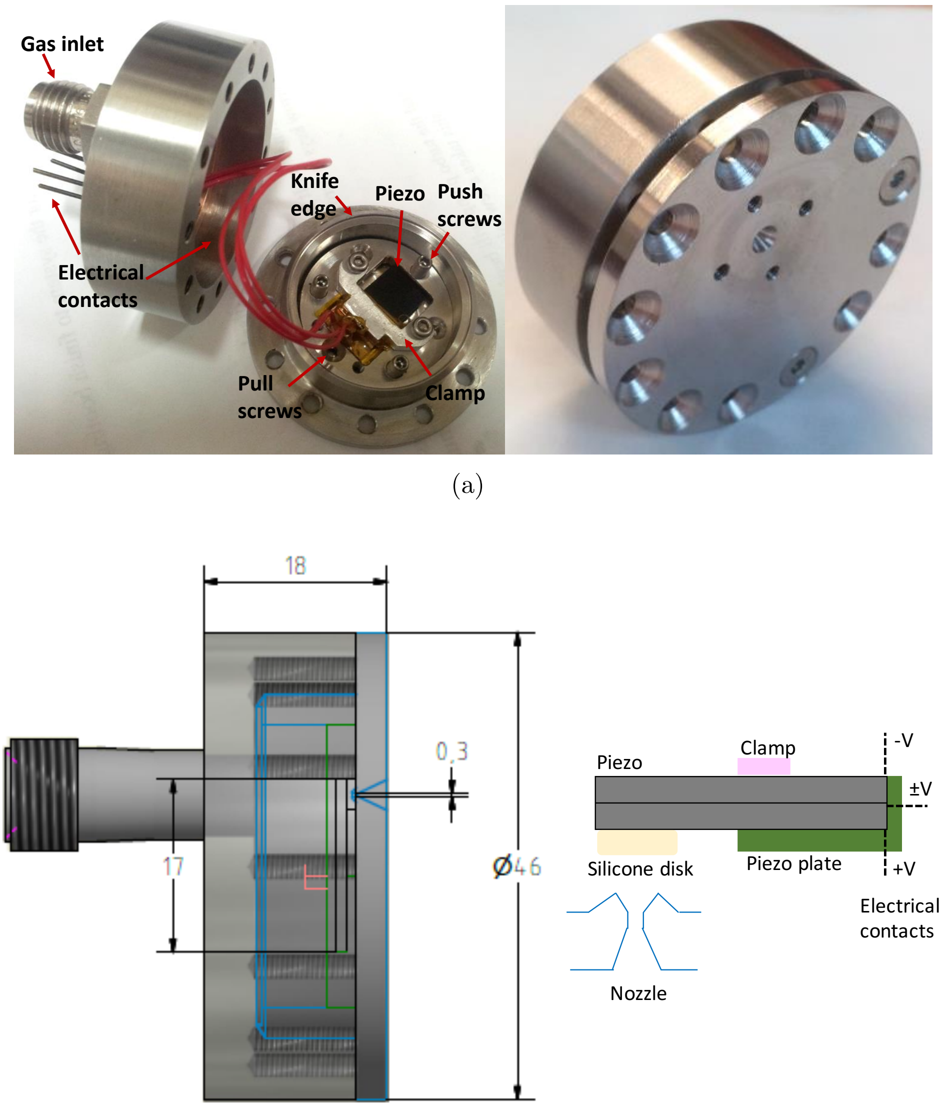

(a)

(b)

Figure 3.2: a) A photograph of our homebuilt cantilever piezo valve with the opened valve on the left, showing the electric contacts on the clamped piezo, and the closed valve on the right with an outer body diameter of 46 mm. The adjustment screws ("push" and "pull") used to adjust the nozzle-to-silicone disk distance are labelled. The silicone disk, which forms a vacuum seal to the nozzle, is glued onto the back-side of the piezo. b) Left: a schematic diagram of the inside of the valve, showing the relevant valve dimensions (in mm). Right: a schematic of the piezo as it is clamped inside the valve. The the nozzle is shown in blue, the plate the piezo sits on in green, the nozzle-sealing silicone disk in beige and the clamp in pink. The width of the piezo is 10 mm, the total length is 17 mm and the free length is 9-10 mm. The nozzle has an opening diameter of 0.3 mm, and a conical shape with a full angle of 40°.

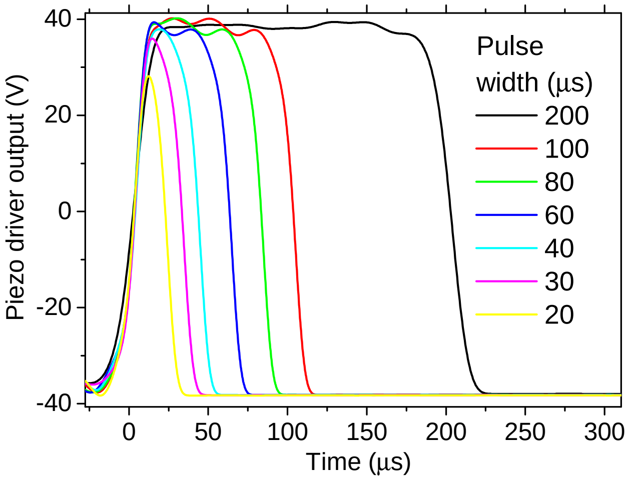

Figure 3.3: The measured voltage output from our homebuilt piezo-driver box for different input trigger pulse widths when switching between -38 V and +38 V.

valve design has sufficient space inside in order to ease the clamping of the piezo, furthermore, the free length of the cantilever can also be varied since the stage on which the piezo rests can be changed. The adjustment screws ("push" and "pull") used to adjust the distance from the sealing silicone disk to the nozzle can also be seen. Figure 3.2b shows a schematic diagram of the valve, showing the relevant valve dimensions, the piezo in black, the nozzle in blue, the step the piezo sits on in green and the clamp in pink. The total length of the piezo is 17 mm whereas the free length is 9-10 mm. The nozzle has an opening diameter of 0.3 mm, and a conical shape with a full angle of 40°. The cantilever and the sealing silicone pad attached to the tip are the only moving parts. The nozzle geometry was found to have an effect on the gas pulse properties in the measurements carried out by Even *et al.* Using the Even-Lavie valve, it was concluded that a conical shape of about 40° is a good compromise between the maximum forward centre line beam intensity and efficient translational cooling. [118]

Our homebuilt piezo-driver box requires a trigger pulse. In all of our experiments, we use the same pulse generator (*Quantum Composers*) in order to produce a square pulse whose width can be adjusted. The amplitude of the driver pulse determining the applied electric field strength can be varied on the homebuilt piezo-driver box. The output from our homebuilt piezo-driver box has been plotted for different trigger pulse widths in figure 3.3; the voltage pulse switches from a negative voltage to a positive voltage for short time durations. The piezo valve is pulsed by applying a voltage pulse from the piezo-driver box alternately to each piezo layer by applying a constant voltage to the top and bottom layers (at $+V$ and $-V$) and switching the middle contact between $-V$ and $+V$, as illustrated on the right in figure 3.2b. In this arrangement, the field being applied is always in the same direction as the poling field. The driven layer contracts when an electric field is applied, while the other layer remains the same, forcing the piezo to bend. A silicone disk seals the nozzle when the piezo bends downwards, on the application of a negative voltage to the middle layer. With our piezo dimensions, and using our homebuilt piezo-driver box, the highest voltages applied result in fields of around 1400 V/mm. In figure 3.3, it can be seen that, for the shorter pulses, the pulse is not at the set high voltage since the rise time is not fast enough to supply the peak voltage for the specified time duration.

3.3 Operation and Characterisation of the Valve

The first step towards making the valve operational was to seal the nozzle, and then the valve body. The molecular beam machine used was described in some detail in the previous chapter and will be described in more technical detail in chapter four. The nozzle-sealing silicone disk was glued onto the tip of the piezo using torr-seal. An adaptor was made to allow the sealing of the valve nozzle against the chamber in order to use it as a leak tester. This enables the adjustment of the silicone-pad-to-nozzle distance outside the vacuum, while the valve is open by using both sets of the adjustment screws displayed in figure 3.2a. First, the valve nozzle was sealed against a vacuum chamber down to the base pressure of our source chamber (10^{-7} mbar). In order to seal the nozzle, the "push" and "pull" screws that were shown in figure 3.2a were adjusted in such a way that the nozzle was sealed to the base pressure of the chamber; the piezo driver was switched on i.e. a DC voltage was applied to one layer such that the piezo was bent towards the nozzle, consequently sealing it. The two set of screws were then adjusted in such a way that when the valve was pulsed with a 100 μs opening time, the pressure increased, and when this width was varied, the pressure increased or decreased accordingly.

Once the piezo valve was sealed, the temporal profile of the gas pulse was characterised by using our homebuilt FIG detector inside the source chamber,

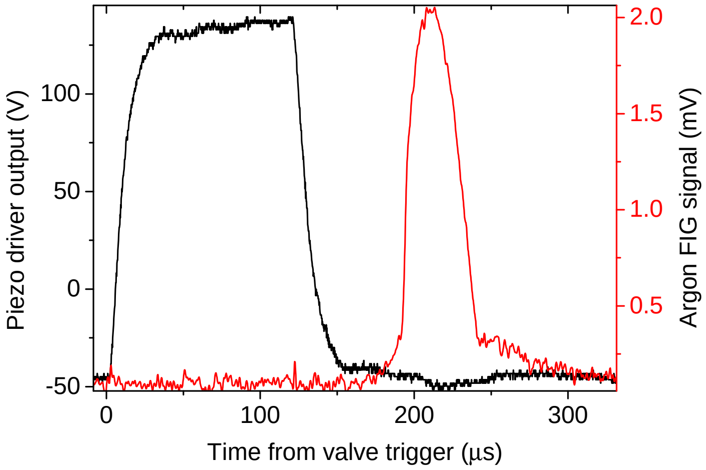

Figure 3.4: Piezo-driver box output with a trigger pulse width of 120 μs (black line), and the detected FIG signal showing the temporal profile of the gas pulse with a FWHM of 32 μs at a distance of 20 mm from the nozzle. The applied electric field strength across the piezo was 727 V/mm. The backing pressure behind the nozzle was 2.1 bar.

positioned at about 20 mm from the nozzle, as it was described in chapter two. The FIG was rotated in such a way that it was positioned at the point where the most intense signal was seen. When the valve was placed inside the chamber, the electrical feedthroughs were found to be leaky from over pressing them, and therefore torr-seal had to be used in order to seal the valve body. When the valve was operating at 10 Hz, the source chamber pressure was 1×10^{-5} mbar. The graph in figure 3.4 shows the high voltage pulse output from our homebuilt driver (in black) and the detected argon FIG signal (in red); the opening trigger pulse width was 120 μs with a total applied electric field across piezo of 727 V/mm, giving a pulse width with a FWHM of 32 μs. The backing pressure behind the nozzle was 2.1 bar.

We characterised the valve by comparing two different gases since the valve behaviour is also gas dependent as the viscosity of the gases are different. Initially, the valve was characterised by using nitrogen gas due to occasional sparking of the piezo, which produced more discharges at higher electric fields than those when argon gas was used. When we were driving the piezo at high field strengths for argon, we observed some irregular behaviour, and at times, the failure of the piezo. In order to avoid any irregular behaviour, the piezo was driven at lower applied electric fields when necessary. Figure 3.5a shows the effect of changing the pulse width on the temporal profile of the gas pulse for nitrogen. The applied electric field strength across the

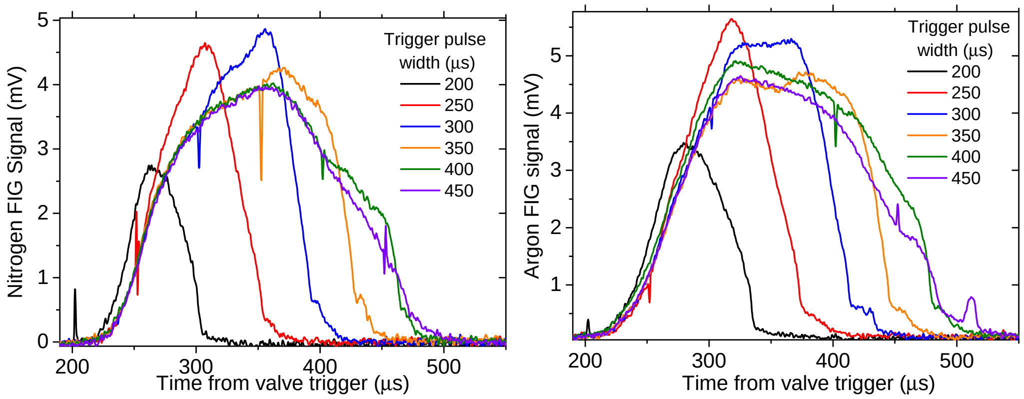

(a) (b)

Figure 3.5: a) Nitrogen FIG signal for different opening trigger pulse widths at an applied electric field of 869 V/mm and a backing pressure of 3.1 bar. b) Argon FIG signal for different driving trigger pulse widths at an applied electric field of 727 V/mm and a backing pressure of 2.1 bar.

piezo valve was 869 V/mm. The gas pulse intensity and width increases with increasing driver pulse width as increasing the duration of the voltage pulse allows the piezo to move further away from the nozzle, allowing more gas through the nozzle. The symmetry starts to be more distorted for longer opening durations, where a shoulder starts to emerge on the closing of the valve. After a trigger pulse width of 400 μs, the gas pulse does not appear to change as the piezo does not bend any further at this fixed voltage, and therefore, the detected gas pulse does not change. At this point, the piezo has enough time to reach the maximum possible displacement from which one could conclude that the highest flow has been achieved. This trend was repeated for argon, as shown in figure 3.5b, as the trigger pulse width is increased from 170 μs, the width of the gas increases as well as the intensity since the piezo moves further back. The intensity no longer increases after a driving pulse width of 300 μs after which only the width increases. As seen in the measurements with nitrogen, the increase in the width stops between 350 μs and 400 μs. The integrated area for these traces has been plotted in figure 3.6a, which further illustrates that the gas flow reaches a maximum for a driving pulse width of at least 400 μs.

One thing which can be noticed in figures 3.5a and b are the spikes in all of the traces which correspond to the falling edge of the applied voltage pulse. Another thing which can be noticed for both sets of data is that the signal

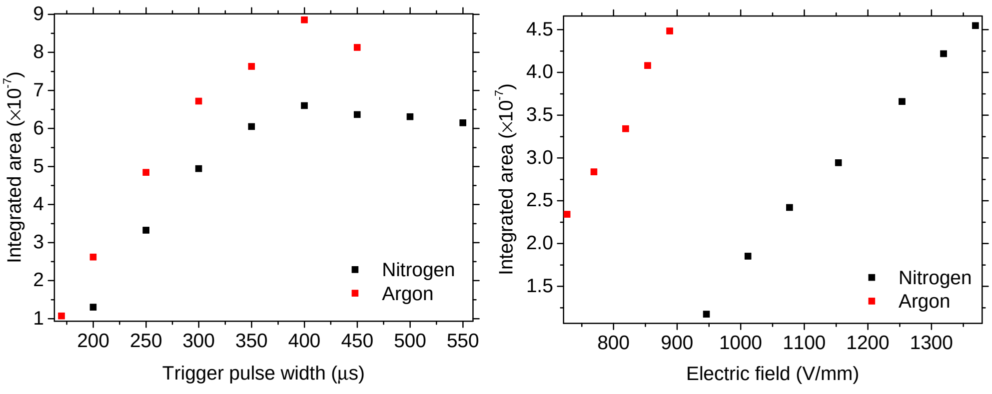

(a) (b)

Figure 3.6: Integrated area of the FIG signal for nitrogen (black squares) and argon (red squares) at a) different driving pulse widths and b) different applied electric field strengths. The operating conditions for a) are given in the caption of figure 3.5. The operating conditions for b) for nitrogen were: 200 μs driving pulse width, and 3.1 bar backing pressure, and for argon: 200 μs driving pulse width, and 2.1 bar backing pressure.

after the spike changes in the same manner for both data sets. This can be explained by considering how the piezo responds to the voltage pulse. If we consider argon, the terminal velocity at room temperature is 550 m/s, thus the gas pulse would take about 36 μs to travel a distance of 20 mm from the nozzle to the FIG. Figure 3.5b clearly shows that the signal begins to rise 200 μs after the valve trigger. Therefore, the response time of the piezo is around 160 μs. For the shorter applied voltage pulses in the range 200-300 μs, there is a clear overshoot after the apparent spike in the traces. For the longer voltage pulses in the range 350-450 μs, a shoulder appears after the spike. This is because when the piezo starts to respond to the voltage pulse, the applied voltage bends the piezo to the position that the piezo can be deflected to at that voltage. The deflection of the piezo tip is linearly proportional to the applied electric field strength (applied voltage). Once the trigger pulse switches off, the applied voltage no longer holds the piezo at that position, thus the piezo is able to bend further from the momentum, resulting in the increased signal, as seen in all traces in figures 3.5a and b.

Examining figure 3.5 again, the height of the almost flat region in the gas pulse for some of the traces does not increase in intensity if the driving pulse width is increased further. For short pulses, the gas pulse shape is more triangular. It has been argued that the true indication of choked flow is not just from the presence of a plateau in the gas profile, but also a constant translational temperature and velocity in this plateau region. [104] Christen *et al.* showed that stationary flow conditions could be experimentally determined in pulsed supersonic beams. Two universal conclusions were made by Christen et al: the first is that continuous flow should be linked to constant flow velocity rather than constant density while the second is that the opening times are much longer than the standard practice for fast acting valves. It was found that the translational temperature and the mean terminal velocity are more important in determining this criterion. They also discovered that constant density was reached faster than maximised cooling and constant velocity. Our FIG detector was placed too close to the nozzle exit in order to determine the time-of-flight profile from which translational temperatures could be determined. Furthermore, for short opening times, a uniform particle density is difficult to judge with a small resolution, i.e. thin slicing with high resolution is required.

The piezo tip displacement can be increased by increasing the applied electric field strength. Figure 3.6b shows the integrated area of the FIG signal at different applied electric field strengths for argon (red squares) and nitrogen (black squares). As expected, more gas is released for both species with increasing electric field strength as the piezo can bend further away from the nozzle, allowing more gas through the nozzle for a longer time. If the electric field could be further increased, one would expect to see the points levelling off. This would indicate that a maximum flow has been reached. However, a higher electric field could not be used due to occasional sparking.

Figure 3.7 shows the shortest gas pulse produced for nitrogen which has a FWHM width of 27 μs using a driving pulse width of 150 μs. The shortest gas pulse width produced with argon is given by the orange line with a FWHM of 32 μs, which is, as expected, longer than that of the lighter nitrogen gas, being a heavier gas.

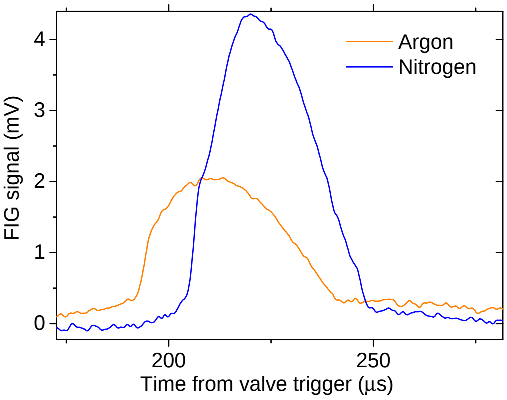

Figure 3.7: Blue line: nitrogen FIG signal for the shortest driving pulse width of 150 μs at an applied field of 896 V/mm and 3.1 bar backing pressure. The FWHM is 27 μs. Orange line: argon FIG signal for the shortest driving pulse width of 120 μs, at an applied field of 727 V/mm and 2.1 bar backing pressure. The FWHM 32 μs. The FIG mission current was set to the highest value of 5 mA to detect the shortest pulses.

3.4 Conclusions and Outlook

In conclusion, we have constructed and characterised a homebuilt cantilever piezo valve which has been optimised at room temperature to produce gas pulses with a FWHM as short as 27 μs for nitrogen gas at a distance of 20 mm from the nozzle. With the simple design of the cantilever piezo, an identical valve can be manufactured by other groups where it could be applied broadly in areas where short gas pulses are desired. A parallel-poled bimorph of PZT507 from *Morgan Electroceramics* with a large transverse piezoelectric coefficient was chosen for our cantilever piezo valve, allowing the operation of the valve at high electric fields, which give large displacements. The piezo valve was characterised by using our homebuilt FIG detector by examining the gas profile of nitrogen and argon under different conditions. By varying the driving pulse width, the detected FIG signal revealed that after a driving pulse width of 400 μs, at an electric field of 869 V/mm for nitrogen, the flow no longer increased, implying a choked flow. Compared to the General Valve that was characterised in chapter two, the piezo valve can produce shorter pulses that are more intense.

To date, our homebuilt cantilever piezo valve has been optimised and characterised to be operated at room temperature. Piezoelectric ceramics have been demonstrated to operate down to very low temperatures but with a reduced piezoelectric effect by a factor of 3 at 77 K and a factor of 8 at 4 K. [119] The limit of working temperature is 193 K for current silicone disks we use for sealing. A new potential material for the sealing disk could be polychlorotrifluoroethylene (PCTFE). The body of the valve was designed to seal with a copper gasket to allow the operation at cryogenic temperatures. We have not at present tested the piezo valve, but, based on our design considerations, it is expected to be operational even at cryogenic temperatures.

Chapter 4

The Building of the Decelerator

Zeeman decelerators are used to manipulate the motion of paramagnetic atoms and molecules using magnetic fields produced by time-dependent high currents. The limitations of the pulsed-type Zeeman decelerators, as discussed in chapter one, motivated the building of a decelerator that uses moving 3D magnetic traps. These traps confine the species of interest throughout the deceleration process, with independent transverse and longitudinal confinement. This new approach to the magnetic deceleration of supersonic beams is based on the generation of a propagating magnetic wave travelling at a desired velocity in the direction of the supersonic beam. Any atoms or molecules with a magnetic dipole moment in low-field-seeking quantum states are trapped around the node of the propagating wave. The design of our decelerator is based on the one by Trimeche *et al.* [75] with several modifications. This chapter starts by discussing our design and how it produces magnetic fields which are spatially and temporally sinusoidal. Next, the vacuum-system design is addressed with more detailed specifications, followed by the presentation of the three sections of the decelerator comprising of the source section, the detection section, and the technical design of the decelerator coils. Finally, the electronics feeding the current to all of the decelerator coils are described.

4.1 Our Decelerator Design

In deciding a design for the decelerator, the movement of the traps was first simulated by a previous member of the group (Ulrich Krohn) to compare the different designs by Trimeche *et al.*, by Ofir *et al.*, [65] and our own. The design by Ofir *et al.* was found to lead to the erratic movement of the traps due to the asymmetries of the field, resulting in a reduction in the phase-space acceptance. The Trimeche *et al.* design is more compact, resulting in a higher field strength and a velocity acceptance for similar currents, but a smaller spatial acceptance. Given that a major aim of the MMQA programme was to finish with as many molecules as possible in the quantum simulator, we decided to proceed with increasing the scale of the design by Trimeche *et al.* in order to maximise the phase-space acceptance of our decelerator. Additionally, this design allows independent longitudinal and transverse control of the atoms and molecules.

We will now compare our design with the one by Trimeche *et al.*, as described in chapter one, where the wires are arranged in blocks of 2×8 wires. Here, for the same total current through a wire block in each design, the contribution to the magnetic field from that block is larger in our design. Therefore, the separation between the top and bottom coils can be made larger by using a larger diameter tube. This in turn means that the spatial acceptance of the decelerator is increased, whilst maintaining the same field gradient, and thus the velocity acceptance along the vertical axis. Another difference in our design is that we use copper wire (AWG 18) with a total diameter of 1.2 mm compared with the $345\,\mu m$ wire of Trimeche *et al.* This allows us to push more current (up to 1000 A) through each wire to maintain, or increase, the velocity acceptance along the molecular beam axis. Furthermore, the Trimeche *et al.* design uses two overlapped quadrupole traps in each period length, which has the effect that the potential well changes shape and depth in three-dimensions markedly as the well propagates through the decelerator. However, our design uses four overlapped quadrupole traps in each period, maintaining the shape and depth of the potential well. A final alteration from the Trimeche *et al.* design is the quadrupole guide used for the transverse guiding, as will be discussed in the following sections. Compared with other Zeeman decelerators, there is the challenging difference in

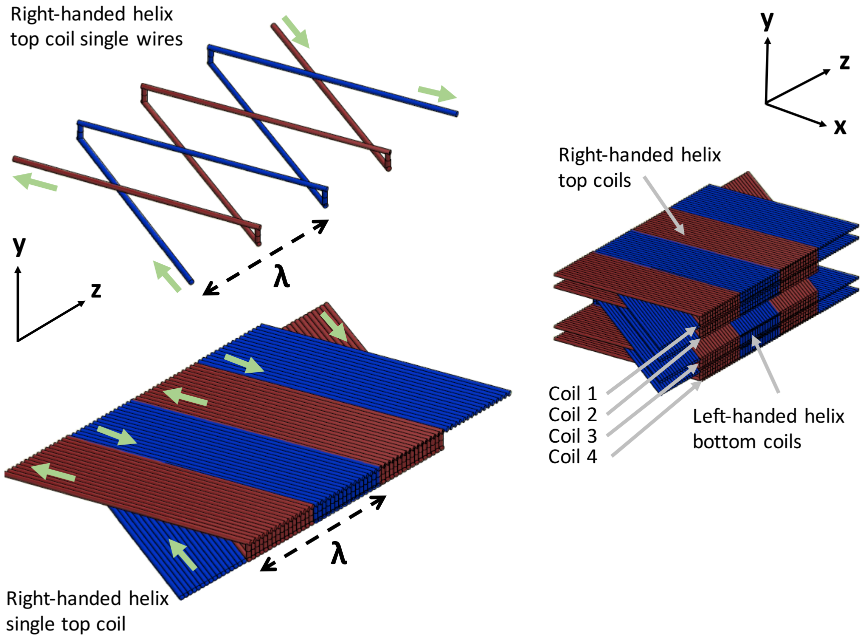

Figure 4.1: Display of the spatial arrangement of the decelerator coils. Top left: a right-handed helix made from two single wires. The green arrows indicate the direction of the current. Bottom left: a single right-handed helical coil with the two groups of 16 wires wrapped around each other. Bottom right: four coils as arranged in a single decelerator coil. The two bottom coils are a mirror image of the two top coils in the xz plane.

the electronics supplying the high currents to the coils at high frequencies, as will be discussed in the following sections.

Figure 4.1 displays the spatial arrangement of the decelerator coils. The diagrams in figure 4.2 show the geometry of our coils and the cross section in the in the xy, yz, and xy-planes. Figure (a) depicts a cross-sectional view through our coil geometry in the xy-plane showing the thin-walled decelerator tube, and around it the quadrupole wires sandwiched between the two pairs of flat helical coils. The decelerator coils are wound in double helixes, as seen in figure 4.1, that are flattened. The flat helical coils provide confinement in the z-direction and in the y-direction while the quadrupole guide independently produces transverse fields in the x and y directions, together forming a three-dimensional magnetic trap. In (c), the flat helical top and bottom coils are illustrated. The colours of blue and red indicate opposing current directions, while the shading corresponds to grouped wires, each carrying the current with a different magnitude. The angle, α, in figure 4.2b was found to affect the efficiency of the decelerator, therefore it was chosen to be 70° as this

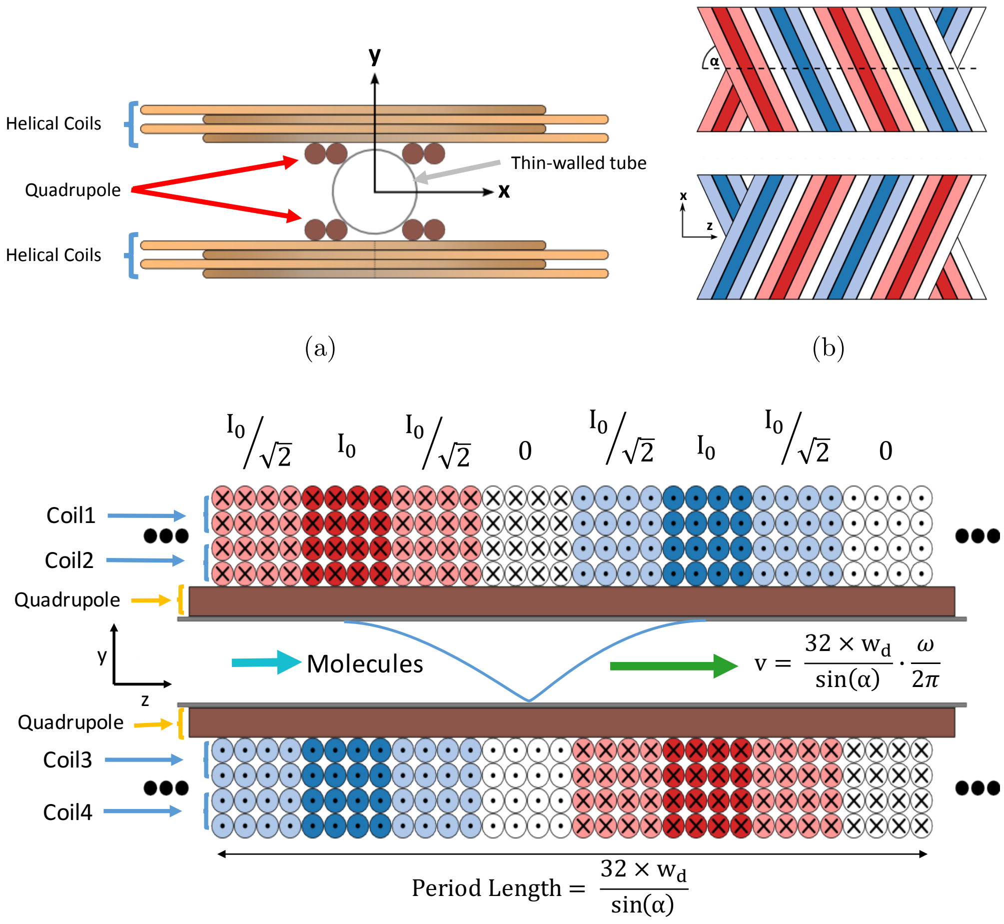

(a) (b)

(c)

Figure 4.2: a) A cross-sectional view of the quadrupole guide coil and the flat decelerator coils in the xy-plane, as it is arranged around the decelerator tube. b) The right-handed and left-handed helical decelerator coils as seen in the xz-plane with the colour and the shading of the current in the 4×4 groups of wires indicating the current direction and magnitude, respectively (α=70°). c) The view of the decelerator coils and quadrupole guide in the yz-plane when the coils are cut at the dashed line. The colour, as well as the dots and crosses indicate the current direction. The shading of the current in the 4×4 groups of wires indicates the current magnitude. This configuration forms a an anti-Helmholtz coil along the beam axis; the z-component of the magnetic field magnitude is as indicated by the blue line with a minimum at the lowest point. The wire diameter, W_d, is 1.2 mm, giving a period length of 40.9 mm for an individual coil.

crossing angle was found to be the optimum angle to give a high efficiency and a big spatial extent of the traps in the z-direction. To obtain the 4×4 blocks of wire, we place two flattened helical coils on top of one another, both for the top and bottom set of coils.

A schematic view of the vertical cross-section of the coil arrangement in the yz-plane (a cut through the dashed line in figure 4.2b) can be seen in figure 4.2c. Each one of the four coils consist of groups of 16 wires that are interleaved in a right-handed double helix. The bottom two coils are identical to the top ones but with the opposite handedness. The identically-shaded wire groups are connected in such a way that the current in them is equal in magnitude but opposite in direction at any given time. The wire geometry is arranged in such a way that, effectively, there is a minimum from the current running into and out of the page, as in an anti-Helmholtz coil. Time-dependent currents are driven through both sets of coils sinusoidally at a certain frequency. This results in a travelling sinusoidal magnetic wave propagating in the z-direction with a series of confining potentials along the z-direction at the velocity of the travelling wave. The calculated magnetic field component in the z-direction for a single decelerator module is illustrated in figure 4.3a and, the contour plot showing the magnetic field in the yz-plane in figure 4.3b. Here, one can see the series of minima of the traps along the z-direction. In our design, for a peak current of 500 A the trap depth is just under 0.7 T. These calculations were carried out by Lewis McArd.

The moving trap is created with an initial velocity that matches the centre of mass velocity of the atomic or molecular supersonic beam. The velocity of the trap, v, is related to the frequency, ω, of the sinusoidal current according to

$$v = \frac{32\mathrm{w}_d}{\sin(\alpha)} . \frac{\omega}{2\pi}, \tag{4.1}$$

where the pre-factor is the length of the period of the coil and hence, d, is the diameter of the wire and, α, the half angle between the sixteen sets of wires. The graph in figure 4.4a shows a plot of the initial velocity at different frequencies for a wire of diameter 1.2 mm and a half angle of 70°. For a beam of Argon travelling at 360 m/s, a frequency of 9 kHz is required for the initial trap velocity. When applying a constant angular frequency, the

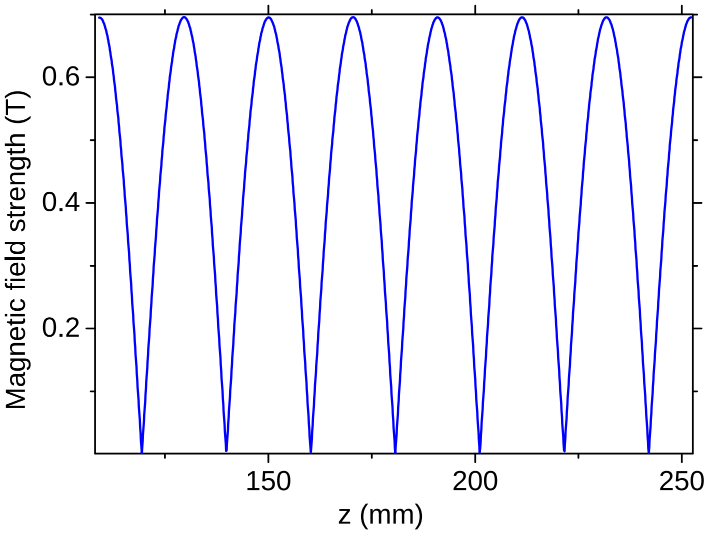

(a)

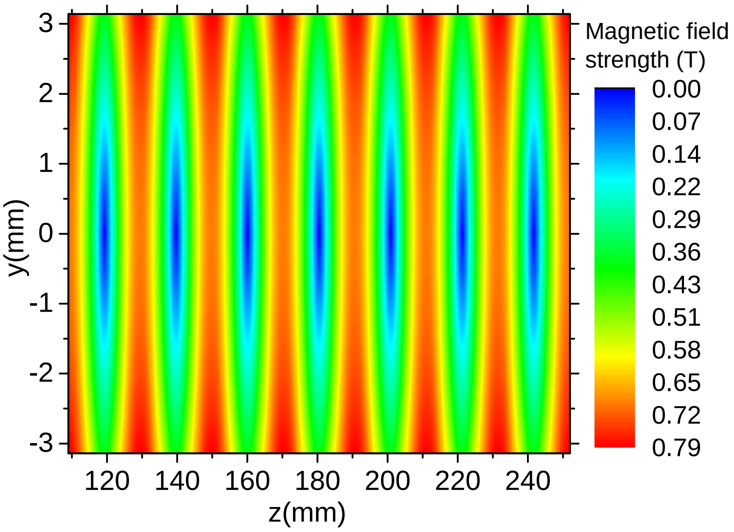

(b)

Figure 4.3: a) Calculated magnetic-field component along the z-direction for a single decelerator module using a peak current of 500 A which comprises of three periods with a total length of 120 mm. b) A contour plot of the magnetic field which includes the y-direction, showing the series of trap minima.

potential well moves at a constant speed that can be matched to the speed of the incoming molecules. Chirping-down the frequency allows the moving potential well along with the molecules trapped within to be decelerated. Figure 4.4b shows a typical constant velocity waveform of a fixed frequency and a chirped-down waveform. The decelerator is modular, with each module having separate set of coils that are powered by an independent generator. Therefore, in a deceleration experiment when the sinusoidal wave is chirped down, as in figure 4.4b, the first module will provide short current pulses at high frequencies while those downstream will be generating longer pulses at lower frequencies.

A synchronous atom is defined as one having the same velocity and position which exactly coincides with the bottom of the trap and always stays in the same position. In a moving frame with the same velocity as the magnetic wave, the synchronous atom does not feel the presence of the potential. But a non-synchronous molecule does see the potential. Decelerated particles in a co-moving trap can be treated in a non-inertial frame of reference by adding a fictitious force. This force is the product of the mass of the particle and the deceleration and acts in the propagation direction, generating a scalar potential which can be expressed in units of magnetic field gradient (T/m). The additional potential tilts the magnetic field potential in the co-moving frame in such a manner that it lowers the front barrier and increases the back one. The greater the deceleration, the greater effect this has. Figure 4.5 illustrates the tilted longitudinal potential due to deceleration, for several deceleration values. Here, the effective magnetic field in the z-direction has been calculated for a guided trap travelling at 360 m/s without any deceleration force (black line) which is then decelerated over a fixed length of 1 m to different final velocities. The remaining barrier height defines the velocities that can be slowed and therefore this effect reduces the acceptance of the trap. For this reason, it is important to have a deep trap to start off with.

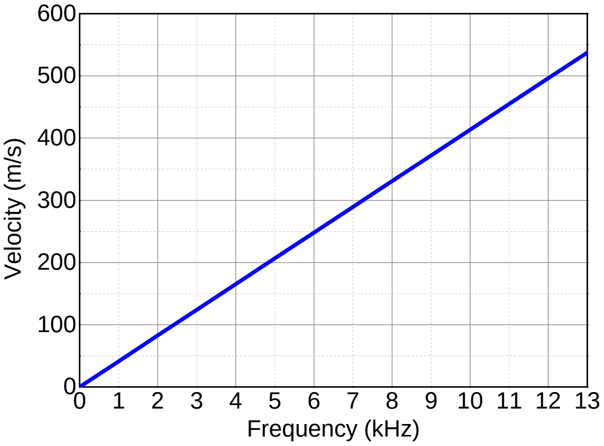

(a)

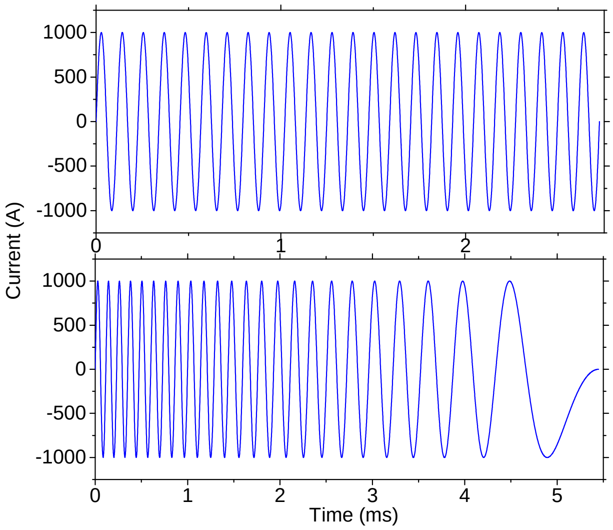

(b)

Figure 4.4: a) Calculated initial velocity at different frequencies for a wire of diameter 1.2 mm and a half angle of 70° using equation 4.1. b) Top: a sinusoidal current wave with a 1000 A peak current at a fixed velocity of 360 m/s and Bottom: a chirped sinusoidal current wave which produces decelerated magnetic traps from an initial velocity of 360 m/s down to 0 m/s over a distance of 1 m.

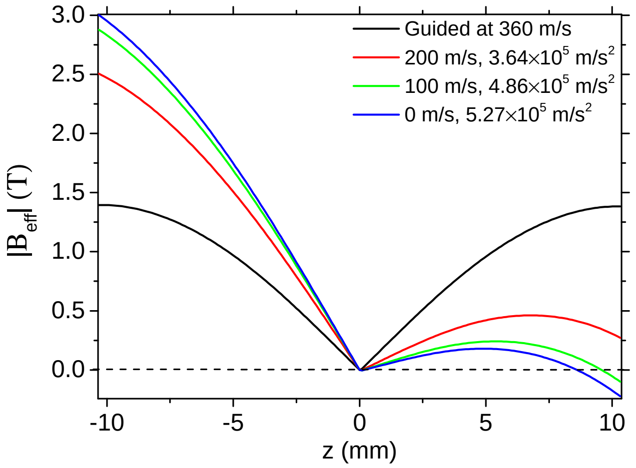

Figure 4.5: The calculated effective magnetic field using 1000 A peak current in the z-direction for Ar* atoms in the $M_J = 2$ magnetic-state. The traps are decelerated from an initial velocity of 360 m/s down to a final velocity indicated by the legend over the same distance of 1 m. The deceleration values employed are also stated in the legend. The fictitious force leads to a reduction in the trap depth from the non-decelerated trap (black line) to the decelerated traps from the tilting of the traps.

4.1.1 Quadrupole Guide Design

The quadrupole guide is independent of the deceleration coils. The quadrupole guide consists of four pairs of wires arranged around the decelerator tube, as depicted in figure 4.6. The wires run parallel to the decelerator tube and are connected in such a way that the current runs in opposite directions for the diagonally opposing pairs of wires, as in an anti-Helmholtz configuration. In this arrangement, there is a zero magnetic field at the centre that then increases linearly in the radial direction. The central region of the guide will be the trapping region for LFS state atoms or molecules. Without the quadrupole guiding and confinement, the beam of atoms or molecules would diverge as it moves due to the presence of a non-zero velocity spread in the radial direction. Without transverse confinement, the only atoms reaching the detector from the valve will be those with a small enough transverse velocity. The greater the magnetic field strength in the radial direction, the higher the velocity components along the radial direction which will be guided. The transverse velocity acceptance in the beam gradually increases with the increase in the guiding current. The magnetic fields have been calculated in the x and y transverse directions as illustrated

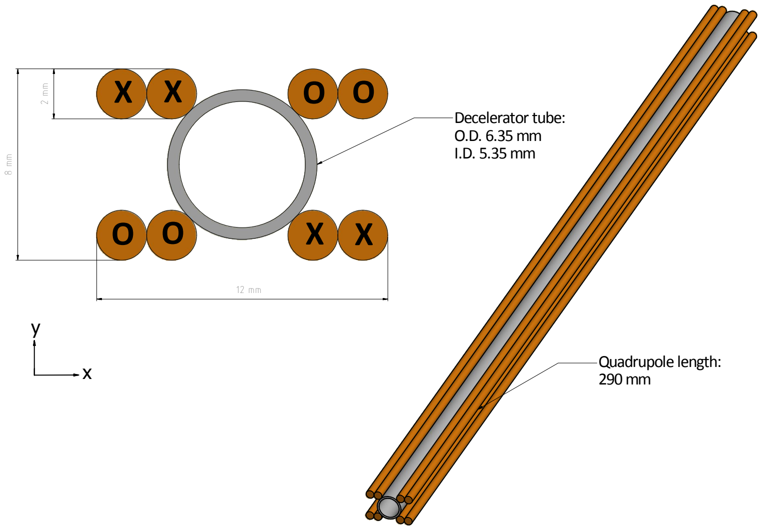

Figure 4.6: Left: cross-sectional view of the quadrupole guide used in our decelerator showing the four pairs of 2 mm diameter wires arranged around the stainless-steel decelerator tube. The circles and crosses indicate the direction in which the current flows i.e., into and out of the page. The relevant dimensions are illustrated. Right: side view of the quadrupole guide, showing the wires running along the decelerator tube for a quadrupole with a length of 290 mm. The quadrupole guide operates with a pulsed current with a variable length and an amplitude up to 900 A.

in figure 4.7. One can see a contour plot of the magnetic field strength in the x and y directions, the white solid circles indicate the positions of the wires, the decelerator tube is also indicated with white circular lines. The trap depth in the x-direction is 119.4 mT giving a gradient of 45.3 $\mathrm{T m^{-1}}$ and in the y-direction the trap depth is 104.6 mT giving a gradient of 39.6 $\mathrm{T m^{-1}}$. Independent decelerator coils and quadrupole guide coils allow us to tune the transverse properties of the traps independently to the deceleration, and velocity properties of the travelling magnetic wave.

The design of the quadrupole guide was decided upon having first considered the electronic capabilities i.e. what power supply was available within our budget. Simulations (by Lewis McArd) showed that the number of guided molecules increases with increasing current. We decided 700 A was sufficient enough based on simulations. There are a few commercial power supplies which are capable of supplying such high current. The design of the quadrupole guide required the resistance to be maintained at a low value in order to allow the use of an effective guiding current without the use of

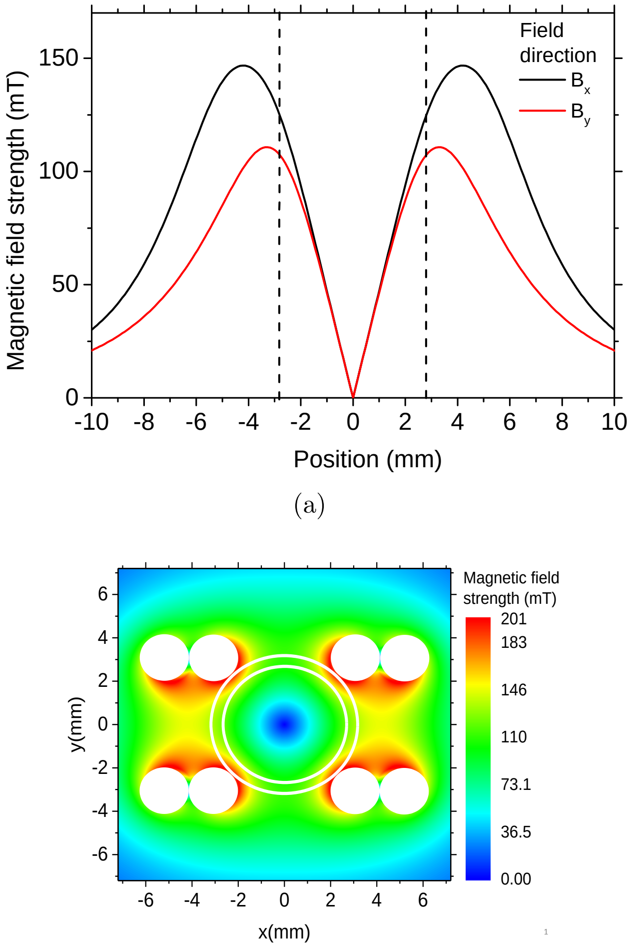

(a)

(b)

Figure 4.7: a) Calculated magnetic field strength at 700 A for the x and y components from the quadrupole guide which provides confinement in the transverse direction for our wire geometry. The trap depth in the x-direction is 119.4 mT giving a gradient of 45.3 $\mathrm{T m^{-1}}$ while in the y-direction the trap depth is 104.6 mT giving a gradient of 39.6 $\mathrm{T m^{-1}}$. b) Contour plot of the magnetic field strength in the x and y directions, the white solid circles indicate the positions of the wires. The decelerator tube is also indicated with white circular lines.

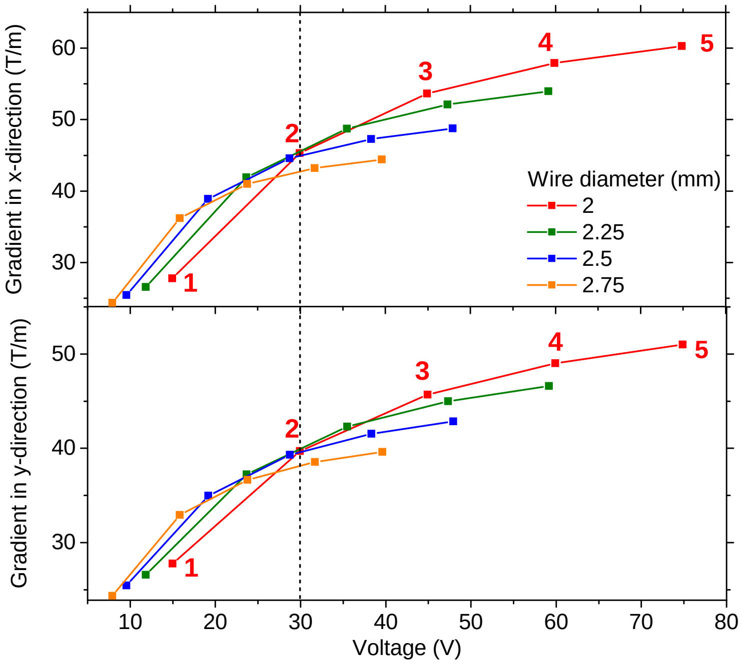

Figure 4.8: Calculated magnetic-field gradient in the x-direction (top) and the y-direction (bottom) attained using our power supply where different voltages are required to drive a current of 700 A through a 1 m long quadrupole. The colour indicates the radius of the wire and the number next to each point indicates the number of wire windings i.e. for '2' the wires are arranged as in figure 4.6.

an excessively high-rated power-supply. Initially, we considered using a bar quadrupole guide with a large cross-sectional area that greatly lowers the resistance and heating at the high current of 700 A. However, increase in the cross-sectional area also means that the current is not localised close to the decelerator tube, giving a low field gradient. The choice in the best wire geometry to use was made by performing simulations (by Lewis McArd), where the field gradient was maximised while taking heating into consideration and the ability to push 700 A through a 1 m long quadruple. The two plots in figure 4.8 show the magnetic field gradient in the x and y-directions at different voltages for different wire diameters. The colour indicates the diameter of the wire and the number for a particular point indicates the number of windings going from left to right. For example, for our arrangement the number is '2' as there are two windings, as shown in figure 4.6. In the end, we decided to make a quadrupole consisting of two windings of copper wire with a diameter of 2 mm. This is the point where a 30 V power supply can supply 700 A for this particular quadrupole design. The 30 V power-supply is indicated by the vertical dashed line which crosses the red line at this point.

4.2 The Vacuum System

The first task in the building of the decelerator was to design and construct a vacuum system for a molecular beam machine. An overview schematic diagram of the vacuum system can be seen in figure 4.9. The vacuum pumps were chosen based on a budget and the source and detection chambers were chosen to allow maximum pumping of the volume for these pumps. Figure 4.9 shows the three main sections of the vacuum system: the source chamber, the detection chamber and the deceleration chamber; currently a tube linking the two end chambers together. For molecular beam experiments, vacuum levels in the lower 1×10^{-7} mbar pressures are sufficient depending on the molecular beam pulse width. When the pulsed valve is in operation, background pressures can be as high as 1×10^{-5} mbar and still give a decent expansion. However, the lower the background pressure in the region of the supersonic expansion, the lower the translational temperature of the pulsed beam. Moreover, lower pressures are required in the deceleration chamber to prevent losses of the decelerated atoms or molecules by collisions with the background gas. Table 4.1 contains a summary of the different pumps and the relevant specifications and the pressure gauges chosen for the decelerator vacuum system; all were purchased from *Pfeiffer Vacuum.* All pressure gauges (C1, C2, C3, C4, and C5) are connected to a MaxiGauge digital pressure reader (TPG 256 A) which allows the pressures to be monitored.

	Turbo pump	**Rotary pump**	**Pressure Gauge**
Source	T1: TPU521PC (300 l/s)	R1: DUO 20MC (24 m^3/h)	C2: PKR 251 C1: TPR 280
Detection	T2: HiPace300 C (245 l/s)	R2: DUO 20 M (24 m^3/h)	C4: PBR 260 C3: TPR 280
Deceleration	T3: HiPace300 C (245 l/s)	R2: DUO 20 M (24 m^3/h)	N/A C3: TPR 280
Gasline	N/A	R3: DUO 5M (6 m^3/h)	C5: APR 267

Table 4.1: Table summarising the model names of the various pumps and pressure gauges schematically depicted in figure 4.9. All five pressures in the systems are monitored on a MaxiGauge digital pressure reader (TPG 256 A). All of the apparatus were purchased from Pfeiffer.

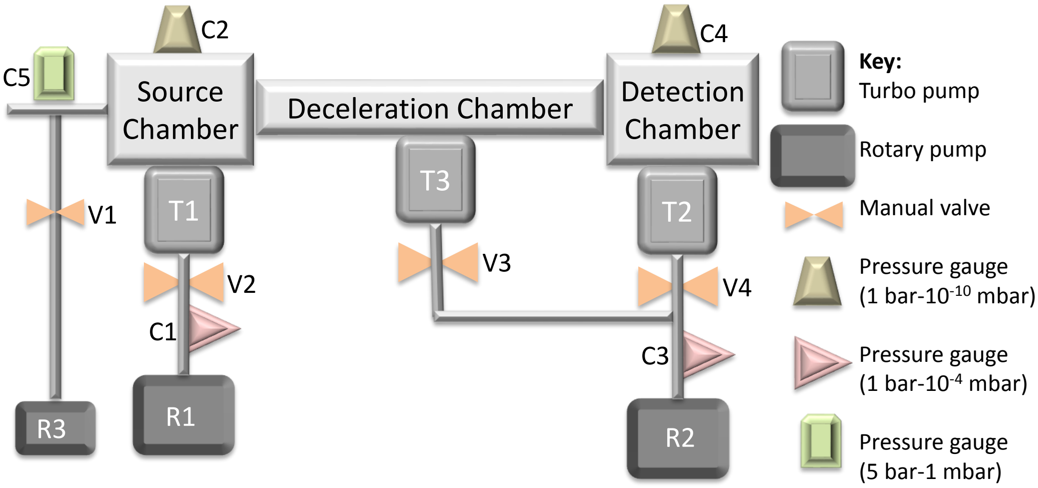

Figure 4.9: A schematic diagram of the decelerator vacuum system showing the source chamber which is connected to the detection chamber via the deceleration chamber (currently a tube). The key on the right defines the symbols used in the schematic diagram. The manual valves allow different sections of the vacuum system to be disconnected from one another. Table 4.1 lists the specifications of all of the pumps and pressure gauges.

The source chamber is kept under vacuum by the turbo pump (T1) with the fastest pumping speed (300 l/s) which is backed by a rotary pump; since this is the chamber which will have the bigger gas load from the molecular beam. The source chamber pressure after a long pump-down period, read by a full-range cold-cathode pressure gauge (C2) can be as low as 5×10^{-8} mbar. The detection chamber is pumped by a smaller pump with a pumping speed of 245 l/s, which is backed by an identical rotary pump. There is a tube connecting the source and detection chambers, providing differential pumping due to the conductance of the gas through the decelerator tube. If a single pumping system is used, one would require a big pump with a very large pumping speed, massively increasing the cost. With differential pumping, a higher vacuum can be achieved in the detection region using a smaller pump with a lower pumping speed. Pressures in the detection chamber can be as low as 5×10^{-9} mbar and are measured by a full-range hot-filament pressure gauge (C4). Currently, the decelerator tube in the middle section is only 317 mm long since we have only used a single decelerator module. In the future, when the decelerator length is extended, there might be a need for pumping in the deceleration chamber. In figure 4.9, a third turbo-pump (T3) is illustrated for the deceleration section, backed by the same rotary pump as T2 since the gas load is much smaller at this end.

The gas-line feeding the pulsed-valve has a small rotary pump (R3) with a pumping speed of 6 m^3/h which allows the pumping of the gas-line and the mixing bottle when needed. We chose the piezo transducer pressure gauge as it can measure pressures to a high accuracy across a big enough range (5.5 bar-1 mbar), allowing the seeding of the species of interest in a carrier gas with an accurate measure of the partial pressure.

The vacuum system was designed with the fail-safe operation in mind. The source chamber's turbo pump, T1, is connected to a relay box, which allows it to communicate with the two rotary pumps, R1 and R2. In case of a power cut, all pumps shut down and all turbo pump venting valves opens to safely vent the system. The rotary pumps do not switch back on unless manually instructed to do so. In the unlikely event that any one of the turbo pumps fails, the pumps will shut down and vent the system with dry-nitrogen which is connected to the venting valves of the turbo-pumps. The rotary pumps, R1 and R2, will switch off through the relay box. In the more likely scenario of a leak in the vacuum system, the turbo pumps will all overload and shut down, venting the system. The rotary pumps, R1 and R2, will switch off through the relay box connected to T1. An override switch for the relay box allows us to switch on the rotary pumps independently to the turbo pumps, when this is required.

4.3 The Decelerator Design

Figure 4.10 shows more detailed drawings of the decelerator from different angles. Photographs of the whole experiment can be seen in *Appendix D*. There are three main sections. The first is the source section (yellow), devoted to the production of atomic and molecular beams. The second is the decelerator section (green), a narrow steel tube along which the deceleration and guiding coils will run outside vacuum. This is connected to the third section, the detection section (red), where the decelerated particles are detected. The source chamber is supported by an aluminium-profile frame (beige) which hangs-off the optical table. The vertical distance between the molecular beam axis and the optical table was chosen to match the height of the output of our dye laser, which is at 255 mm above the optical table. Custom-made clamps were designed and machined to support the detection

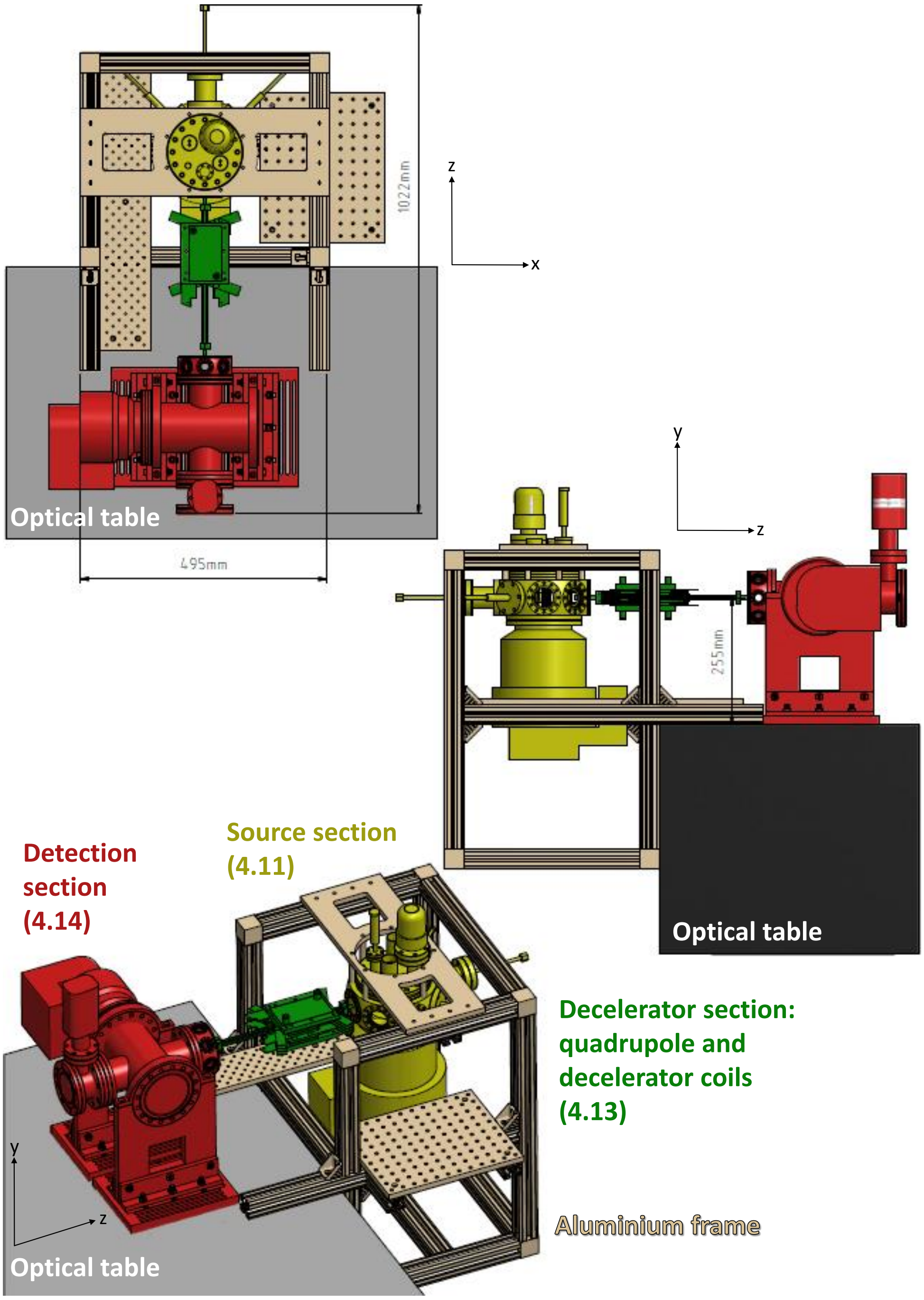

Figure 4.10: Drawings of the decelerator as viewed from different angles, top: looking down at the xz-plane, middle: side view in the yz-plane, bottom: three-dimensional view of the whole experiment. The source section (yellow) is supported by the aluminium frame (in beige) which is fixed to the optical table. The detection section (in red) is held by clamps which are also fixed to the optical table. The deceleration section (in green) hangs in the middle, and is supported by the source and detection chambers as well as some bars which support the weight. The specified dimensions illustrate the overall extent of the experiment. Each section will be expanded to illustrate the design in more detail in the figure specified in the brackets. The source and detection chambers are separated by 317 mm.

section with the chamber centre at the same vertical distance. These clamps allow flexibility in moving the detection chamber in order to align the molecular beam axis. The detection section can be moved further downstream with increasing decelerator length. The precise alignment of the detection chamber to the source was carried out by passing a laser beam through the molecular-beam axis and then fixing the clamps. The deceleration section hangs in the middle, and is supported by the source and detection chambers, as well as some bars which support the weight. The quadrupole electronics (not shown) sit close to the quadrupole guide, while the decelerator electronics (not shown) hang from above the decelerator, positioning them as close as possible the decelerator coil wires. This is to minimise the resistance from longer connections. Each section will be expanded to illustrate the design in more detail in the following sections: the source section will be described in figure 4.11, the detection section in figure 4.14, and the deceleration section in figure 4.12.

4.3.1 Source Section

The purpose of the source chamber was described in detail in chapter two, where the pulsed valve and discharge source were characterised for a metastable argon atomic beam. Figure 4.11 shows detailed drawings of the source section. The source chamber is made of a commercially bought spherical octagon (Kimball Physics Inc., MCF600-SphOct-F2C8-A), consisting of a hollow sphere intersected by two DN100CF sealing surfaces and eight DN40CF sealing surfaces. The top is sealed by a custom-made DN100CF flange and the bottom, by a turbo-pump with an identical flange. In this arrangement, the compact source chamber only has a small volume which needs to be pumped away, thus, with the pump sitting very close to where the expansion occurs, it results in very good background pressures between pulses.

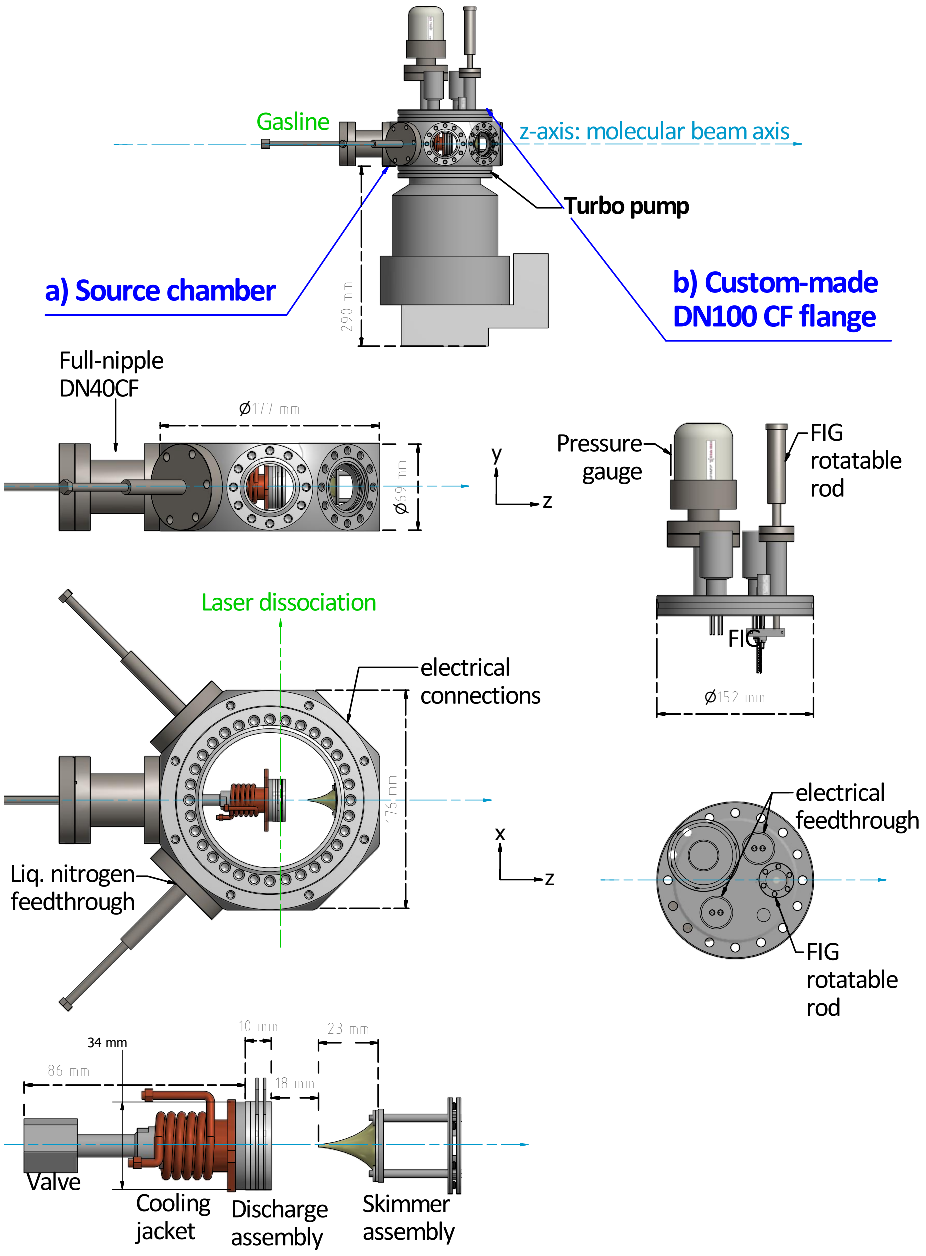

Figure 4.11: Drawings of the source section showing the various views. The source section consists of a spherical octagon with two DN100CF flanges; the top is sealed by a custom-made DN100CF flange and the bottom by the turbo-pump. All flanges comprise of CF-type flanges with knife edges. a) The source chamber consists of a spherical octagon with two DN100CF flanges and eight DN40CF sealing surfaces. Two DN40CF surfaces are for the liquid nitrogen feedthroughs, two are for the optical axis of the dissociation laser, two are electrical feedthroughs and the last two are for the gas-line and the decelerator tube, both aligned along the molecular beam axis (light blue dashed arrow). b) The custom-made DN100CF flange sits on top of the spherical-octagon and was designed to fit a half nipple to hold the source chamber pressure gauge, two electrical feedthroughs, one feeding the required current and voltage to the FIG, and another smaller half nipple for a rotatable rod that holds the FIG detector. The FIG can be rotated into and out of the way of the molecular beam.

Although the compact design of the source chamber allows us to keep the cost down with pumping requirements, it introduces the challenge of fitting the various components inside. The valve used in the decelerator experiments (the General Valve) was described in detail in chapter two. It is illustrated in the bottom of figure 4.11. The valve nozzle exit was positioned to coincide with the laser dissociation axis (green dashed line). Due to the fixed length of the general valve (85 mm), it was necessary to attach a full nipple on one of the DN40CF surfaces. This was to provide extra length in order to attach the general valve gas-line to an adaptor and then to a Let-Lok fitting on the gas-line flange along the molecular beam axis (figure 4.11a). Once the valve was positioned, the skimmer (*Beam Dynamics Inc.*, Model 2, 1 mm orifice) orifice was then positioned in such a way that the gas pulse's transverse spatial spread would match the inner-diameter of the decelerator tube at the point where the first trap was expected to be. Each DN40CF sealing surface has a pair of grooves for which Kimball Physics Inc. provides clamps that can be fixed to the grooves called "groove-grabbers". The skimmer's rim is sandwiched between two plates, which are fixed to four bars, that are themselves screwed into tapped holes in the groove-grabbers. For photographs of the source chamber see *Appendix D.*

The valve is cooled by passing liquid nitrogen through a copper tube that is wrapped around a cooling jacket (figure 4.11). The cooling jacket slides onto the valve body before the front-face flange is attached. In this way both the valve body and the front face-plate with the nozzle are cooled. A cryogenic vacuum compatible grease (Apiezon) was used to fill gaps in order to improve the thermal contact between the cooling jacket and the valve. Two of the spherical octagon's DN40CF surfaces are used for liquid nitrogen feedthroughs. The remaining DN40CF surfaces are used for electrical feedthroughs and the decelerator tube which is aligned with the molecular beam axis (light blue dashed arrow). The custom-made DN100CF flange sits on top of the spherical octagon and was designed to fit a half nipple to hold a pressure gauge, two electrical feedthroughs, one that feeds the required current and voltage to the FIG, and another smaller half nipple used for a rotatable rod that holds the FIG detector. A small clamp was designed to fix the FIG to the rotatable rod in such a manner that it can be rotated into and out of the way of the molecular beam axis.

4.3.2 Deceleration Section

The source and detection chambers are connected by a stainless steel tube (6.35 O.D., 0.5 mm wall thickness) which is under vacuum. The deceleration coils sit outside vacuum above and below this tube. The flanges at either end are thin flanges. The reason for this at the detection end was to minimise the distance between the end of the decelerator and the MCP detector; reducing the transverse spread of the gas on its free-flight towards the detector. For each flange, a hole of I.D. 6.35 mm was made to allow the tube to slide in. Torr-Seal was then applied to fix the tube and form a secure vacuum seal down to pressures as low as $1{\times}10^{-8}$ mbar (see *Appendix D*, figure D.3). This way, we can replace the tube easily with a longer one when extending the length of the decelerator. Care must be taken not to apply too much force or pressure to the Torr-seal to avoid leaks in the vacuum.

The quadrupole guide geometry was described earlier. Clamps were designed to position the wires in the correct location around the decelerator tube, also held by the clamps (figure 4.12). The quadrupole guide was wound by using a single straightened wire. Once positioned correctly, the wires were then glued together using a two-part epoxy (See *Appendix D*). In order to produce magnetic traps as close as possible to the theoretical simulations, i.e. trap depth, shape and a smooth movement, it was necessary to produce a near to perfect set of coils. This means that all coils must have minimum discrepancies, such as large gaps between the wire blocks and unwanted bending on the flat faces of the coils. The decelerator coils were wound by a member of the group (Lewis McArd) using a home-made automated motorised coil winder by feeding 16 wires from each side onto a thin plate around which the wires are wrapped. The next stage was to press the coils flat in the central region of the coil to remove the 3 mm gap left by the process of wrapping the wires around the 3 mm thick plate. The coils are pressed while a thermally conductive epoxy resin is applied to them (Stycast 2850FT with catalyst 9). The epoxy holds the coil in shape once it is pressed as well as allowing good thermal contact between it and the cooling apparatus. The photograph in figure 4.13 shows one of the coils before it was pressed. The connections between the wires were made using crimp connectors. Figure D.7 in *Appendix* D shows the different connectors which were tested to find the best one with the smallest resistance.

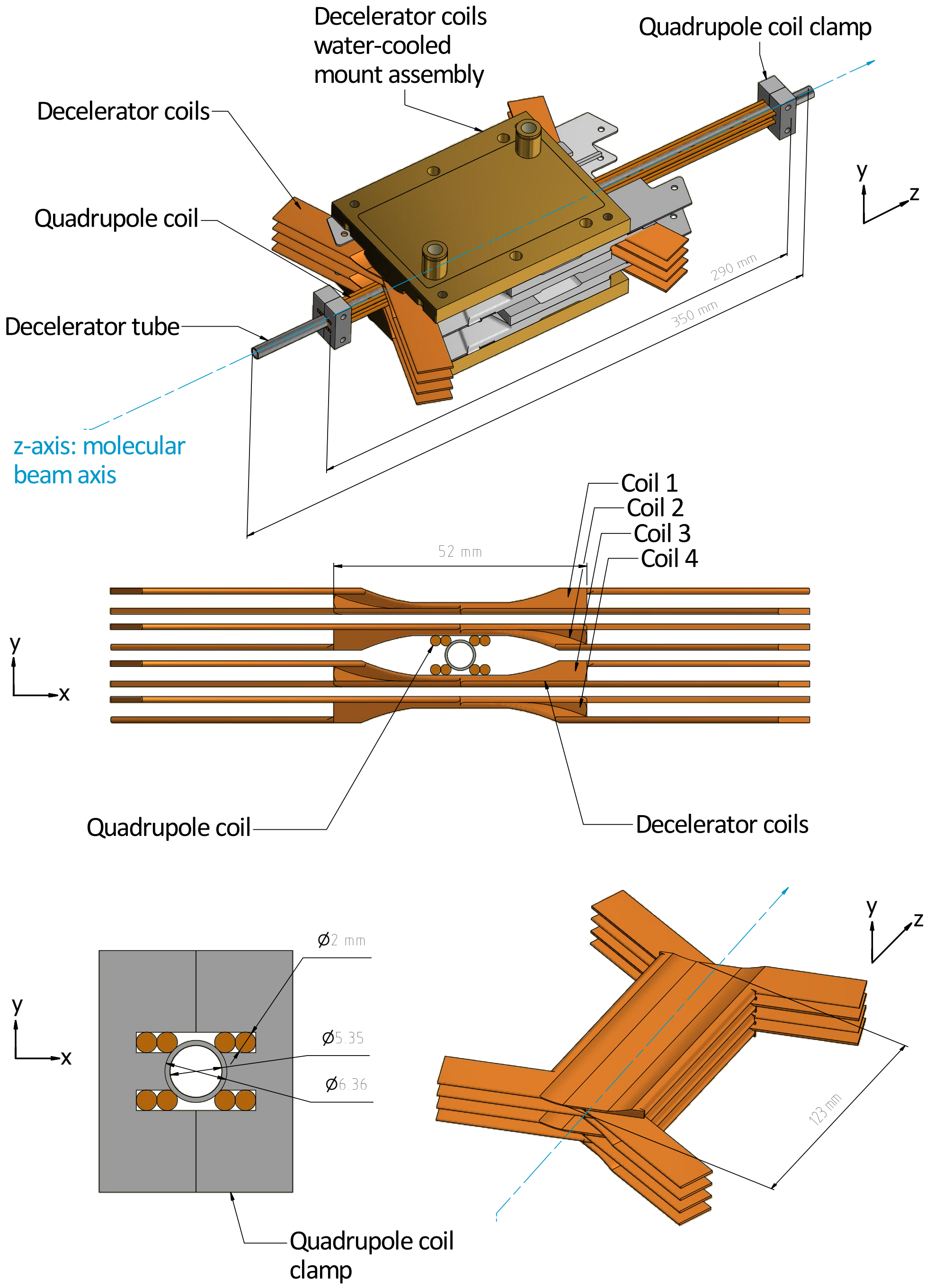

Figure 4.12: Drawings of the decelerator section from different angles. Top: a single, fully-constructed decelerator module with all four flattened helical coils in place. The quadrupole guide sits around the decelerator tube. The coil mounts hold the coils which are sandwiched between two water-cooled plates. Both the quadrupole guide and the decelerator coils sit outside vacuum, the decelerator tube is the only volume under vacuum. The coil mounts allow a modular design. There are also stands that fix the module to the optical table in order to support its weight. The quadrupole wires are correctly positioned around the decelerator tube by the quadrupole clamp. Middle: cross sectional view of both the decelerator coils and quadrupole guide around the decelerator tube. Bottom: the quadrupole guide alone with the clamp (left) and the decelerator coils (right).

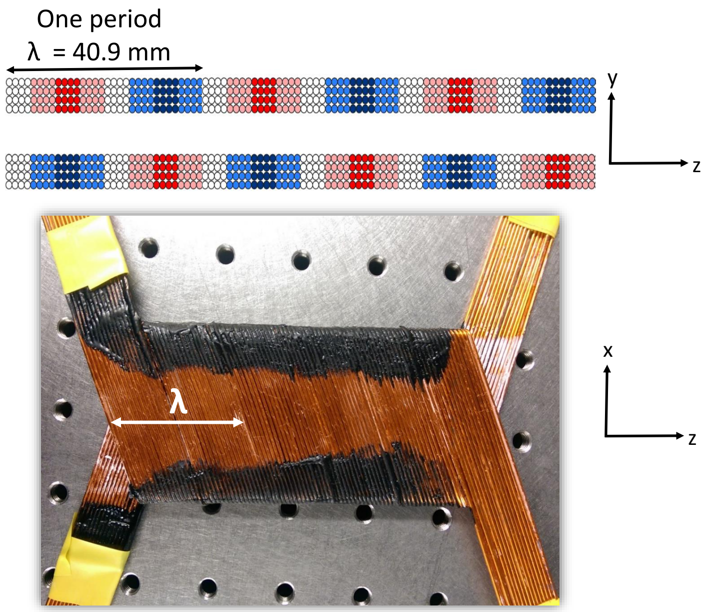

Figure 4.13: A photograph of a single decelerator coil. The thermally conductive epoxy holding the wired together is seen in black. There are three period lengths for each coil, each with a length of 40.9 mm.

The diagram in figure 4.12 shows the decelerator section from different angles. At the top, one can see a single, fully-constructed decelerator module with all four flat helical coils in place and the quadrupole guide around the decelerator tube. There are also clamps at either end, positioning the wires in the correct geometry around the decelerator tube. When passing the high currents through the decelerator coils and quadrupole guide, heat is generated. There are also forces generated by the coils. With this design, the heat and forces generated are mitigated by mounting on top and below the coils water-cooled heat exchangers. This ensured that the coils are mounted in a robust frame. The coil mounts were designed to allow access for additional vacuum pumping which might be required when we extend the decelerator length. The design of the coil mounts and clamps holding the decelerator coils is modular, allowing us to extend the decelerator length by slotting together multiple modules which can be fixed together. The coil mounts are sandwiched between the cooling plates. The plates have tapped holes which are used to fix Thorlab stands and clamps to it, allowing the module to be fixed to the optical table.

4.3.3 Detection Section

The detection section consists of a smaller spherical octagon which is identical to the source chamber but has smaller sealing surfaces (MCF450-SphOct-E2A8). The drawings in figure 4.14 show the detection section at different angles. At one end of the spherical octagon, the decelerator tube is connected to a thin DN63CF flange. The other end is connected to a 4-way cross in order to attach the turbo pump. Finally, a custom-made T-piece is attached downstream along the molecular-beam axis, which ensures a fixed, desired distance to the optical axis for reasons which will be explained below. The T-piece also allows us to attach a pressure gauge. The detection chamber has been designed in such a manner that three different methods of detection can be used: micro-channel plate (MCP), quadrupole mass spectrometer (QMS) and cavity-enhanced laser-induced fluorescence (CELIF). The MCP detector was discussed in detail in chapter two. When the MCP detector is used, the assembly sits on a plate that is held perpendicularly to the molecular beam axis on two groove-grabbers. Photographs of the detection chamber can be seen in *Appendix D*. In order to detect molecules, we have the necessary axes to use LIF simultaneously with CRD since we have two perpendicular axes, as depicted at the bottom of figure 4.14. This technique is called CELIF and it can be used to measure absolute densities of molecules coming out of the decelerator. The cavity mirrors of CRD will be aligned along the CRD-axis. Chapter six is devoted to the development and successful demonstration of the detection of SD molecules using CELIF.

The QMS is another detector which can be used in the decelerator's detection chamber but has only been tested to date to ensure that it functions well. It is a commercial quadrupole mass spectrometer with a custom ion source (*Hiden analytical*, HAL/3F RC 301 PIC, see *Appendix D* for a schematic diagram). This allows the detection of selected masses of different atomic states using electron impact or photo-ionisation. The detection chamber length along the molecular beam axis was designed in such a way that the ionisation volume coincides with the optical axis of the spherical octagon of the detection chamber, as illustrated in the middle of figure 4.14. The QMS is a type of mass analyser used in mass spectrometry that filters ions based on their mass-to-charge ratio (m/z). It consists of four cylindrical rods, set parallel to each other. The opposing pairs are electrically connected and

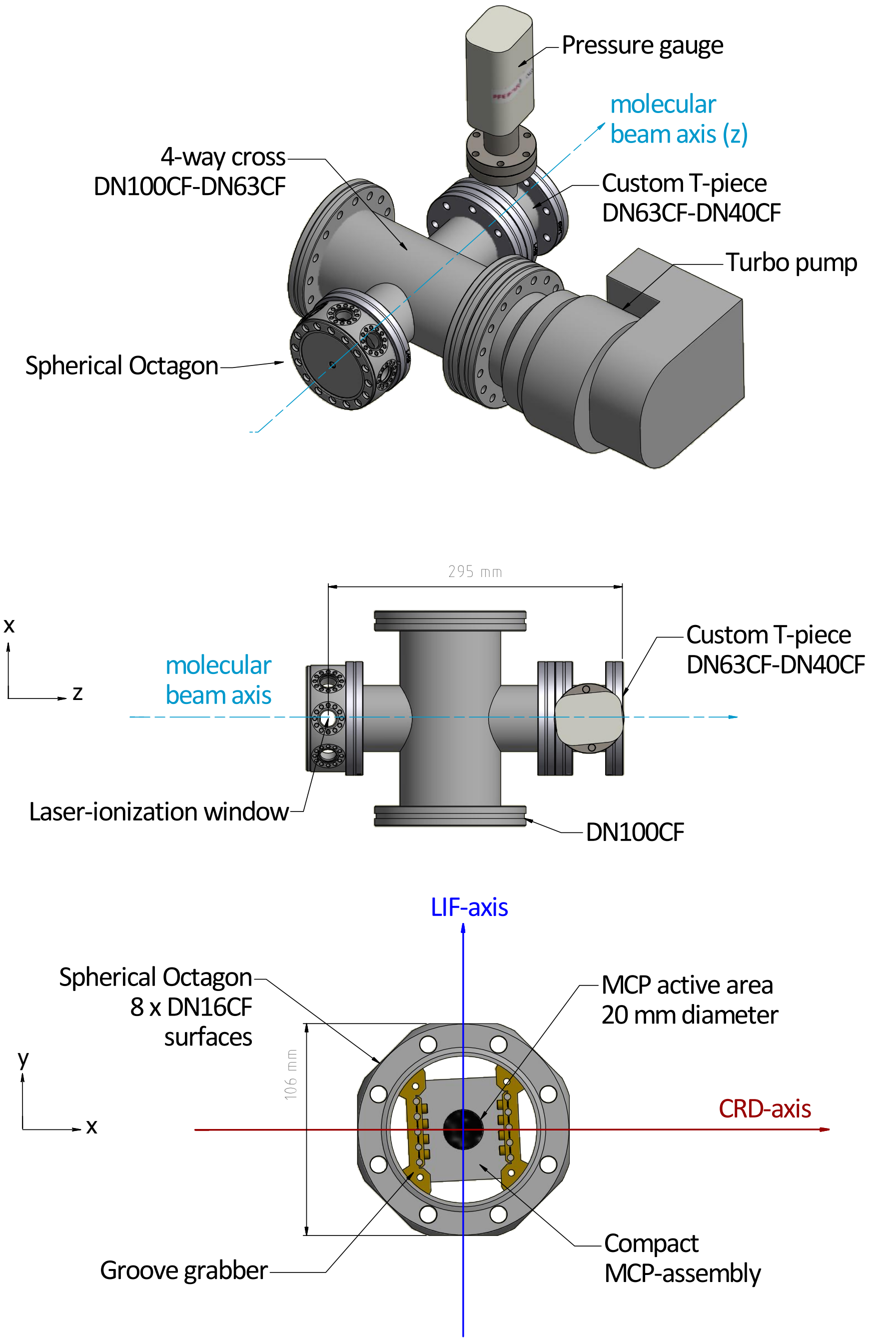

Figure 4.14: Drawings of the detection section from different angles showing the various components. Top: overall diagram showing the 4-way cross connecting the spherical octagon to the T-piece with the pressure gauge and the turbo pump. The molecular-beam axis is depicted by a dashed light-blue line. Middle: top view (xz-plane) with the length of the QMS-detector arranged in such a way that the ionisation volume coincides with the flanges of the detection chamber for photo-ionisation. Bottom: the detection-chamber, a spherical-octagon with two DN63CF surfaces and eight DN16CF surfaces. The MCP assembly sits on a plate that is held perpendicularly to the molecular beam axis on two groove-grabbers. There are axes for LIF detection as well as CRDS. Photographs of the detection chamber can be seen in *Appendix D*.

a radio frequency (RF) voltage is applied between each pair in addition to a DC voltage, which is superimposed onto it. Any ions travelling along the quadrupole between the rods will accelerate away from the centre line towards the rods due to the DC bias. The rate of acceleration will be dependent on their m/z ratio, thus allowing the selection of a specific m/z ratio. For a given ratio of RF and DC voltages, only ions of a certain m/z ratio will reach the detector. Other ions will have unstable trajectories and thus collide with the metal rods. By continuously varying the applied voltage, one can scan for a range of m/z values.

4.4 Decelerator Electronics

To decelerate atoms and molecules, the decelerator requires deep traps with high magnetic field gradients which are time-dependent and whose velocity can be varied. The production of these three-dimensional magnetic traps requires the generation of controllable time-dependent high currents. The flat decelerator coils and the quadrupole guide coil are independent, with separate electronics with different requirements and specifications. The requirement for the quadrupole electronics is to produce a square, high-current pulse with a variable width. The 'on-time' of the pulse can be matched to the duration of the time-of-flight of the atoms or molecules. For a 1 m decelerator and a deceleration from an initial velocity of 360 m/s to a final velocity of zero, this would have to be on for 5.56 ms. For the current quadrupole guide length of 290 mm the pulse would have to be on only for 1.6 ms. Pulsing the quadrupole on and off offers three advantages: minimising the power consumption and heat dissipation and avoiding fringe fields. These magnetic fields produced at the ends of the quadrupole can perturb the motion of the atoms or molecules on entrance and exit of the decelerator. Therefore, it is best to avoid them by switching the quadrupole on only when the molecules are within the quadrupole guide. To achieve this, fast switching is required, giving a square high-current pulse.

Figure 4.15 shows a schematic diagram describing the operation principle of the electronic circuit used to generate the high current pulse for the quadrupole. The design of the circuit was inspired by the electronics driving the conventional Zeeman decelerator of Merkt's group. [72] The cir-

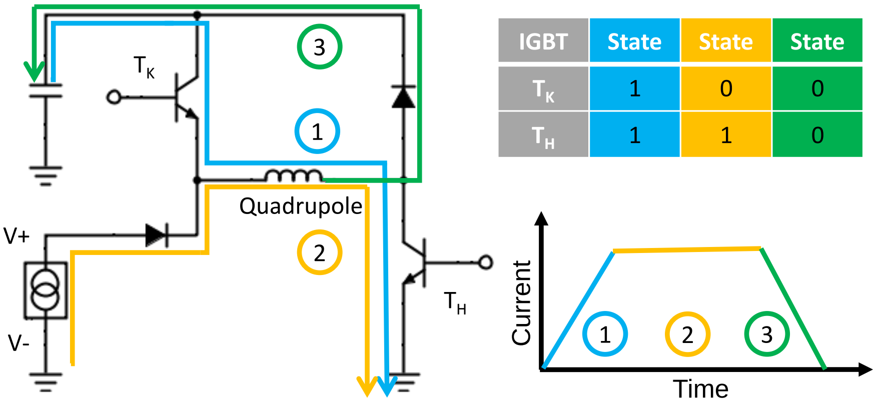

IGBT	State	State	State
T_K	1	0	0
T_H	1	1	0

Figure 4.15: Left: a schematic diagram of the electronics circuit used to generate the high current pulse for the quadrupole. The different colours indicate the different switching phases. Top right: a table showing the logical states of the IGBT switches during the three switching phases with 0 representing an open switch and 1 a closed switch. Bottom right: schematic plot of the temporal evolution of the current pulse across the quadrupole.

cuit uses a capacitor and two Integrated Gate Bipolar Transistors (IGBTs, SKM600GB066) for the fast switching, and two high-current power supplies in parallel (Sorensen SGA 375 A x 40 V) in order to maintain the current during the 'on-time'. The capacitor (10 mF rated to 100 V) provides the current 'kick', allowing the fast initial rise time. There are three switching phases indicated by three different colours. The table shows the logical states of the IGBT switches during the three switching phases with '0' representing an open switch and '1' a closed switch. At the bottom right is a schematic plot of the temporal evolution of the current pulse through the quadrupole. The current is rapidly ramped up through the coil by having switches T_K and T_H initially closed (blue phase), thus releasing the charge on the kick capacitor. Once the capacitor is discharged, switch T_K is then opened, and the power-supply maintains a constant current for the chosen pulse duration (yellow phase). Finally, switch T_H is opened (green phase), consequently ending the hold phase. The presence of the capacitor drives out the current from the quadrupole, therefore aiding in its recharge.

Figure 4.16 shows a square high current pulse measured via a current sensor. The peak current measured was 700 A with a rise time of 477 μs. However, we are not currently using the kick, hence the very slow rise and fall times.

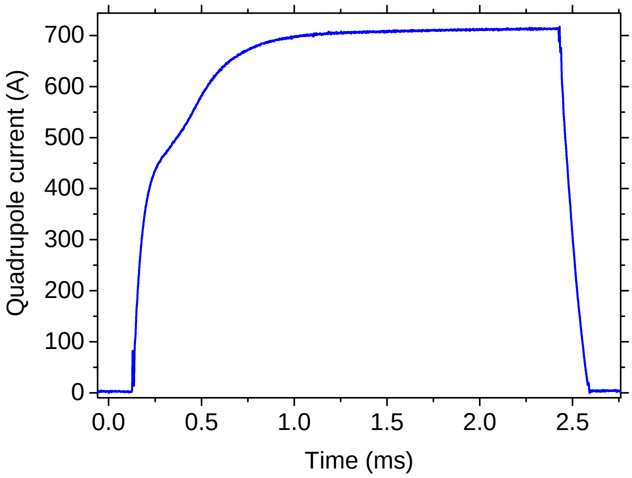

Figure 4.16: The observed quadrupole current pulse measured via a current sensor through the quadrupole showing a peak of 700 A and with a 477 μs rise time. This was without using an effective 'kick'.

For the shorter pulses, we need faster rise and fall times, and this can be achieved by having a separate high-voltage power-supply (100 V) to provide the necessary voltage for the kick capacitor to give rapid rise and fall times of the current. The current can be varied using the power supply, and the pulse width can be varied using the pulse generator. By fitting an analytical expression to the rising edge, the quadrupole guide resistance was determined to be 16.9±0.3 mΩ and the inductance 2.92±0.04 μH. These were later measured to be 16.0±0.5 mΩ and 4.2±0.1μH using a multimeter.

The magnetic confinement in the z-direction is produced by passing current in the flat helical-coils. The current is fed to the four groups of wires for the four separate phases. This is varied sinusoidally with a frequency that can be varied to attain the desired beam velocity, giving a continuous travelling-wave. The atoms and molecules with a magnetic dipole moment, in the LFS states, can be trapped and decelerated inside this trap. To synthesise the alternating-current, we use H-bridges for each current phase which consists of four high current IGBT switches. The decelerator coils circuit was designed by Barry Moss, an expert in the filed of high current and voltage electronics for use in the mining industry.

The supply electronics for a single phase is displayed in figure 4.17. A coil has inductive and resistive properties, which can be modelled using an inductor and resistor in series. The H-bridge IGBT switches (SKM400GB12T4) are capable of the fast switching of the high currents required for our application.

The operation of the H-bridge is as follows. Current is made to flow in one direction by closing switches Q1 and Q4 simultaneously. To reverse the current direction, switches Q2 and Q3 are closed while Q1 and Q4 are opened. When these switches are either fully open (when resistance is infinite) or fully closed (when resistance is zero), then the power dissipated is zero. However, the resistance is finite for all other times, and therefore, we cannot continuously increase the current sinusoidally, as this would generate a large amount of heat, destroying the switches. This problem is overcome using Pulse-Width-Modulation (PWM), which uses switches only in the preferred 'on' or 'off' states. The fast current switching required for the initial high frequencies is provided by the kick capacitors C2 (1.5 mF rated to 850 V). The hold capacitors, which act as the supply capacitors to supply the high current for the decelerator are indicated by C1 (2.2 mF, rated at 450 V). The power supply (Tdk Lambda ALE 202A series, 3 kV 2000 J/s) is connected to the positive and negative terminals. To allow the full 800 V from the power supply to be dropped across the pair, two of these are connected in series. Finally, the resistors indicated by R1 (10 kΩ) are discharge resistors for the supply capacitors. Figure 4.18 shows a schematic diagram of the complete decelerator electronics required to control the four separate blocks (labelled as 'coil a' etc.) that form a single coil with time-dependant modulated currents.

In PWM, a specific sequence of pulses is synthesised to drive the IGBTs to create the desired current waveform. This method encodes an analogue signal into a digital pulse sequence. This is done by sending the IGBTs a string of pulses of the correct length and by making use of the way an inductor and resistor in series draw current. This is because a coil has inductive and resistive properties, which can be modelled using an inductor and resistor in series. This is illustrated in figures 4.19 for a velocity of 150 m/s (frequency 3.5 kHz). The PWM sequence is generated as follows. Figure 4.19 shows a reference sine wave (red) and two copies (green), which are offset in both vertical directions by a certain percentage of the peak current of 1000 A of the reference sine wave. The amount of offset, typically in the range of 8-12%, was chosen based on the quality of the sine wave and the crossing of the sine wave with the horizontal axis. A representation of the reference signal is then created within the tolerance envelope using the analytic expressions for the charge and discharge of an inductor, shown in blue. For the positive half of the sine wave, when the current through the coils is greater or equal

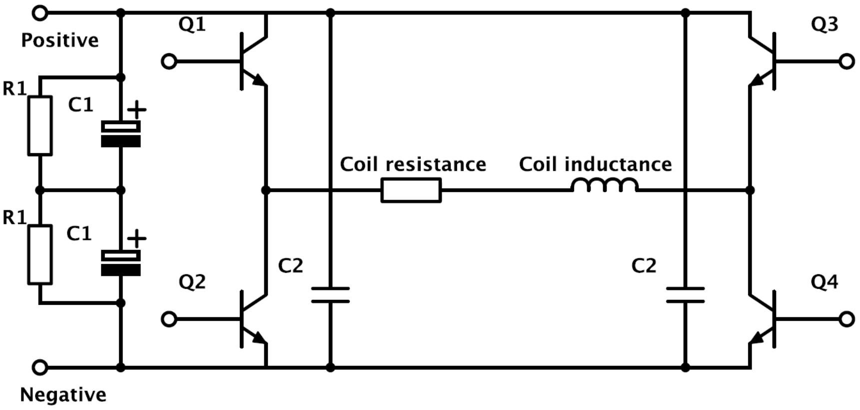

Figure 4.17: A schematic diagram of the H-bridge required for a single coil domain to drive a single phase. The coil is separated into its inductive and resistive components. The IGBTs are represented by the letter Q. Capacitors labelled as 'C1' are supply capacitors (2.2 mF rated to 450 V); two are connected in series to allow the 800 V from the supply to be dropped across the pair. Capacitors labelled as 'C2' (1.5 mF rated to 850 V) are the kick capacitors for the IGBT pairs. The positive and negative terminals are connected to a high-voltage power-supply. Components labelled as 'R1' (10 kΩ) are discharge resistors for the supply capacitors.

to the upper tolerance (upper vertically offset green sine wave), the voltage is switched off, causing the inductor to discharge. When the current falls below the lower tolerance, the voltage is switched on, and the inductor will begin charging as current is drawn again. The orange trace in 4.19 shows the resulting sequence of pulses required to create the synthesised current waveform. To achieve the required synthesised current sine wave, the pulse sequence carrying information about activation of the IGBTs and the pulse duration is first translated into a binary string. This is then encoded onto an FPGA which itself generates the pulses fed to the IGBTs via a driver card.

The coil in the circuit diagrams is separated into its inductive (L) and resistive (R) components, which it has intrinsically. The maximum current that can be drawn by the coil resistance has an associated rise time once a DC voltage is applied to the coils due to coil's inductance. This results from the fact that the voltage dropped across the coil equals the sum of the voltage dropped across the inductor and resistor. The ratio L/R is the time constant of the circuit and determines how fast the current changes in the circuit before reaching a steady state value. The current reaches this maximum steady state value after five time constants (transient time) after which the voltage across the inductance of the coil reduces to zero, effectively removing it from

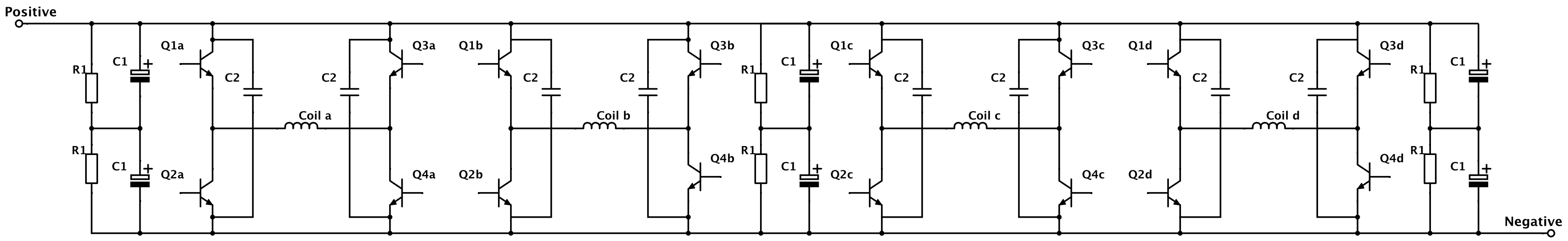

Figure 4.18: A schematic diagram of the complete decelerator electronics required to control the four separate blocks (labelled as 'coil a' etc.) that form a single coil with time-dependant modulated currents. The IGBTs are represented by Q. The letter indicates which coil block the H-bridge controls i.e. the IGBT indicated by Q1a is in position 1 and controls coil block a. Capacitors labelled as C1 are supply capacitors (2.2 mF rated to 450 V); two are connected in series to allow the 800 V from the supply to be dropped across the pair. Capacitors labelled as C2 (1.5 mF rated to 850 V) are the kick capacitors for the IGBT pairs. The positive and negative terminals are connected to a high-voltage power-supply. R1 (10 kΩ) are discharge resistors for the supply capacitors.

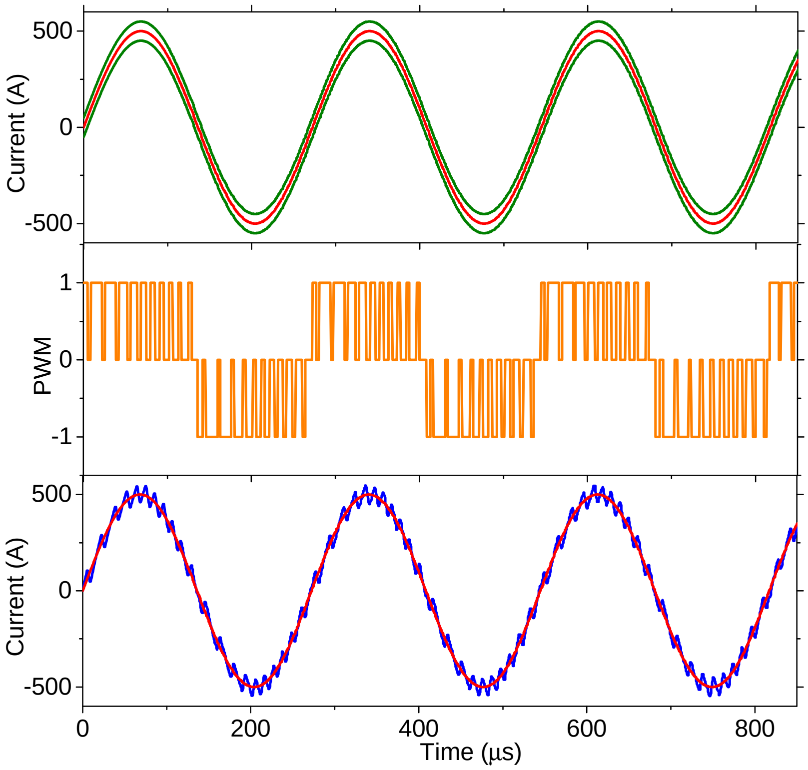

Figure 4.19: Digital pulse sequence used to produce the analogue sine waveform required for the decelerator coils for a trap velocity of 150 m/s (frequency= 3.5 kHz). Top: a reference sine wave (red) enclosed with the tolerance envelope (green). Middle: the digital voltage pulse width modulated sequence required to generate the synthesised wave. Bottom: the synthesised waveform (blue) is projected on top of the reference sine wave (red).

the circuit. At this point, the current only depends on the resistor. The average resistance and inductance of the four phases of the decelerator flat coils were measured (by Lewis McArd) to be 369±3 mΩ and 28.7±0.2 μH. This gives a time constant of $\sim$77.9±0.9μs.

The graph in figure 4.20 shows the measured sinusoidal current (black traces) via a current probe, achieved using pulse width modulation. The supply voltage used was 650 V and the repetition rate was 5 Hz. The two waveforms show how the quality of the sine wave improves as the frequency of the generated sine wave is decreased from a 8.5 kHz (velocity of 350 m/s) down to 3.5 kHz (velocity of 150 m/s). The difference in quality for the two sine waves is due to the time constant. The time constant limits how fast the current can be switched and the peak current that can be achieved. For the lower frequency/velocity, the switching is fast enough to have multiple on

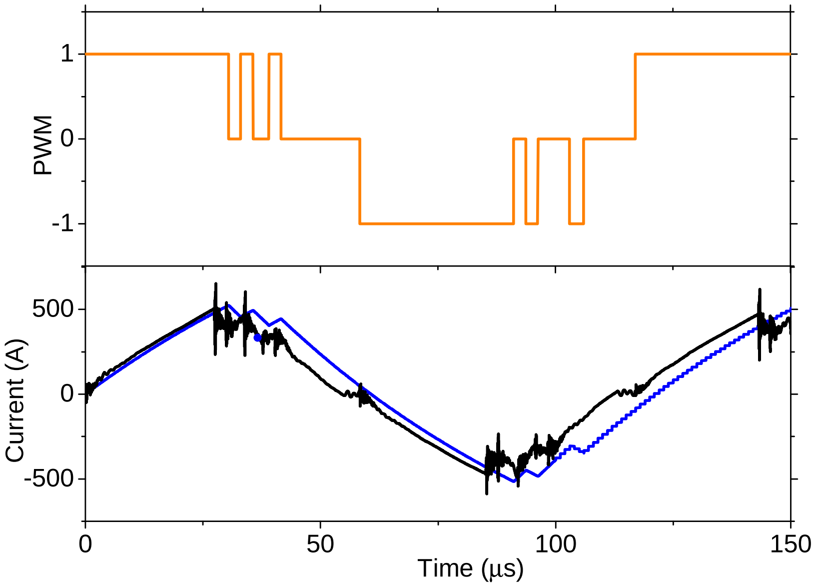

(a)

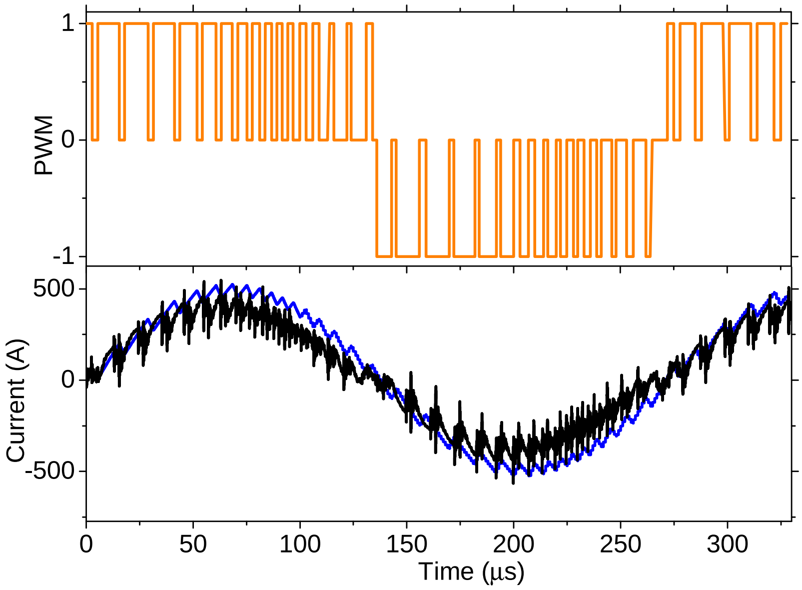

(b)

Figure 4.20: The synthesised sinusoidal current (blue) and the measured sinusoidal current (black) at roughly 500 A peak (650 V supply voltage) using a pulse width modulated sequence (yellow) for a trap velocity of a) 350 m/s and b) 150 m/s.

and off switching of the current, producing a smoother sine wave. However, for the higher frequency, the time constant needs to be shorter in order to be able to have a better representation of the sine wave.

4.5 Conclusions

To conclude, we have designed and built a modular moving-trap Zeeman decelerator that can produce moving magnetic traps to capture and decelerate short gas pulses that can then be detected. This chapter reviewed the operation principle of the decelerator and the demonstration of the generation of the high currents and magnetic fields required for deep traps. The final coil geometry for the decelerator coils and quadrupole guide were decided after performing simulations (by Ulrich Krohn and Lewis McArd). The decelerator vacuum system was designed to be compact, reducing the cost. The source chamber and cooled pulsed discharge valve assembly was designed to produce short gas pulses which can be characterised and optimised with a FIG. A skimmer allows the partial spatial matching of the source emittance to the decelerator acceptance. The detection chamber was designed to allow different means of detecting atoms and molecules: MCP, single-pass LIF, CELIF and using a QMS with the ability to photo-ionise.

By designing an automated coil-winder, we can construct decelerator coils with very few discrepancies. One of the major achievements of this project was to overcome the great challenge of pulsing high currents at high frequencies. The electronics driving the quadrupole guide can supply currents up to 700 A for a variable duration. The electronics and power supplies of the flat helical decelerator coils, to date, are capable of delivering sinusoidal currents up to 600 A peak current in each wire at frequencies ranging from 8.8 kHz to DC for durations of a few milliseconds at repetition rates up to 10 Hz. We have not yet achieved a peak current of 1000 A at the required high velocities or frequencies since the ratio of inductance to resistance is high. One way in which this can be improved is by using connections between the wires with a smaller resistance and inductance. We could also start with a slower beam from a buffer gas source, as discussed in the first chapter. With slower beams, lower frequencies are required. At lower frequencies the sinusoidal currents are of better quality and higher currents can also be achieved for a given time constant.

Chapter 5

Magnetic Guiding and Experiments Towards the Deceleration of Ar*

In this chapter, the first set of results from our moving-trap magnetic decelerator are presented. The transverse 2D-guiding of the Ar* atoms in our decelerator is carried out by the quadrupole guide. This is done independently to the deceleration which is in the longitudinal direction, along the molecular beam axis, and is achieved by the planar decelerator coils. In the presentation of our results, we first demonstrate the 2D-guiding of Ar* using the quadrupole guide followed by the 3D guiding and the first attempt at the deceleration of Ar* atoms in a travelling magnetic wave.

5.1 Atoms in Magnetic Fields

Central to our experiment is the Zeeman effect; without it, we would not be able to apply a force to the atoms. The Zeeman effect describes the splitting of atomic energy levels in the presence of an external magnetic field, $\vec{B}$. This is the potential energy associated with the magnetic moment of the system, $\vec{\mu}$, when placed in a uniform magnetic field, $\vec{B}$, and is given by [120]

$$V = -\vec{\mu} \cdot \vec{B}, \tag{5.1}$$

or in the case of a magnetic field only along the z-direction, it is given by

$$V = -\mu_z \, B_z. \tag{5.2}$$

This effect can be used to exert a force on particles by applying inhomogeneous magnetic fields according to

$$\vec{F}_z = -\nabla V. \tag{5.3}$$

The total magnetic moment of the electrons, $\vec{\mu}$, can be written in terms of the sum of the intrinsic magnetic moment, μ_s, associated with the intrinsic spin angular momentum, s, and the magnetic moment, μ_l, associated with the orbital angular momentum, l. These are given by

$$\vec{\mu}_s = -g_s \, \mu_B \, \vec{s} \tag{5.4}$$

$$\vec{\mu}_l = -g_l \, \mu_B \, \vec{l} \tag{5.5}$$

where $\mu_B = e\hbar/2m_e c$=9.27×10^{24} J/T is called the Bohr magneton, g_l is the gyromagnetic ratio of the electron's orbital angular momentum and is equal to 1, and g_s is the gyromagnetic ratio of the electron's spin and is roughly equal to 2 according to Dirac's relativistic theory of electron spin. [120] In the case of argon, the nuclear spin is zero, and therefore there is no magnetic moment associated with the nuclear spin.

For many electron atoms, the terms s and l are replaced with S and L to denote the sum of the angular momenta. Therefore, the total magnetic moment of the electrons is given by

$$\vec{\mu} = -\mu_B \, (2\vec{S} + \vec{L}) = -\mu_B(\vec{J} + \vec{S}) \tag{5.6}$$

where $\vec{J} = \vec{L} + \vec{S}$. Substituting equation 5.6 into 5.1 we obtain

$$V = -\mu_B(\vec{J} + \vec{S}) \cdot \vec{B}. \tag{5.7}$$

The Zeeman interaction is treated as a small perturbation. The weak field approximation is made, meaning that the Zeeman splitting produced by the external field is small compared with the fine structure (i.e. the spin-orbit interaction) or the applied field is weak compared to the field internal to the atom. In this weak field regime, the eigenstates are described in the coupled angular momentum basis sets.

Using first-order perturbation theory, the Zeeman energy splitting of the state $|\gamma LSJM_J\rangle$, where γ specifies the configuration, is

$$\Delta E = \langle \gamma LSJM_J \,|\, V \,|\, \gamma LSJM_J \rangle \,. \tag{5.8}$$

The matrix elements can be evaluated by projecting onto the quantisation axis, and by doing so, one eventually ends up with the Zeeman energy shift (Refer to page 149 in the given reference for the full derivation [120])

$$\Delta E = g\mu_B M_J B_z, \tag{5.9}$$

where g is the Landé g-factor and is given by

$$g = 1 + \frac{J(J+1) + S(S+1) - L(L+1)}{2J(J+1)}. \tag{5.10}$$

The electronic configuration of the ground state of argon is $1s^2 2s^2 2p^6 3s^2 3p^6$, giving the single state of ${}^1S_0$. The next higher energy electronic configuration is $1s^2 2s^2 2p^6 3s^2 3p^5 4s^1$. This configuration has four energy levels from the LS-coupling. The four states are ${}^1P_1$, ${}^3P_0$, ${}^3P_1$, and ${}^3P_2$. The next higher energy electronic configuration is $1s^2 2s^2 2p^6 3s^2 3p^5 4p^1$. This configuration has ten energy levels from the LS-coupling. The ten states are given by ${}^1S_0$, ${}^3S_1$, ${}^1P_1$, ${}^3P_0$, ${}^3P_1$, ${}^3P_2$, ${}^1D_2$, ${}^3D_1$, ${}^3D_2$, and ${}^3D_3$. The ${}^3P_2$ and ${}^3P_0$ states are the two lowest energy states that are metastable and are accessible using electric discharge excitation. The energies of these two states are $93143.8\,\mathrm{cm}^{-1}$ and $94553.7\,\mathrm{cm}^{-1}$, respectively. [121] Typical Zeeman splitting in our experiments are a couple of cm^{-1} (see figure 5.1), which is much smaller than the spin-orbit (fine-structure) splitting, thus, the weak field regime applies and the Zeeman effect is linear, as given by equation 5.9.

For metastable argon in the ${}^3P_2$ state, all five M_J magnetic sub-level quantum states ($M_J = 2, 1, 0, -1, -2$) are equally populated. In the absence of a magnetic field, all the M_J sub-levels are degenerate but this degeneracy is broken in the presence of a magnetic field. When the degeneracy is broken, the energy splitting of the sub-levels depends on whether the projection

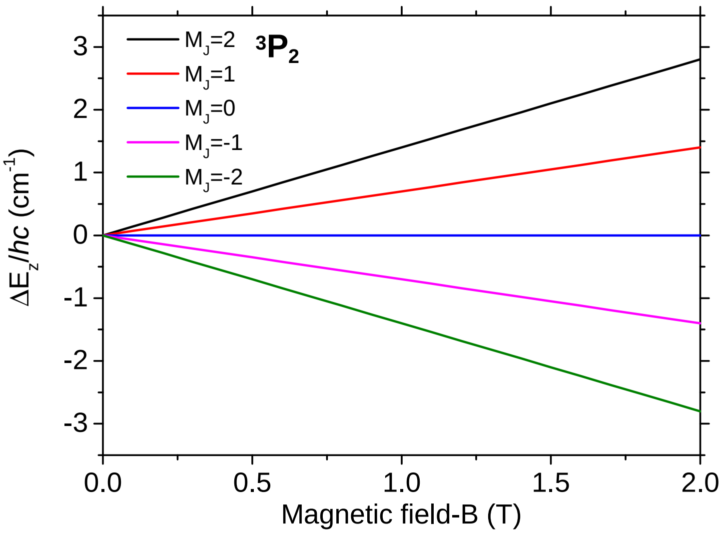

Figure 5.1: The Zeeman effect in the $^3P_2$ state. The low-field-seeking state $M_J = 2$ with the largest magnetic moment is depicted in black. Plotted using equation 5.9.

of the spin is parallel or anti-parallel to the applied magnetic field. Figure 5.1 (as seen in chapter one) illustrates the Zeeman effect in the $^3P_2$ state, as calculated using equation 5.9. The different M_J Zeeman sub-levels are divided into two groups: high-field-seeking states (HFS, $M_J = -1, -2$) and low-field seeking states (LFS, $M_J = 1, 2$). The HFS states minimise their energy in high magnetic fields while the LFS state minimise their energy in low magnetic fields. The overall effect on LFS states is that the inhomogeneous magnetic field exerts a force, according to equation 5.3, on the atom and pushes it back towards the low field region and vice versa for the HFS.

5.2 2D Guiding of Ar*

Once the decelerator machine and the source were built, the first test to be carried out was the 2D-guiding of Ar* atoms using the magnetic fields produced by the quadrupole guide. The schematic diagram in figure 5.2 shows the experimental setup used in the 2D-guiding experiments. The metastable atoms are produced by the electric excitation of the liquid-nitrogen cooled argon gas pulse exiting the valve, which supersonically expands into the source chamber. The driving pulse width for the cold valve was 126 μs. A typical

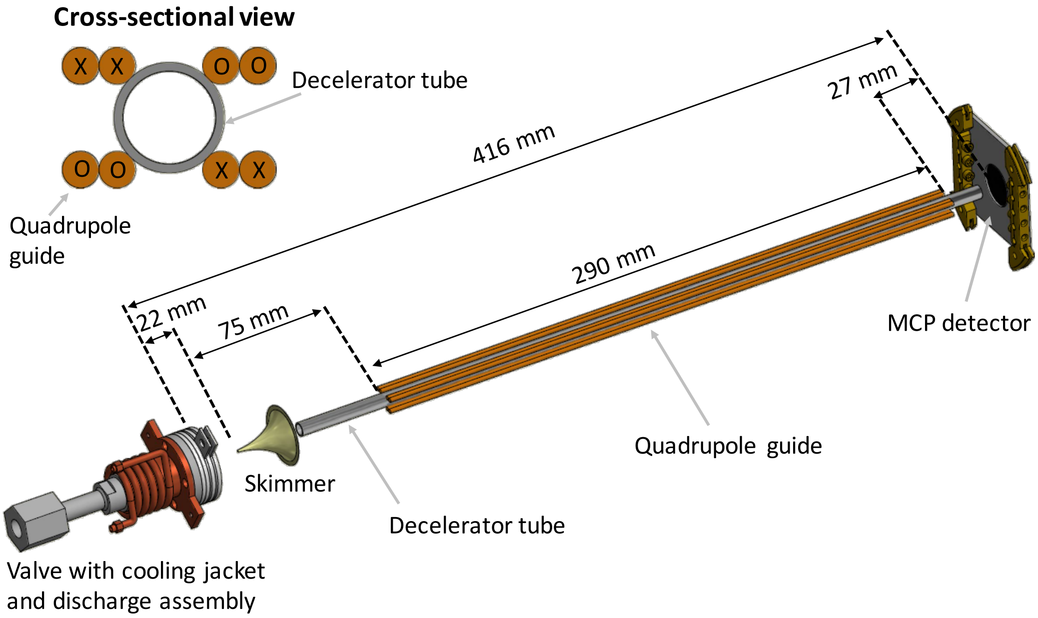

Figure 5.2: A schematic diagram of the experimental setup used in the 2D-guiding experiment. The supersonically expanded pulse of argon atoms is produced by the pulsed valve which is cooled with liquid nitrogen. The discharge assembly excites the argon atoms to metastable states (Ar*). The skimmer orifice with a 1 mm diameter, is positioned at a distance of 22 mm downstream from the midpoint between the discharge electrodes. The beam passes through the 350 mm long, 5.35 mm I.D. stainless-steel tube. The MCP detector is placed 416 mm downstream from the point where the metastable atoms are created. The 290 mm long quadrupole wires (2 mm O.D.) run parallel to this tube, starting at 75 mm and ending at 365 mm from the skimmer orifice. The free-flight distance from the quadrupole end to the MCP detector is only 27 mm. A cross-sectional view of the quadrupole and the decelerator tube is also shown. The circles and crosses indicate the direction of the currents flowing through the quadrupole wires.

argon backing pressure that was used was 2.7 bar. Once cooled, the nozzle temperature was measured to be 120 K using the thermocouple attached to the valve's front-face flange. The electric excitation occurs between the two discharge electrodes, this is taken as the point of creation for the metastable state atoms. A voltage of 500 V was applied with a 20 μs pulse width for the electric discharge. The delay between the valve triggering and the high-voltage discharge pulse was 274 μs. The discharge-stabilising filament current was set to 1.5 A. The data was averaged over 40 shots.

Once excited by the electric discharge, the argon gas pulse travels through the 1 mm orifice of the skimmer positioned at a distance of 22 mm downstream, and then into the stainless-steel decelerator tube. The quadrupole guide

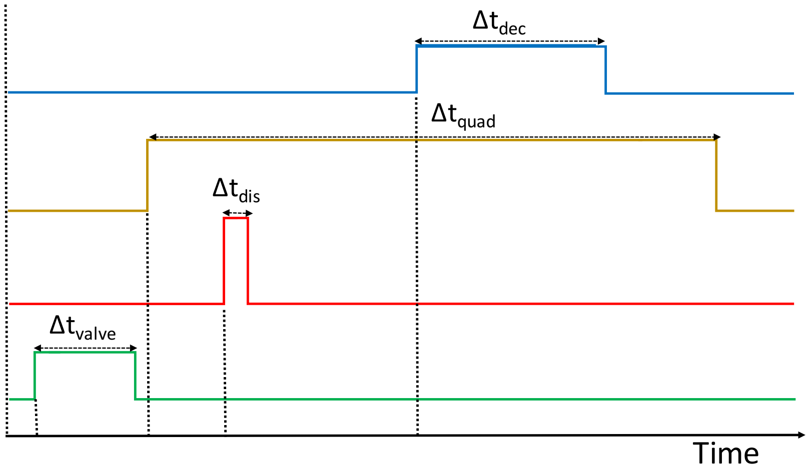

Figure 5.3: An illustration of a typical pulse sequence used in each repetition pulse of the guiding and deceleration experiment. The green trace represents the opening pulse for the valve with a pulse width of around 126 μs. The red trace represents the high-voltage discharge pulse with a pulse width of 20 μs. The middle of this pulse marks the zero of time. This is applied after a delay of around 274 μs from the valve opening trigger pulse. The quadrupole is triggered before the discharge pulse (yellow trace) with a guiding pulse width of around 2.3 ms. The sinusoidal current through the decelerator coil is applied later and lasts around 400 μs.

starts at a distance of 75 mm from the skimmer orifice (figure 5.2). In the 2D-guiding experiments, the currents driving the quadrupole guide were in the range 0-900 A. The MCP detector, placed at a distance of 416 mm from the point where the metastable atoms are created, detects the arrival times of the guided atoms. The mean velocity and the translational temperature of the beam can be extracted from the time-of-flight (TOF) distribution by fitting it with a distribution, as described in chapter two.

The driver electronics of the quadrupole were discussed in chapter four. Figure 5.3 shows a typical pulse sequence of the guiding and deceleration experiments. The green trace represents the opening pulse for the valve with a pulse width of around 126 μs. The red trace represents the high voltage discharge pulse with a pulse width of 20 μs. The middle of this pulse marks the zero of time. This is applied after a delay of around 274 μs from the valve trigger pulse since this was found to be the optimum delay to produce the greatest number of metastable atoms. The quadrupole is triggered 150 μs before the discharge pulse (yellow trace) with a guiding pulse width of around 2.3 ms. This is to ensure the peak current is reached before the beam reaches the beginning of the quadrupole guide. The finite rise-time of the quadrupole (477 μs) is also taken into consideration. As previously explained, this long rise-time may pose a problem with the atoms experiencing fringe fields as they approach the first decelerator trap. However, this is a risk we have to take since we are currently unable to switch the quadrupole currents sufficiently fast. For the 3D-guiding and attempted deceleration experiments, the sinusoidal current applied to the decelerator coils is triggered after a certain delay and lasts around 400 μs, this is roughly the flight time through the 123 mm long single module. The deceleration and 3D-guiding experiment will be discussed in the next section.

The magnetic fields produced by the quadrupole guide were illustrated and discussed in chapter four. The magnetic field strength is zero along the axis, through the centre of the decelerator tube and increases in strength with increasing radial distance. The atoms in low-field-seeking (LFS) states are guided towards the detector along the length of the quadrupole. Figures 5.4a and 5.4b show the measured and the theoretical quadrupole fields at 500 A. The magnetic fields were measured by using a home-made Hall probe that was constructed of a Hall effect sensor (Honeywell SS39ET) which was glued onto a rod. The sensor was calibrated against a commercial Hall probe (model GM04) by measuring the magnetic field of a permanent magnet. The sensor that was glued onto the tip of the rod was translated along the x and y direction by clamping the rod onto a translation stage. The x direction is close to theory but the y direction differs. It is suspected that the problem is coming from the wires not being perfectly positioned due to them not being well clamped in place in the region where the Hall probe was measuring. For a driving current of 500 A through the quadrupole, the measured magnetic trap depth at the wall in the x-direction is 85 mT giving a gradient of 32 Tm^{-1} and in the y-direction the trap depth is 70 mT giving a gradient of 26 Tm^{-1}.

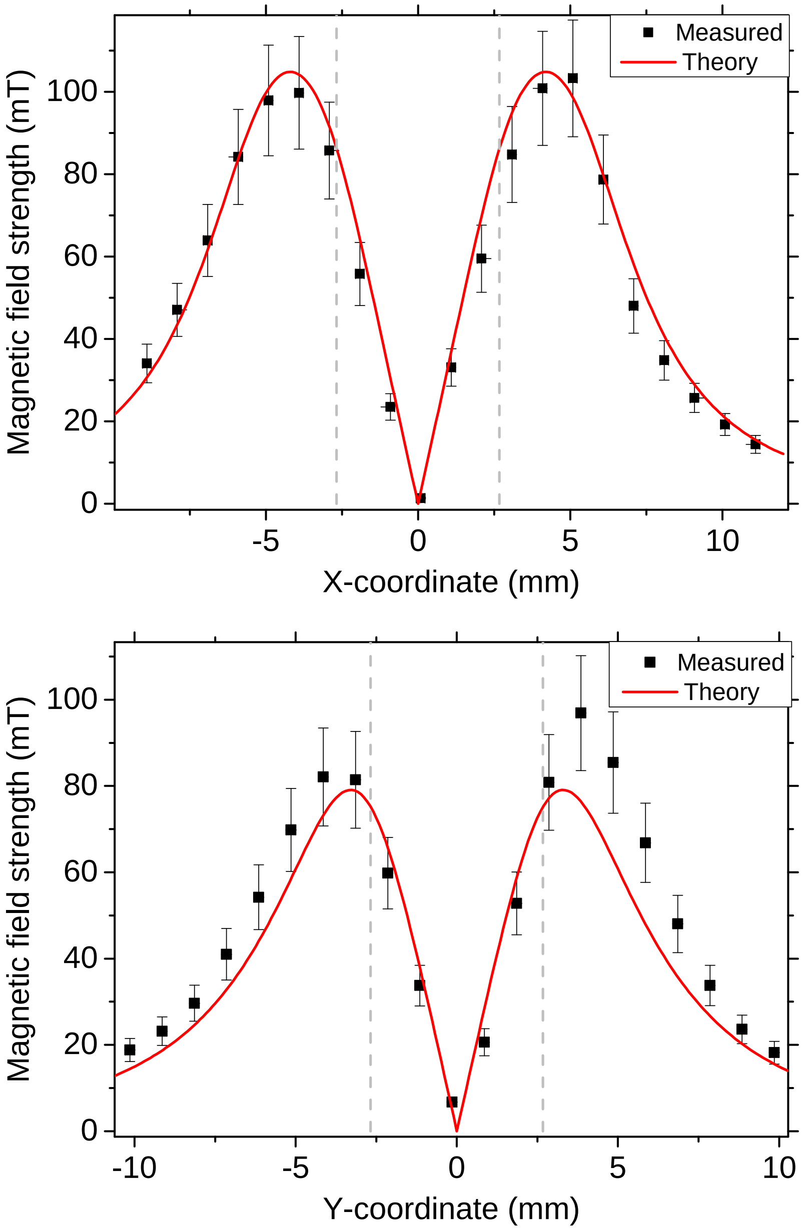

Figure 5.4: Measured magnetic field strength (black squares) at a current of 500 A along the X-coordinate (a) and Y-coordinate (b). The red traces are the calculated fields from theory. The grey dashed lines mark the walls of the quadrupole.

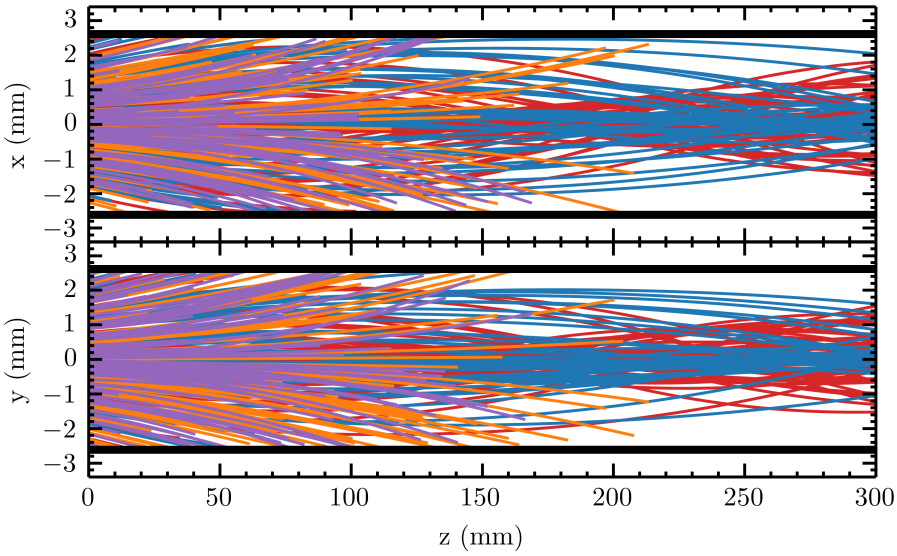

Figure 5.5: Simulated particle trajectories for the different M_J sub levels of the $^3P_2$ metastable state of argon along the x-direction (top) and the y-direction (bottom). The quadrupole current used was 700 A and the beam speed was 335 m/s with a FWHM of 66 m/s. Red $\mathrm{M}_J = 2$, blue $M_J = 1$, orange $\mathrm{M}_J = -1$, purple $M_J = -2$. The $M_J = 0$ state is not shown.

Figure 5.5 shows the simulated particle trajectories for the HFS and LFS M_J sub levels of the $^3P_2$ metastable states of argon. Each state is represented by a different colour. Only the LFS states ($M_J = 2, 1$) are confined by the magnetic fields of the quadrupole. All HFS states ($M_J = -2, -1$) are repelled and crash into the walls of the decelerator tube. The two $M_J = 0$ states (not seen in the figure) of both $^3P_2$ and $^3P_0$ have no magnetic dipole-moment, and therefore, pass through the tube without feeling the effect of the quadrupole magnetic field. The ones that do make it to the end of the tube also contribute to the MCP signal. Therefore, from the six magnetic sub-levels, only a third is lost from crashing into the walls. Without the transverse confinement provided by the quadrupole guide, most of the atoms would eventually crash into the inner walls of the decelerator tube. This is because the argon atomic beam diverges after it moves towards the MCP detector due to the transverse spread in velocity. The quadrupole guide effectively acts like a focussing lens for the LFS states where the focal length depends on the effective dipole moment, and therefore, the state. The confinement strength is proportional to the state's Zeeman shift.

Comparing the trajectories in the x-direction to those in the y-direction, there is slightly more confinement in the x-direction due to the pole geometry used. Therefore, greater velocities can be focussed and guided. The magnetic fields from the quadrupole guide manipulate the atoms in the transverse direction, causing them to oscillate around the molecular beam axis due to the restoring force towards the beam axis until they reach the detector. The atoms in the $M_J = 2$ (red) state complete 1.5 oscillations while the atoms in the $M_J = 1$ (blue) state only complete half an oscillation. For a longer quadrupole, the atoms will have longer time to oscillate and complete more oscillations.

The traces in figure 5.6a show the observed effect of the magnetic fields from the quadrupole guide on the measured Ar* signal. The black trace shows the transmission peak (without any current through the quadrupole guide) and all other traces are for the guided peaks using different driving currents. The mean velocity of the beam is 330 ± 9 m/s with a FWHM velocity spread of 94 m/s. The intensity of the signal increases with increasing quadrupole current. This is expected, since increasing the current increases the magnetic field gradient, which means that atoms with greater transverse velocities can be guided by the greater force. One might also notice that the slower tail of the distribution (with the longer arrival times) experiences a bigger change in signal than the faster part of the distribution. This is due to the fact that the slower atoms spend more time in the magnetic field of the quadrupole, and therefore, experience the force for longer. The measured change in signal will be even greater with increasing quadrupole or decelerator length, since the transverse guiding becomes more important for longer flight times. Although a higher current leads to a greater enhancement in the intensity of the detected metastable argon peak, greater currents also lead to more heating of the wires. At the higher current, the heating leads to an increase of resistance which results in a drop of current.

To verify the measured TOF traces, Monte-Carlo trajectory simulations were performed (by Lewis McArd). For the quadrupole, the infinite straight wire equations were used to calculate the quadrupole magnetic field, which was generated on a grid (1550 points per mm^2). For the flat decelerator coils, the decelerator fields were calculated using the Biot-Savart law. A 3D cubic interpolator was used to fill between the grid points. The spatial extent was chosen to be within the outer diameter of the tube (± 3.175 mm in the x and

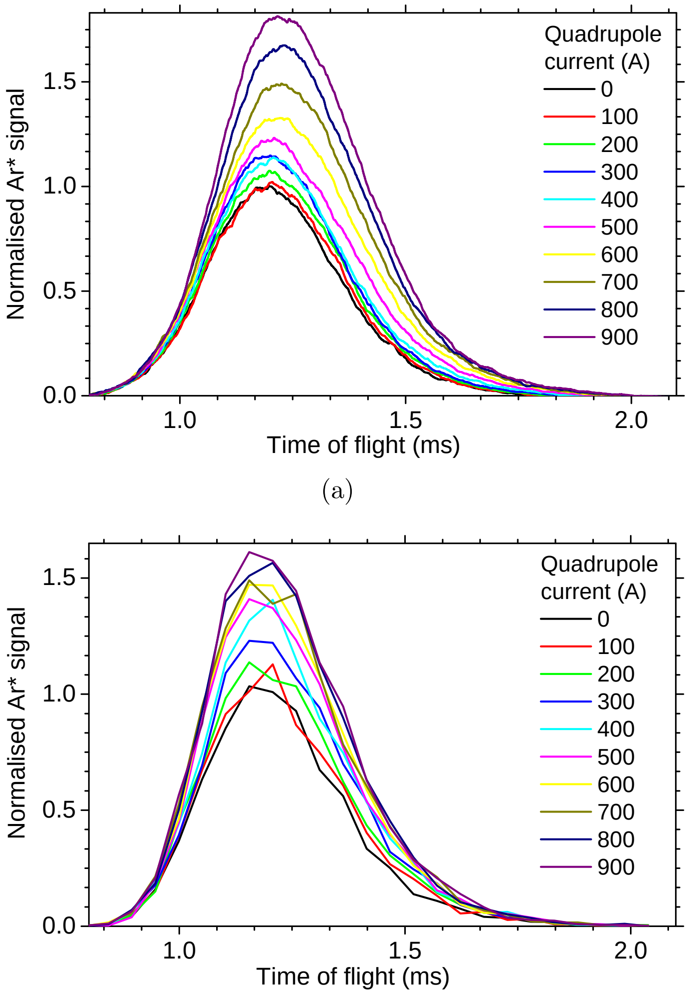

(a)

(b)

Figure 5.6: a) Measured and b) simulated 2D guiding of Ar* atoms at different currents for a nozzle temperature of 120 K. The initial beam travels at 330±9 m/s with a FWHM spread of 94 m/s (3.8 K). The data is normalised to the transmission peak.

y directions) that marks a position cut-off beyond which particles are lost. The magnetic field between the grid points was determined by interpolation. From this, the field derivatives were calculated for the force. In the TOF plots, the initial distribution of the atoms was chosen to simulate the source setup. The spatial and temporal width of the source at the discharge electrodes was assumed to be a point source due to the relatively long TOF of the beam to the detector. Furthermore, the expansion of the gas pulse due the finite longitudinal temperature was found to be bigger than any other contributions. The velocity spread in the z-direction was set to the experimental FWHM. The transverse x and y spatial and velocity distributions were determined geometrically from the skimmer aperture, the valve nozzle and their separations. Firstly all particles are given a random point at the nozzle aperture (a random radial position and a random angle relative to the x axis). Next, the particles are given another random point at the skimmer aperture (again a random radial position and a random angle). Initially, the particles are uniformly distributed throughout the valve aperture. A vector is drawn between the nozzle and skimmer points. Then, using the known z and the velocity along the z direction, the transverse velocity components can be calculated. Therefore the transverse velocity is determined through geometrical constraints imposed by the skimmer and nozzle. The particle trajectories are then simulated. The particle motions are then calculated by numerically solving the differential equations using a fourth order Runge-Kutta algorithm.

Figure 5.6b shows the simulated TOF traces for the data in figure 5.6a using an initial beam with the same mean velocity and spread as the measured transmission signal (0 A quadrupole guide current). The first thing to note is that the intensity increases as expected. However, some obvious differences can also be seen. To better compare the differences, the signals were analysed to give the integrated area, mean velocity, and the translational temperature. The integrated area of the measured and simulated signals is plotted in figure 5.7. The measured signal (black trace) shows an increase by nearly a factor of two from 0 A to 900 A. The area increases with increasing current linearly from 0 A to 300 A. After a current of 300 A, this increase becomes faster with a bigger gradient. The stronger the field, the bigger the maximum transverse velocity which can be guided by the quadrupole guide. We would expect a

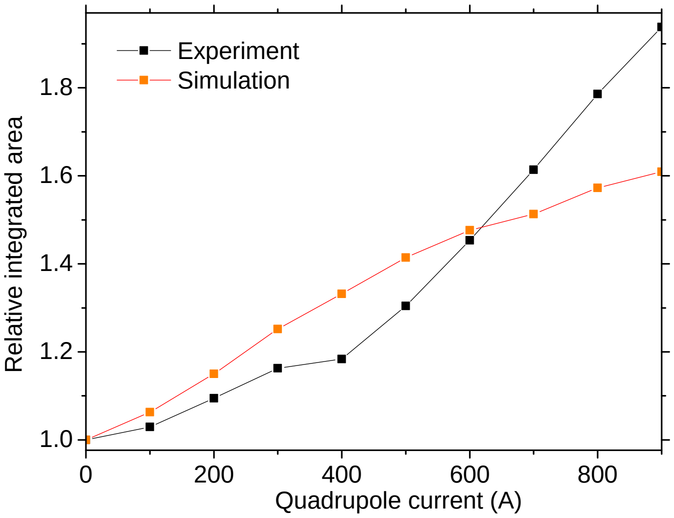

Figure 5.7: The integrated area of the metastable argon peak traces in figures 5.6a and b for the experimental and simulated TOF traces at different quadrupole currents.

linear increase which should saturate at some point, as expected from the simulations (orange trace).

When the TOF traces in figure 5.6a are carefully examined, one can see a slight shift in the peak arrival time and therefore the mean velocity. The traces in figure 5.6a and b were analysed to extract both the mean velocity and translational temperature of the distribution. The results are presented in figure 5.8a and b. The simulated data shows the expected behaviour, the mean velocity is not altered by varying the quadrupole current. For the measured data, it can be seen that the mean velocity changes by 15 m/s as the current is increased from 0 A to 900 A. Just as with the integrated area, the mean velocity is constant from a 0 A to 300 A, as one would expect, since the transverse quadrupole fields should have no effect on the arrival times of the atoms. However, further increase from 300 A and above seems to cause a shift in the velocity distribution, giving a mean velocity that is around 10 m/s slower at 700 A. The increase in the translational temperature also seems to occur at currents higher that 300 A. For the simulated data, the very small change in the translational temperature is a result of the fitting of the simulated data which is not perfectly smooth.

One might think that the appearance of slower atoms in the TOF distribution when the guide is active may be because under these conditions the slower atoms can travel through the device without being lost by collisions with

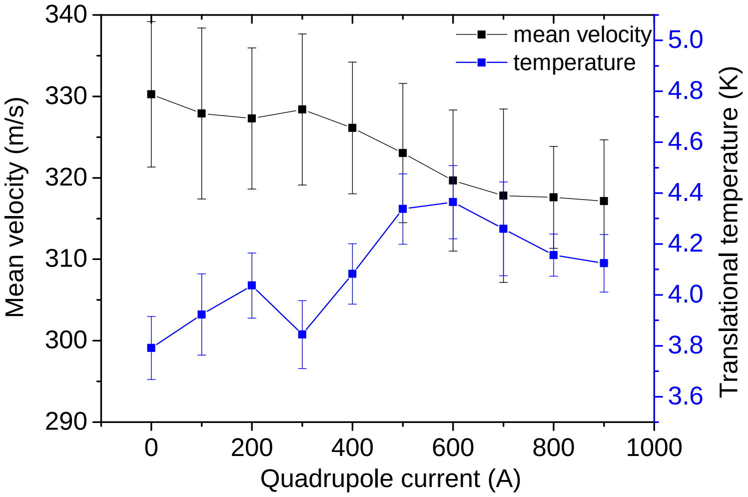

(a)

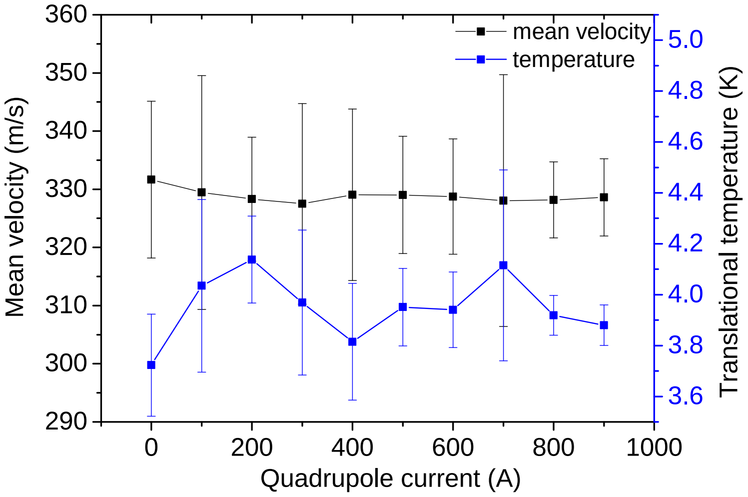

(b)

Figure 5.8: The mean peak velocity (black) and the translational temperature (blue) for the a) experimental and b) simulated TOF data presented in figures 5.6 a and b.

the walls, as would be the case when the guide is off. This is supported by the fact that the drop in the apparent mean velocity of the beam occurs at a similar current for the point where integrated area increases differently to the simulated data. One must also note that the velocities of the measured and simulated data do agree within the error. However, the greater increase in the relative integrated area in the Ar* in the measurements compared to the simulations suggest that there is another factor affecting the atom's trajectories which was not considered in the simulations. One possible explanation for this difference is due to the fringe fields produced both at the entrance and the exit of the quadrupole guide. The quadrupole is made from a single wire that is wound in the required arrangement, therefore there are bends at either end. There is a distance of 97 mm from the discharge electrodes to the beginning of the quadrupole. As the atoms travel through this distance, the atoms can be affected by the fringe fields on entrance to the quadrupole. The quadrupole current pulse has a finite rise time of 477 μs, and is therefore switched on in advance in such a manner that the peak current is reached by the time the atoms reach the beginning of the quadrupole.

The fringe fields are a likely suspect for this effect since they produce a field gradient in the z-direction that is not accounted for in the simulations. Figure 5.9 shows the calculated fringe fields at the beginning and the end of the 290 mm long quadrupole at 700 A. The size of the wire loop was close to 5 mm. The sudden drop in the magnetic field in the z-direction at the end of the quadrupole is a numerical calculation error. Looking at this field, one can appreciate that the atoms are decelerated as they climb up the potential hill on entrance to the quadrupole. These atoms then climb back down the potential hill and are accelerated back to the initial velocity. The same thing occurs at the end of the quadrupole. Though the atoms' initial velocity does not change, the arrival time is longer due to the extra flight time gained when they were decelerated and accelerated by the potential hill. The mean velocities calculated and illustrated in figure 5.8a were calculated based on the mean arrival time of the peaks after fitting the TOF distributions. The calculation does not account for the changes in the velocity of the atoms due to the fringe fields during the flight time of the atoms. If we approximate the fringe fields as linear, using the gradient of the field we can approximate the deceleration and acceleration experienced by the atoms due to the fringe fields. This was found to give a longer time of flight which gives a velocity

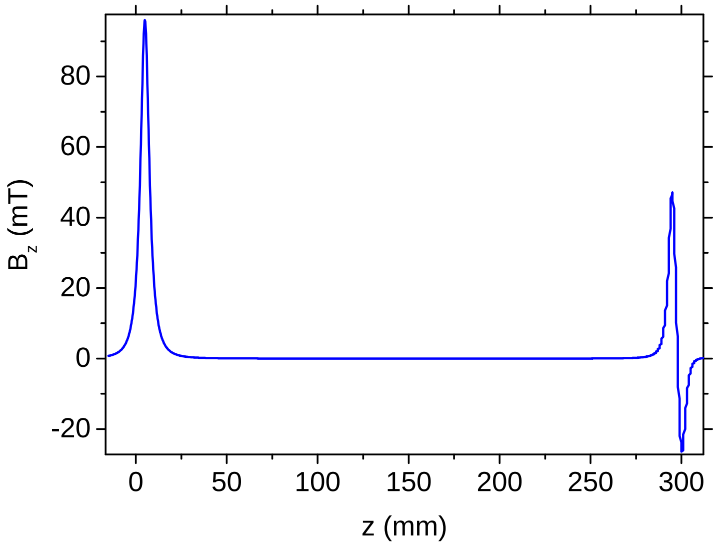

Figure 5.9: Calculated fringe fields at the beginning and the end of the 290 mm long quadrupole at 700 A. z=0 marks the beginning of the straight part of the quadrupole while z=290 marks the end.

that is slower by 20 m/s. This is an overestimate doe to the approximation of the field as linear, therefore this is not far from the 10 m/s drop in velocity seen at 700 A, as seen in figure 5.8.

These fringe fields can be avoided by rapidly switching on the current to the peak value with fast switching times of around 10 μs, at a time when the atoms are within the quadrupole. This will require the addition of another power supply to the quadrupole circuit described in chapter four. Currently, the on-time of the quadrupole is excessively longer. For the 290 mm long quadrupole, a beam with a mean velocity of 330 m/s only requires a current on time of 1.76 ms. However, in our measurements, the electrical noise from the fast switching and the rise and falling edges of the quadrupole current pulse are superimposed on the Ar* MCP signal. Therefore, it was necessary to use a longer pulse to avoid overlap of this noise on the Ar* MCP signal. To date, we have attempted to reduce this noise by eliminating earth loops, using shielding on signal cables and by using a shielded box for the voltage follower of the MCP detector. However, this still remains a work in progress. Once this noise issue is eliminated, we can use the fast switched current pulse in such a way that the atoms completely avoid the fringe fields from the quadrupole guide.

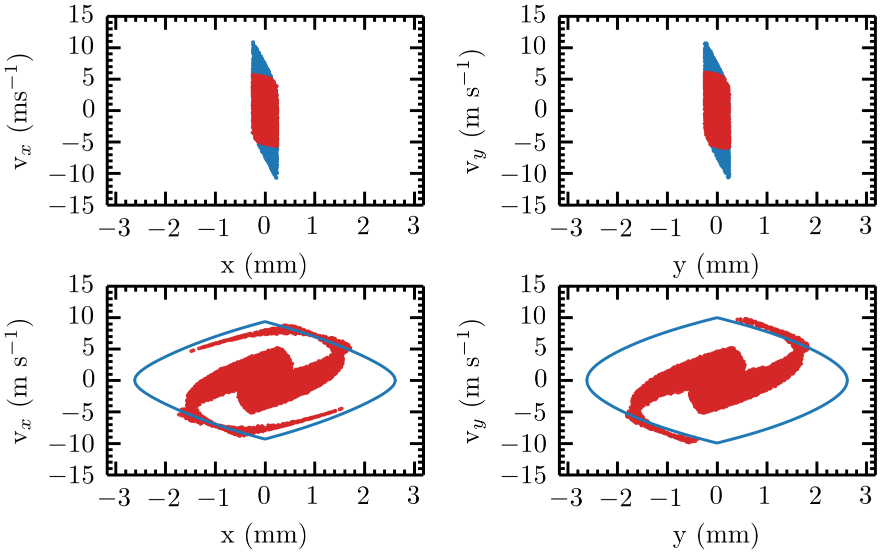

Figure 5.10: Initial (top) and final (bottom) phase-space distribution in the x (left) and y (right) dimension of a Monte Carlo simulation of 25,000 particles for the $M_J = 2$ state. Particles that will be rejected are plotted in blue, and are no longer plotted once they have collided with the beam tube wall. Simulation were carried for a beam travelling the length of the quadrupole (∼300 mm, 700 A) at 335 m/s with a FWHM spread of 66 m/s in the z-direction.

The top of figure 5.10 shows the phase-space distribution at the skimmer. The initial distribution, or source emittance distribution has this specific starting shape due to the geometry of the system. The particles with a large position must have a large velocity in the opposite direction (away from the tube wall). The bottom phase-space distributions show the final phase-space distribution in the x and y directions, at the end of the quadrupole with the 1D-model separatrix indicated by a blue line. This is for atoms in the $M_J = 2$ state. The separatrix determines the highest positions and velocities that can be accepted or captured by the magnetic fields, in this case from the quadrupole guide alone. Any particle within the separatrix will follow a closed trajectory. Particles within the acceptance will make it to the detector, while those outside will crash into the walls of the decelerator tube. After passing through the quadrupole guide, the phase-space distribution rotates clockwise. This is due to the anharmonicity of the potential, which means that the outer orbits have longer periods than the inner ones, resulting in spiral structures. The particles spread away from the separatrix due to free flight expansion.

From figure 5.10 we can see that the velocity acceptance in the radial direction for the argon atoms in the $^3P_2$, $\mathrm{M}_J = 2$ quantum state is about $\pm 10\,\mathrm{m/s}$ in the x and y directions. The radial spatial distribution was selected by completely filling the internal diameter of the delivery tube. The transverse velocity was selected through the geometrical constraints imposed by the skimmer and nozzle. So for the gas pulse described, the emittance is $2.46 \times 10^4\,(\mathrm{mm\,m/s})^2$, the zero field acceptance is $6.11 \times 10^2\,(\mathrm{mm\,m/s})^2$, and the acceptance at 700 A is $3.00 \times 10^3\,(\mathrm{mm\,m/s})^2$.

Figure 5.11 shows the phase-space distribution evolution for atoms in the $\mathrm{M}_J = 2$ state at four different points along the quadrupole, starting at the entrance of the quadrupole (a), at 100 mm from the entrance (b), at 300 mm from the entrance (c), and at the end of the decelerator (d). The clockwise rotation of the phase-space distribution can be clearly seen. Figure 5.12 shows the phase-space distribution evolution at the same points, but showing all five M_J states, indicated by different colours. The behaviour of the $\mathrm{M}_J = 2$ state is repeated here in red. The $\mathrm{M}_J = 1$ state shows similar behaviour, however, the phase-space distribution rotates less as this state feels a smaller force from the quadrupole magnetic field gradient. Initially, the HFS state phase-space distribution starts to rotate anticlockwise (opposite to the LFS). The $\mathrm{M}_J = -2$ state disappears in the third frame while the $\mathrm{M}_J = -1$ state is no longer visible in the last frame. There is no rotation in the trajectories of the $\mathrm{M}_J = 0$ state, since, without a magnetic dipole moment, these experience no force from the magnetic field gradient of the quadrupole.

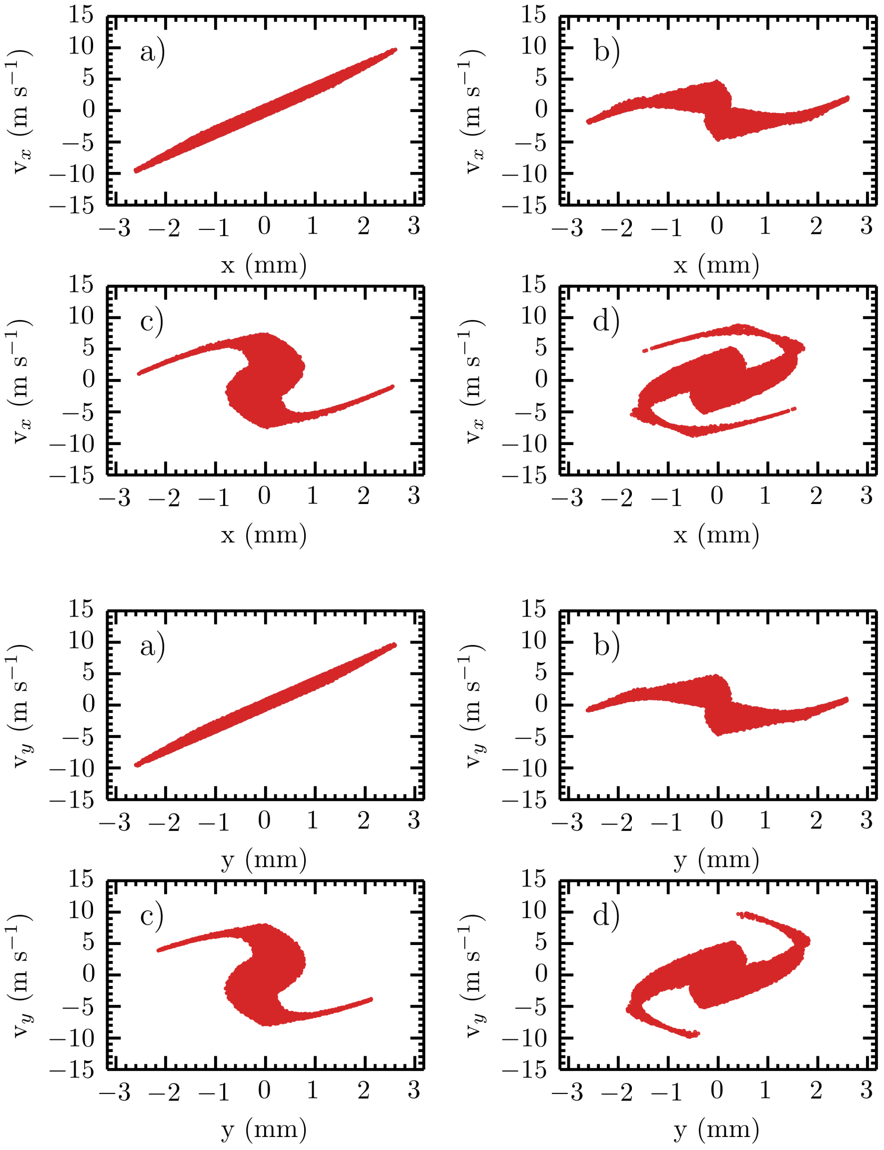

Figure 5.11: Phase space evolution in the x (top) and y (bottom) dimension of a Monte Carlo simulation of 25,000 particles for the for the $M_J = 2$ state and 700 A in the quadrupole guide. Particles that will be rejected are not plotted. The same simulation parameters were used as in figure 5.10. a) At the quadrupole entrance, b) at 100 mm from the quadrupole entrance, c) at 200 mm from the quadrupole entrance, d) at the end of the decelerator.

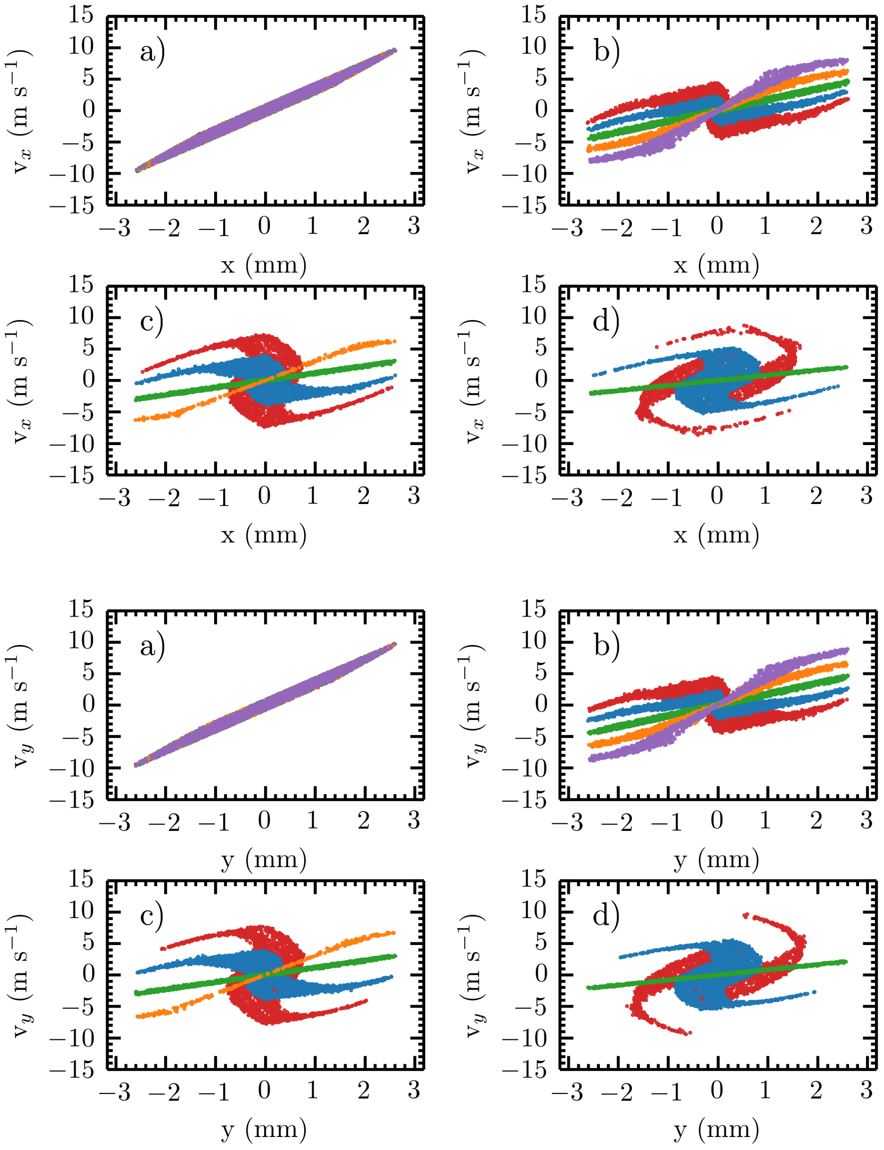

Figure 5.12: Phase space evolution in the x (top) and y (bottom) dimension of a Monte Carlo simulation of 25,000 particles. Particles that will be rejected are not plotted. Red $M_J = 2$, blue $M_J = 1$, green $M_J = 0$, orange $M_J = -1$, purple $M_J = -2$. The same simulation parameters were used as in figure 5.10. a) At the quadrupole entrance, b) at 100 mm from the quadrupole entrance, c) at 200 mm from the quadrupole entrance, d) at the end of the decelerator.

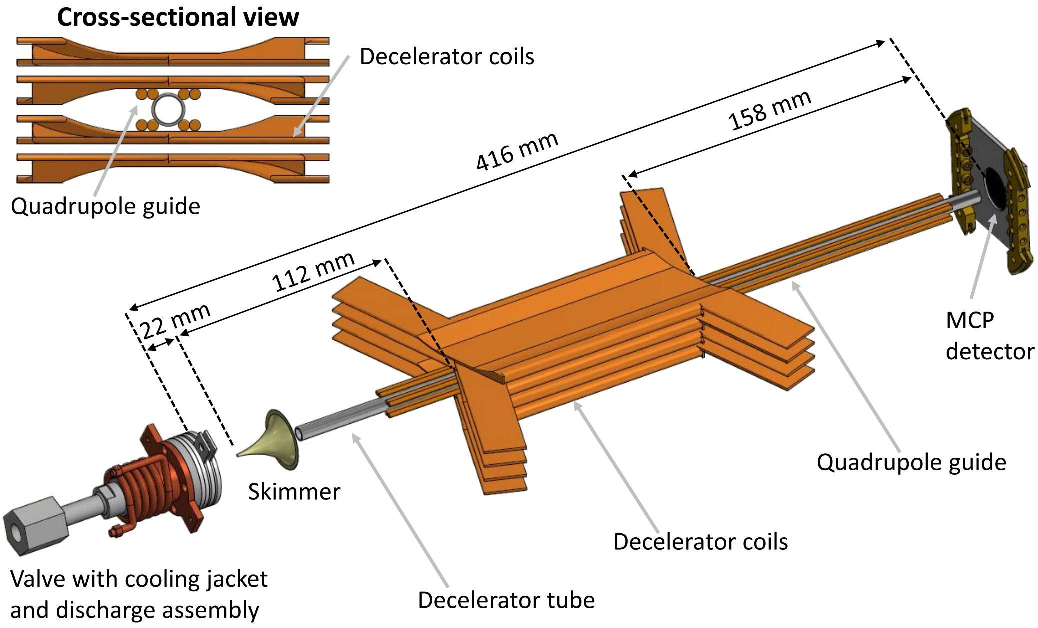

Figure 5.13: A schematic diagram of the experimental setup used in the 3D-guiding experiment. The supersonically expanded pulse of argon atoms is produced by the pulsed valve, which is cooled with liquid nitrogen. The discharge assembly excites the argon atoms to the metastable states. The skimmer orifice with a 1 mm diameter, is positioned at a distance of 22 mm downstream from the midpoint between the discharge electrodes. The beam passes through the 350 mm long, 5.35 mm I.D. stainless-steel tube. The MCP detector is placed 416 mm downstream from the point where the metastable atoms are created. The 123 mm long decelerator coils start at 112 mm from the skimmer orifice. The free-flight distance from the end of the decelerator planar coils to the MCP detector is 158 mm. A cross-sectional view of the planar decelerator coils sitting above and below the quadrupole guide sandwiching the decelerator tube is also shown.

5.3 3D Guiding and Experiments Toward the Deceleration of Ar*

To demonstrate that the decelerator works according to how it should, we first demonstrated the 3D-guiding of Ar*. Figure 5.13 shows a schematic diagram of the experimental setup used in the 3D-guiding and attempts at deceleration experiments. The operating conditions of the source were identical to the ones used for the 2D-guiding measurements described earlier. Figure 5.3 on page 111 illustrated the pulse sequence in each repetition of the experiment. For these measurements, the quadrupole guide was applied as described in the figure (2.3 ms long, 150 μs before discharge). The sinu-

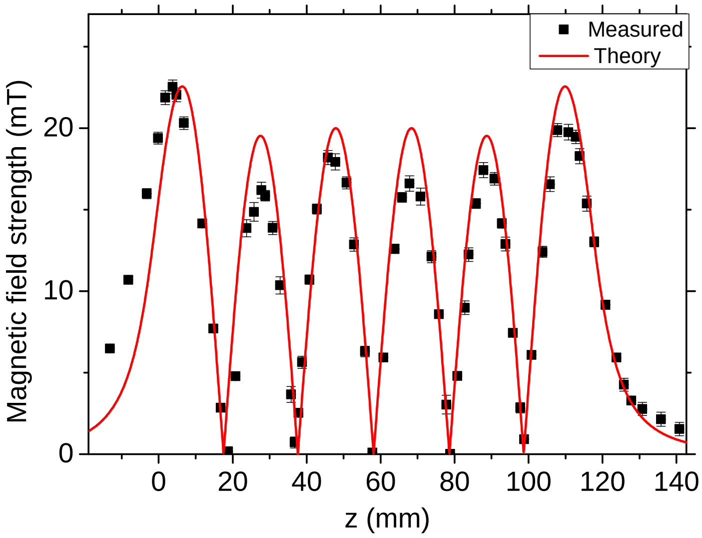

Figure 5.14: Measured magnetic field strength (black squares) at a current of 16 A along the z-coordinate. The red trace is the calculated field from theory.

soidal current pulse was about ∼400 μs and the delay between the discharge and decelerator traps switch-on time was ∼300 μs. The quadrupole is not thermally bonded properly to the cooling block, thus, the experiment was running at 2 Hz due to the heating of the quadrupole guide. The quadrupole guide current was 700 A. The flat decelerator coil current was limited to 500 A (650 V). The data was averaged over 40 shots.

Figure 5.14 shows the measured and calculated magnetic field strength at 16 A, along the z-direction. The way the magnetic fields were measured was described for the quadrupole guide in section 5.2. There are clear discrepancies between the measured and calculated fields. One reason could be due to the coils not being perfectly aligned. This could lead to a reduction or shift in the maxima. A magnetic wave with a constant velocity is produced by keeping the frequency of the AC current constant. The travelling wave captures the gas pulse with the velocity class with the same velocity as the travelling wave, if the atoms are perfectly coupled into the trap. Figure 5.15 shows the arrival times of Ar* at the MCP detector after the discharge trigger. The first peak corresponds to the photons created by the electric discharge and the second to the Ar* signal. The red trace shows the transmission through the decelerator tube without any magnetic fields. There are two small peaks, one positioned before the photon peak and one after the Ar* peak. These correspond to the noise from the on and off switching of the quadrupole elec-

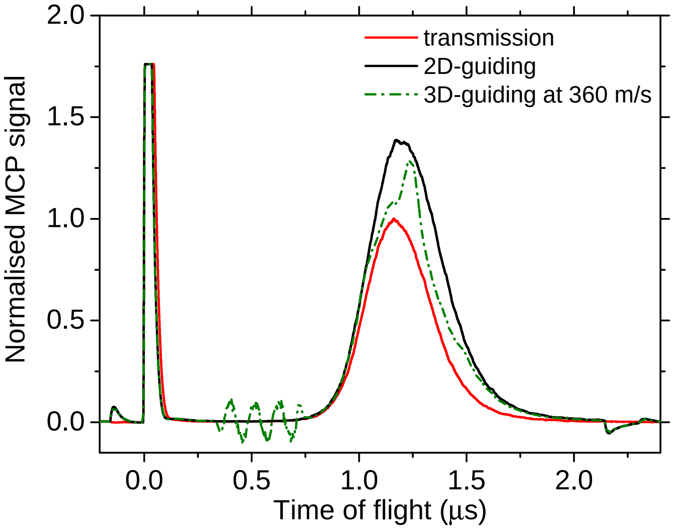

Figure 5.15: Red trace: detected Ar* signal for when no fields are switched on giving the transmission peak. The first peak corresponds to the photon signal. Black trace: 2D-guided Ar* atoms. Green trace: 3D-guided trap with a set velocity of 360 m/s.

tronics. Another noise superimposed onto the detected MCP signal is the sinusoidal current pulse, which is seen just before the Ar* peak. The mean velocity of the transmission (zero field) peak is 335 ± 9 m/s with a translational temperature of 4.2 K (99 m/s FWHM velocity spread). When the quadrupole is switched on (black trace), the detected intensity is increased from the guiding of the LFS states of the $^3P_2$ state of Ar*. The green trace shows the signal when the decelerator coils were switched on, with a set trap velocity of 360 m/s. A bunched peak is visible around 1.25 ms. By fitting a Gaussian to this peak, the mean velocity is calculated to be 336 ± 13 m/s and a translational temperature of 479 ± 19 mK (30 m/s FWHM velocity spread). At 500 A, we expect trap depths of 1.4 K. This is higher by a factor of three. The most likely explanation for this is because the calculated trap depth is based on a 1D model of the trap depth, whereas in the measurements the atoms move in a 3D space where the trap depth could be shallower in the other dimensions. This was also observed by Lavert-Ofir *el al.* in their moving trap Zeeman decelerator. [65] Another contribution is the misalignment of the coils, as was seen from figure 5.14.

Figure 5.16a shows the 3D-guiding of Ar* at different velocities, in comparison with the transmission peak (black dotted line). The mean velocity of the transmission peak is 335 ± 9 m/s, with a translational temperature of

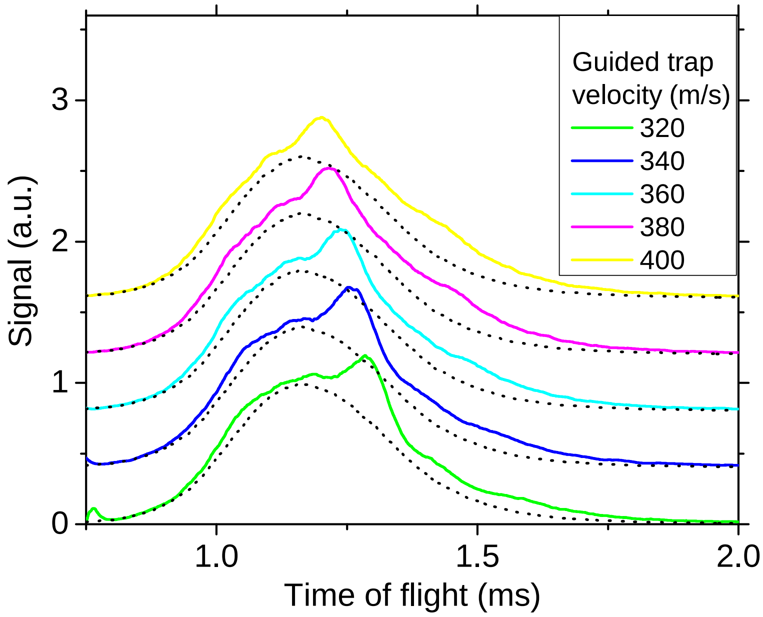

(a)

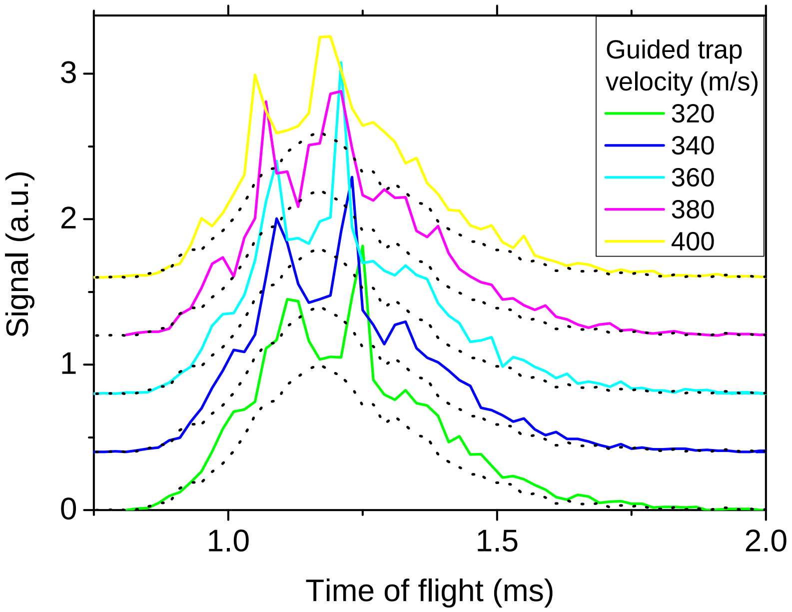

(b)

Figure 5.16: Measured (a) and simulated (b) 3D-guiding of Ar* at different velocities. The data is vertically offset for clarity. The dashed line shows the transmission through the decelerator tube while the magnetic fields are switched off. The data is normalised to the transmission peak.

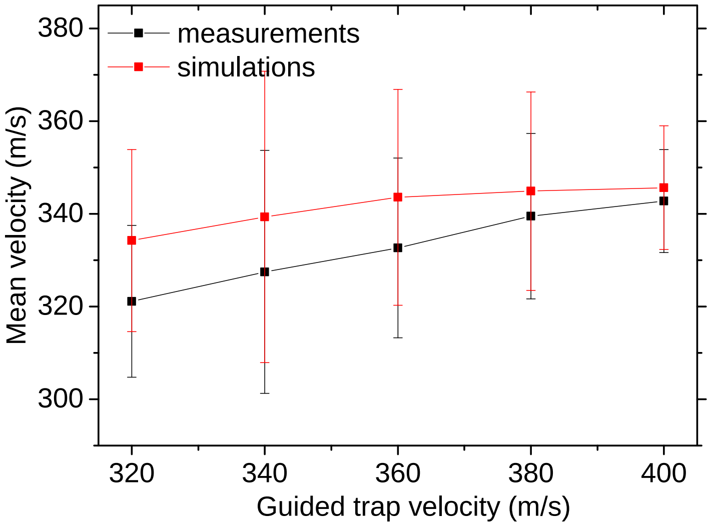

Figure 5.17: The guided mean velocity for different trap velocities for the measured (red) and simulated (black) data in figure 5.16.

4.2 K (99 m/s FWHM velocity spread). The measurements clearly show that the guided peaks at different velocities arrive earlier in time for the faster trap velocities, as expected. Figure 5.16b shows the simulations (performed by Lewis McArd) for the data in figure 5.16a. Although the trends are reproducible, the main peak in each simulated time-of-flight profile does not match the measured peak. To further examine this, we look at the velocity of the peaks in figure 5.17, calculated from their arrival time. The velocity appears to increase almost linearly with increasing guided trap set velocity, both for the measured, and simulated data. The two data sets do however agree within the error. This is a very good indication that the decelerator is working well. The second thing that is noticed is that the simulated peaks are narrower than the measured peaks. The integrated area, a measure of the number of atoms, determined after the subtraction of the transmission peaks are plotted in figure 5.18. The presence of only a small variation in the integrated areas indicated that the measured peaks have been spread out, leading to broader peaks. Furthermore, the simulations in figure 5.16b show a second peak to the left of the main peak, which corresponds to the neighbouring trap which is filled. In the measured data, there is only a slight bump. This peak arrives earlier in time, thus, it is from atoms that are travelling faster.

First, we will consider why the set trap velocity does not match the calculated trap velocity of the bunched peak from the arrival time. Figure 5.19

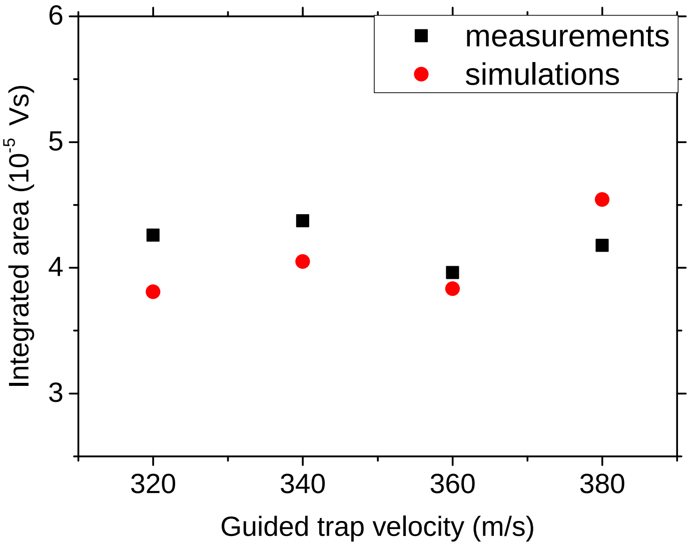

Figure 5.18: The integrated area of the peaks for the measured (black) and simulated (red) data in figure 5.16.

shows the distribution of the longitudinal velocity versus the TOF, for the simulated TOF measurements for a guided beam at 360 m/s. The highlighted regions with a box correspond to the two main peaks in figure 5.16b in the simulated TOF profiles. The main bunched region just after 1.2 ms has a velocity centering around 345 m/s. This means that for the trap moving at 360 m/s, we captured the atoms moving at 345 m/s. These atoms, with a mean velocity of 360 m/s are not coupled to the trap because the delay between the discharge and the switching on of the trap was not optimised. These atoms have a relative velocity of 15 m/s, relative to the trap minimum. Thus, the atoms still feel the force as they spend some time in the trap, and are therefore bunched. When varying the delay, we are spatially picking different velocity classes. Figure 5.20 shows the effect of changing this delay on the Ar* signal. The guided trap velocity was set to 330 m/s. The transmission peak's (dotted black line) mean velocity was calculated to be 343±15 m/s from the mean arrival time (vertical grey dashed line). Two peaks can be seen in all traces. Depending on the initial spatial or temporal length of the gas pulse and the separation between consecutive traps, either a single trap or multiple traps can be filled. The separation between the trap minima is 19.2 mm. The distance from where the Ar* atoms are created and the first trap is about 134 mm. For a beam travelling at 343 m/s, it takes 400 μs to travel this distance. With a FWHM of 98 m/s, this gas pulse has

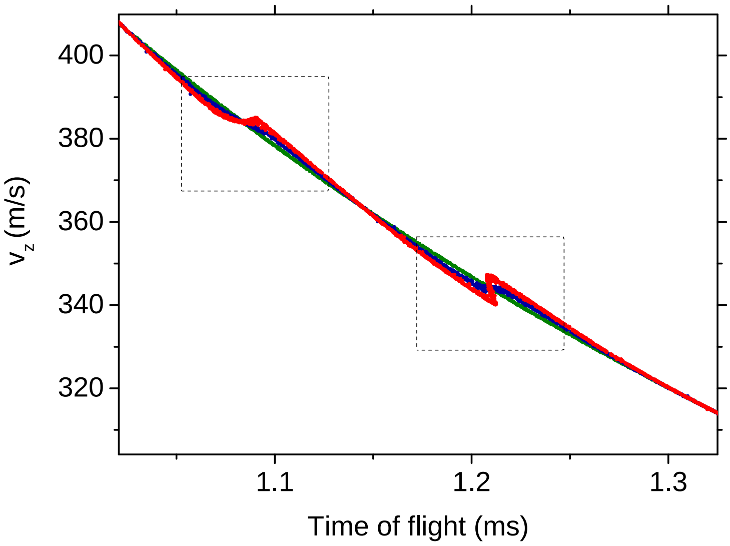

Figure 5.19: Distribution of the longitudinal velocity with respect to the time from the valve trigger for a trap that is guided at 360 m/s. Red $M_J = 2$, blue $M_J = 1$, green $M_J = 0$.

a spatial spread of 28 mm (assuming a size of 0 mm in the z-direction at the point of creation). For the shorter delays, the first trap is capturing the faster atoms while the second trap is capturing the slower atoms, at a less intense part of the gas pulse. With increasing delay, the main trap captures the slower atoms and the peak's intensity reduces. Eventually, the main trap is at the slower tail of the distribution. At this point, the second peak is more intense, because, it is the one which is switched on, spatially, further downstream where the gas intensity is greater and the atoms are faster. In these measurements, the set trap velocity is 330 m/s, by comparing with the calculated velocities of the main peak (shown in the legend), a delay between 320-340 μs would be optimum, as it could coincide with the set trap velocity. To conclude, for such a short decelerator length, the time the trap is switched on needs to be optimised to ensure the trap captures the part of the beam with a velocity that matches the set trap velocity.

To understand the difference between the simulated and the measured TOF traces we must first consider all the effects which have not been taken into account in the simulations which could affect the deceleration process. Firstly, Majorana transitions have not been taken into account in the simulations. Majorana transitions are spin-flip, state-changing transitions which could lead to losses in a decelerator if the atoms are transferred into the non-trappable HFS states. These Majorana transitions are driven by the motion

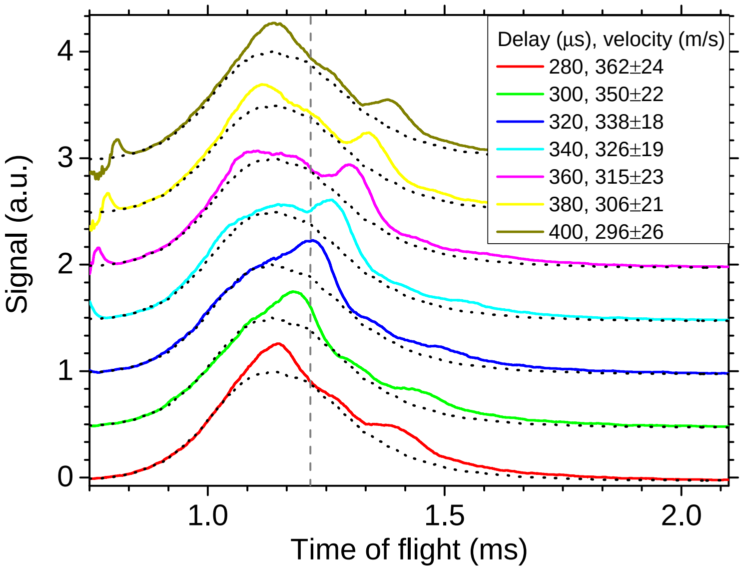

Figure 5.20: Guided trap at a velocity of 330 m/s with different discharge-decelerator trap delays. The data is vertically offset for clarity. The velocity of the peaks with a clear shift from 280 μs delay to 400 μs is specified in the legend. The dotted black line is the transmission signal. The grey vertical dashed line marks the mean arrival time of the transmission peak.

of the particles through regions where the magnetic field is close to zero. Since our trap is a quadrupole trap, the atoms spend very little time in the trap minima where the field is close to zero, and thus we do not expect Majorana losses in our Zeeman decelerator. The effect of Eddy currents is another thing which has not been taken into account in the simulations. Eddy currents are loops of electrical current which are induced within conductors by a changing magnetic field due to Faraday's law of induction which generates magnetic fields that reduce the overall field. However, the decelerator tube that the atoms travel through was made of Stainless steel 316 which is negligibly responsive to magnetic fields, therefore we do not expect any losses due to effects from Eddy currents. Another possible loss mechanism is through collisions with possible gas trapped in the decelerator tube. However, it was calculated by another member of the group that under the conditions of the valve and the pumping capabilities of the vacuum system, the decelerator tube is sufficiently evacuated to low pressures, making collisions with background gas within the decelerator tube unlikely. Furthermore, losses via collisions with background gas would affect both peaks in the same way, which is not what we see in our data.

As mentioned earlier, the simulations do not take into account the imperfections in the alignment of the pairs of the decelerator coils as well as the heat conducting epoxy used to hold the coils together. This could affect the shape of the traps and their depth due to the variation in the magnetic field. The movement of the traps was simulated and animated to examine the variation in the trap depth. It was seen that some peaks do drop below where they should. It is also worth noting that the simulations used the theoretical current through the coils i.e. the current predicted by the PWM code which is not an idealised current. The rapid oscillation in the synthesised currents fed to the decelerator coils are pretty fast, thus the average potential the atoms see is close to what we expect. Though the measured current could have been used, this was easier because the current probe was very noisy. Nonetheless, all these effects only lead to a reduction in trap depth, and not the apparent unequal broadening of the two peaks.

We will now consider the signal-to-noise ratio of the simulated data. The trajectories from the simulations are output as velocity and time at the detector for each one of the 25,000 particles. The TOF traces are obtained by binning all the particles' arrival times. The signal-to-noise ratio in the simulated data sets depends on how the particles are binned. Running more trajectories would reduce the noise associated with the binning. From the 25,000 particles, only around 1% make it through to the end. Running more trajectories would reduce the error associated with binning.

Lastly and probably most importantly, the simulations use hard edges for the switching of the decelerator trap. In reality, there is around a 25 μs build-up time and decay time for the current in the decelerator coils. This means that on entrance, the trap loading is not represented. As seen in figure 5.20, the delay affects which velocity class is bunched by the traps. A 25 μs delay alone was enough to cause a change of 10 m/s in the mean velocity of the guided peak. Thus this is the most likely reason to why the simulations do not agree with the measured TOF traces in figures 5.16a and b. This delay also means that the fields at the exit of the decelerator coils are still on as the bunched packets leave the decelerator coil.

We will now try and understand why the measured peaks are broadened and why the neighbouring faster trap is made broader than the main trap, to a point where it is almost not visible. Again, we believe that the fringe fields are

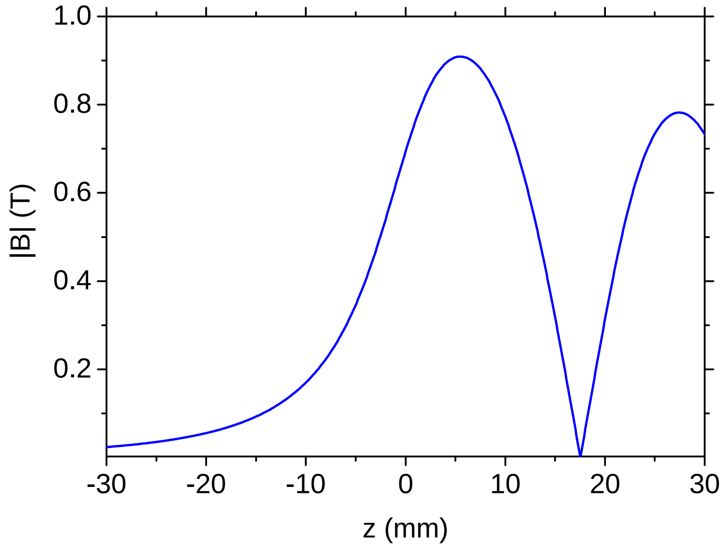

Figure 5.21: Calculated fringe field on entrance to the decelerator coil at 500 A. The edge of the coil along the centre, which is the crossing point is z=0. The coil is symmetric and therefore the field at the exit of the decelerator coil is an mirror image of this through z=0.

the most likely cause for this. Figure 5.21 shows the calculated fringe fields at the entrance of the decelerator coil. The fields at the exit are a mirror image of this. As can be see, there is an accelerating field as one travels from the last trap minima towards the exit of the coil. Let us first consider the main peak in the TOF distribution which is the slower one with the longer TOF. The peak consists of bunched atoms with a range of velocities centred around a specific velocity. While the main peak travels through the region of the fringe fields, the current in the decelerator coils is decaying, thus reducing the field gradient and the acceleration experienced by the atoms. Thus, the atoms that are faster travel further down the potential hill and are more accelerated while the slower ones experience less acceleration due to the decaying current. This means atoms with different velocities are accelerated by different amounts, causing the atoms to have a greater spread in velocities, which results in broadened peaks on the detector. When comparing the simulations with the measured TOF traces, it was seen that the faster peak was more broadened. The faster packet travels in the region of the fringe fields of the decelerator on exit from the decelerator coil, before the decelerator coils are switched off. The faster peak experiences a larger magnitude of acceleration as the current decays with time. The result is, that the faster peak with the shorter

TOF is very broadened in the results, to an extent where it is not very distinguishable.

Once we observed a peak that was guided, we decided to chirp down the frequency of the travelling wave in order to attempt to decelerate the atoms. We first started with an arbitrary deceleration down to a final velocity of 330 m/s. Having seen a peak that arrived later in time, we pushed it further and saw the peak arrive later in time. Figure 5.22a shows the results of our attempt at decelerating our trap from an initial velocity of 360 m/s down to final velocities of 330 m/s, 280 m/s, 250 m/s, and 220 m/s. The transmission peak is illustrated with a dotted black line to help see the change in velocity. The mean velocity of the transmission peak is 335 ± 9 m/s and with a translational temperature of 4.3 K (100 m/s FWHM velocity spread). Figure 5.22b shows the simulations (performed by Lewis McArd) for the data in figure 5.22a. Again, although trends are reproduced, the simulated data's main peaks do not match the measured peak. To examine this, again, we look at the peak velocity from the arrival time in figure 5.23. The velocity decreases linearly with decreasing final trap velocity both for the measured and simulated data. Comparing the measured (black) points to the simulated (red) points, there is a clear offset which reduces with increasing final trap velocity. As was seen in the 3D-guiding, the peaks are also shifted in this case for the same reasons. Furthermore, figure 5.22b shows secondary peaks which are more enhanced for reasons explained earlier. As seen in the 3D-guiding measurements, the integrated areas of the peaks, illustrated in figure 5.24 follows a similar trend with a small variation in the value. Again, this is due to the fact that the atom packet is spread in time by the fringe fields, giving broader peaks.

One might notice that the guided trap at 360 m/s in figures 5.16 and 5.22 look slightly different. However, this is because they were taken from two separate data sets at different times of the day. Therefore, the source would have changed over the long time duration. Furthermore, the delay between the discharge and decelerator switch-on time was slightly different, this might account for slight different in the shape of the traces.

Initially it appeared like we were decelerating. However, if we consider our trap depth of 0.7 T and the deceleration force that adds a pseudo potential that lowers the trap depth, then the traps are open for all the deceleration

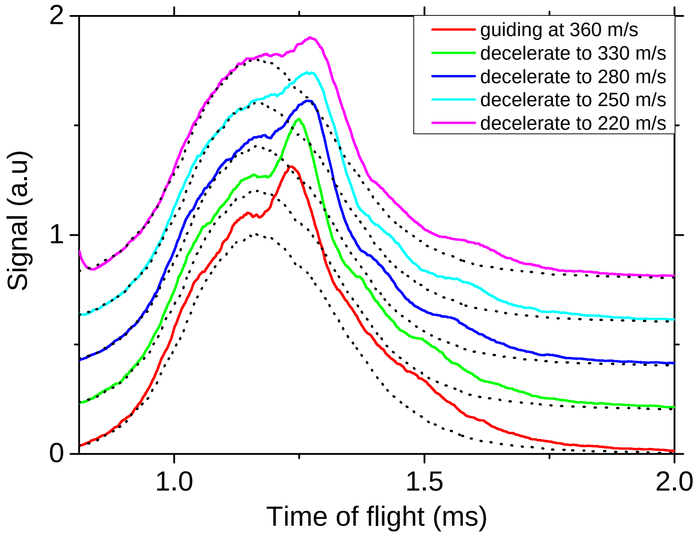

(a)

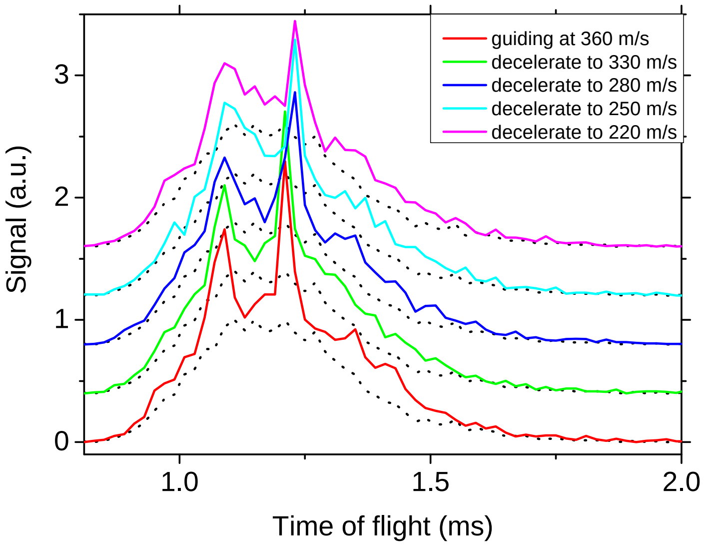

(b)

Figure 5.22: Measured (a) and simulated (b) deceleration of a trap from an initial velocity of 360 m/s (red trace) down to different final velocities with the value indicated in the legend. The data is vertically offset for clarity. The dotted black line is the transmission argon signal when no fields are switched on. The data is normalised to the transmission peak.

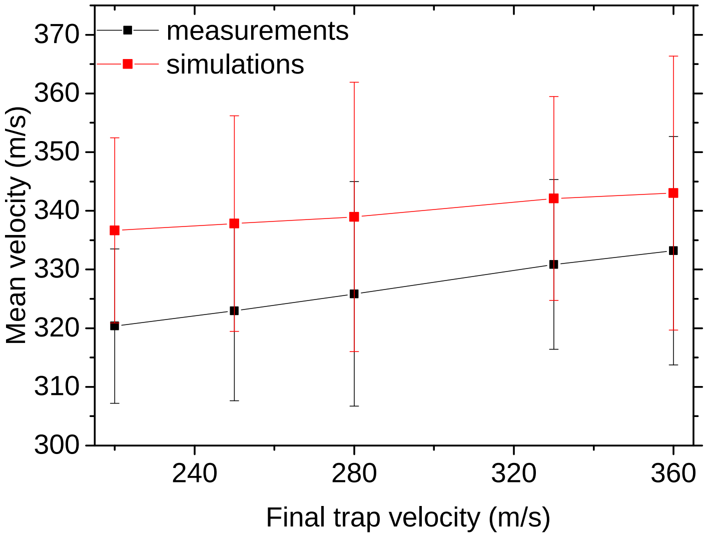

Figure 5.23: The mean velocity for the guided traps at 360 m/s and the traps decelerated to different final velocities for the measured (black) and simulated (red) data in figure 5.22.

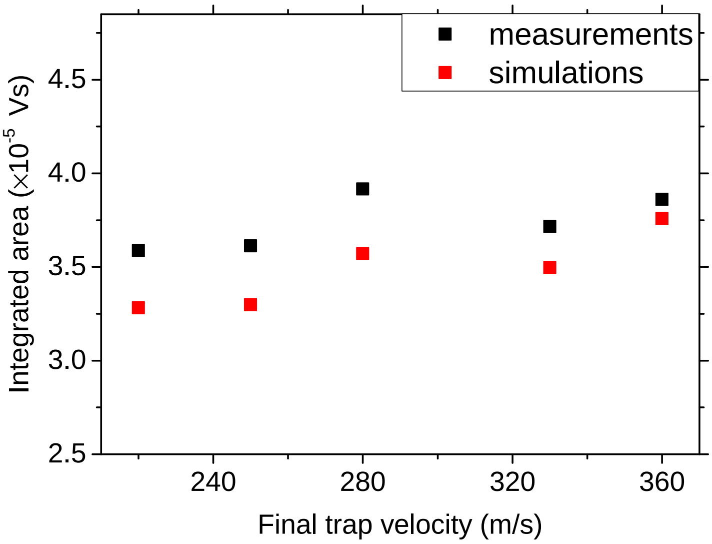

Figure 5.24: The integrated area of the peaks for the measured (black) and simulated (red) data in figure 5.22.

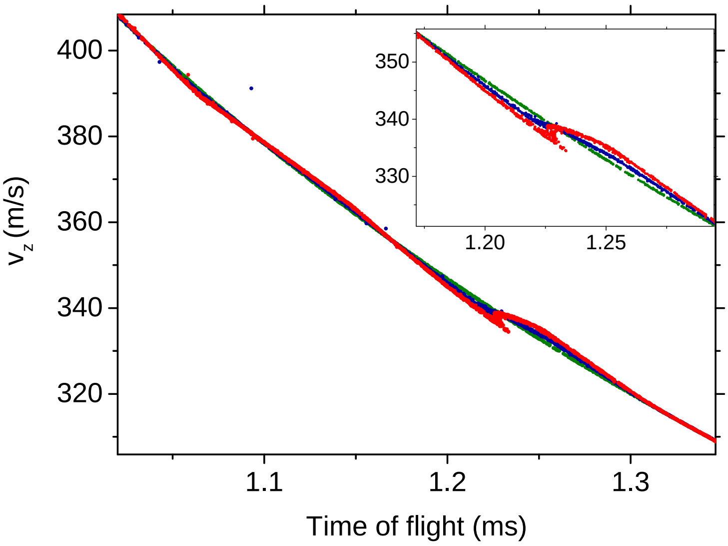

Figure 5.25: Distribution of the longitudinal velocity with respect to the time from the valve trigger for a trap that is decelerated from 360 m/s to 220 m/s. Red $M_J = 2$, blue $M_J = 1$, green $M_J = 0$.

attempts. Over our rather short decelerator length of 123 mm, the minimum final trap velocity which can be set to, and still see a closed trap is 350 m/s where the deceleration is at 1.45×10^4 m/s^2. Therefore, we do not really expect to see any deceleration. Furthermore, the length of time the force is applied for is an important factor that determines the change in velocity that can be achieved. The gradient of the magnetic trap (70 T/m) causes the acceleration or deceleration of the atoms. Depending on where the atoms are positioned with respect to the trap minimum, they might experience an increase or decrease in the velocity. During the time any atom is in the vicinity of the trap, it will experience the same force from the gradient of the magnetic fields. Here, the change in velocity which can be applied for our trap depth of 0.7 T is only about 12 m/s for a trap which is on for $\sim$400μs. This is the maximum change in velocity that can be obtained by this trap.

Figure 5.25 shows the distribution of the longitudinal velocity versus the TOF for the simulated TOF measurements for the decelerated trap from 360 m/s to 220 m/s. Looking at the $M_J = 2$ states (red), it can be seen that there is no bunching at 220 m/s. The bunched atoms are distributed around a centre closer to 337 m/s. In comparison to the green $M_J = 0$ states which are not influenced by the field, the relative change in velocity for the $M_J = 2$ states is $\sim$5 m/s. As you would expect, this is smaller than the maximum change from the impulse force of the trap. This is due to the fact that the atoms are only exposed to the trap for a short duration of time, even shorter that the ‘on-time’ of the trap because of changing the relative velocity. The trap is initially at a velocity of 360 m/s, and thus, travels past the slower atoms. As the trap is decelerated, the slower atoms catch-on with the trap, and are thus spatially in the vicinity of the trap for long enough to feel a force. The change in velocity is the same order of magnitude that you would expect for if the decelerator is on for $\sim 400 \mu$s.

To better understand why we observe bunching, despite the open traps, we look at the phase-space distributions at the beginning and the end of the decelerator. For this, Monte Carlo trajectory simulations with 35000 atoms were performed (by Lewis McArd). Figure 5.26 shows the phase-space distributions in the x, y, and z at the beginning (top) and the end (bottom) of the decelerator for a guided beam at 360 m/s. The blue region shows the uniform initial phase-space distribution fed into the decelerator while the red points show the trajectories that were in the trap at the end of the decelerator module. The acceptance in the y-direction is slightly bigger than the x from the addition of the fields from the flat decelerator coils to the quadrupole guide fields. The red region is centred around the guided trap velocity of 360 m/s, as expected. The phase-space distribution at the end of the decelerator does not fill in the separatrix because the decelerator length is very short. For a longer decelerator, the atoms outside the separatrix would not make it to the end of the decelerator. The guided trap at 360 m/s was found to have an efficiency of 7.8% with an acceptance of 1.1×10^7 (mm m/s)^3.

We now look at deceleration to a final trap velocity of 220 m/s in figure 5.27. Here, the trap is fully open, and it is clear that no atoms centred around the initial 360 m/s or 345 m/s velocity are captured and decelerated. Thus, it is clear from this figure that we are not decelerating the atoms. Nonetheless, we still see bunching, as indicated by the measured and simulated peaks in figure 5.22. The red atoms which make it to the end of the decelerator are ones that were in the vicinity of the trap in their flight time as the trap was decelerated to a point where these slower atoms caught up with it, and had a relative velocity that was small relative to the trap minimum. This means that they had enough time to feel an effect from the force applied by the trap. Any atoms that were there when the trap was first switched on already overtook the trap as it was quickly decelerated. Only atoms that

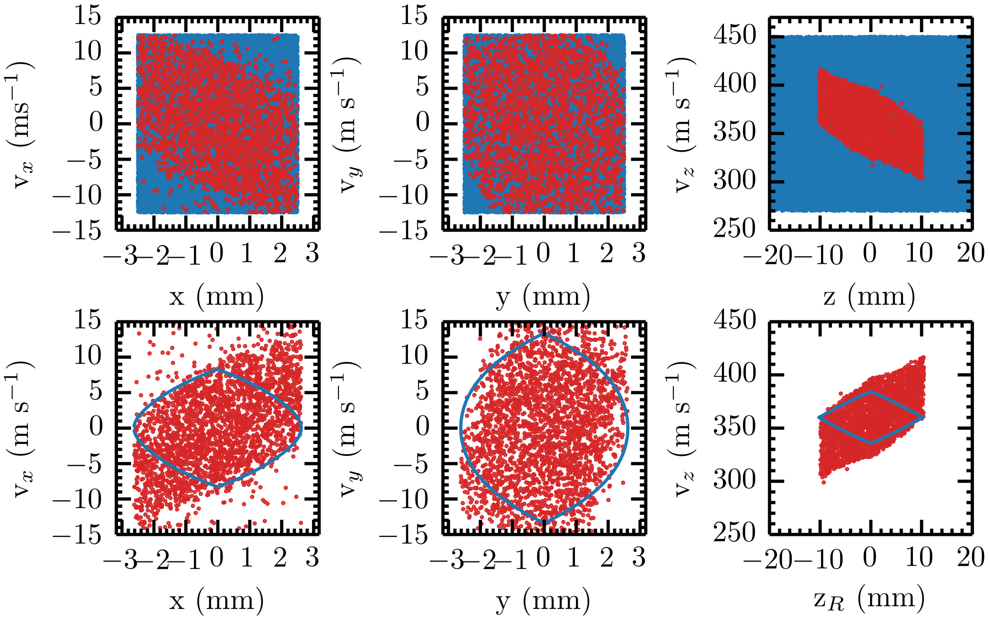

Figure 5.26: Phase space distributions at the beginning of the decelerator coils (top) and at the end of the decelerator (bottom) for a guided trap velocity set to 360 m/s, along all three dimensions. z_R is the relative position with respect to the trap minimum. The 1D separatrix is plotted in blue. The blue points show the initial phase space points fed into the decelerator while the red points show what makes it to the end of the decelerator.

are spatially in the region of the trap could experience a change in velocity. There are some atoms that are not exposed to the trap for a very long time at all. The global change in shape, because of the 12 m/s attainable change in velocity, is therefore, very small. The manipulation of the motion can be seen from the change in the shape. Each individual atom will only change velocity by up to 12 m/s. Some atoms might have started outside the trap, then were inside and felt the force, and then left the trap.

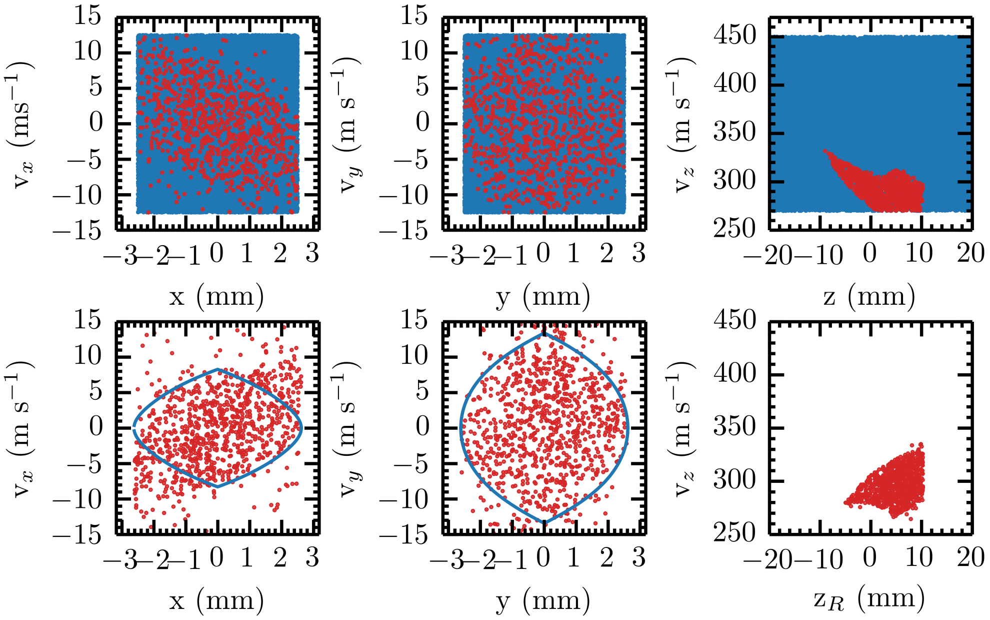

Figure 5.27: Phase space distributions as described in figure 5.26 for a decelerated trap, from an initial velocity of 360 m/s to a final velocity of 220 m/s.

5.4 Conclusions

In this chapter we presented our proof-of-principle experimental results where we demonstrated the manipulation of Ar* atoms in the $^3P_2$ metastable state using 2D and 3D magnetic fields. Our 3D traps use continuously modulated magnetic fields which produce a travelling potential. It was successfully shown that the Ar* signal intensity is greatly increased, nearly by a factor two (at 900 A) by using a 290 mm long quadrupole magnetic guide which provides transverse confinement of the atoms in the LFS states. The greater the current through the quadrupole guide, the more intense the detected Ar* MCP signal and the integrated area. The unexpected change in the mean velocity due to the longer effective TOF and translational temperature was suspected to be due to the fringe fields from the two ends of the quadrupole.

With the addition of the decelerator coils, magnetic confinement along the longitudinal molecular beam axis was achieved, forming 3D-traps. It was shown that the paramagnetic Ar* atoms can be guided at a chosen constant velocity along our rather short single coil with a length of 123 mm. The 3D-guiding of the LFS states of $^3P_2$ state of Ar* atoms, was carried out at constant velocities ranging from 320 m/s up to 400 m/s. The longitudinal temperatures were ~500 mK. While attempting the deceleration of the traps, though no real deceleration was observed for this short deceleration length, the fields did show a manipulation effect. This gives us the confidence that with a longer decelerator, we will see very prominent bunching.

Once the decelerator is extended in length, other paramagnetic species such as CaF, SD, CH_3 radicals can also be decelerated. One problem to overcome is the effect of electrical noise while the decelerator is active. A lot of work has been done to increase shielding and break any earth loops (including building an optical coupler for the FPGA), however, this is still a work in progress. The next step would be to add a second module to decelerate down to lower velocities. With a longer decelerator, the observed effect of the slower molecules which are not initially trapped but contribute to the signal should be eliminated. Therefore, the simulations should be able to replicate what is observed experimentally, which is an important validation of results. Furthermore, the fringe fields, which are not taken into account in the simulations are the reason for the differences in the measured and simulated signals. It is important to note that the region of "deceleration" and the region of "fringe fields" are nearly equal in size. Therefore, for our longer decelerator, the effect of the fringe fields will be less significant. In conclusion, these first set of proof of principle experiments and simulations that were carried out show that there is yet work do be done to improve the simulation to better match the measured TOF traces.

Chapter 6

Measuring Absolute Densities of Molecules Using CELIF

This chapter starts off by discussing standard, well established detection techniques, used to measure absolute densities in gas samples. Laser-induced fluorescence (LIF) and cavity ring-down spectroscopy (CRDS) are explored first, followed by cavity-enhanced laser-induced fluorescence (CELIF), a cross-correlated combination of the two methods. The chapter explains the methodology of CELIF with the presentation of published work where we measured the absolute density of SD radicals in a supersonic jet down to $(1.1\pm0.1)\times10^{5}\,\mathrm{cm}^{-3}$ in a modestly specified apparatus. [82] The CELIF technique can be used to determine absolute quantities: absorption cross sections, sample densities and fluorescence quantum yields. [122] For the purpose of the decelerator and the MMQA project, the ability to measure absolute densities of molecules in the molecular traps is important. In addition, CELIF allows the time evolution of absolute trap densities to be measured.

6.1 Direct Absorption and CRDS

Absolute molecular number density, ρ, can be determined in a direct absorption measurement, where the change in intensity of light, I, is measured, as it passes through a sample of a known path length, l, for a species of a known frequency-dependent absorption cross-section, σ, at the particular wavelength of the light. This relationship is represented in the Beer-Lambert law, which gives the relationship between the intensity of a spectral feature and the frequency-dependent absorption properties of the sample according to

$$I = I_0 e^{-\sigma\rho l} = I_0 e^{-\alpha l}, \tag{6.1}$$

where I_0 is the initial intensity travelling through the sample, I is the emerging reduced light intensity and $\alpha = \sigma\rho$ the absorption coefficient.

In experiments where the gas sample has a high density, as found in standard cold atom experiments, absolute densities are calculated from direct absorption measurements with the single pass of the light through the sample. However, in experiments involving molecular beams, densities are low and absorption cross sections are smaller for molecules than atoms, preventing the detection of an appreciable change in the light intensity for a specific path length. Nevertheless, equation 6.1 shows that a reduction in density can be compensated by an increase in path length, thus making the detection more sensitive. This is achieved in CRDS via multiple passes of the same laser pulse through the sample volume by placing two highly reflective mirrors around the sample on the laser axis. Path lengths can be on the order of many kilometres. However, this does not apply to molecular beams.

CRDS is a well-established, widely used laser-based direct absorption technique for direct quantitative measurements of molecules in gas, liquid and solid-phase samples. [123,124] Traditional laser absorption spectroscopy techniques cannot be used to detect inherently weak absorptions, as the change in intensity of the light as it passes though the sample is very small compared with the initial laser intensity, thus, the sensitivity is usually limited by fluctuations in initial laser intensity. CRDS is based on the measurement of the rate of absorption, rather than the magnitude of absorption, of light circulating in an optical cavity, where the decay time is measured, instead of the total intensity. CRDS is a general technique with the single requirement that the absorbing particles can absorb the laser light. The only experimental restriction is that the high-reflectivity mirrors required for the CRDS can be obtained in the wavelength region of the absorption.

Figure 6.1 shows a schematic diagram of a standard ring-down cavity with two highly reflective mirrors that confine the light pulse from a pulsed laser

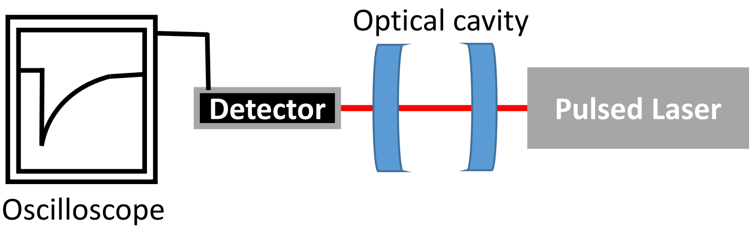

Figure 6.1: Schematic diagram of a standard set-up of a CRD experiment consisting of a pulsed laser light source, two highly reflective mirrors for the optical cavity, and a detector for the photons transmitted through the cavity. The exponential ring-down signal is displayed on a fast oscilloscope.

within the optical cavity. As the light pulse enters the cavity, most of it is reflected directly back from the input mirror (typically $\geq$99.9 % depending on the mirror's reflectivity), but the small fraction coupled into the cavity through transmission is reflected off the surface of the mirrors hundreds, if not thousands of times. A small fraction of the light leaks out of the mirrors and exits the cavity with each successive reflection and is detected with a photon detecter (e.g. a photomultiplier tube, PMT), placed on the cavity axis. If the laser pulse is temporally shorter than the round-trip time of the cavity, a fast detector could observe a train of discrete pulses at the exit mirror, with an exponential envelope. However, if the response-time of the detection electronics is not fast enough, this will be smoothed into an exponential decay. The scope can also be bandwidth limited to smooth out the laser pulse train to give better exponential decays.

The confinement time of the pulse within the cavity is called the ring-down time, and is the inverse of the decay rate of the signal that can be determined by fitting an exponential to the CRD transient. The CRD transient is the momentary increase in the detected light intensity by the detector which decays exponentially over a short period of time. This occurs for every laser pulse of light that enters the cavity. Measurements of the ring-down time in CRDS are independent of the laser intensity, and thus, any shot-to-shot fluctuations in the pulse intensity. This immunity to shot-to-shot variations in the laser intensity, along with the extremely long effective path-lengths (up to tens of kilometres) through the sample, makes CRDS very sensitive. A spectrum of the molecule can be produced by scanning the wavelength of the laser with the sample placed inside the cavity. The molecules introduce another loss mechanism for the light, causing a more rapid decay of the light.

The measured variation of the ring-down time with wavelength results in a spectrum with absolute absorbances at the wavelengths at which the laser is in resonance with a molecular transition.

As the pulse enters the cavity and bounces between the two highly reflective mirrors, with mirror reflectivity R, a fraction (1-R) leaks out of the exit mirror with each reflection. The intensity of the initial light pulse inside the cavity, I_0, is reduced by a factor of R with each reflection and R^2 with each round trip, and after k round trips, I_0 is reduced by

$$I_k = I_0 R^{2k} = I_0 e^{2klnR}. \tag{6.2}$$

Substituting in the time it takes the light pulse (moving at the speed of light, c) to complete k round trips, $t = 2Lk/c$, inside a cavity of length L, the initial intensity reduction becomes

$$I(t) = I_0 e^{\frac{tclnR}{L}}. \tag{6.3}$$

lnR can be approximated to $-(1 - R)$ since $R \approx 1$, giving

$$I(t) = I_0 e^{-\frac{tc(1-R)}{L}} = I_0 e^{-t/\tau_0}, \tag{6.4}$$

where the term in the exponent, τ_0, is the empty cavity ring-down time of the light pulse and is the time taken for the light pulse intensity to drop to $1/e$ ($\approx$0.37) of the initial intensity. It is only dependent on the cavity length and the mirrors' reflectivity according to

$$\tau_0 = \frac{L}{c(1 - R)}. \tag{6.5}$$

When an absorbent that absorbs at the laser frequency is introduced into the cavity, an extra loss mechanism exists for the light, therefore the exponential time profile of the light decays at a faster rate with a reduced time constant, τ, given by

$$\tau = \frac{L}{c(1 - R + \alpha d)}, \tag{6.6}$$

where d is the path length. We can write the reduced time constant in terms of the empty cavity ring-down time for a path length equal to the cavity length

$$\frac{1}{\tau} = \frac{1}{\tau_0} + \alpha c, \tag{6.7}$$

which can be re-written as

$$\alpha = \sigma\rho = \frac{1}{c}\left(\frac{1}{\tau} - \frac{1}{\tau_0}\right). \tag{6.8}$$

Thus, in CRD, absolute absorption coefficients, $\alpha = \sigma\rho$, are measured and, absolute densities, ρ, can be determined, if the frequency-dependent absorption cross-section, σ, is known. Equation 6.8 assumes that the whole cavity is filled by the sample, thus, for molecular beam where this is not the case, the right hand side needs to be multiplied by the ratio of the cavity and sample lengths, L/d, in order to account for the higher density in the smaller sample volume.

The condition for Beer's law of absorption must be met for an accurate absorbance measurement, which implies that the absorption feature's spectral width must be wider than the laser line width. This is to ensure all laser wavelengths are equally absorbed or transmitted. Another requirement for an accurate absorbance measurement is a shorter excited state lifetime than the round trip time, i.e. the ground-state population of the absorber molecule must not be significantly depleted by excitation during the time the laser pulse is circulating inside the optical cavity. [125]

CRD measurements are not background free as they are based on the detection of a change in signal. The minimum detectable absorption coefficient, α_{min}, depends on what region of the electromagnetic spectrum is being used since the mirror reflectivity is wavelength dependent. In general, α_{min} increases as one goes from the IR, through the visible region, and into the UV. Other factors that affect the minimum detectable absorption coefficient are the bandwidth of the laser and whether the lasers are CW or pulsed.

Cavity Modes

A CRD optical cavity is basically an etalon with a very high finesse. Thus it will let in only very narrow (few kHz in width) resonant modes from the broad bandwidth of the input laser. The resonant modes are characterised by both the number of transverse and longitudinal modes. To detect a sample, it must have an absorption feature which overlaps with at least one of the active cavity modes. Because the bandwidth of the pulsed laser is broad, there is no issue with the matching of the laser frequency with a single cavity mode, since multiple modes are excited. For narrow bandwidths, as found with CW lasers, one faces the difficulty of coupling the light into the correct mode for the absorption feature. The best sensitivity in a CRDS experiment is obtained when a single longitudinal mode of the ring-down cavity is excited. However, this is very difficult to achieve with lasers that have large bandwidths and bad spatial profiles. For our dye laser, the bandwidth was measured to be 6.4 ± 0.3 GHz, which means that for our measured cavity length of $d = 98.29 \pm 0.05$ cm at least 42 cavity longitudinal modes are spanned for each dye laser wavelength setting.

The spacing, in frequency ($\Delta\nu$), between two longitudinal modes for a cavity of length L, is called the free spectral range (FSR) and is given by

$$\Delta\nu = \frac{c}{2L}. \tag{6.9}$$

The first transverse mode is called TEM_{00} which has a Gaussian intensity distribution with respect to the laser axis, for a stable optical cavity. The cavity is optimised when the TEM_{00} mode is maximised and all others are minimised. Higher order transverse modes, TEM_{nm}, have n radial and m angular nodal planes. By ‘mode-matching’ the cavity i.e. shaping the input beam such that the wavefront radii closely matches the size and radius of curvature of the TEM_{00} modes of the cavity (curvature of the entrance mirror), excitation of higher order transverse modes can be dramatically reduced (but not eliminated).

If the laser light deviates from the path directly along the cavity axis, higher order modes are excited. Higher order transverse modes have different exponential decay constants, resulting in a multi-exponential ring-down transient. It can also lead to mode beating, caused by different cavity modes interfering with one another, seen as oscillations in the exponential decay time profile of the intensity.

6.2 Laser-Induced Fluorescence (LIF)

Laser-induced fluorescence (LIF) is a well established technique for sensitively detecting very low densities of suitable species. It can be performed using different media e.g. molecular beams, liquids and solids and is widely used in quantitative measurements of species in flames due to the technique's high sensitivity, spatial resolution, and non-invasive nature. It is far more sensitive than CRDS since it is not detecting a change in signal. LIF is, in theory, background free with the exception of scattered light from optical surfaces or Rayleigh scattering, making it very sensitive. With careful attenuation of stray light and photon-counting over very long acquisition times, single figure numbers of molecules can be detected in the probe laser volume. Stray light can be discriminated against by time gating the signal, if the fluorescence lifetime is long compared to the pulse length or by using a frequency filter if the fluorescence is off resonance. However, for short fluoresce lifetimes compared to the laser pulse width, stray light leads to very small signal-to-noise ratios. The detection limit of a LIF setup is determined by the base-line noise of the detection system.

In LIF, an atom or molecule is exposed to light and excited to a higher energy state when the wavelength of the light corresponds to the energy separation of two of its electronic energy levels. Excitation occurs from the absorption of photons from a specific ro-vibrational state in the lower electronic state to a specific ro-vibrational state in the upper excited electronic state. In a LIF measurement the photons can be detected on a PMT to record the fluorescence intensity. A fluorescence excitation spectrum can thus be produced by measuring the fluorescence signal as a function of the wavelength of the excitation laser, which reveals the population of the different states. Or, by fixing the excitation laser wavelength on a single transition, the population of the chosen state can be monitored over time.

However, LIF only provides relative quantities and it is well known that calibrating a LIF setup to give absolute densities can be very difficult and imprecise. Kirste *et al* managed to make absolute measurements using LIF

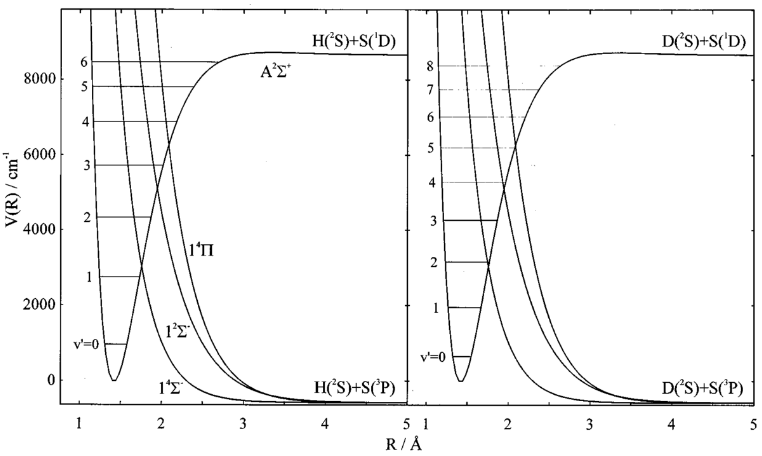

Figure 6.2: Potential energy curves of SH and SD molecules. The vibrational levels of the A $^2\Sigma^+$ state of SH and SD are displayed as horizontal lines. The repulsive states $1^4\Pi$, $1^2\Sigma^+$ and $1^4\Sigma^-$ are also shown. [124]

over nearly 4 hours to determine the densities of OH radicals as low as 200 molecules cm^{-3} in their 0.03 cm^3 probe volume, with a relatively large 30% error. The absolute density measurements were obtained by painstakingly calibrating their detection system and the fluorescence process including; fluorescence quantum yield, solid angle observed by the detector, and transmission efficiency of optical components in front of the detector. [126]

The difficulty in calibrating a standard LIF setup to give absolute densities motivated us to further test the CELIF method following the work of Sanders *et al.* using SD molecules. The choice of SD molecules was because we already had experience with the production and detection of the molecule. More importantly, it is paramagnetic in its absolute ground state. The heavier isotope was chosen over the SH due to its longer fluorescence lifetime, making its detection easier. The diagram in figure 6.2 shows potential energy curves of the excited electronic states of SH and SD molecules involved. The longer lifetime of SD molecules is a result of the predissociation rates of the vibrational energy levels of the excited state. The most significant contribution to the predissociation of the low vibrational levels of the A$^2\Sigma^+$ state of the SD and SH molecules is their interaction with the repulsive $1^4\Sigma^-$ state. The rate depends on the extent of overlap of these vibrational state energy levels and the repulsive state potential. This is the case in both molecules, however, since the vibrational levels of SD lie lower

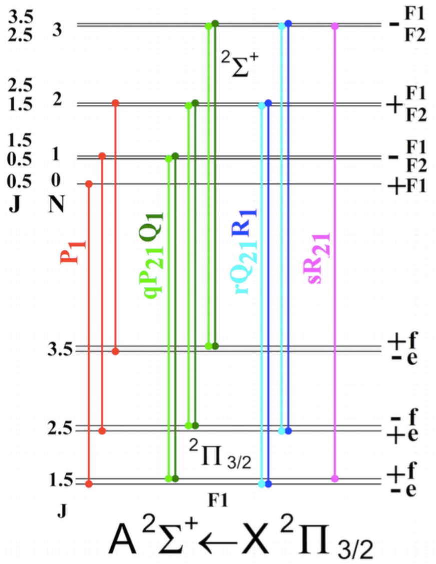

Figure 6.3: Energy level diagram of the electronic ground state $X^2\Pi_{3/2}$ and the first excited state $A^2\Sigma^+$ of SD. Both electronic states are in the vibrational ground state, $v = 0$. J is the total angular momentum, N is the total orbital rotation quantum number. The Λ-doublet splitting and ρ-doublet splitting are exaggerated for clarity and are indicated by the lower-case and upper-case of the letter 'f', respectively. P, Q and R are used to label transitions with $\Delta J = -1, 0, +1$, respectively. For more details see [126].

in potential than those of SH with the same vibrational quantum number, the pre-dissociation is faster for SH resulting in a shorter lifetime.

There are selection rules that that determine which electronic, vibrational and rotational transitions are allowed. In our SD measurements, we excite on the $A^2\Sigma^+(v' = 0) \leftarrow X^2\Pi_{3/2}(v'' = 0)$ transition (see figure 6.3). Transitions from the rotational levels of the lowest vibrational state of the lower electronic state up to the rotational levels of the lowest vibrational state of the excited electronic state are labelled by letters which correspond to different branches, depending on the change in the rotation quantum number, J. The absorption fluorescence spectrum of SD molecules can be seen in figure 6.4.

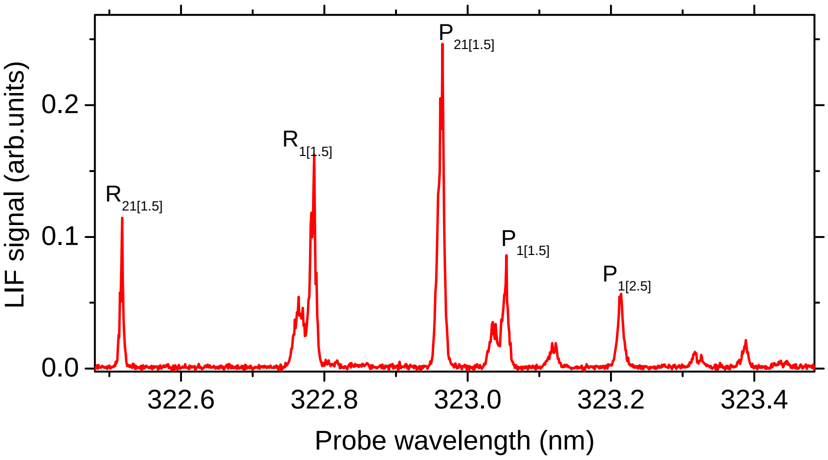

Figure 6.4: A conventional, single-pass LIF excitation spectrum of the $A^2\Sigma^+(v' = 0) \leftarrow X^2\Pi_{3/2}(v'' = 0)$ of jet-cooled SD.

6.3 Measuring Absolute Densities of SD Radicals Using CELIF

Sanders *et al.* [122] first used the CELIF technique described in this chapter, a method that combines the absolute absorption capabilities of CRDS and the sensitivity of LIF to measure absolute absorption coefficients. They showed that the technique was particularly effective for molecules like 1,4-bis(phenylethynyl)benzene (BPEB), which has a short fluorescence lifetime of 500 ps for the $S_1(\pi\pi*)$ excited state. This was because short lifetimes inflict challenges on the conventional single-pass LIF since the LIF signal is obscured by the stray light of the excitation laser and the Rayleigh scattered light, and therefore cannot be easily discriminate against by simply gating the signal. Measurements were carried out on the molecules in a supersonic jet using a pulsed laser at 10 Hz in the UV (320 nm). A minimum absorption coefficient ($\alpha_{\min}$) of $< 1.5 \times 10^{-9}\,\text{cm}^{-1}$ was reached in 250 s. The limit-of-detection (LOD) in these experiments was quoted as an upper limit because it could not be rigorously assessed due to difficulties in controlling the BPEB source and instabilities in the BPEB source at low concentrations.

The experiments by Sanders et al. showed that by adding cross-correlated LIF detection to a standard CRD setup, the LIF measurement extends the dynamic range of the CRD measurement from three, to at least 6 orders of magnitude. The dynamic range is defined by the minimal and maximal detectable change in ring-down time. [122] The dynamic range of absorbance

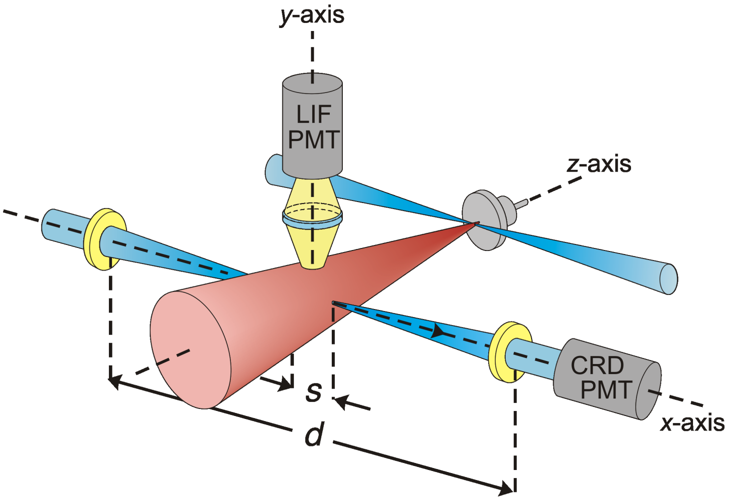

Figure 6.5: CELIF experimental setup. SD radicals generated by photodissociation of D_2S in the expansion of the supersonic beam (z-axis) are excited by the CRD laser (x-axis) and the fluorescence signal S^{LIF} is detected (y-axis) simultaneously with the ring-down signal I^{CRD}.

measurements is determined by saturation at the higher end and by the LOD at the other end, where the lowest absorbance that can be measured needs to give a signal change that is greater than the noise on the trace.

The CELIF technique is the first of its kind to cross correlate the ring-down and fluorescence signals in such a way that both techniques are enhanced. The combination of these two techniques has been previously used to measure fluorescence quantum yields and quenching rates. [127–129] However, this was not necessarily done with a single laser beam, and not in a cross-correlated manner CELIF uses. Figure 6.5 illustrates the CELIF setup, it is a standard LIF measurement with fluorescence collected perpendicularly to the molecular beam axis, where normalisation is achieved using the simultaneously measured CRD signal along the third perpendicular axis which also provides absolute calibration of the signal. The normalisation eliminates shot-to-shot fluctuations in the laser intensity and the simultaneous ring-down measurement is used for the absolute calibration of the normalised LIF signal. The calibration is very robust since both LIF and CRD measurements use the same laser photons and molecules in the sample as both signals are recorded simultaneously on a shot-to-shot basis.

CRD benefits from the long path length for a filled cavity, but when the sample is localised, as in molecular beams, the effective path length can be reduced by orders of magnitude. The technique is applicable to any gas-phase, liquid and even solid samples as with CRDS, provided the fluorescence light can be extracted from the sample volume. If the photon loss per pass is high, stand-alone CRDS can be used. The advantage of using CELIF is from the challenges it deals with that are usually faced with single-pass LIF. The cavity can, in principle, eliminate any stray light and thus reduce scattered background signal, giving an improved signal-to-noise ratio and allowing the detection on the laser excitation wavelength. This may eliminate the need for baffles and optical filters that are sometimes required in LIF setups in order to suppress the stray light. The cavity also reduces saturation from the decreased laser intensity of the probe laser pulse as the pulse is effectively stretched in time. In single-pass LIF, short fluorescence lifetimes raise challenges as the fluorescence signal is obscured by the stray light of the excitation pulse and the Rayleigh scattered light from the sample cannot be easily discriminated against by gated detection. In contrast, CELIF is equally applicable to short and long fluorescence lifetimes compared to the laser pulse length.

6.3.1 CELIF Methodology

The reader is referred to a detailed description of the methodology for CELIF which has been described in detail in the original article by Sanders *et al.* [122] The main points will be more briefly described here. The LIF signal detected along the y-axis in figure 6.5 is given by

$$S^{\mathrm{LIF}} = I^{\mathrm{LIF}}\,\alpha\,\Gamma\,g, \tag{6.10}$$

where I^{LIF} is the light intensity that has interacted with the molecules within the probe volume, $\alpha = \sigma\rho$ is the absorption coefficient, where σ is the bandwidth corrected absorption cross section and ρ is the absolute molecular number density, Γ is the fluorescence quantum yield and g is an instrument factor, and is the product of the fraction of fluorescence photons created in the probe volume that hit the LIF PMT, the quantum efficiency of that PMT and a factor quantifying the convolution of the detection system solid angle with the angular distribution of the fluorescence or scattering process.

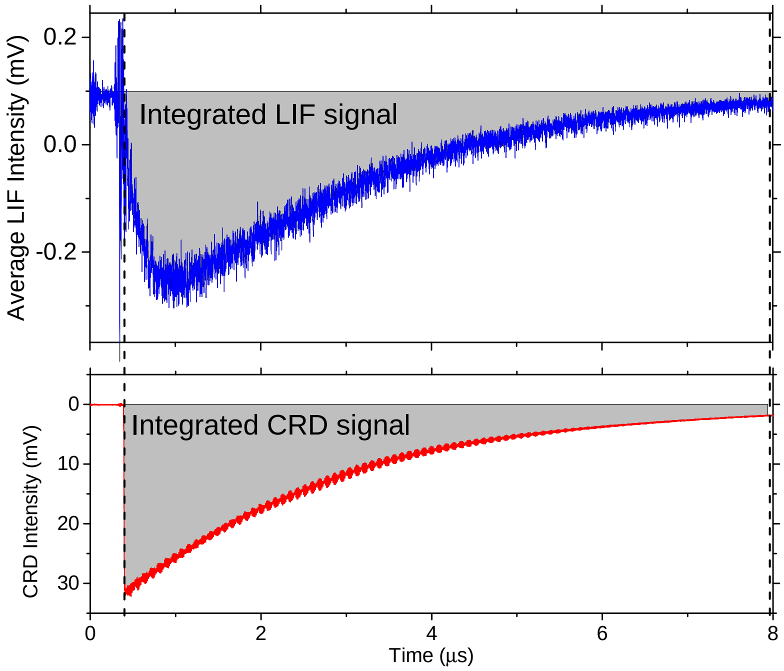

Figure 6.6: Simultaneously recorded LIF (blue) and CRD (red) transients of SD molecules. The ns laser pulse is stretched to the $2\,\mu$s decay of the cavity. An arbitrary offset is included between $t = 0$ and the time the laser pulse arrives in the cavity in order to have a baseline for better fitting of the exponential.

For highly reflective mirrors ($\approx 100\%$) and low photon loss per cavity pass (*i.e.* $\alpha\, d \ll 1$) one can make the approximation.

$$I^{\mathrm{LIF}} \simeq 2I^{\mathrm{CRD}}/T, \tag{6.11}$$

where I^{CRD} is the time-integrated CRD intensity and T is the transmission of the cavity exit mirror. [122] Therefore, the CELIF signal

$$S^{\mathrm{CELIF}} = \frac{S^{\mathrm{LIF}}}{I^{\mathrm{CRD}}} = \sigma\,\rho\,\Gamma\,\frac{2g}{T}, \tag{6.12}$$

is the integrated LIF signal normalised shot-to-shot to the integrated CRD intensity. Figure 6.6 shows simultaneously recorded LIF (blue) and CRD (red) transients in SD molecules. The integrated ring-down signal shown is used to normalise the integrated LIF signal, giving the CELIF signal. The I^{CRD} provides a very robust shot-to-shot normalisation of the LIF signal against the light intensity, eliminating the shot-to-shot fluctuations in the laser intensity. More importantly, it provides a precise way of determining the laser intensity in the cavity. The factor g/T is difficult to determine because it contains factors that depend on the instrument. For the CELIF method to deliver absolute absorption coefficients, the instrument dependent factor must be robustly calibrated. Ideally, this would be done by simultaneously measuring the LIF signal and a CRD absorption where the change in ring-down time is used to determine α, and thus, the absolute density and the calibration factor. The calibration proportionality factor is determined from rearranging equation 6.12 and substituting in equation 6.8 to give

$$\kappa = \frac{\alpha}{S^{\mathrm{CELIF}}} = \frac{T}{2\Gamma g} = \frac{I^{\mathrm{CRD}}}{S^{\mathrm{LIF}}} \frac{1}{c} \left(\frac{1}{\tau} - \frac{1}{\tau_0} \right). \tag{6.13}$$

Therefore, by measuring the LIF signal, then normalising this using the integrated ring-down intensity for a CRD measurement, where a sufficient reduction in ring-down time can be detected, the calibration factor which eliminates the need to determine all instrument dependent factors can be found.

In our measurements for SD molecules, however, the density 12 cm from the nozzle, a distance constrained by our vacuum chambers, was too low to measure a CRD absorption. As an alternative, a separate Rayleigh CELIF scattering measurement was required, leaving all other experimental parameters unchanged. In our measurements we used dry N_2 gas. To relate the Rayleigh scattering measurements to the SD measurements, we take the ratio between the two CELIF measurements for the two different molecules which gives

$$\frac{S_{\mathrm{SD}}^{\mathrm{CELIF}}}{S_{\mathrm{N_2}}^{\mathrm{CELIF}}} = \frac{\sigma_{\mathrm{SD}}}{\sigma_{\mathrm{N_2}}} \frac{\rho_{\mathrm{SD}}}{\rho_{\mathrm{N_2}}} \frac{\Gamma_{\mathrm{SD}}}{\Gamma_{\mathrm{N_2}}} \frac{g}{g'}. \tag{6.14}$$

The fluorescence from the SD radicals does not necessarily have the same angular distribution as Rayleigh scattering, therefore one must account for the difference in intensities of scattered light and fluorescence light due to their angular distribution. This was achieved by setting the angle between the linear polarisation of the probe light and the LIF detection axis to the "magic angle", $\theta = 54.7°$ where any difference in intensities would vanish. [130] The instrument dependent factors are the same for both measurements, thus $g = g'$. For Rayleigh scattering $\Gamma_{\mathrm{N_2}} = 1$. On the other hand, $\Gamma_{\mathrm{SD}} \neq 1$, because predissociation of the SD radical competes with fluorescence. [124] Therefore, equation 6.14 can be rearranged to give

$$\alpha_{\mathrm{SD}} = \sigma_{\mathrm{SD}}\rho_{\mathrm{SD}} = \frac{\rho_{\mathrm{N_2}}}{S_{\mathrm{N_2}}^{\mathrm{CELIF}}}\frac{\sigma_{\mathrm{N_2}}}{\Gamma_{\mathrm{SD}}}S_{\mathrm{SD}}^{\mathrm{CELIF}}, \tag{6.15}$$

which no longer contains the instrument dependent factors.

6.3.2 Details of the Experiment and Measurements

First, the D_2S molecules that were photodissociated into the SD molecules were synthesised in the lab according the reaction

$$2\,\mathrm{D_3PO_4} + 3\,\mathrm{FeS} \longrightarrow 2\,\mathrm{D_2S} + \mathrm{Fe(PO_4)_2}.$$

The synthesised D_2S gas was stored in a small cylinder. This cylinder was connected to a gas mixing assembly that was constructed to allow the mixing of the molecules in the neon carrier gas, as depicted in figure 6.7. The assembly consists of taps that separate the different supply gases, a piezo transducer gauge (Pfeiffer Vacuum, APR 265) to accurately measure pressure, and a rotary pump. There are two loops of pipe of unequal length each entering the bottom and exciting the top of the gas mixing bottle feeding the valve. This, together with the heating tape wrapped around the pipes, generates a convection current. This assembly allowed the sequential dilutions of the mixtures to obtain different concentrations for the dilution measurements, as will be described the following sections. The entire mixing bottle and gas-line was deuterated by exposure to D_2O in order to prevent isotope exchange with H_2O. The assembly was constructed carefully to ensure it was leak proof since D_2S is highly poisonous.

The CELIF measurements presented in this chapter were undertaken in a separate molecular beam machine. The optical cavity mirrors acted as the vacuum chamber windows that formed a vacuum seal were held by mounts. The mounts holding the mirrors were designed with screws in order to allow the precise alignment of the mirrors to trap the laser pulse inside the cavity. The operating pressure in the chamber was $< 10^{-5}$ mbar. The distance between the nozzle and the cavity axis was 12 cm.

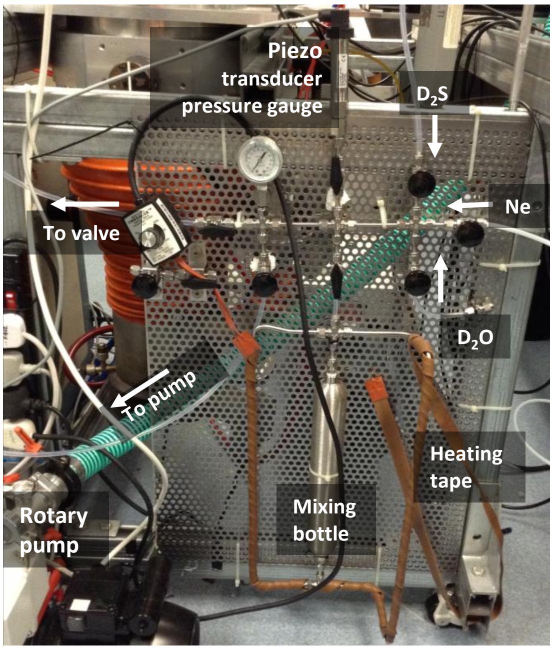

Figure 6.7: Gas mixing assembly used to supply the D_2S and Ne carrier gas mixture the solenoid valve, including a mixing bottle where the mixtures are made and a piezo transducer gauge to accurately measure the pressures.

The SD molecules were formed in a supersonic jet of varying densities of D_2S molecules seeded in Ne (2 bar backing pressure) propagating along the z-axis, as in figure 6.5, from a pulsed solenoid valve (Parker, General Valve Series 9). The SD radicals were created by photodissociation of D_2S molecules, mixed at varying partial pressures in the Ne carrier gas before expansion, using an ArF excimer laser (GAM LASER, EX5, 193 nm, *ca.* 4 mJ per pulse). The excimer laser beam was aligned through the windows in such a way that it was just at the nozzle exit, where the D_2S density was highest.

A pulse generator was used to control the triggering of the whole experiment. To optimise the trigger timing for the time when the molecular beam arrives within the probe volume, the delay between the firing of the dissociation laser and the probe laser was scanned and the integrated LIF signal recorded. The delay was scanned by controlling the timing using a LabVIEW programme. The black trace in figure 6.8 shows a scan for a fixed valve (nozzle) to dissociation laser delay of 290 μs, and a fitted gaussian (in red). The peak is at 150 μs, which gives a terminal velocity of around 800 m/s for a nozzle to probe volume distance of around 12 cm.

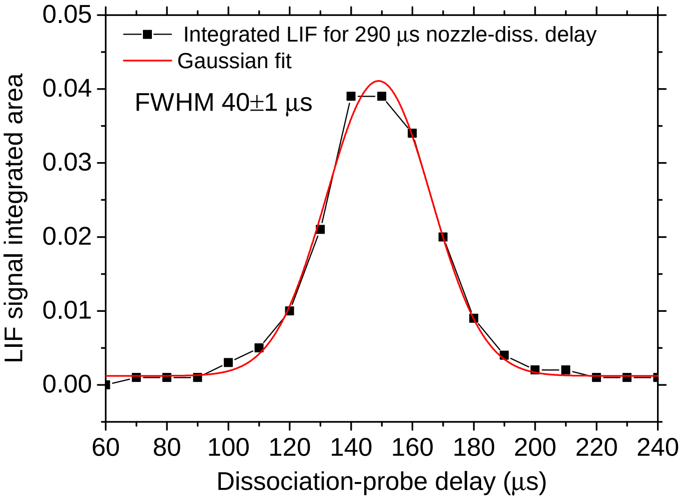

Figure 6.8: Integrated LIF signal for varied delays between the triggering of the dissociation and probe lasers (black) for a fixed nozzle to dissociation laser delay of 290 μs fitted with a gaussian (red).

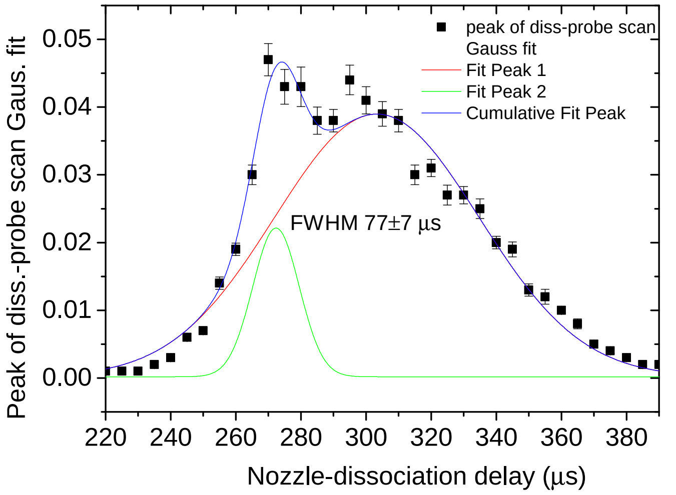

Figure 6.9: Integrated LIF signal for varied delays between the valve opening and the firing of the dissociation laser (black squares), with two single gaussians fitted to the two peaks (green and red), and a double cumulative peak fit (blue).

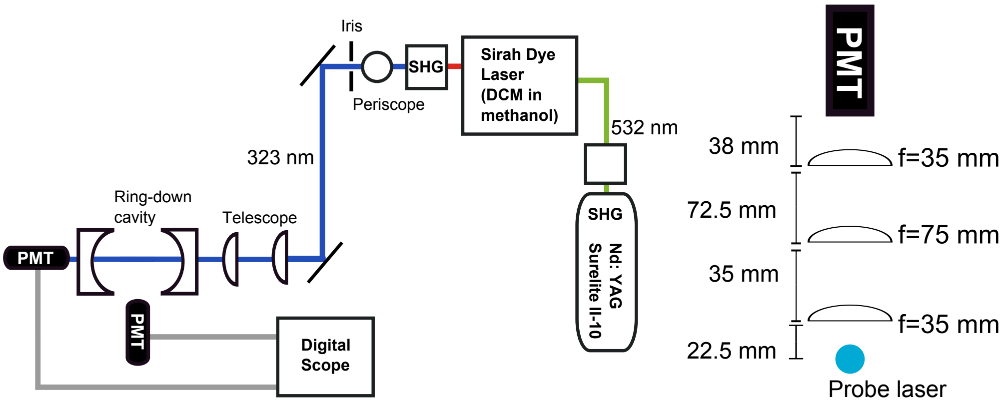

(a) (b)

Figure 6.10: a) Schematic diagram of the set-up used in the CELIF measurements. b) LIF collection optics.

The dissociation-probe delay scan was repeated for different valve-dissociation laser delays, and the results fitted with a gaussian. Figure 6.9 shows the peak of the gaussian fit for the different scans (black squares). From the figure, the optimum delay showing the highest number of SD molecules produced, where the density is more stable is at around 270 μs. In is clear from the data that the points are best fitted with a cumulative double peak with two single gaussians fitted to the two peaks (green and red), and a double cumulative peak fit (blue).

The diagram in figure 6.10a shows the a schematic representation of the detection system and how the probe beam was steered along the CRD cavity axis. A nanosecond pulsed Nd:YAG (Continuum Surelite II-10, 532 nm, repetition rate $f_{\mathrm{rep}} = 10$ Hz, 5 ns pulse length) pumped a dye laser (Sirah Cobra Stretch), tuned to the $\mathrm{P}_1(1.5)$ line of the $(0,0)$-band of the $\mathrm{A}^2\Sigma^+ \leftarrow \mathrm{X}^2\Pi_{3/2}$ transition at 323.17 nm (200 μJ typical pulse energy), was coupled into a standard ring-down cavity. This particular spectroscopic feature was used as it is an isolated peak. Beam shaping optics (a telescope) were used to best match the beam wavefront radius to the curvature of the entrance mirror. Polarisation rotating optics were also used to set the angle between the linear polarisation of the probe light and the LIF detection axis to the 'magic angle', as described earlier. The length of the cavity, L, and the radius of curvature of the mirrors were chosen such that the confocal cavity is optically stable. In order to align the cavity, the mirrors are placed in adjustable mirror mounts that allow the mirrors to be tilted and aligned. A three-lens

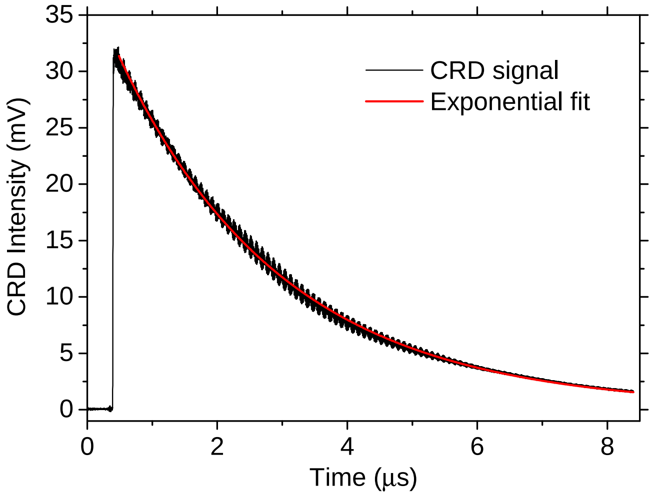

Figure 6.11: Measured ring-down transient (black) and the fitted first order exponential (red). The short laser pulse trace can be seen as the high frequency oscillations of the CRD transient. The lower frequency oscillation seen is a result of the interference between different modes.

LIF detection optical system (figure 6.10b) was aligned along the y-axis and has a field of view that restricts the probe volume to 1.9×10^{-3} cm^3 over a length of $d = 1.2$ cm. This probe volume was calculated using ray tracing matrices by another member of the group.

The ring-down transient was measured with a PMT (Hamamatsu, H7732-10) along the x-axis which orthogonally intersects the molecular beam along the z-axis. The trace in figure 6.11 shows a typical ring-down transient that was measured by the CRD PMT for the cavity used in our setup, with an exponential decay of the light intensity exiting the cavity. By fitting a first-order exponential to the ring down signal (red trace in figure 6.11), a cavity ring-down time of $2.236 \pm 0.002\,\mu$s was determined by comparison with equation 6.4.

To optimise the optical cavity for the TEM$_{00}$ mode, a fast Fourier transform (FFT) of the ring-down trace was monitored on the oscilloscope while adjusting the screws of the mirror mounts in the mirror alignment. The frequency that corresponds to the TEM$_{00}$ mode is at 167 MHz and is the peak whose amplitude must be maximised while all others minimised. From the FFT, the cavity length was measured to be $L = 98.29 \pm 0.05$ cm, by using equation 6.9. Using this value and equation 6.5, the cavity mirrors (Layertec) reflec-

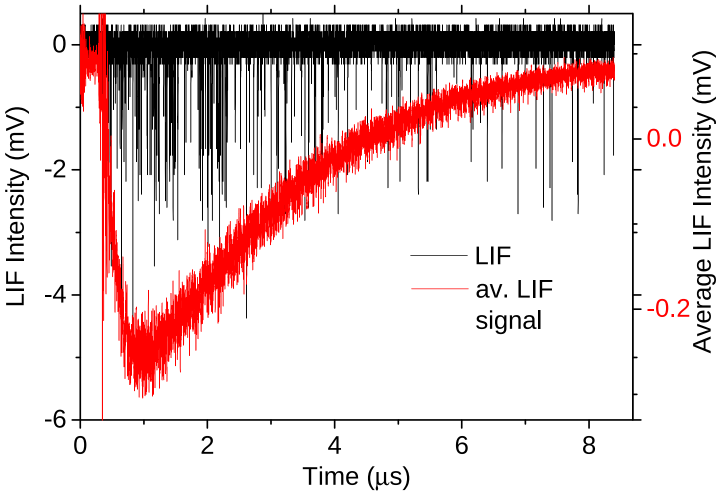

Figure 6.12: Raw LIF signal measured showing photons (black), some of which overlap and the average signal (red) over 200 laser shots with a transient that follows the ring-down transient with a ring-down time of about 2 μs.

tivity was measured to be $\geq$ 99.87%. The quoted mirror transmission was given as 0.01–0.015%. The radius of curvature of the mirrors is 1 m, which gives a $1/e^2$ beam waist radius of 0.023 cm. To eliminate the high frequency oscillations in the exponential, which results from the short laser pulse train, the CRD signal was bandwidth limited on the oscilloscope to 20 MHz, in order to give exponentials of higher quality.

For the LIF signal, photons were counted with another PMT (Hamamatsu, H3695-10). Both signals were digitised with an oscilloscope (LeCroy, WaveRunner 610Zi). The detected signal from the LIF PMT can be seen in figure 6.12. The raw signal is shown in black, where individual photons, as well as overlapped photons can be seen. The red trace shows the average signal over 200 laser shots. It is clear that the laser light pulse is effectively stretched by the cavity by comparison with the ring-down transient in figure 6.11 with a ring-down time characteristic of the cavity. For a simultaneously recorded CRD and LIF transients, the effective number of photons in the cavity can be determined by calculating the area under the ring-down signal curve.

Recording the LIF signal by integrating the area of the LIF transient can only be done accurately for a relatively strong signal, as shown in figure 6.12. When the signal levels are low, as they are found at the lower SD concentrations, individual photons are seen and their rate of appearance is too low for area integration to give an accurate measurement. This point was validated by scanning the probe laser wavelength and recording the LIF using area-integration, followed by photon counting. The two graphs in figure 6.13 show the absorption spectra of the $\mathrm{A}^2\Sigma^+(v' = 0) \leftarrow \mathrm{X}^2\Pi_{3/2}(v'' = 0)$ of jet-cooled SD for two different means of recording the photon signal: photon counting (top) and area integration (bottom). It is clear that the signal to noise ratio for the area integration spectrum is worse than that for the same scan repeated with photon counting.

A LabVIEW programme was written by a member of the group with an algorithm that counts photons correctly. A photon was only counted if the signal was between two pre-assigned noise thresholds; an upper one and a lower one. To set the threshold values, individual shots were observed and the photons counted by eye, in such a way that the correct photon count was given by the LabVIEW programme. The photons were correctly counted, provided they were not close in time. To prevent this, the probe laser intensity was reduced sufficiently to ensure that the number of signal counts was not under-represented due to photon coincidences on the detector. Figure 6.14 shows the excitation spectra of the $\mathrm{A}^2\Sigma^+(v' = 0) \leftarrow \mathrm{X}^2\Pi_{3/2}(v'' = 0)$ of jet-cooled SD for a conventional, single-pass LIF (bottom), and the CELIF signal (top) where photon counting was used. The signal to noise ratio of the scans is similar and the same features appear in both scans. One difference seen is that the peaks are more well defined in the CELIF scan. The probe beam was expanded for the single-pass LIF spectrum scan measurement to reduce saturation. However, power broadening was still observed.

6.3.3 Data Acquisition and Error Analysis

A LabVIEW programme was written by a member of the group for the data acquisition and analysis. For each diluted mixture of $\mathrm{D_2S}$ in the Ne carrier gas that was photodissociated into SD, the number of photon counts on the LIF PMT $S^{\mathrm{LIF}}_{\mathrm{tot},i}$ for each ith shot was recorded for n laser shots to give the "total" signal counts originating from SD molecules and from background sources. Simultaneously, the cavity ring-down (CRD) transient was recorded for each ith laser shot. Each CRD transient was fitted with an exponential to obtain the amplitude $A^{\mathrm{CRD}}_{0,i}$ and the ring-down time τ_i and the integrated

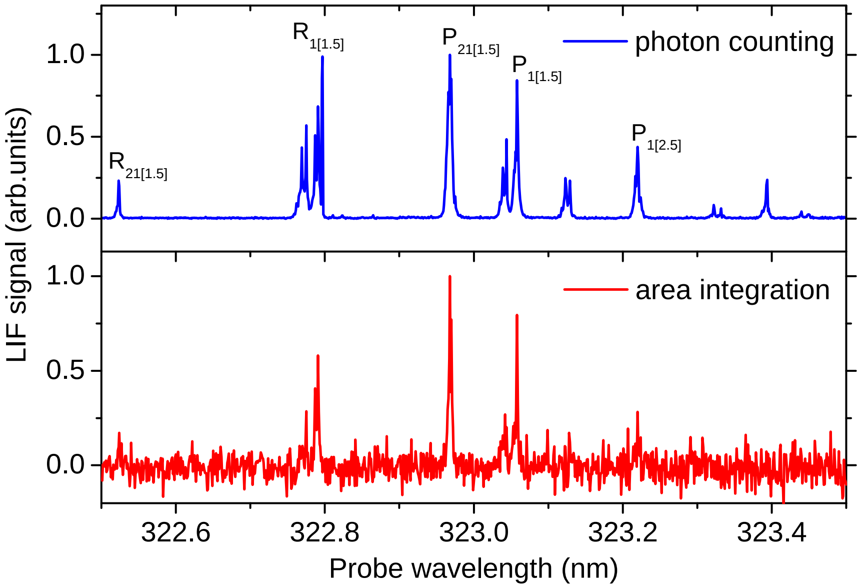

Figure 6.13: Comparison of CELIF excitation spectra of the $A^2\Sigma^+(v' = 0) \leftarrow X^2\Pi_{3/2}(v'' = 0)$ of jet-cooled SD molecules using photon counting (top) and area integration (bottom).

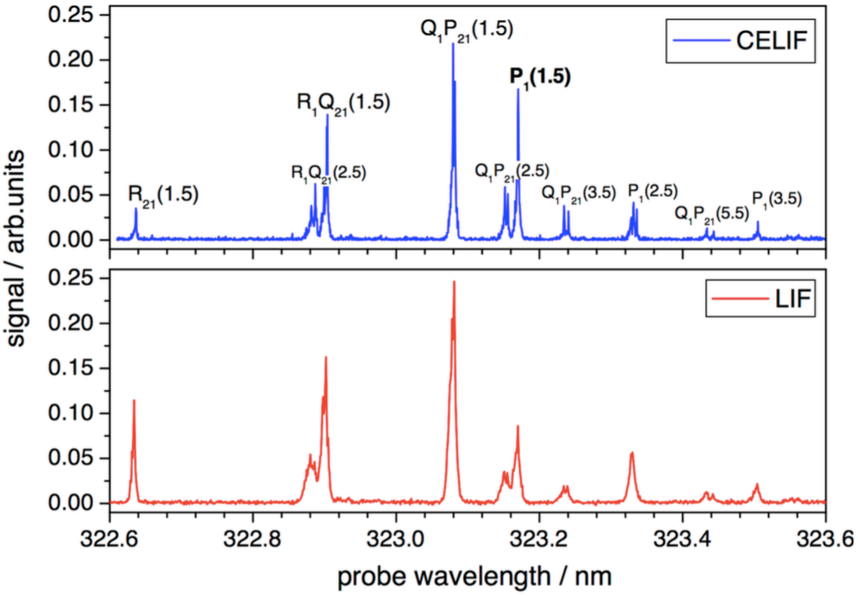

Figure 6.14: Photon counting comparison of CELIF (top) and conventional, single-pass LIF (bottom) excitation spectra of the $A^2\Sigma^+(v' = 0) \leftarrow X^2\Pi_{3/2}(v'' = 0)$ of jet-cooled SD.

CRD intensity calculated

$$I^{\mathrm{CRD}}_{\mathrm{tot},i} = A^{\mathrm{CRD}}_{0,i}\tau_i. \tag{6.16}$$

The total CELIF signal for each laser shot

$$S^{\mathrm{CELIF}}_{\mathrm{tot},i} = \frac{S^{\mathrm{LIF}}_{\mathrm{tot,i}}}{I^{\mathrm{CRD}}_{\mathrm{tot},i}}, \tag{6.17}$$

was then calculated and averaged over all laser shots to give the average total CELIF signal per shot $S^{\mathrm{CELIF}}_{\mathrm{tot}}$. This procedure was found to give the same result as using

$$S^{\mathrm{CELIF}}_{\mathrm{tot}} = \frac{S^{\mathrm{LIF}}_{\mathrm{tot}}}{I^{\mathrm{CRD}}_{\mathrm{tot}}}, \tag{6.18}$$

where the subscript i has been dropped because $S^{\mathrm{LIF}}_{\mathrm{tot}}$ is the average number of photon counts per laser shot and $I^{\mathrm{CRD}}_{\mathrm{tot}}$ is the average integrated CRD intensity per shot.

Immediately following n laser shots, the dissociation laser was blocked and the same procedure above was repeated for another n laser shots to arrive at the average CELIF signal per shot from background sources $S^{\mathrm{CELIF}}_{\mathrm{bg}}$. The average CELIF signal per shot originating from SD molecules was thus determined by the background subtraction

$$S^{\mathrm{CELIF}}_{\mathrm{SD}} = S^{\mathrm{CELIF}}_{\mathrm{tot}} - S^{\mathrm{CELIF}}_{\mathrm{bg}}, \tag{6.19}$$

and is plotted in figure 6.16 on page 170. The CELIF normalisation of the background is justified when one considers the sources of the background signal. Even though the cavity is an effective discriminator of scattered light compared to a standard LIF setup, 99% of $S^{\mathrm{LIF}}_{\mathrm{bg}}$ originated from scattered light from the probe laser, most likely from UV fluorescence of the UV grade fused silica substrate of the cavity entrance mirror. $S^{\mathrm{LIF}}_{\mathrm{bg}}$ was found to be proportional to $I^{\mathrm{CRD}}_{\mathrm{bg}}$.

The error bars in figure 6.16 for $S^{\mathrm{CELIF}}_{\mathrm{SD}}$ were determined as follows. The relative fitting error on $A^{\mathrm{CRD}}_{0,i}$ and τ_i, was

$$\beta(A_{0,i}) = \frac{\delta A^{\mathrm{CRD}}_{0,i}}{A^{\mathrm{CRD}}_{0,i}} = 0.1\% \qquad \text{and} \qquad \beta(\tau_i) = \frac{\delta\tau_i}{\tau_i} = 1\%, \tag{6.20}$$

respectively. The relative fitting errors, $\beta(A_{0,i})$ and $\beta(\tau_i)$, were found on analysis to vary insignificantly over all laser shots because the cavity was set up such that the ring-down transients were good quality single exponential decays with electronic noise that did not vary significantly shot-to-shot. Thus, $\beta(A_{0,i})$ and $\beta(\tau_i)$ are treated as constants, $\beta(A_0)$ and $\beta(\tau)$, where $\beta(A_0) \ll \beta(\tau)$. The resulting relative error $\beta(I)$ on the determination of each $I^{\mathrm{CRD}}_{\mathrm{tot},i}$ only depends on the fitting errors and is, therefore

$$\beta(I) = \sqrt{\beta(A)^2 + \beta(\tau)^2} \approx \beta(\tau), \tag{6.21}$$

$\beta(I)$ is the only relevant error with respect to $I^{\mathrm{CRD}}_{\mathrm{tot},i}$ because an important point of CELIF is to remove noise caused by shot-to-shot fluctuations in laser intensity. The quantum noise from counting LIF photons over n laser shots was

$$\delta S^{\mathrm{LIF}}_{\mathrm{tot}} = \left(\frac{S^{\mathrm{LIF}}_{\mathrm{tot}}}{n}\right)^{1/2}, \tag{6.22}$$

and comes from Poisson statistics. Therefore, the combined noise in $S^{\mathrm{CELIF}}_{\mathrm{tot}}$ is

$$\delta S^{\mathrm{CELIF}}_{\mathrm{tot}} = \left[\frac{1}{nS^{\mathrm{LIF}}_{\mathrm{tot}}} + \beta(\tau)^2\right]^{1/2} S^{\mathrm{CELIF}}_{\mathrm{tot}}. \tag{6.23}$$

An equivalent to equation 6.23 for the background CELIF signal can be derived in the same way except the error is dominated by the quantum noise because $S^{\mathrm{LIF}}_{\mathrm{bg}}$ is very small, *i.e.*

$$\delta S^{\mathrm{CELIF}}_{\mathrm{bg}} \approx \left(\frac{1}{nS^{\mathrm{LIF}}_{\mathrm{bg}}}\right)^{1/2} S^{\mathrm{CELIF}}_{\mathrm{bg}}. \tag{6.24}$$

The noise in $S^{\mathrm{CELIF}}_{\mathrm{SD}}$ from equation 6.19 is

$$\delta S^{\mathrm{CELIF}}_{\mathrm{SD}} = \left[\left(\delta S^{\mathrm{CELIF}}_{\mathrm{tot}}\right)^2 + 2\left(\delta S^{\mathrm{CELIF}}_{\mathrm{bg}}\right)^2\right]^{1/2}, \tag{6.25}$$

where the factor 2 comes from the fact that $S^{\mathrm{CELIF}}_{\mathrm{tot}}$ contains $S^{\mathrm{CELIF}}_{\mathrm{bg}}$.

To derive an expression for the limit of detection (LOD) of $S^{\mathrm{CELIF}}_{\mathrm{SD}}$, which is the horizontal line in figure 6.16, the approximation that $I^{\mathrm{CRD}}_{\mathrm{tot}} = I^{\mathrm{CRD}}_{\mathrm{bg}} = I^{\mathrm{CRD}}$ is made such that

$$S^{\mathrm{LIF}}_{\mathrm{SD}} = S^{\mathrm{LIF}}_{\mathrm{tot}} - S^{\mathrm{LIF}}_{\mathrm{bg}}, \tag{6.26}$$

so the noise in $S_{\mathrm{SD}}^{\mathrm{LIF}}$ is

$$\left(\delta S_{\mathrm{SD}}^{\mathrm{LIF}}\right)^2 = \left(\delta S_{\mathrm{tot}}^{\mathrm{LIF}}\right)^2 + 2\left(\delta S_{\mathrm{bg}}^{\mathrm{LIF}}\right)^2 = \frac{1}{n}\left(S_{\mathrm{SD}}^{\mathrm{LIF}} + 2S_{\mathrm{bg}}^{\mathrm{LIF}}\right). \tag{6.27}$$

At the LOD, $S_{\mathrm{SD}}^{\mathrm{LIF}} = S_{\mathrm{SD}}^{\mathrm{LIF,LOD}} = \delta S_{\mathrm{SD}}^{\mathrm{LIF}}$, therefore

$$n\left(S_{\mathrm{SD}}^{\mathrm{LIF,LOD}}\right)^2 = S_{\mathrm{SD}}^{\mathrm{LIF,LOD}} + 2S_{\mathrm{bg}}^{\mathrm{LIF}}. \tag{6.28}$$

Solving for $S_{\mathrm{SD}}^{\mathrm{LIF,LOD}}$ gives

$$S_{\mathrm{SD}}^{\mathrm{LIF,LOD}} = \frac{1}{2n} + \left(\frac{1}{4n^2} + \frac{2S_{\mathrm{bg}}^{\mathrm{LIF}}}{n}\right)^{1/2}, \tag{6.29}$$

which, in the limit of large n, gives

$$S_{\mathrm{SD}}^{\mathrm{LIF,LOD}} \approx \left(\frac{2S_{\mathrm{bg}}^{\mathrm{LIF}}}{n}\right)^{1/2}. \tag{6.30}$$

The CELIF signal at the LOD is therefore

$$S_{\mathrm{SD}}^{\mathrm{CELIF,LOD}} \approx \left(\frac{2S_{\mathrm{bg}}^{\mathrm{LIF}}}{n\left(I^{\mathrm{CRD}}\right)^2}\right)^{1/2}, \tag{6.31}$$

which, when compared to equation 6.24, reveals that

$$S_{\mathrm{SD}}^{\mathrm{CELIF,LOD}} \approx \sqrt{2}\delta S_{\mathrm{bg}}^{\mathrm{CELIF}}. \tag{6.32}$$

6.3.4 Results and Discussions

The measurements of $S_{\mathrm{SD}}^{\mathrm{CELIF}}$ presented in this chapter had to take place in a regime where the photodissociation of the D_2S molecules was saturated, which ensures that any shot-to-shot instabilities or long-term drifts in the laser pulse energy do not contribute to the noise in $S_{\mathrm{SD}}^{\mathrm{CELIF}}$ signal. Figure 6.15a shows $S_{\mathrm{SD}}^{\mathrm{CELIF}}$ as a function of photodissociation laser pulse energy. The signal varies linearly at low laser pulse energies and begins to enter a saturated regime at around 3.5 mJ per pulse. However, for the fluorescence signal, the opposite is true; the fluorescence from the SD radicals must not

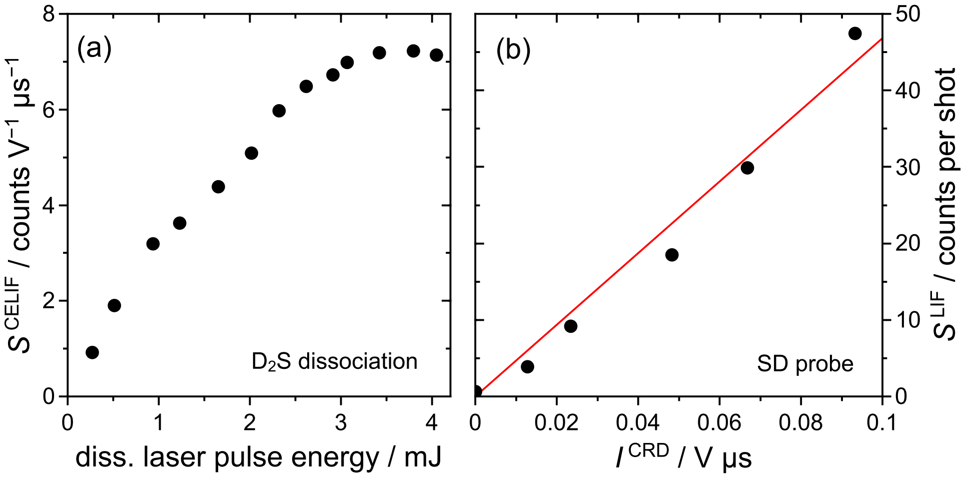

Figure 6.15: (a) Dependance of the SD CELIF signal on the pulse energy of the D_2S dissociation laser showing saturation at 3.5 mJ and above. (b) Dependance of the average LIF counts per shot on the probe laser pulse energy as measured by the time-integrated ring-down signal. The statistical error bars are smaller than the symbols.

be saturated for the shot-to-shot normalisation of the CELIF to be valid. Figure 6.15b shows that the dependence of $S_{\mathrm{SD}}^{\mathrm{CELIF}}$ on the intensity of the probe light in the cavity is linear thus proving that the experiment is not in the LIF saturation regime.

Figure 6.16 shows a plot of $S_{\mathrm{SD}}^{\mathrm{CELIF}}$ versus the mole fraction of D_2S mixed in the Ne carrier gas before expansion. Starting from the highest value, the mole fraction was lowered by sequentially diluting the previous mixture by pumping away a fraction of the 2 bar total pressure and adding Ne until the total pressure returned to 2 bar. After each dilution, the gas mixture was “stirred” for 20 minutes using the gas mixing assembly that was illustrated in figure 6.7. Each black data point in figure 6.16 is the CELIF signal for each separate dilution with the background subtraction according to equation 6.19 and was obtained as discussed in the previous section.

The horizontal line in figure 6.16 represents the LOD of the CELIF signal, plotted using the expression for the LOD of $S_{\mathrm{SD}}^{\mathrm{CELIF}}$, where the signal to noise ratio is unity, as given by equation 6.31 with $n = 1000$ shots and $n = 2000$ shots at the higher and lower D_2S mole fractions, respectively.

The $S_{\mathrm{SD}}^{\mathrm{CELIF}}$ axis in figure 6.16 has been converted into α_{SD} using equation 6.15. To do this, the ratio $\rho_{\mathrm{N}_2}/S_{\mathrm{N}_2}^{\mathrm{CELIF}}$ had to be measured. This was done by taking separate measurements for the Rayleigh scattering from nitro-

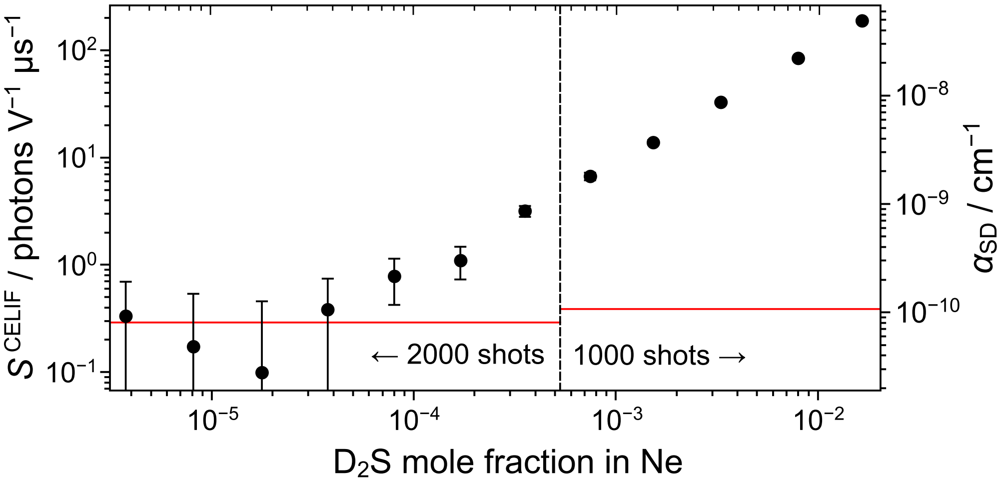

Figure 6.16: Determination of the limit of detection of the SD CELIF measurement and, therefore, of α_{SD} by successive dilution of the D_2S/Ne gas mixture. The red horizontal line shows the limit of detection where the signal to noise ratio is unity.

gen gas. The results are presented in figure 6.17. As per the SD CELIF measurements, the probe laser intensity was reduced sufficiently to ensure good photon counting statistics. The N_2 pressures in the chamber above and below 48 mbar were measured using a calibrated piezo transducer gauge (Pfeiffer Vacuum, APR 265) and a calibrated Pirani gauge (Pfeiffer Vacuum, PBR 260), respectively. Pressures were converted into densities via the van der Waals equation.

The N_2 density could have been measured by CRD, had it not been for the fact that the alignment of the cavity mirrors changed between the measurement of the reference empty cavity ring-down time and the measurement with N_2 gas present, because of the changing pressure differential. Fortunately, the CELIF technique does not rely on a stable cavity alignment because the normalisation only depends on knowing I^{CRD} for a given measurement. To ensure an accurate determination of I^{CRD}, the cavity was realigned for each N_2 pressure to obtain a good quality exponential decay.

The ratio $\rho_{\text{N}_2}/S^{\text{CELIF}}_{\text{N}_2}$ required for equation 6.15 was measured to be $(1.31 \pm 0.02) \times 10^{15}$ counts per shot V μs cm^{-3} from the inverse of the slope of the number density dependence of the N_2 Rayleigh scattering shown in figure 6.17. The slope and the error were determined from a linear χ^2 fit. The same procedure as described above to evaluate $S^{\text{CELIF}}_{\text{SD}}$, and associated errors, was also used to evaluate the average N_2 Rayleigh scattering CELIF signal per

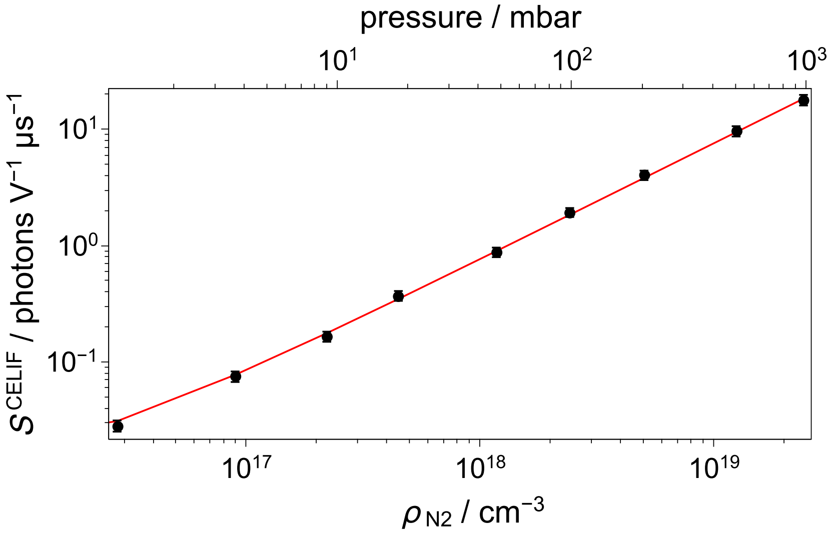

Figure 6.17: Determination of the ratio $\rho_{\mathrm{N}_2}/S_{\mathrm{N}_2}^{\mathrm{CELIF}}$ from measurements of the CELIF signal from N_2 Rayleigh scattering at varying N_2 pressures. The line is a linear χ^2 fit of the data.

shot $S_{\mathrm{N}_2}^{\mathrm{CELIF}}$ and its error $\delta S_{\mathrm{N}_2}^{\mathrm{CELIF}}$, with the exception that no background subtraction was required as it did not affect the slope of the graph in figure 6.17.

The minimum detectable absorption coefficient according to equation 6.15 is, $\alpha_{\mathrm{SD}}^{\mathrm{LOD}} = (7.9 \pm 0.6) \times 10^{-11}$ cm^{-1}, using the values $\sigma_{\mathrm{N}_2}(323.17$ nm$) = (4.1{\pm}0.2){\times}10^{-26}$ cm^2, [131] and $\Gamma_{\mathrm{SD}} = 0.20{\pm}0.01$ [124,132], PGOPHER [133] was used, inputting known spectroscopic constants [134–136], to obtain a cross section for SD of $(4.5 \pm 0.2) \times 10^{-15}$ cm^2 GHz. Using a measured laser bandwidth of (6.4 ± 0.3) GHz, measured from the FWHM of the of the spectral features of the SD spectrum in figure 6.14, the bandwidth corrected cross section is $\sigma_{\mathrm{SD}} = (7.0 \pm 0.5) \times 10^{-16}$ cm^2. The noise at the LOD is dominated by the quantum-noise in the LIF signal, therefore, the quantum-noise-limited density of SD radicals at our LOD is $\rho_{\mathrm{SD}}^{\mathrm{LOD}} = 1.1 \times 10^5$ molecules cm^{-3} and has an error of only 10%. Given the very small probe volume, this density corresponds to an average of just 215 ± 21 molecules in the probe volume at any given time.

6.4 Conclusions and Outlook

The work of Sanders *et al.* did not prove that CELIF would be as effective as it was for BPEB at measuring the absolute absorption coefficients of molecules with relatively long fluorescence lifetimes, such as SD. [122] In this chapter, we have shown that the CELIF detection technique, which combines a modest CRD and LIF setup and using a standard UV pulsed dye laser, can be an effective detection method for molecules with fluorescence lifetimes on the order of hundreds of nanoseconds. Using CELIF we measured the absolute density of SD radicals in a pulsed supersonic jet down to the LOD of 10^5 cm^{-3}. In the 0.002 cm^3 probe volume, this corresponds to *ca.* 200 molecules, a quantum-noise-limited absorption coefficient, $\alpha_{\text{min}} = 7.9 \times 10^{-11}$ cm^{-1} in 200 s.

The CELIF technique is limited to molecules that are suitable to LIF, since at the heart of CELIF, is a fluorescence measurement. Another requirement is that the molecules must fluoresce on a timescale less than the time it takes for a molecule to leave the field of view of the LIF detection optics. For the SD molecules in our experiments, the fluorescence lifetime is *ca.* 200 ns and the time the molecules take to leave the field of view of the LIF detection optics from the point of excitation is around 7 μs. Also, the molecule must absorb in a wavelength region $>$ 200 nm where CRD mirrors can be fabricated. However, many important molecules of interest in many fields fall into this category (*e.g.* NO). CELIF measurements are potentially of use to those wishing to determine absolute cross sections in molecular beam scattering experiments. [126]

Given the modest setup used in these experiments, there is much room to improve the LOD. Examining the terms in equation 6.31, one can see that the LOD of the of the set-up can be lowered by maximising n and I^{CRD}, and minimising $S_{\text{bg}}^{\text{LIF}}$. Although the cavity is an effective discriminator of scattered light compared to a standard LIF setup, 99% of $S_{\text{bg}}^{\text{LIF}}$ originated from scattered light from the probe laser, as explained earlier. One could could effectively eliminate the scattered light by using thin mirrors with a low absorbance allied with light baffles and low reflectivity surfaces inside the cavity chamber, as is done routinely in standard LIF measurements. This would leave only dark counts on the PMT as the source of background signal. Another improvement would be to use a photon-counting PMT (*e.g.*

Hamamatsu H7360-01, 2 pA dark current), which could lower the dark counts by a further factor of 10^3. This would result in the lowering of the LOD density to *ca.* 400 cm^{-3}. This corresponds to, on average less than 1 molecule in the probe volume at any given time. One final improvement would be to use a narrow bandwidth laser of, say, 120 MHz [126] which would increase the bandwidth corrected SD absorption cross-section by a factor of 50 and commensurately lower the LOD density to $< 10\ \text{cm}^{-3}$.

Chapter 7

Final Conclusions and Outlook

In the first chapter of this thesis, an introduction was given to the field of cold molecules and their applications. The route towards the production of microKelvin cold polar molecules, for the application in a quantum simulator device was outlined. The decelerator is one of the stages in this route. Based on the limitations of conventional pulsed-type Zeeman decelerators described in chapter one, we decided to proceed with building a new type of Zeeman decelerator which uses real, 3D moving traps. It was decided to go with a similar design to that developed by Trimeche *et al.*. [75] This thesis presented the work carried out towards the building of the decelerator and the successful demonstration of the 3D guiding and attempted deceleration of Ar* atoms in LFS states.

The second chapter of this thesis presented the work on the development of a source of Ar* atoms for the decelerator. A homebuilt FIG was developed to allow the characterisation of the General Valve (series 99) at different temperatures, in order to operate it at optimum conditions. The chapter also presented the development and characterisation of a controllable discharge-based source of Ar* atoms. The excitation source developed was an electric discharge. The introduction of a hot filament near the discharge electrodes enabled the discharge to operate more stably at voltages as low as 400 V, and discharge pulse durations as short as 20 μs, which combine to create a cold packet of Ar* atoms. The optimised slow beam of Ar* had a velocity of 306±8 m/s and a translational temperature of 4 K.

Chapter three described our homebuilt cantilever piezo valve which we constructed, characterised and optimised using our homebuilt FIG detector at room temperature to produce short gas pulses. The piezo valve was characterised by examining the gas profile of nitrogen and argon under different conditions. Compared to the General Valve that was characterised in chapter two, the piezo valve can produce shorter pulses that are more intense. The valve was optimised at room temperature to produce gas pulses with a FWHM as short as 27μs for nitrogen gas at a distance of 20 mm from the nozzle. To date, our homebuilt cantilever piezo valve has been optimised and characterised to be operated at room temperature. We have not at present tested the piezo valve, however, based on our design considerations, it is expected to be operational even at cryogenic temperatures.

The fourth chapter presented the design of the decelerator. The biggest advantage of this type of decelerator is in the fact that the paramagnetic atoms are confined in all three dimensions, continuously throughout the length of the decelerator. The chapter explained the operation principle of the decelerator and demonstrated the generation of the high currents and magnetic fields required for deep traps. The final coil geometry for the decelerator coils and quadrupole guide were justified. The chapter also outlined the detailed specifications of the decelerator. The decelerator vacuum system, described in detail in this chapter, was built to be compact, reducing the cost. The source chamber and the cooled pulsed discharge valve assembly were designed to produce short gas pulses that can be characterised and optimised with a FIG. A skimmer allows the partial spatial matching of the source emittance to the decelerator acceptance. The detection chamber was designed to allow different means of detecting atoms and molecules: MCP, single-pass LIF, CELIF and QMS with the ability to photo-ionise.

One of the major achievements of this project was to overcome the great challenge of pulsing high currents at high frequencies. The confined atoms within the trap can be brought to a standstill by chirping the modulated high frequency all the way down to zero. The electronics driving the quadrupole guide can supply currents up to 900 A for a variable duration. The electronics and power supplies of the flat helical decelerator coils, to date, are capable of delivering sinusoidal currents up to 600 A peak current in each wire at frequencies ranging from 8.8 kHz to DC for durations of a few milliseconds at repetition rates up to 10 Hz. We have not yet achieved a peak current of 1000 A at the required high velocities or frequencies since the ratio of inductance to resistance is high. One way in which this can be improved is by using connections between the wires with a smaller resistance and inductance. We could also start with a slower beam from a buffer gas source, as discussed in the first chapter. With slower beams, lower frequencies are required. At lower frequencies, the sinusoidal currents are of better quality and higher currents can be achieved for a given time constant. Another way to obtain slow beams is to feed a slowed beam into the moving 3D traps from a conventional Zeeman decelerator. The conventional pulsed-type Zeeman decelerator is good at higher velocities and relatively easy to implement. This was done by Quintero-Perez *et al.* where a combination of a traditional Stark decelerator and a traveling wave decelerator were used to achieve high throughput of ammonia molecules. [137, 138]

In chapter five, we presented our proof-of-principle experimental results where we demonstrated the manipulation of Ar* atoms in the $^3P_2$ metastable state using 2D and 3D magnetic fields. It was successfully shown that the Ar* signal intensity is greatly increased, nearly by a factor two (at 900 A) by using a 290 mm long quadrupole magnetic guide which provides transverse confinement of the atoms. With the addition of the decelerator coils, magnetic confinement along the longitudinal molecular beam axis was achieved, forming 3D-traps. It was shown that the paramagnetic Ar* atoms in LFS states can be guided at a chosen constant velocity. The 3D-guiding of the LFS states of $^3P_2$ state of metastable argon atoms was carried out at constant velocities ranging from 320 m/s up to 400 m/s. The longitudinal temperatures were ∼500 mK. While attempting the deceleration of the traps, though no real deceleration was observed for this short deceleration length, the fields did show a manipulation effect. This gives us the confidence that with a longer decelerator, we will see very prominent bunching.

Once the decelerator is extended in length, other paramagnetic species such as CaF, SD, CH_3 radicals can also be decelerated. A beam of CaF molecules from a buffer gas source, starting at an initial velocity of 150 m/s, could be decelerate to a standstill using a 1 m long decelerator. This would only require eight decelerator modules. By multiplexing, we can use one electronics unit to drive more than one decelerator module. One problem which remains to be overcome is the effect of electrical noise while the decelerator is active. A lot of work has been done to increase shielding and break any earth loops (including building an optical coupler for the FPGA), however, this is still a work in progress. The next immediate step would be to add a second module to decelerate down to lower velocities. With a longer decelerator, the observed effect of the slower molecules, which are not initially trapped but contribute to the signal, should be eliminated. Therefore, the simulations should be able to replicate what is observed experimentally, which is an important validation of results. For such a short decelerator (12.3 cm), it was clear from the comparison of the simulations with the measured results that further work needs to be done to confirm the measured data with the simulations.

In chapter six, we showed that the CELIF detection technique, which combines a CRD and LIF setup and using a standard UV pulsed dye laser, can be an effective detection method for molecules with fluorescence lifetimes on the order of hundreds of nanoseconds or shorter. Using CELIF, we measured the absolute density of SD radicals in a pulsed supersonic jet down to the LOD of 10^5 cm^{-3}. In the 0.002 cm^3 probe volume, this corresponds to *ca.* 200 molecules, and the quantum-noise-limited absorption coefficient is $\alpha_{\mathrm{min}} = 7.9 \times 10^{-11}$ cm^{-1} in 200 s of acquisition time. We have already considered the implementation of the CELIF detection into the decelerator chamber.

When it comes to the deceleration of atomic and molecular beams, the decelerator is only as good as the source. The ideal source for a decelerator is a slow beam with a small translational temperature that allows the trapping of most of the molecules in the beam. The higher the phase space density, the better the source. The phase-space density of the decelerated packet of atoms or molecules is limited by the phase-space density of the initial supersonic beam. The phase-space density can be increased by having more effective cooling in the expansion. More cooling can be achieved by more collisions which would occur at higher pressures. The General Valve we have used in our experiments so far was not designed to be operated at high pressures or at cryogenic temperatures. There is another widely-used valve which is based on the same operation mechanism of the General Valve, called the Even-Lavie valve. Unlike the General Valve, this valve was designed and optimised for use at cryogenic temperatures and at high backing pressures to give high-density beams.

One modification which is currently being made to the decelerator is the implementation of our recently purchased Even-Lavie valve. In a paper by Luria *et al.*, simulations and experiments were performed to quantify the effects of nozzle shape and skimmer placement on high-density supersonic jets. [118] It was revealed that changes in skimmer design and positioning are required to allow intense supersonic beams to propagate in typical supersonic beam setups. At high beam densities, the skimmer orifice is required to be placed at a distance of 1000 nozzle diameters, in order to avoid interference with the skimmer, which would lead to the heating of the beam, as the reflected shock waves would interact with the expansion. [118] Skimmer interference not only degrades the temperature by increasing it, but also the beam intensity and angular spread. It is a standard practice to use trumpet-shaped skimmers. However, this is based on past studies made with continuous beams. The article in question point out that this cannot be copied to pulsed beams. Furthermore, the orifice of the skimmer must have a larger diameter when using high beam densities. [118] We have therefore purchased a cone-shaped skimmer from *Beam Dynamics* with a 4 mm diameter orifice. With the new Even-Lavie valve, the source chamber had to be redesigned with a short extension to enable us to position the valve nozzle at a distance of 15 cm from the skimmer orifice.

Another addition to the Even-Lavie valve is a dielectric barrier discharge (DBD) that is capable of producing a colder plasma. [139] It uses a different discharge mechanism to excite the gas by using a dielectric material between the electrodes. The live electrode is fed with a high voltage RF burst to operate the discharge. Breakdown is initiated in a large number of independent current filaments or micro-discharges that cover the dielectric uniformly. This prevents arcing produced by hotspots and sputtering. In the Even-Lavie valve, this excitation discharge source can create a very cold plasma at the nozzle itself since the DBD source is contained within the front flange of the valve. Therefore, the metastable state atoms are created before the expansion, where the densities are high. Consequently, they can be cooled from the collisions as the gas supersonically expands into the vacuum chamber. Using this valve-discharge assembly, cooling of large molecules to $<1\,\mathrm{K}$ is routinely achieved. [66]

The decelerator developed in the realm of this thesis was initially built to slow-down polar molecules to a velocity which can be captured by a molecular MOT. This is one of the steps in the route towards building a quantum simulator device, as described in chapter one. Apart from its use in a quantum simulator device, this new type of decelerator can be used for the various applications mentioned in chapter one. One of these is in cold chemistry. Through the collaboration with the group of Momose in Vancouver, the magnetic deceleration and focussing of methyl radicals was recently demonstrated. [76] The methyl radical is an interesting choice since it is an important species in combustion reactions and is also a good candidate to investigate reaction dynamics. It is one of the most important and fundamental intermediates in chemical reactions. With regards to magnetic deceleration, the methyl radical has a similar magnetic moment to mass ratio to argon, so with an appropriate choice of a seed gas we should be able reproduce the results we have so far with argon and demonstrate deceleration of our first molecule.

Appendix A

Home-Made Valve Driver

We have also constructed a home-made valve driver which allows more flexibility in manipulating the beam characteristics. Using the home-made driver, the kick-voltage amplitude and width can both be varied in addition to the hold voltage width. The traces in figure A.1a show that the voltage pulses from the our home-made valve including: a higher kick voltage which provides the initial force required to move the mass of the armature against the closing spring and a lower hold voltage that keeps the valve open. For the commercial valve driver, IOTA-ONE the driver triggers the valve with a fixed high voltage pick pulse of approximately 275 V (DC) with a standard set maximum length of 180 μs and a constant hold voltage amplitude of 10 V. The only parameter which can be varied is the total 'on-time' which is the hold voltage width.

Figure A.1b shows the temporal profile of the gas pulse for the optimum gas pulse using the home-made driver in terms of minimising the source chamber background pressure and keeping a complete looking expansion and a comparison with the IOTA-ONE driver trace. The trigger for the IOTA-ONE driver and the kick and hold voltage pulses used for the home-made driver are displayed in figure A.1a. As can be seen, the valve opens later and is broader using the home-made driver with a FWHM of 319 μs for the home-made driver and 147 μs for the IOTA-ONE driver. Attempts were made to produce identical traces for the output using the home-made and commercial valve drivers. Identical traces could not be achieved due to the sensitivity of the valve behaviour to even very small differences in the kick and hold and the combination of the two. When investigating the gas profile at lower

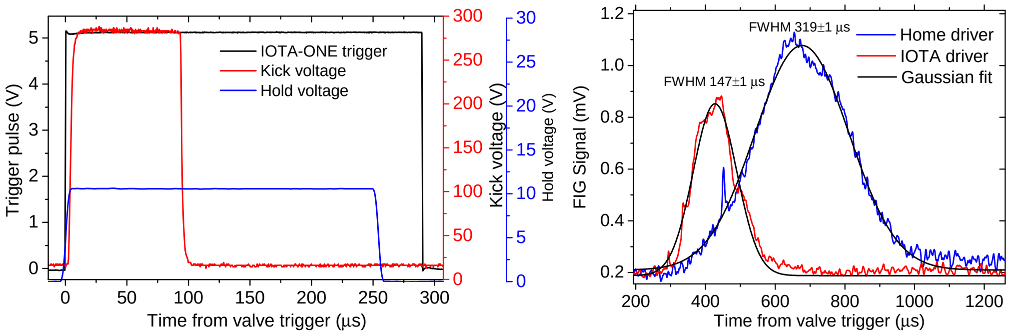

(a) (b)

Figure A.1: The higher voltage 'kick' voltage pulse (red) and lower voltage 'hold' voltage pulse (blue) output from the home-made valve driver. The black trace is the pulse generator opening trigger pulse fed to the commercial IOTA-ONE valve driver. b) Argon FIG signal from the home-made driver (blue) and the IOTA driver (red) using a trigger pulse 290 μs for the IOTA-ONE driver, and a 100 μs kick at 280 V and a 255 μs hold at 10 V for the home-made driver.

temperatures with the home-made driver, the valve behaviour was even more sensitive with even a few volts or microsecond changes leading to dramatic changes in the gas profile. The background pressures in the source chamber were too high for a clean supersonic expansion, thus, it was decided to stick to the IOTA-ONE driver.Identical traces could not be achieved due to the sensitivity of the valve behaviour to even very small differences in the kick and hold and the combination of the two.

Figure A.2a shows the gas temporal profile at different kick voltage pulse widths using the home-made driver. It can be seen that, with increasing kick voltage width, the valve opens with a high force for increasing lengths of time, pushing the armature and poppet further back, releasing more gas. However, it also starts to deteriorate the gas pulse as the valve appears not to be closing properly if the kick pulse width is higher that 71 μs. In figure A.2b the effect of varying the kick voltage amplitude can be seen on the gas profile. Similarly to figure A.2a, the valve opens faster, but this time due to a greater force that pushes the armature and poppet back. The gas profile also gets broader as the poppet retract further back and takes longer to retreat into the nozzle.

When investigating the gas profile at lower temperatures with the home-made driver, the valve behaviour was even more sensitive with even a few volts or microsecond changes leading to dramatic changes in the gas profile.

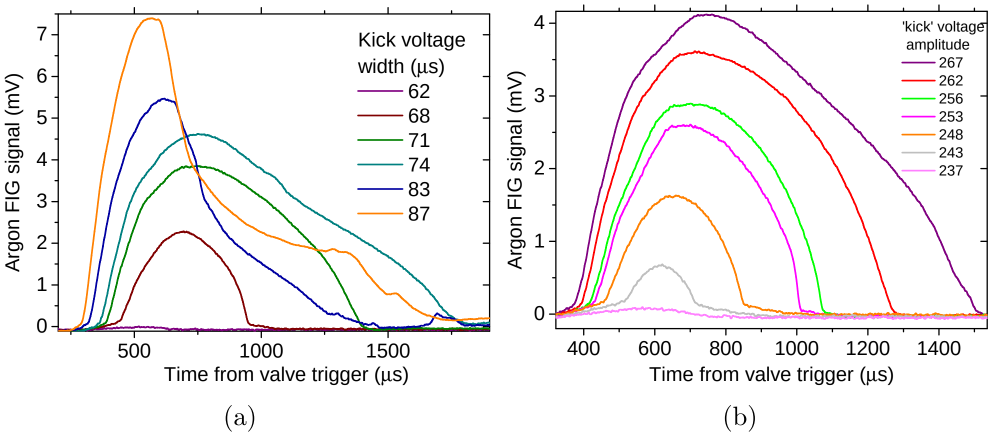

(a) (b)

Figure A.2: Argon FIG signal showing the gas profile using the home-made driver at a hold voltage pulse length of 230 μs at a) different kick voltage widths using an amplitude of 236 V, and b) for different amplitudes of the kick voltage pulse using a kick voltage pulse length 64 μs.

The background pressures in the source chamber were too high for a clean supersonic expansion, thus it was decided to stick to the IOTA-ONE driver.

Appendix B

Voltage Follower

Our MCP has high output input impedance ($1\,\mathrm{M}\Omega$). If we directly connect the output of MCP to the BNC (characteristic impedance $50,\Omega$ or $75\,\Omega$), the acquired signal would be reduced by a factor of 5×10^{-5} $(50/(1000000 + 50))$ because of the voltage divider. This is illustrated in figure B.1 a.

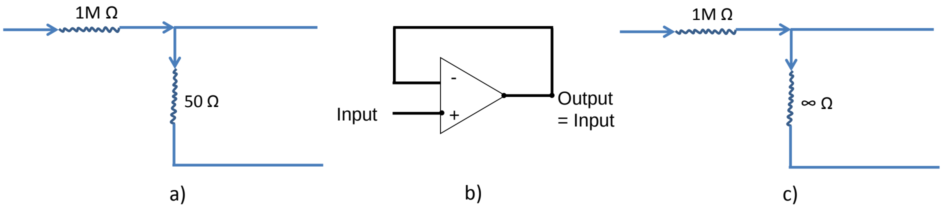

Figure B.1: a) The high output impedance of the MCP connected to the low impedance of the signal BNC cable which divides the voltage. b) Buffer amplifier schematic diagram. c) The high output impedance of the MCP connected to the high impedance of the input of the amplifier.

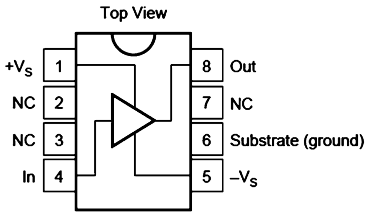

Figure B.2: Pin configuation of the buffer amplifier. Taken from data sheet of the high speed buffer amplifier (*Burr Brown, OPA633*).

A simple solution to this is the use of a voltage follower (also called buffer amplifier with gain 1), as shown in figure B.1 b. An operational amplifier

(OPAMP) has high input impedance (ideally infinity) and low out impedance (ideally zero). Therefore, if a voltage follower is connected between the MCP and the BNC cable, one can get [$\infty/(1000000 + \infty) = 1$] the entire MCP output.

Appendix C

Detailed FIG Drawings

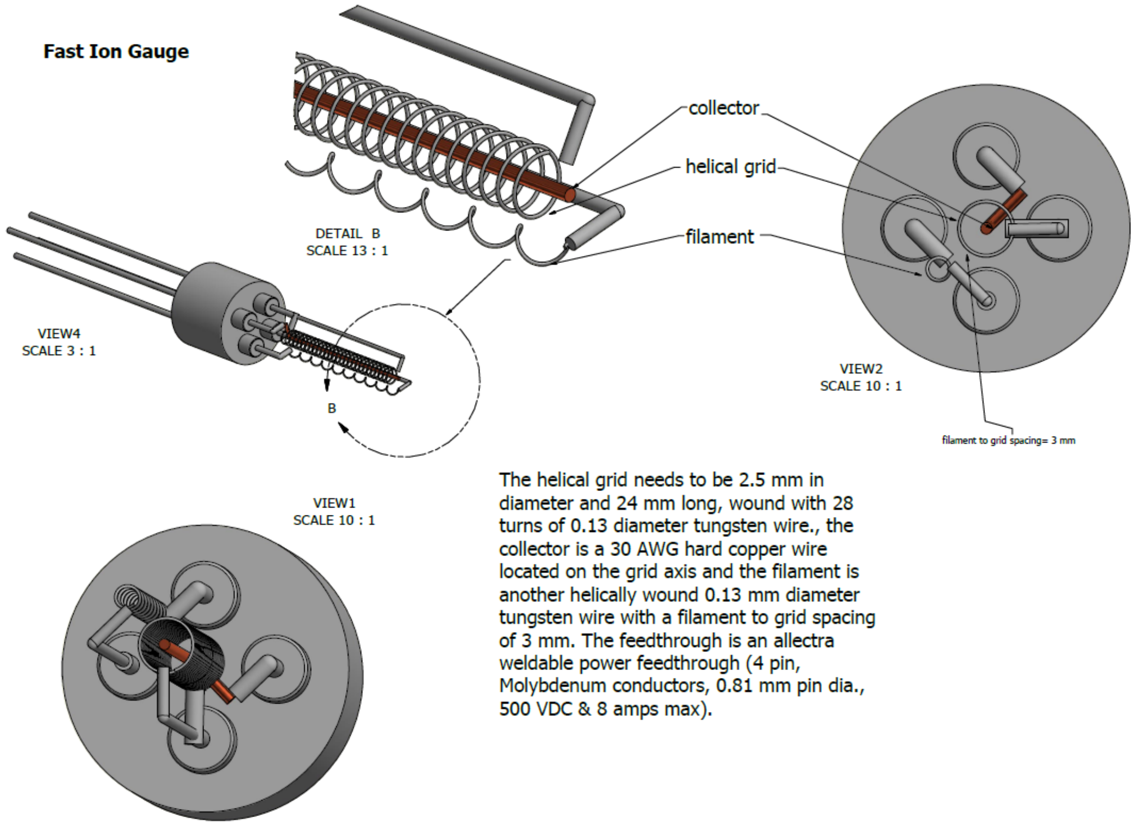

The helical grid needs to be 2.5 mm in diameter and 24 mm long, wound with 28 turns of 0.13 diameter tungsten wire., the collector is a 30 AWG hard copper wire located on the grid axis and the filament is another helically wound 0.13 mm diameter tungsten wire with a filament to grid spacing of 3 mm. The feedthrough is an allectra weldable power feedthrough (4 pin, Molybdenum conductors, 0.81 mm pin dia., 500 VDC & 8 amps max).

Figure C.1: Detailed drawing of the FIG.

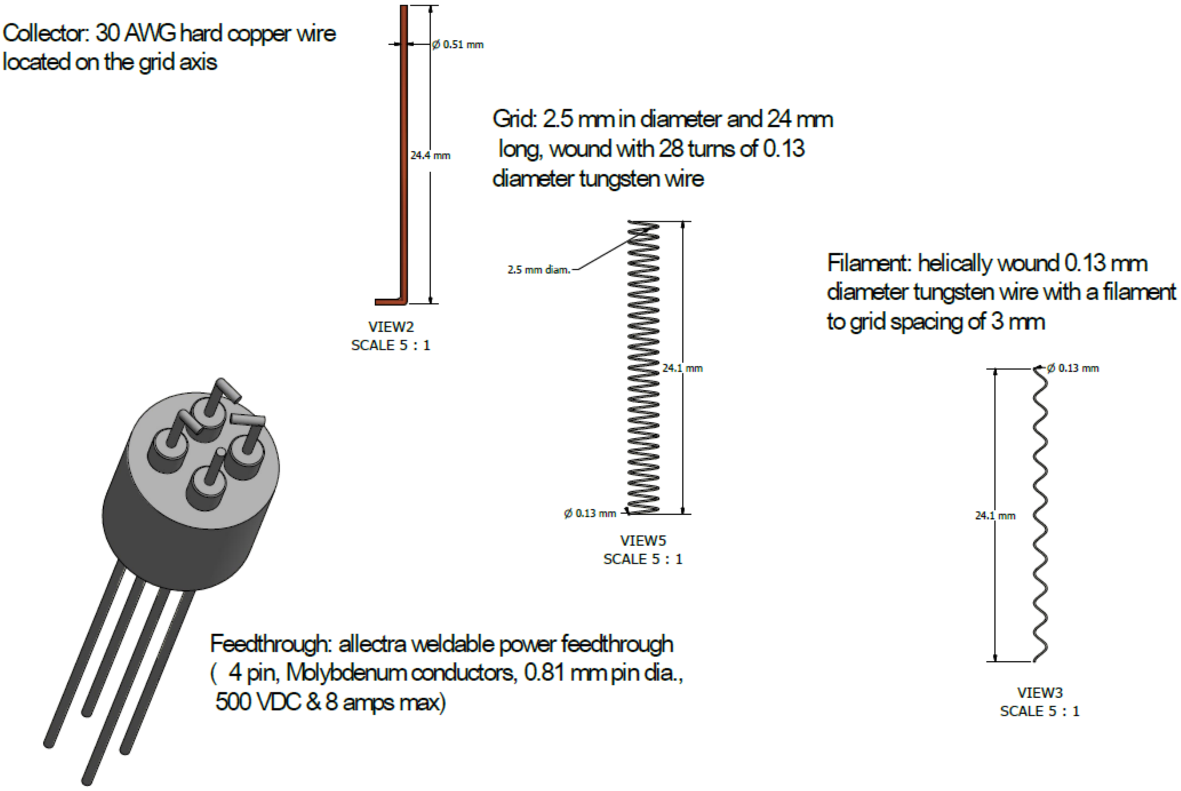

Collector: 30 AWG hard copper wire located on the grid axis

Grid: 2.5 mm in diameter and 24 mm long, wound with 28 turns of 0.13 diameter tungsten wire

Filament: helically wound 0.13 mm diameter tungsten wire with a filament to grid spacing of 3 mm

Feedthrough: allectra weldable power feedthrough (4 pin, Molybdenum conductors, 0.81 mm pin dia., 500 VDC & 8 amps max)

Figure C.2: Detailed drawing of the FIG.

Appendix D

Decelerator Design

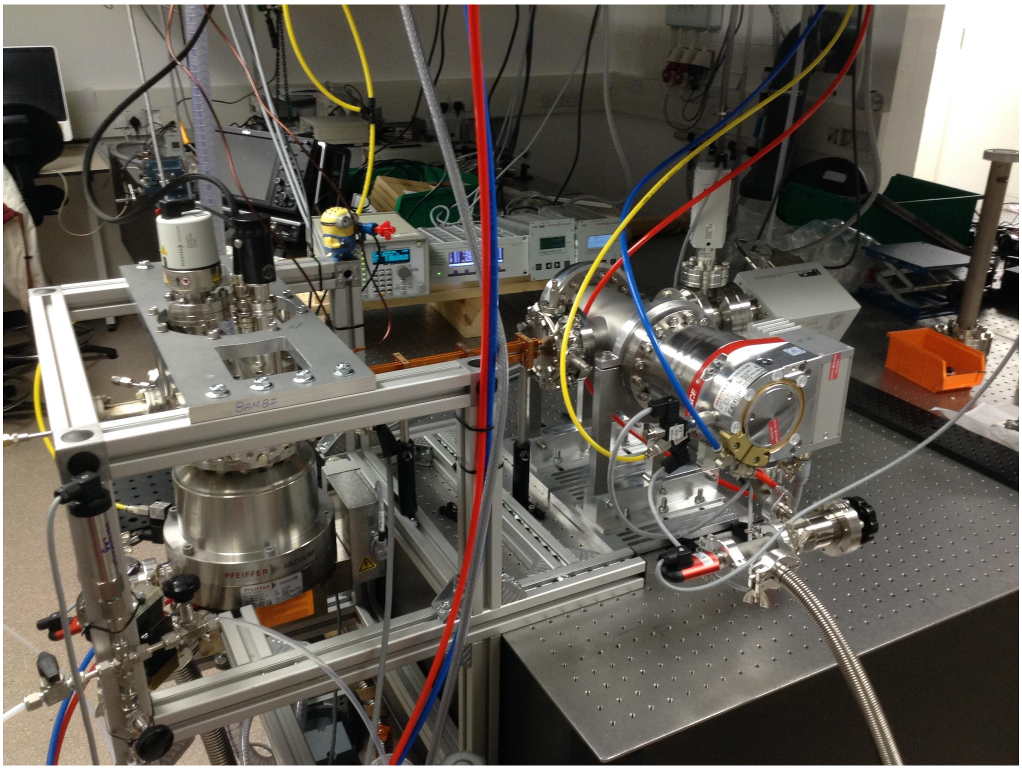

Figure D.1: Photograph of the decelerator vacuum system from three different angles.

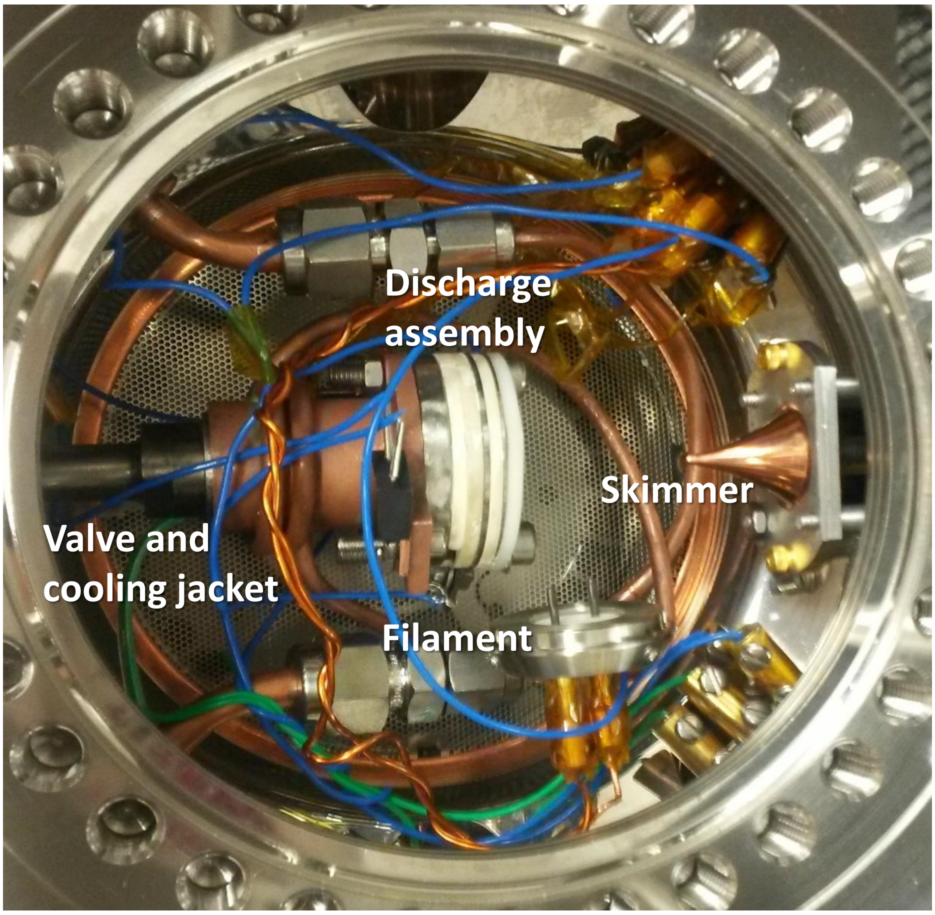

Figure D.2: A photograph showing the inside of the compact spherical-octagon source chamber, showing the valve and discharge assembly, the skimmer with its orifice positioned at about 2 cm downstream from the source. The cooling jacket is wrapped around the valve body, with liquid nitrogen fed through the copper tubing through arms that are bend at a certain radius. The discharge-stabilising filament is positioned about 1 cm off the molecular beam axis.

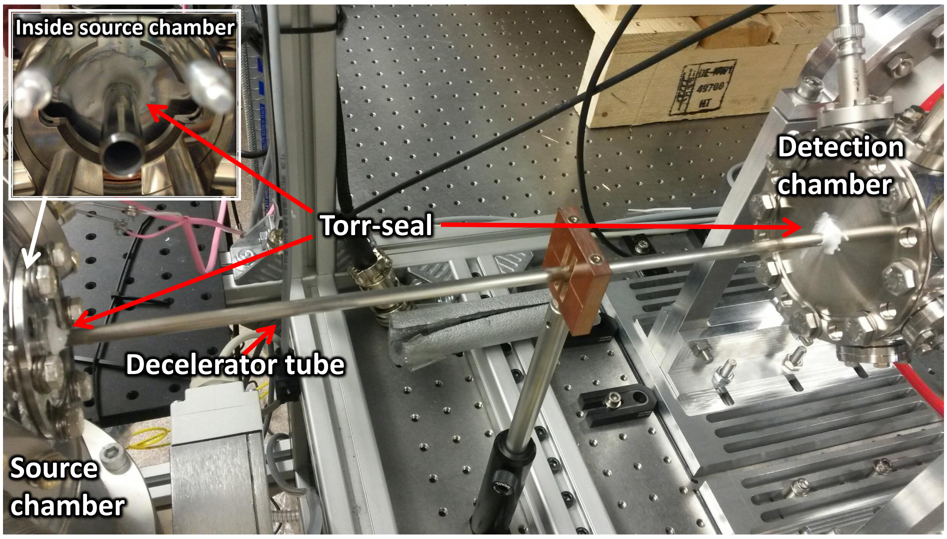

Figure D.3: A photograph showing how the decelerator tube, which is under vacuum connects the source and detection chambers together. At each end there is a thin flange with a hole of I.D. 6.35 mm to allow the tube to slide in. Torr-Seal was then used to fix the tube and form a secure vacuum seal down to pressures as low as $1{\times}10^{-8}$ mbar. The clamp holding the tube ensures the correct positioning of the tube until the Torr-Seal sets and hardens. The total tube length is 350 mm, and the separation between the two thin flanges is 317 mm.

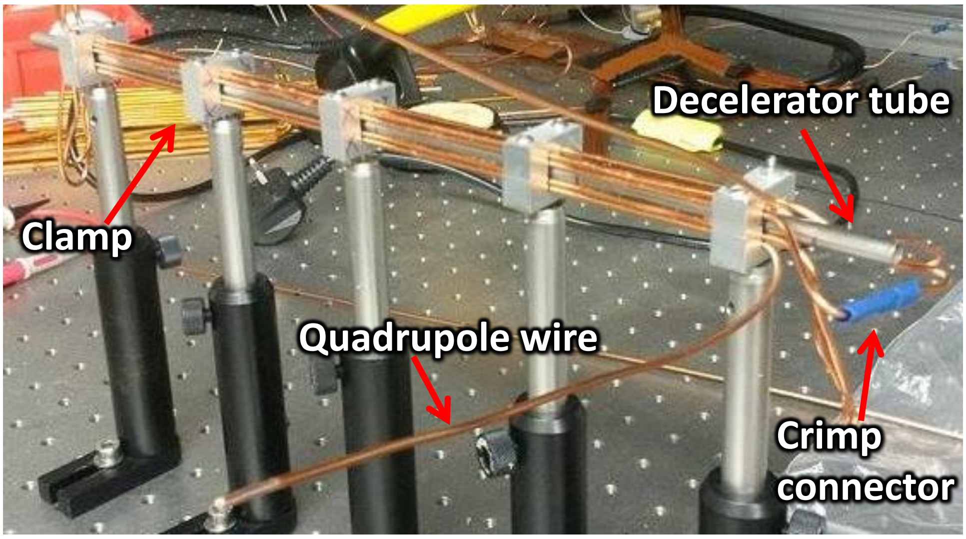

Figure D.4: A photograph showing the setup used in one of the attempts made to wind the quadrupole guide using the designed clamps in such a way that the four pairs of wires are positioned correctly around the decelerator tube, which is also held by the clamp.

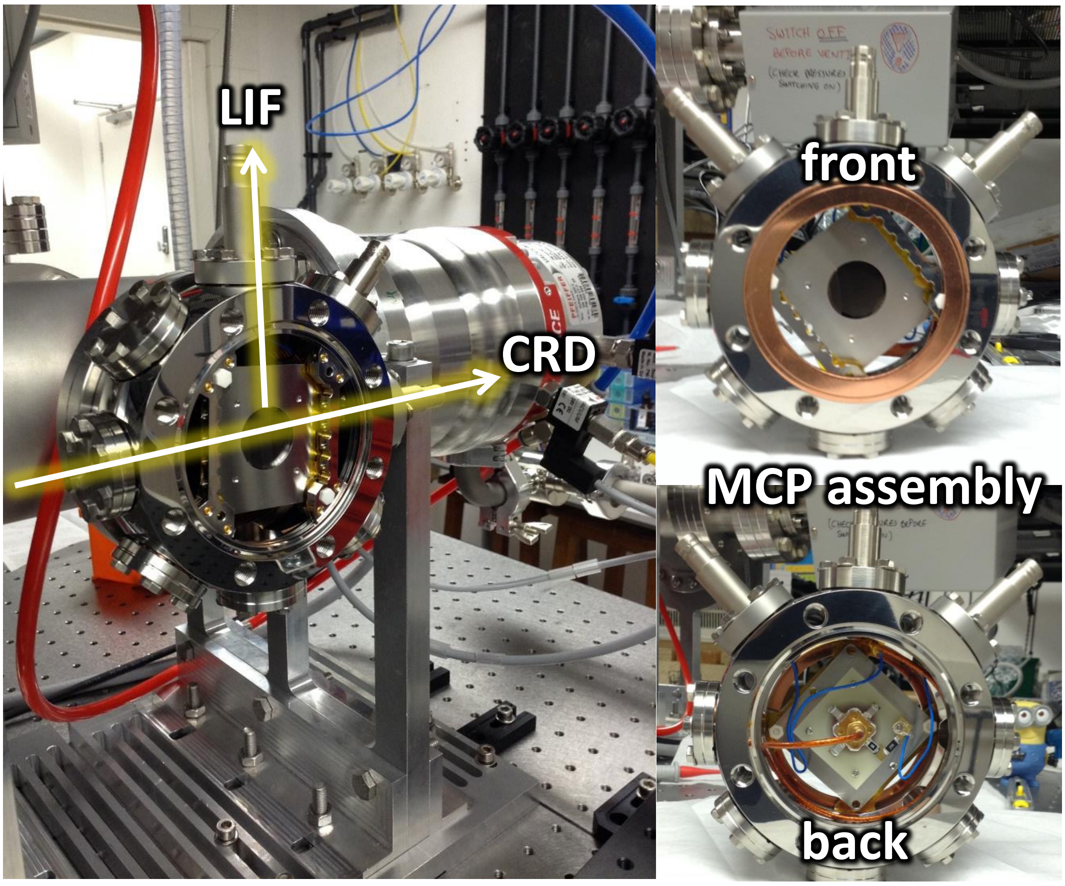

Figure D.5: Photographs of the detection chamber. Left: side view of the spherical octagon as it is mounted on the 4-way cross without the thin flange where the LIF and CRD axis are indicated by arrows. Top right: front view of the spherical octagon showing the MCP active area in black. Bottom right: back view of the spherical octagon showing the back of the MCP-assembly with the high-voltage, earth wires and the SMA cable for the MCP signal.

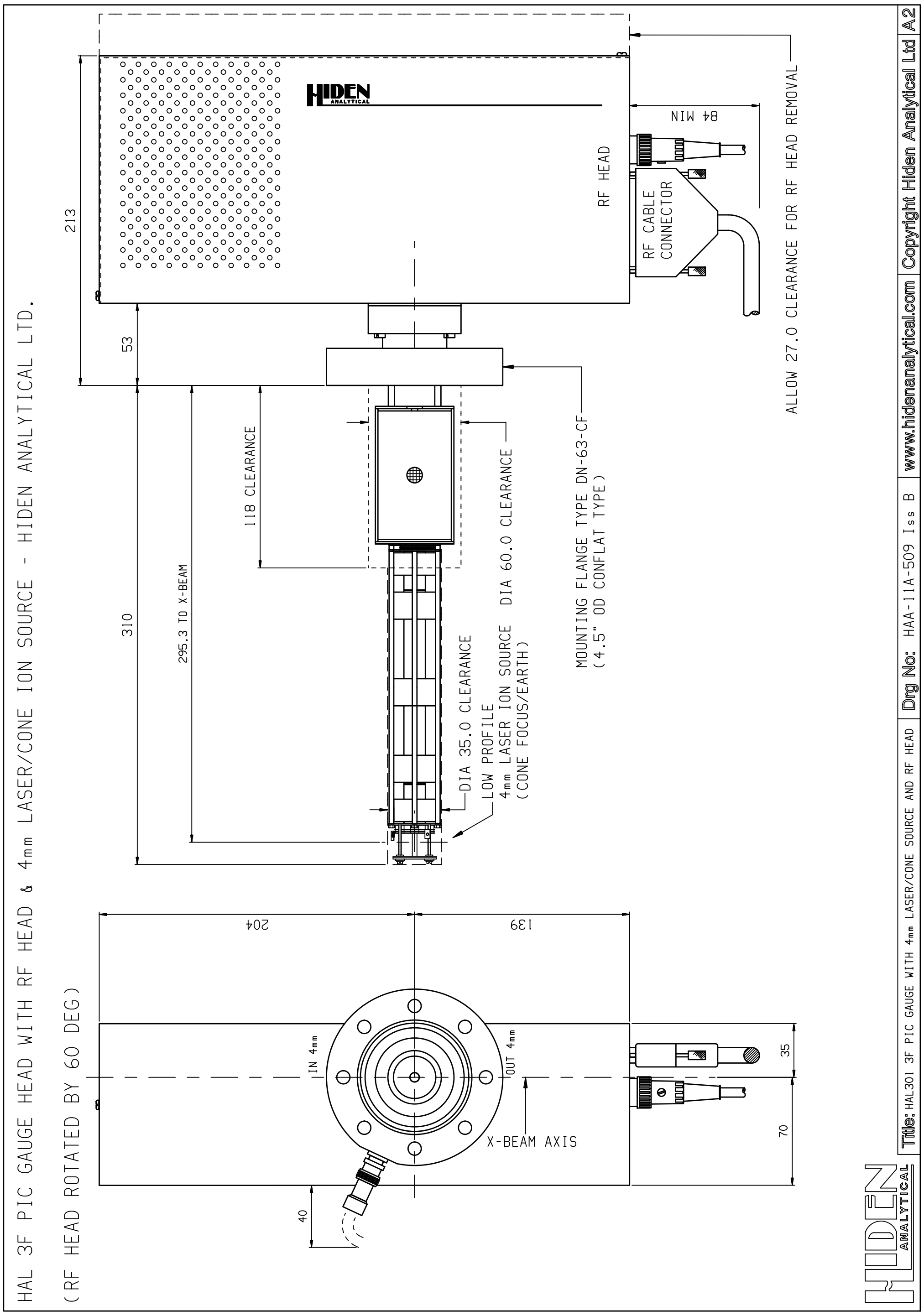

Figure D.6: A schematic diagram of our custom-made quadrupole mass spectrometer which includes a 4 mm diameter hole for laser ionization. Drawing made by Hiden.

Coil Description	Resistance (mΩ)	Inductance (μH)	Time constant (μs)	Estimated Peak Current (A)
Coil 1 phase 1, crimped connections	447	26.8	60.1	604
Coil 1 phase 1, flattened	484	31.0	64.1	522
Coil 1 phase 2, soldered joints	632	42.1	66.6	387
Coil 2 phase 1, Ulrich style wiring	468	38.4	82.2	438
Coil 2 phase 2, blue crimps	471	37.5	79.6	447
Coil 2 phase 3, red crimps	429	30.5	71.0	540
Coil 2 phase 4, shorten red crimps	421	28.5	67.8	573
Coil 2 phase 1, extra resistance	487	28.8	59.2	554

Figure D.7: Top: photographs of the different attempts made for connecting the wires together to test different types of connections. Bottom: the resistance, inductance, time constant, and the estimated current achieved using these values for the different types of connections.

Bibliography

[1] D. Wineland, R. Drullinger, and F. Walls, *Radiation-Pressure Cooling of Bound Resonant Absorbers*, Physical Review Letters **40**, 1639 (1978).

[2] M. Kasevich, E. Riis, S. Chu, and R. DeVoe, *RF spectroscopy in an atomic fountain*, Physical Review Letters **63**, 612 (1989).

[3] M. Greiner, O. Mandel, T. Esslinger, T. W. Hänsch, and I. Bloch, *Quantum phase transition from a superfluid to a Mott insulator in a gas of ultracold atoms*, Nature **415**, 39 (2002).

[4] M. H. Anderson, J. R. Ensher, M. R. Matthews, C. E. Wieman, and E. A. Cornell, *Observation of Bose-Einstein Condensation in a Dilute Atomic Vapor*, Science **269**, 198 (1995).

[5] L. D. Carr, D. DeMille, R. V. Krems, and J. Ye, *Cold and ultracold molecules: science, technology and applications*, New Journal of Physics **11**, 055049 (2009).

[6] B. K. Stuhl, M. T. Hummon, and J. Ye, *Cold State-Selected Molecular Collisions and Reactions*, Annual Review of Physical Chemistry **65**, 501 (2014).

[7] H. R. Thorsheim, J. Weiner, and P. S. Julienne, *Laser-induced photoassociation of ultracold sodium atoms*, Physical Review Letters **58**, 2420 (1987).

[8] E. R. I. Abraham, N. W. M. Ritchie, W. I. McAlexander, and R. G. Hulet, *Photoassociative spectroscopy of long-range states of ultracold* $^6Li_2$ *and* $^7Li_2$, The Journal of Chemical Physics **103**, 7773 (1995).

[9] A. Fioretti, D. Comparat, A. Crubellier, O. Dulieu, F. Masnou-Seeuws, and P. Pillet, *Formation of Cold* Cs_2 *Molecules through Photoassocia-*

tion, Physical Review Letters **80**, 4402 (1998).

[10] M. D. Rosa, *Laser-cooling molecules*, The European Physical Journal D **31**, 395 (2004).

[11] B. K. Stuhl, B. C. Sawyer, D. Wang, and J. Ye, *Magneto-optical Trap for Polar Molecules*, Physical Review Letters **101**, 243002 (2008).

[12] E. S. Shuman, J. F. Barry, and D. Demille, *Laser cooling of a diatomic molecule*, Nature **467**, 820 (2010).

[13] D. J. McCarron, E. B. Norrgard, M. H. Steinecker, and D. DeMille, *Improved magneto-optical trapping of a diatomic molecule*, New Journal of Physics **17**, 1 (2015).

[14] M. T. Hummon, M. Yeo, B. K. Stuhl, A. L. Collopy, Y. Xia, and J. Ye, *2D Magneto-Optical Trapping of Diatomic Molecules*, Physical Review Letters **110**, 143001 (2013).

[15] M. Yeo, M. T. Hummon, A. L. Collopy, B. Yan, B. Hemmerling, E. Chae, J. M. Doyle, and J. Ye, *Rotational State Microwave Mixing for Laser Cooling of Complex Diatomic Molecules*, Physical Review Letters **114**, 223003 (2015).

[16] V. Zhelyazkova, A. Cournol, T. E. Wall, A. Matsushima, J. J. Hudson, E. a. Hinds, M. R. Tarbutt, and B. E. Sauer, *Laser cooling and slowing of CaF molecules*, Physical Review A - Atomic, Molecular, and Optical Physics **89**, 1 (2014).

[17] E. A. Donley, N. R. Claussen, S. T. Thompson, and C. E. Wieman, *Atom-molecule coherence in a Bose-Einstein condensate*, Nature **417**, 529 (2002).

[18] J. Cubizolles, T. Bourdel, S. J. J. M. F. Kokkelmans, G. V. Shlyapnikov, and C. Salomon, *Production of Long-Lived Ultracold Li_2 Molecules from a Fermi Gas*, Physical Review Letters **91**, 240401 (2003).

[19] S. Jochim, M. Bartenstein, A. Altmeyer, G. Hendl, C. Chin, J. H. Denschlag, and R. Grimm, *Pure Gas of Optically Trapped Molecules Created from Fermionic Atoms*, Physical Review Letters **91**, 240402 (2003).

[20] K. Xu, T. Mukaiyama, J. R. Abo-Shaeer, J. K. Chin, D. E. Miller, and

W. Ketterle, *Formation of Quantum-Degenerate Sodium Molecules*, Physical Review Letters **91**, 210402 (2003).

[21] P. K. Molony, P. D. Gregory, Z. Ji, B. Lu, M. P. Köppinger, C. R. Le Sueur, C. L. Blackley, J. M. Hutson, and S. L. Cornish, *Creation of Ultracold* $^{87}Rb^{133}Cs$ *Molecules in the Rovibrational Ground State*, Physical Review Letters **113**, 255301 (2014).

[22] J. K. Webb, V. V. Flambaum, C. W. Churchill, M. J. Drinkwater, and J. D. Barrow, *Search for Time Variation of the Fine Structure Constant*, Physical Review Letters **82**, 884 (1999).

[23] C. G. Parthey *et al.*, *Improved Measurement of the Hydrogen 1S-2S Transition Frequency*, Physical Review Letters **107**, 203001 (2011).

[24] A. Libson, S. T. Bannerman, R. J. Clark, T. R. Mazur, and M. G. Raizen, *The atomic coilgun and single-photon cooling*, Hyperfine Interactions **212**, 203 (2012).

[25] E. Hinds, M. Tarbutt, J. Hudson, and B. Sauer, *Preparation and Manipulation of Molecules for Fundamental Physics Tests*, in *Cold Molecules*, p. 22, CRC Press, 2009.

[26] J. J. Hudson, D. M. Kara, I. J. Smallman, B. E. Sauer, M. R. Tarbutt, and E. a. Hinds, *Improved measurement of the shape of the electron*, Nature **473**, 493 (2011).

[27] N. E. Bulleid, R. J. Hendricks, E. A. Hinds, S. A. Meek, G. Meijer, A. Osterwalder, and M. R. Tarbutt, *Traveling-wave deceleration of heavy polar molecules in low-field-seeking states*, Physical Review A **86**, 021404 (2012).

[28] J. Veldhoven, J. Kupper, H. L. Bethlem, B. Sartakov, A. J. A. Roij, and G. Meijer, *Decelerated molecular beams for high-resolution spectroscopy*, The European Physical Journal D **31**, 337 (2004).

[29] A. B. Henson, S. Gersten, Y. Shagam, J. Narevicius, and E. Narevicius, *Observation of resonances in Penning ionization reactions at sub-kelvin temperatures in merged beams*, Science (New York, N.Y.) **338**, 234 (2012).

[30] I. R. Sims and I. W. M. Smith, *Gas-Phase Reactions and Energy Transfer at Very Low Temperatures*, Annual Review of Physical Chemistry

46, 109 (1995).

[31] J. J. Gilijamse, S. Hoekstra, S. Y. T. van de Meerakker, G. C. Groenenboom, and G. Meijer, *Near-Threshold Inelastic Collisions Using Molecular Beams with a Tunable Velocity*, Science **313**, 1617 (2006).

[32] B. C. Sawyer, B. K. Stuhl, D. Wang, M. Yeo, and J. Ye, *Molecular Beam Collisions with a Magnetically Trapped Target*, Physical Review Letters **101**, 203203 (2008).

[33] M. Kirste, L. Scharfenberg, J. Kłos, F. Lique, M. H. Alexander, G. Meijer, and S. Y. T. van de Meerakker, *Low-energy inelastic collisions of OH radicals with He atoms and* D_2 *molecules*, Physical Review A **82**, 042717 (2010).

[34] G. Quéméner and P. S. Julienne, *Ultracold Molecules under Control!*, Chemical Reviews **112**, 4949 (2012).

[35] M. Schnell and G. Meijer, *Cold Molecules: Preparation, Applications, and Challenges*, Angewandte Chemie International Edition **48**, 6010 (2009).

[36] M. Lemeshko, R. V. Krems, J. M. Doyle, and S. Kais, *Manipulation of molecules with electromagnetic fields*, Molecular Physics **111**, 1648 (2013).

[37] G. Meijer, *Cold Molecules*, in *CHEMPHYSCHEM*, edited by W. Stwalley, R. Krems, and B. Friedrich, volume 3, pp. 495–501, CRC Press, 2009.

[38] R. P. Feynman, *Simulating physics with computers*, International Journal of Theoretical Physics **21**, 467 (1982).

[39] A. Micheli, G. K. Brennen, and P. Zoller, *A toolbox for lattice-spin models with polar molecules*, Nature Physics **2**, 341 (2006).

[40] M. Lewenstein, A. Sanpera, V. Ahufinger, B. Damski, A. Sen(De), and U. Sen, *Ultracold atomic gases in optical lattices: mimicking condensed matter physics and beyond*, Advances in Physics **56**, 243 (2007).

[41] G. Pupillo, H. P. Büchler, A. Micheli, and P. Zoller, *Condensed Matter Physics with Cold Polar Molecules*, arXiv:0805.1896v1 [cond-mat.other] (2009).

[42] E. Hinds, *Private communication, MMQA meeting*, 2012.

[43] S. M. Skoff, R. J. Hendricks, C. D. J. Sinclair, J. J. Hudson, D. M. Segal, B. E. Sauer, E. a. Hinds, and M. R. Tarbutt, *Diffusion, thermalization, and optical pumping of YbF molecules in a cold buffer-gas cell*, Physical Review A **83**, 023418 (2011).

[44] N. E. Bulleid, S. M. Skoff, R. J. Hendricks, B. E. Sauer, E. a. Hinds, and M. R. Tarbutt, *Characterization of a cryogenic beam source for atoms and molecules*, Physical Chemistry Chemical Physics **15**, 12299 (2013).

[45] M. Tarbutt, *Private communication, MMQA meeting*, 2013.

[46] J. F. Barry, D. J. McCarron, E. B. Norrgard, M. H. Steinecker, and D. DeMille, *Magneto-optical trapping of a diatomic molecule*, Nature **512**, 286 (2014).

[47] P. Barletta, J. Tennyson, and P. Barker, *Creating ultracold molecules by collisions with ultracold rare-gas atoms in an optical trap*, Physical Review A **78**, 052707 (2008).

[48] D. DeMille, D. R. Glenn, and J. Petricka, *Microwave traps for cold polar molecules*, European Physical Journal D **31**, 375 (2004).

[49] D. P. Dunseith, S. Truppe, R. J. Hendricks, B. E. Sauer, E. a. Hinds, and M. R. Tarbutt, *A high quality, efficiently coupled microwave cavity for trapping cold molecules*, Journal of Physics B: Atomic, Molecular and Optical Physics **48**, 045001 (2014).

[50] J. Lim, M. D. Frye, J. M. Hutson, and M. R. Tarbutt, *Modeling sympathetic cooling of molecules by ultracold atoms*, Physical Review A **92**, 053419 (2015).

[51] B. K. Stuhl, M. T. Hummon, M. Yeo, G. Quéméner, J. L. Bohn, and J. Ye, *Evaporative cooling of the dipolar hydroxyl radical*, Nature **492**, 396 (2012).

[52] H. Bethlem, G. Berden, and G. Meijer, *Decelerating Neutral Dipolar Molecules*, Physical Review Letters **83**, 1558 (1999).

[53] S. D. Hogan, M. Motsch, and F. Merkt, *Deceleration of supersonic beams using inhomogeneous electric and magnetic fields*, Physical Chemistry Chemical Physics **13**, 18705 (2011).

[54] H. L. Bethlem, G. Berden, F. M. H. Crompvoets, R. T. Jongma,

A. J. A. van Roij, and G. Meijer, *Electrostatic trapping of ammonia molecules*, Nature **406**, 491 (2000).

[55] L. Scharfenberg, H. Haak, G. Meijer, and S. Y. T. van de Meerakker, *Operation of a Stark decelerator with optimum acceptance*, Physical Review A **79**, 023410 (2009).

[56] H. L. Bethlem, A. J. A. van Roij, R. T. Jongma, and G. Meijer, *Alternate Gradient Focusing and Deceleration of a Molecular Beam*, Physical Review Letters **88**, 133003 (2002).

[57] S. Meek, H. Bethlem, H. Conrad, and G. Meijer, *Trapping Molecules on a Chip in Traveling Potential Wells*, Physical Review Letters **100**, 153003 (2008).

[58] A. Osterwalder, S. A. Meek, G. Hammer, H. Haak, and G. Meijer, *Deceleration of neutral molecules in macroscopic traveling traps*, Physical Review A **81**, 051401 (2010).

[59] R. Fulton, A. I. Bishop, and P. F. Barker, *Optical Stark Decelerator for Molecules*, Physical Review Letters **93**, 243004 (2004).

[60] S. D. Hogan, *Rydberg-Stark deceleration of atoms and molecules*, EPJ Techniques and Instrumentation **3**, 2 (2016).

[61] S. Merz, N. Vanhaecke, W. Jäger, M. Schnell, and G. Meijer, *Decelerating molecules with microwave fields*, Physical Review A - Atomic, Molecular, and Optical Physics **85**, 6 (2012).

[62] E. Narevicius, C. G. Parthey, a. Libson, J. Narevicius, I. Chavez, U. Even, and M. G. Raizen, *An atomic coilgun: using pulsed magnetic fields to slow a supersonic beam*, New Journal of Physics **9**, 358 (2007).

[63] E. Narevicius, A. Libson, C. G. Parthey, I. Chavez, J. Narevicius, U. Even, and M. G. Raizen, *Stopping Supersonic Beams with a Series of Pulsed Electromagnetic Coils: An Atomic Coilgun*, Physical Review Letters **100**, 093003 (2008).

[64] E. Narevicius, A. Libson, C. Parthey, I. Chavez, J. Narevicius, U. Even, and M. Raizen, *Stopping supersonic oxygen with a series of pulsed electromagnetic coils: A molecular coilgun*, Physical Review A **77**, 051401 (2008).

[65] E. Lavert-Ofir, L. David, A. B. Henson, S. Gersten, J. Narevicius, and E. Narevicius, *Stopping paramagnetic supersonic beams: the advantage of a co-moving magnetic trap decelerator*, Physical Chemistry Chemical Physics **13**, 18948 (2011).

[66] N. Akerman, M. Karpov, L. David, E. Lavert-Ofir, J. Narevicius, and E. Narevicius, *Simultaneous deceleration of atoms and molecules in a supersonic beam*, New Journal of Physics **17**, 065015 (2015).

[67] N. Vanhaecke, U. Meier, M. Andrist, B. H. Meier, and F. Merkt, *Multistage Zeeman deceleration of hydrogen atoms*, Physical Review A **75**, 031402 (2007).

[68] S. Hogan, D. Sprecher, M. Andrist, N. Vanhaecke, and F. Merkt, *Zeeman deceleration of H and D*, Physical Review A **76**, 023412 (2007).

[69] S. D. Hogan, A. W. Wiederkehr, M. Andrist, H. Schmutz, and F. Merkt, *Slow beams of atomic hydrogen by multistage Zeeman deceleration*, Journal of Physics B: Atomic, Molecular and Optical Physics **41**, 081005 (2008).

[70] S. D. Hogan, A. W. Wiederkehr, H. Schmutz, and F. Merkt, *Magnetic Trapping of Hydrogen after Multistage Zeeman Deceleration*, Physical Review Letters **101**, 143001 (2008).

[71] A. W. Wiederkehr, S. D. Hogan, B. Lambillotte, M. Andrist, H. Schmutz, J. Agner, Y. Salathé, and F. Merkt, *Trapping deuterium atoms*, Physical Review A **81**, 021402 (2010).

[72] A. W. Wiederkehr, M. Motsch, S. D. Hogan, M. Andrist, H. Schmutz, B. Lambillotte, J. a. Agner, and F. Merkt, *Multistage Zeeman deceleration of metastable neon*, The Journal of Chemical Physics **135**, 214202 (2011).

[73] A. Wiederkehr, H. Schmutz, M. Motsch, and F. Merkt, *Velocity-tunable slow beams of cold* O_2 *in a single spin-rovibronic state with full angular-momentum orientation by multistage Zeeman deceleration*, Molecular Physics **110**, 1807 (2012).

[74] M. Motsch, P. Jansen, J. A. Agner, H. Schmutz, and F. Merkt, *Slow and velocity-tunable beams of metastable* He_2 *by multistage Zeeman deceleration*, Physical Review A **89**, 043420 (2014).

[75] A. Trimeche, M. N. Bera, J. P. Cromières, J. Robert, and N. Vanhaecke, *Trapping of a supersonic beam in a traveling magnetic wave*, The European Physical Journal D **65**, 263 (2011).

[76] T. Momose, Y. Liu, S. Zhou, P. Djuricanin, and D. Carty, *Manipulation of translational motion of methyl radicals by pulsed magnetic fields*, Phys. Chem. Chem. Phys. **15**, 1772 (2013).

[77] Y. Liu, S. Zhou, W. Zhong, P. Djuricanin, and T. Momose, *One-dimensional confinement of magnetically decelerated supersonic beams of O_2 molecules*, Physical Review A **91**, 021403 (2015).

[78] K. Dulitz, M. Motsch, N. Vanhaecke, and T. P. Softley, *Getting a grip on the transverse motion in a Zeeman decelerator*, The Journal of Chemical Physics **140**, 104201 (2014).

[79] K. Dulitz, A. Tauschinsky, and T. P. Softley, *Zeeman deceleration of electron-impact-excited metastable helium atoms*, New Journal of Physics **17**, 35005 (2015).

[80] A. W. Wiederkehr, S. D. Hogan, and F. Merkt, *Phase stability in a multistage Zeeman decelerator*, Physical Review A **82**, 043428 (2010).

[81] J. Liouville, *Mémoire sur la classification des transcendantes, et sur l'impossibilité d'exprimer les racines de certaines équations en fonction finie explicite des coefficients*, Journal de Mathématiques Pures et Appliquées , 56 (1837).

[82] A. Mizouri, L. Z. Deng, J. S. Eardley, N. H. Nahler, E. Wrede, and D. Carty, *Absolute density measurement of SD radicals in a supersonic jet at the quantum-noise-limit*, Physical Chemistry Chemical Physics **15**, 19575 (2013).

[83] D. R. Miller, *Atomic and Molecular Beam Methods: Volume 1*, pp. 14–53, Oxford University Press, USA, 1988.

[84] M. D. Morse, *Atomic, Molecular, and Optical Physics: Atoms and Molecules, volume 29*, pp. 21–47, Academic Press, 1996.

[85] S. DePaul, D. Pullman, and B. Friedrich, *A pocket model of seeded supersonic beams*, The Journal of Physical Chemistry **97**, 2167 (1993).

[86] J. B. Anderson and J. B. Fenn, *Velocity Distributions in Molecular Beams from Nozzle Sources*, Physics of Fluids **8**, 780 (1965).

[87] W. R. Gentry and C. F. Giese, *Ten-microsecond pulsed molecular beam source and a fast ionization detector.*, The Review of scientific instruments **49**, 595 (1978).

[88] D. Irimia, D. Dobrikov, R. Kortekaas, H. Voet, D. A. van den Ende, W. A. Groen, and M. H. M. Janssen, *A short pulse (7μs FWHM) and high repetition rate (dc-5 kHz) cantilever piezovalve for pulsed atomic and molecular beams*, Review of Scientific Instruments **80**, 113303 (2009).

[89] C. E. Otis and P. M. Johnson, *A simple pulsed valve for use in supersonic nozzle experiments*, Review of Scientific Instruments **51**, 1128 (1980).

[90] M. G. Liverman, S. M. Beck, D. L. Monts, and R. E. Smalley, *Fluorescence excitation spectrum of the* $^1A_u(n\Pi) \leftarrow^1 A_g(0-0)$ *band of oxalyl fluoride in a pulsed supersonic free jet*, The Journal of Chemical Physics **70**, 192 (1979).

[91] A. Auerbach and R. McDiarmid, *Modified pulsed valve for supersonic jet applications*, Review of Scientific Instruments **51**, 1273 (1980).

[92] R. A. Smith, T. Ditmire, and J. W. G. Tisch, *Characterization of a cryogenically cooled high-pressure gas jet for laser/cluster interaction experiments*, Review of Scientific Instruments **69**, 3798 (1998).

[93] L. Abad, D. Bermejo, V. J. Herrero, J. Santos, and I. Tanarro, *Performance of a solenoid-driven pulsed molecular-beam source*, Review of Scientific Instruments **66**, 3826 (1995).

[94] N. E. Bulleid, *Slow, cold beams of polar molecules for precision measurements*, PhD thesis, Imperial College London, 2013.

[95] M. C. V. Beek and J. J. Meulen, *An intense pulsed electrical discharge source for OH molecular beams*, **337**, 237 (2001).

[96] *Prepared for IAU Symposium 210 (Uppsala Sweden, June 2002), Ionization Energies (eV) of Atoms and Ions*, https://dept.astro.lsa.umich.edu/∼cowley/ionen.htm .

[97] E. E. Muschlitz, *Metastable Atoms and Molecules: Measurements of their unusual properties in highly excited states reveal a new area for investigation*, Science **159**, 599 (1968).

[98] S. B. Nagel, C. E. Simien, S. Laha, P. Gupta, V. S. Ashoka, and T. C. Killian, *Magnetic trapping of metastable* $^3P_2$ *atomic strontium*, Physical Review A **67**, 011401 (2003).

[99] S. Davis, D. T. Anderson, G. Duxbury, and D. J. Nesbitt, *Jet-cooled molecular radicals in slit supersonic discharges: Sub-Doppler infrared studies of methyl radical*, The Journal of Chemical Physics **107**, 5661 (1997).

[100] T. Halfmann, J. Koensgen, and K. Bergmann, *A source for a high-intensity pulsed beam of metastable helium atoms*, Measurement Science and Technology **11**, 1510 (2000).

[101] J. Ladislas Wiza, *Microchannel plate detectors*, Nuclear Instruments and Methods **162**, 587 (1979).

[102] H. Lewandowski, E. R. Hudson, J. Bochinski, and J. Ye, *A pulsed, low-temperature beam of supersonically cooled free radical OH molecules*, Chemical Physics Letters **395**, 53 (2004).

[103] W. Christen, T. Krause, B. Kobin, and K. Rademann, *Precision velocity measurements of pulsed supersonic jets*, The journal of physical chemistry. A **115**, 6997 (2011).

[104] W. Christen, *Stationary flow conditions in pulsed supersonic beams.*, The Journal of Chemical Physics **139**, 154202 (2013).

[105] J. B. Cross, *High repetition rate pulsed nozzle beam source*, Review of Scientific Instruments **53**, 38 (1982).

[106] D. Gerlich, G. Jerke, U. Muck, and U. Person, *Schnelles Ventil zur Erzeugung sehr kurzer Gasimpulse, 1990*, http://www.tu-chemnitz.de/physik/ ION/Technology .

[107] T. Udem, R. Holzwarth, and T. W. Hänsch, *Optical frequency metrology.*, Nature **416**, 233 (2002).

[108] D. L. Proctor, D. R. Albert, and H. F. Davis, *Improved piezoelectric actuators for use in high-speed pulsed valves*, Review of Scientific Instruments **81**, 023106 (2010).

[109] U. Even, J. Jortner, D. Noy, N. Lavie, and C. Cossart-Magos, *Cooling of large molecules below 1 K and He clusters formation*, The Journal of Chemical Physics **112**, 8068 (2000).

[110] M. N. Slipchenko, S. Kuma, T. Momose, and A. F. Vilesov, *Intense pulsed helium droplet beams*, Review of Scientific Instruments **73**, 3600 (2002).

[111] V. A. Baturin, A. Y. Karpenko, P. A. Litvinov, S. A. Pustovoitov, and I. I. Chemeris, *A Quick-Acting Pulsed Gas Valve for a Cluster-Beam Source*, Instruments and Experimental Techniques **47**, 417 (2004).

[112] T. Muller and P. H. Vaccaro, *Construction and characterization of a short pulse slit-jet source based upon the current loop-actuated design*, Review of Scientific Instruments **69**, 406 (1998).

[113] K. L. Saenger, *Pulsed molecular beams: A lower limit on pulse duration for fully developed supersonic expansions*, The Journal of Chemical Physics **75**, 2467 (1981).

[114] K. L. Saenger and J. B. Fenn, *On the time required to reach fully developed flow in pulsed supersonic free jets*, The Journal of Chemical Physics **79**, 6043 (1983).

[115] T. Li, Y. H. Chen, F. Y. C. Boey, and J. Ma, *High amplitude vibration of piezoelectric bending actuators*, Journal of Electroceramics **18**, 231 (2007).

[116] Q.-M. Wang, Q. Zhang, B. Xu, R. Liu, and L. E. Cross, *Nonlinear piezoelectric behavior of ceramic bending mode actuators under strong electric fields*, Journal of Applied Physics **86**, 3352 (1999).

[117] *Morgan Electroceramics*, http://www.morganelectroceramics.com .

[118] K. Luria, W. Christen, and U. Even, *Generation and propagation of intense supersonic beams.*, The journal of physical chemistry. A **115**, 7362 (2011).

[119] K. G. Vandervoort, R. K. Zasadzinski, G. G. Galicia, and G. W. Crabtree, *Full temperature calibration from 4 to 300 K of the voltage response of piezoelectric tube scanner PZT-5A for use in scanning tunneling microscopes*, Review of Scientific Instruments **64**, 896 (1993).

[120] G. K. Woodgate, *Elementary Atomic Structure*, Second ed. (Oxford University Press, 1980).

[121] NIST, *Energy Levels of Neutral Argon (Ar I)*, http://physics.nist.gov/PhysRefData/Handbook/Tables/argontable5.htm

.

[122] S. E. Sanders, O. R. Willis, N. H. Nahler, and E. Wrede, *Absolute absorption and fluorescence measurements over a dynamic range of 10^6 with cavity-enhanced laser-induced fluorescence*, arXiv:1308.1989 [physics.chem-ph] (2013).

[123] M. D. Wheeler, S. M. Newman, A. J. Orr-Ewing, and M. N. R. Ashfold, *Cavity ring-down spectroscopy*, Journal of the Chemical Society, Faraday Transactions **94**, 337 (1998).

[124] M. D. Wheeler, A. J. Orr-Ewing, and M. N. R. Ashfold, *Predissociation dynamics*, The Journal of Chemical Physics **107**, 7591 (1997).

[125] P. Zalicki and R. N. Zare, *Cavity ring-down spectroscopy for quantitative absorption measurements*, The Journal of Chemical Physics **102**, 2708 (1995).

[126] M. Kirste, *OH-NO Scattering at the Quantum Level*, PhD thesis, Fritz-Haber-Institut der Max-Planck-Gesellschaft, 2012.

[127] J. J. L. Spaanjaars, J. J. ter Meulen, and G. Meijer, *Relative predissociation rates of OH from combined cavity ring down -Laser-induced fluorescence measurements*, The Journal of Chemical Physics **107**, 2242 (1997).

[128] C. Bahrini, S. Douin, J. Rostas, and G. Taieb, *CRD and LIF spectra of the CaBr and CaI radicals*, Chemical Physics Letters **432**, 1 (2006).

[129] D. Tokaryk, A. Adam, and M. Slaney, *Cavity ring down laser spectroscopy of the transition of the* $\tilde{B}^2\Sigma^+ - \tilde{X}^2\Sigma^+$ *CaCCH*, Chemical Physics Letters **433**, 264 (2007).

[130] R. N. Zare, *Angular Momentum-Understanding Spatial Aspects in Physics and Chemistry* (John Wiley & Sons, 1988).

[131] D. Ityaksov, H. Linnartz, and W. Ubachs, *Deep-UV Rayleigh scattering of* N_2, CH_4 *and* SF_6, Molecular Physics **106**, 2471 (2008).

[132] M. Kawasaki, H. Sato, G. Inoue, and M. Suzuki, *Fluorescence lifetimes of SD(*$A^2\Sigma^+$*, v'=0, N') radicals and rotational distribution of SD(*$X^2\Pi_{3/2}$*, v'=0, J') photofragments generated in photodissociation of* D_2S *and* C_2H_5SD *at 193 nm*, The Journal of Chemical Physics **91**, 6758 (1989).

[133] C. M. Western, *PGOPHER, a program for Simulating Rotational Structure, Version 8.0, http://pgopher.chm.bris.ac.uk.*

[134] J. Senekowitsch, H. J. Werner, P. Rosmus, E. A. Reinsch, and S. V. ONeil, *Ab initio calculations of radiative transition probabilities in SH, SH^+, and SH^-*, The Journal of Chemical Physics **83**, 4661 (1985).

[135] G. W. E. Klisch, T. Klaus, S. P. Belov, A. Dolgner, R. Schieder, *The Rotation Spectrum of SH and SD*, The Astrophysical Journal **473**, 1118 (1996).

[136] D. A. Ramsay, *Absorption Spectra of SH and SD Produced by Flash Photolysis of H_2S and D_2S*, The Journal of Chemical Physics **20**, 1920 (1952).

[137] M. Quintero-Pérez, P. Jansen, T. E. Wall, J. E. van den Berg, S. Hoekstra, and H. L. Bethlem, *Static Trapping of Polar Molecules in a Traveling Wave Decelerator*, Physical Review Letters **110**, 133003 (2013).

[138] M. Quintero-Pérez, T. E. Wall, S. Hoekstra, and H. L. Bethlem, *Preparation of an ultra-cold sample of ammonia molecules for precision measurements*, J. Mol. Spec. **300**, 112 (2014).

[139] K. Luria, N. Lavie, and U. Even, *Dielectric barrier discharge source for supersonic beams*, The Review of scientific instruments **80**, 104102 (2009).